



Aalborg Universitet

AALBORG UNIVERSITY  
DENMARK

## Shark - new motor design concept for energy saving-applied to Switched Reluctance Motor

Tataru, Ana Mari

*Publication date:*  
2004

*Document Version*  
Publisher's PDF, also known as Version of record

[Link to publication from Aalborg University](#)

*Citation for published version (APA):*  
Tataru, A. M. (2004). *Shark - new motor design concept for energy saving-applied to Switched Reluctance Motor*. Institut for Energiteknik, Aalborg Universitet.

### General rights

Copyright and moral rights for the publications made accessible in the public portal are retained by the authors and/or other copyright owners and it is a condition of accessing publications that users recognise and abide by the legal requirements associated with these rights.

- Users may download and print one copy of any publication from the public portal for the purpose of private study or research.
- You may not further distribute the material or use it for any profit-making activity or commercial gain
- You may freely distribute the URL identifying the publication in the public portal -

### Take down policy

If you believe that this document breaches copyright please contact us at [vbn@aub.aau.dk](mailto:vbn@aub.aau.dk) providing details, and we will remove access to the work immediately and investigate your claim.

**Shark**  
**-new motor design concept for energy saving-**  
**applied to Switched Reluctance Motor**

by

Ana-Mari Tataru  
Institute of Energy Technology, Aalborg University







## **Preface**

This thesis is submitted to the Faculty of Engineering and Science at Aalborg University in partial fulfilment of the requirements for the PhD degree in Electrical Engineering.

The project was financed jointly by Danish Energy Agency, Danfoss A/S and Grundfos A/S. The project has been followed by two supervisors: Associate Professor Andrew Ewen Ritchie and Associate Professor Peter Omand Rasmussen, both of the Institute of Energy Technology (IET), at Aalborg University. Finn Jensen (Danfoss A/S) was in the steering group until June 2001, whilst Flemming Buus Bendixen (Grundfos A/S) followed the project until year 2003. I would like to thank them all for their guidance and moral support during and after this work.

Special thanks to Dr. Jasmin Corda, of the School of Engineering, at University of Leeds for being closely involved in the development of the analytical model of Shark Switched Reluctance Machine, during the three months spent at University of Leeds, United Kingdom. I would like to acknowledge the support provided by Steven Watkins, University of Leeds, for providing a comprehensible documentation of the Switched Reluctance Machine by investing passion in developing the Brivit database.

My thanks to Associate Professor Orla Nielsen and to Bjarne Kristensen for their patience and extremely good expertise during the manufacturing of the cylindrical and Shark air gap Switched Reluctance Motors and their assistance during the experimental work reported in this thesis.

Aalborg,  
Ana-Mari Tataru

## **Abstract**

The aim of this thesis is to document and promote a relatively new concept of designing electrical machine with improved efficiency, without using more or better material. The concept, called Shark, consists in replacing the cylindrical air gap by a non-linear shape obtained by translating specific geometrical pattern on the longitudinal axis of the electrical machine. This shape modification increases the air gap area and thus the energy conversion, taking place in the machine. Whilst other methods of improving the efficiency consider the use of more and/or better magnetic material and/or optimisation of the magnetic circuit of the radial cross-section of the machine, the proposed method makes use of the longitudinal cross-section of the machine.

In spite of a few reports claiming the improvement of the efficiency by applying the optimisation of the longitudinal cross-section, none analysis of various air gap shapes and of their influence on the magnetic performance has been reported. Due to a simple geometry, the Switched Reluctance Machine has been selected for demonstration of the Shark principle.

Initially, linear and finite element analysis are considered. They provide the basic knowledge of the manner in which various Shark air gap, having different dimensions, influence the energy conversion in the machine. The saturation mechanisms, specific to each Shark profile are analysed and optimum Shark profile and its dimensions are selected for implementation in a demonstration machine.

Due to the lack of quick analysis tools, an analytical model of the Shark Switched Reluctance Machine is also proposed in this thesis. This model is conceived by modifying one of the existing models of cylindrical air gap Switched Reluctance Machines, such as to account for the presence of the Shark profiles in the air gap.

The calculations are verified by measurement on two demonstration machines, having cylindrical and Shark air gaps. The measurement proved the theory right and measurement of efficiencies proved that the Shark air gap improves the efficiency of a specified machine by two to four % point with respect to a corresponding cylindrical air gap machine. Furthermore, the two Switched Reluctance Machines are compared with other motor technologies such as Induction Motor and Brushless DC Motor.

Analysis of the forces produced in the Shark SRM reveals particular aspects, adding some difficulties to assembly the Shark motor. However, the latest assembly technologies provide solution for a simplified assembly of a Shark machine.

Calculations of economical aspects demonstrate a small difference in saving between the Shark Switched Reluctance Motor and the Brushless DC Motor considered in this project.

## Nomenclature

### ▪ Abbreviations

IM	standard efficiency Induction Motor
SRM	Switched Reluctance Motor
CSRM	Cylindrical air gap Switched Reluctance Motor
Shark SRM	Shark air gap Switched Reluctance Motor
BLDCM	BrushLess DC permanent-magnet Motor
HEM	High Efficiency Motor
MEC	Magnetic Equivalent Circuit
FEA	Finite Element Analysis
FEM	Finite Element Model

### ▪ Symbols

$W$	co-energy
$W_{conv}$	converted energy
$\Delta W$	co-energy variation between the converted energy and the sum of the converted and stored energy
$W_f$	stored energy
$P_{in}$	input power
$P_{out}$	output power
$P_{Cu}$	conductive loss
$P_{Fe}$	core loss
$EC$	conversion ratio
ph	number of phases of the machine
$\omega$	speed [rpm]
$S$	number of strokes
$N_{ph}$	number of turns per phase
$R_{ph}$	phase resistance
$I_{rms}$	the rms value of the phase current
$\mu_0$	permeability of the free space
$\mu$	permeability of the iron
$\mathfrak{R}$	reluctance
–	permeance
$u$	instantaneous voltage



$i$	instantaneous current
$\Psi$	flux linkage
$\phi$	magnetic flux
MMF	magnetomotive force
$D_s$	stator outer diameter
$D_{bs}$	stator pole root diameter
$D_{r1}$	rotor diameter
$D_{br}$	rotor pole root diameter
$D_{g(m)}$	mean air gap diameter of the Shark SRM
$D_{s(m)}$	mean stator diameter of the Shark SRM
$D_{r(m)}$	mean rotor diameter of the Shark SRM
$l_{pole}$	circular stator pole length
$\beta_s$	stator pole arc
$\beta_r$	rotor pole arc
$g$	air gap length
$l_{stk}$	stack length
$l_{stk}'$	equivalent stack length
$h_{pole}$	stator pole height of the cylindrical air gap SRM
$n_t$	number of Shark segments
$\beta$	angle at the basis of the Shark profile
$l_{shk}$	Shark tooth pitch
$h_{shk}$	height of the Shark profile
$\delta_t$	reduction of the pole height due to the Shark teeth
$k_w$	fractional reduction of the pole height due to the Shark teeth
$A$	cross-section
$L$	inductance of the magnetic circuit
$k$	inductance gain
$k_w$	energy gain
$H_g$	air gap magnetic field intensity
$H_{sp}$	stator pole magnetic field intensity
$H_{rp}$	rotor pole magnetic field intensity
$H_{sy}$	stator yoke magnetic field intensity
$H_{ry}$	rotor body magnetic field intensity

$k_\phi$	ratio of electrical loading on rotor and stator
$k_e$	emf factor incorporating the winding distribution factor and the ratio between the area spanned by the salient poles and the total air gap area
$k_i$	current waveform factor
$k_p$	electrical power waveform factor
$w_{sp}$	width of the stator pole
$w_{rp}$	width of the rotor pole
$w_g$	width of the air gap
$w_{sy}$	width of the stator yoke
$w_{ry}$	width of the rotor yoke
$A_{sp}$	area of the stator pole
$A_{rp}$	area of the rotor pole
$A_g$	area of the rotor pole
$A_{sy}$	area of the stator yoke
$A_{ry}$	area of the rotor yoke
$l_{sp}$	length of the stator pole flux path
$l_{rp}$	length of the rotor pole flux path
$l_{sy}$	length of the stator yoke flux path
$l_{ry}$	length of the rotor yoke flux path

- Subscripts

0	cylindrical air gap
saw	saw toothed air gap
square	square-wave air gap
ellipse	elliptical air gap
trap	trapezoidal air gap

- Superscripts

u	unaligned rotor position
a	aligned rotor position







## Table of contents

Preface.....	i
Abstract.....	ii
Nomenclature.....	iii
Chapter 1	
1.1 Background and motivation.....	1
1.2 Introduction to the Shark concept.....	4
1.3 Switched Reluctance Motor –working principle.....	6
1.4 Variations of SRM.....	9
1.5 Area of application of SRM.....	11
1.6 Objectives.....	12
1.7 Outline of the thesis.....	14
Chapter 2 Linear analysis of the Shark Switched Reluctance Motor.....	17
2.1 Shark principle.....	17
2.2 Linear analysis of various Shark profiles.....	22
2.3 Discussion and comparison of the analysed Shark profiles.....	34
2.4 Summary and conclusion.....	37
Chapter 3 Finite Element Modelling of Shark Switched Reluctance Motor.....	39
3.1 Objectives and methodology.....	40
3.2 Solving the magnetic field by the means of the Finite Element Analysis.....	41
3.3 Two-dimensional Finite Element Analysis of the Shark Switched Reluctance Motor.....	42
3.4 Analysis of the Shark air gap Switched Reluctance Motor.....	49
3.5 Summary and conclusions.....	72
Chapter 4 Analytical modelling of the Shark Switched Reluctance motor.....	75
4.1 Motivation and objective.....	75
4.2 Analytical calculation-overview.....	77
4.3 Magnetisation characteristic of the Shark Switched Reluctance Motor in the aligned rotor position.....	78
4.4 Magnetisation characteristic of the Shark Switched Reluctance Motor in the unaligned rotor position.....	92
4.5 Energy conversion and optimum Shark configuration.....	100
4.6 Analytical calculation of the static force in Shark Switched Reluctance Motor.....	104
4.7 Summary and Conclusions.....	115

Chapter 5 Measurement and comparison of different motor types.....	117
5.1 Objectives and methodology.....	117
5.2 Experimental arrangements.....	120
5.3 Results of the steady-state tests.....	121
5.4 Comparison of different motor types.....	131
5.5 Summary and conclusions.....	143
Chapter 6 Manufacturing considerations for the Shark Switched Reluctance Motor.....	145
6.1 Motivation and objective.....	145
6.2 Cutting of lamination and lamination stack for Shark Switched Reluctance Motor.....	146
6.3 Assembly solutions.....	151
6.4 Windings.....	154
6.5 Axial mounting.....	155
6.6 Summary and conclusions.....	156
Chapter 7 Summary and Conclusions.....	157
Appendix A Design data of IM, CSRSM, Shark SRM and BLDCM.....	159
A.1 Induction Motor.....	159
A.2 CSRSM.....	161
A.3 Shark SRM.....	163
A.4 BLDCM.....	165
Appendix B.....	169
B.1 Definition of the air gap layers for FEA.....	169
B.2 Error distribution in the air gap.....	170
B.3 Saw-toothed air gap. Flux density distribution in the air gap.....	172
B.4 Square-wave air gap. Flux density distribution in the air gap.....	174
B.5 Trapezoidal air gap. ....	176
Appendix C.....	180
C.1 Langevin function approach.....	180
C.2 Calculation of the winding area.....	181
C.3 Verification of the analytical model for 6/4 SRM.....	183
C.4 Verification of the analytical model for 12/8 SRM.....	184
C.5 Permeance ratio.....	185
C.6 Radial and axial forces.....	185
Appendix D Estimation of the relative prices of different motor technologies.....	188
References.....	189
List of publications.....	199

# Chapter 1

## Introduction

The research documented in this thesis concerns the area of electrical machines design. It deals with a new design concept, which approaches the electrical machine from the viewpoint of the longitudinal cross-section. The proposed analysis is rooted in the intention to produce more torque without using more material. The new concept, which achieves an increase of the air gap area by modification of the cylindrical air gap of a motor to a non-linear shape, was named Shark [1], due to the similarity of the proposed air gap shape and sharks teeth. Specifically, this study is dedicated to the analysis of the Shark concept, to the development of an analytical model and to the comparison of the performance of the proposed Shark machine with those of the usual cylindrical air gap machines.

The interest for the Shark concept is emphasised by the improvements to performance claimed in references [1], [2], [3], [4], [5], [6]. Seen in the context of the international policy to save energy, the Shark concept may be a potential solution to the reduction of energy usage in electrical machines. Therefore, the present study is aimed to provide a step forward for the introduction of this new concept to the manufacturers of electrical machines.

The significance of the Shark concept, in terms of energy saving potential, is highlighted in the first section of this introductory chapter. The Shark concept is then briefly described in order to define the technical framework of the study. Subsequently, the electrical machine selected as the vehicle for demonstration is considered from two aspects. One aspect is the application area, which also gives an idea of the potential applications for the Shark concept. The second aspect regards the working principle of the demonstration machine and the variables to be used in the evaluation of the discussed concept. Variations of the demonstration machine, having as purpose the improvement of the energy conversion, are presented as well.

Based on the above mentioned presentation of the Shark concept the objectives and methodology of the study are defined. An outline of the thesis concludes this introductory chapter.

## 1.1 Background and motivation

Increasing awareness of the finite global energy resources requires a more efficient approach to its use. In this context, governmental regulations impose new standards [7] for more efficient energy conversion in industrial applications. On the other hand, consumer demand for cheap, energy saving products exerts new pressure on industrial manufacturers. Attempting to satisfy these two



demands, producers perform research to investigate potential solutions to promote the sensible use of electricity and to help eliminate unnecessary and costly waste.

Electric motors are the main consumers of electric energy, with applications ranging from large power plant to domestic appliances. In industry about 70 % of the total energy is consumed by motor driven systems [8]. In this context, a new category of electric motors is being promoted on the market. This new category, High Efficiency Motor (HEM), has a higher efficiency than the majority of the motors in current use.

A HEM refers to the ubiquitous Induction Machine (IM), and employs mainly the same manufacturing technology as a standard motor. The improved efficiency is obtained by using better and/or more material and/or by optimising the geometry of the magnetic circuit. However, both methods are expensive. Forecasts of the savings possible if HEM applied are significant [8], [9].

To encourage these changes a new classification of electric motors according to efficiency has been approved by CEMEP<sup>1</sup> and the General Directorate for Energy within the European Commission, ranking them according to the efficiency [7], [9]. This distributes the motors into three groups: standard efficiency motors (**Eff3**), improved efficiency motors (**Eff2**) and high efficiency motors (**Eff1**) as shown in Fig.1.1 for 2 and 4 pole Induction Machines. Moreover, the manufacturers were committed to reduce the market share of Eff3 motors by at least 50 % by December 2003 [7].

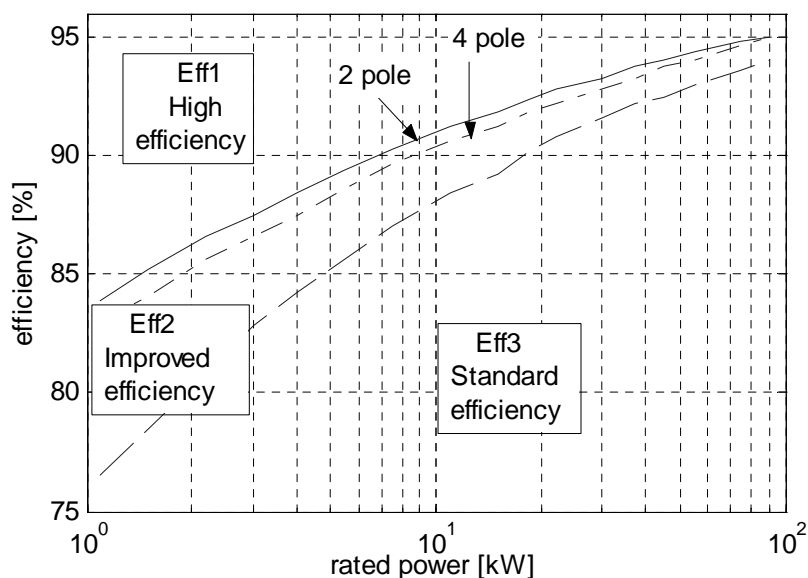


Fig.1.1 Classification of electric motors according to their efficiency [7]

As an extension of these regulations, the Danish Energy Agency (DEA) introduced its own programme for energy saving. The power range included in the DEA efficiency table for energy-saving motors (Table 1.1) was increased to include motors rated at 0.55 [kW] instead of the IEC version, which stops at 1.1 [kW], because motors rated at less than 1 [kW] generally exhibit a lower efficiency than those rated at 1 [kW] or more. Additionally, very large numbers of these small machines are in use in domestic and office equipment. Therefore, any potential improvement of the efficiency of these small motors makes a large difference to global energy consumption.

<sup>1</sup> European Committee of Manufacturers of Electrical Machines and Power Electronics

Table 1.1 Full load efficiencies for High Efficiency Motors with 2 and 4 poles, according to the Danish Energy Agency

Power [kW]		0.55	0.75	1.1	1.5	2.2	3	4
Efficiency (%)	2 poles	80	81	81	82	84	85	86
	4 poles	77	78	78	80	82	84	86
Power [kW]		5.5	7.5	11	15	18.5	22	30
Efficiency (%)	2 poles	87	89	90	91	92	92.5	93
	4 poles	87	88	90	91	92	92	92.5
Power [kW]		37	45	55	75	90	110	
Efficiency (%)	2 poles	93.5	94	94.5	95	95.5	96	
	4 poles	93.5	94	94.5	95	95.5	96	

The topic of energy saving must be approached carefully. Attention must be paid to the fact that improved efficiency does not necessarily means a large energy saving. When considering efficiency and potential energy savings, four facts must be taken into consideration:

- the efficiency of electric machines increases with the power rating as it may be seen in Fig.1.1. This allows more room for improvement in low power motors
- low power motors represent a large proportion of motors in use as may be seen in Fig.1.2 for the USA [11]. A similar situation applies in all developed countries [7]
- the main energy consumers are the large motors as the diagram in Fig.1.3 indicates it, many motors are not operated at full load

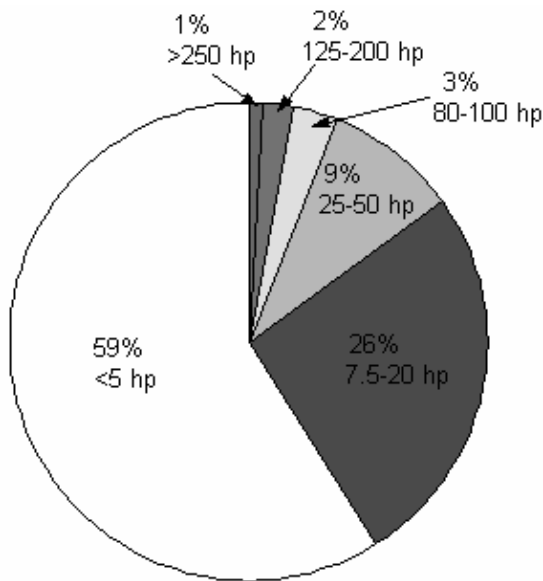


Fig. 1. 2 Motor distribution in USA [11]

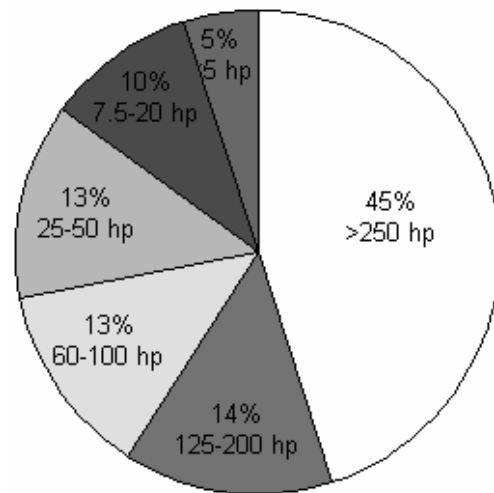


Fig. 1. 3 Energy consumption distribution in USA [11]

Analysis of induction motor efficiency curves reveals that there is a large potential for improvement of the energy conversion process for motors rated in the low power range. Therefore fact (a) considered with the large number of small motors in use (b), may support the idea that the motors rated in the low power range may also afford the main resources for potential energy saving. However, things prove to be different. As already mentioned in (b) and (c), large motors are actually the main energy consumers, despite the lower proportion of the total existing motors in use. The small motors, even though they are greater in number, have the lowest energy consumption.

This fact negates the previous suggestion that small motors should be main focus for energy saving. The energy consumption depends on various factors such as: rated power range of the motor, efficiency, annual operating time of the equipment, load<sup>2</sup> factor and usage<sup>3</sup> factor of the motor. Small motors, although they are sold in large numbers, usually have a lower usage factor than motors rated in the higher power range. This contributes to their lower energy consumption over a defined period. Therefore, more energy may be saved by a slight improvement of the efficiency of large motors than by a significant efficiency improvement of small motors.

In spite of all the international actions intended to promote the use of HEM and in spite of general demand for energy saving products, the market is still reluctant to make changes. The increased initial purchase cost necessary for HEM, caused by the use of improved or more material and by the increased quality of manufacturing, is at the root of this paradox. The selection of a motor by a purchasing agent is dominated by the purchase price and not by the potential lifetime cost saving made possible by the use of HEM. It is often forgotten that the purchasing price represents less than 5% of the lifetime cost of the motor [7]. To encourage the HEM market a subsidy of up to 30% of the HEM price is offered in Denmark [7].

In some reports [12], it is argued that an E-motor (electric motor with incorporated electronics) may bring more advantage than an HEM. This may be true, but any gain in inherent motor efficiency may be valuable for energy saving. The interest of this thesis is restricted to improvements related to the efficiency of the motor itself.

In this introductory section was shown that the general tendency is to reduce the energy used by electric motors because they represent an important energy consumer in industry. To do so new standards were approved by CEMEP and high efficiency motors are promoted on the market. Generally, a better efficiency is achieved by using better or more magnetic material or by optimisation of the radial cross-section of the electric motor. Both methods are expensive. Therefore, consideration of the longitudinal cross-section of an electric motor may further improve the performance of the electric motor or may be considered as an alternative solution to the two methods mentioned above. This new concept was named Shark concept and is introduced in the following section.

## **1.2 Introduction to the Shark concept**

Although the development of electrical machines has long been a well-established commercial enterprise, design investigations and innovations are still in progress. The concept of HEM involves the use of better quality or of more material and optimisation of the magnetic circuit. A tremendous amount of research work dedicated to the optimum design of electrical machines has revealed that the material distribution within the machine is one of the key elements for improving the machine performances.

A common way to improve the design of an electrical machine is by optimisation of the radial cross-section [13], [14], [15]. This is governed by considerations relating the cost of manufacture to the improvement brought by the new geometry of the machine.

---

<sup>2</sup> The load factor is that fraction of the rated load, at which the motor is normally loaded

<sup>3</sup> The usage factor is that fraction of time when the motor actually operates

The magnetic capability of the longitudinal cross-section has not been considered until recently. This new design perspective considers the transformation of the cylindrical air gap (Fig.1.4) into an air gap shaped by the translation of a regular geometrical pattern along the length of the lamination stack as shown in Fig.1.5.

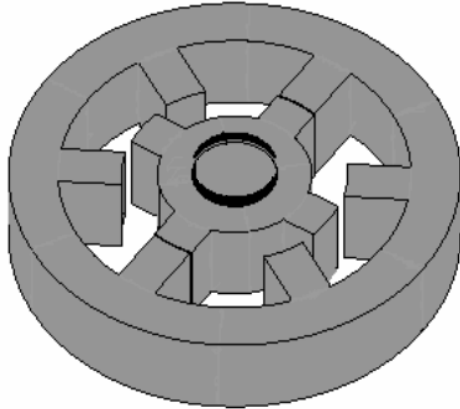


Fig.1.4 Cylindrical air gap SRM

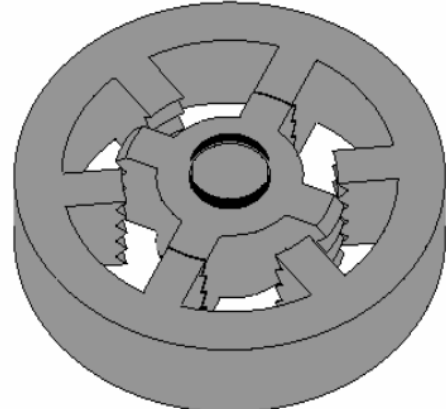


Fig.1.5 SRM with Shark air gap

The ultimate goal of this modification is to improve the conversion of energy by increasing the area of the air gap. The main point is that this goal is reached without using more magnetic material, but simply by redistributing the material between the stator and the rotor bodies. This new philosophy combines the advantages of both axial and radial air gaps [2] and has been called 'Shark' [1]. The geometrical pattern repeated along the length of the machine will be called Shark tooth/segment/profile throughout this work. The Shark profile may take various shapes, the selection being limited only by manufacturing possibilities and cost. Although the Shark concept may, in theory, be applied to any type of electrical machine, in practice this proves difficult. Some configurations of electrical machine, with Shark air gap, present assembly difficulties as it may be imagined by considering Fig.1.5. There are two main problems: the insertion of the rotor stack and the insertion of the windings into slots. Among the existing motor types the Switched Reluctance Motor (SRM) has the simplest magnetic circuit and allows an easier implementation of the Shark concept now when no technological documentation is available. The constructional advantage provided by the concentrated windings, which may be easier to assemble in a Shark Switched Reluctance Motor compared to the distributed windings commonly used in Induction Machines, where assembly may even be impossible. For these reasons it was decided to use the Switched Reluctance Motor as a demonstrator in this work.

### 1.3 Switched Reluctance Motor – working principle

Before developing the theory of the Shark principle, the foundation of the study must be clearly defined. Therefore, the working principle of the SRM is considered in this section. In subsequent discussions, the energy conversion process is described in relevant terms suitable for modelling the effects of the Shark configuration on the performances of the machine. This effect is believed to be dependent on the flux linkage, inductance and converted energy. The magnetisation characteristics and the torque production mechanism are also discussed in this section.

The Switched Reluctance Machine is considered to have the simplest construction and working principle of all rotating electric machine types. The basic structure of an SRM comprises salient stator and rotor poles as shown in Fig.1.6. A coil is wound around each stator pole and no windings or magnets are located on the rotor. Because of this simple configuration, the SRM may be cheaper to manufacture than any other type of electrical machine [44].

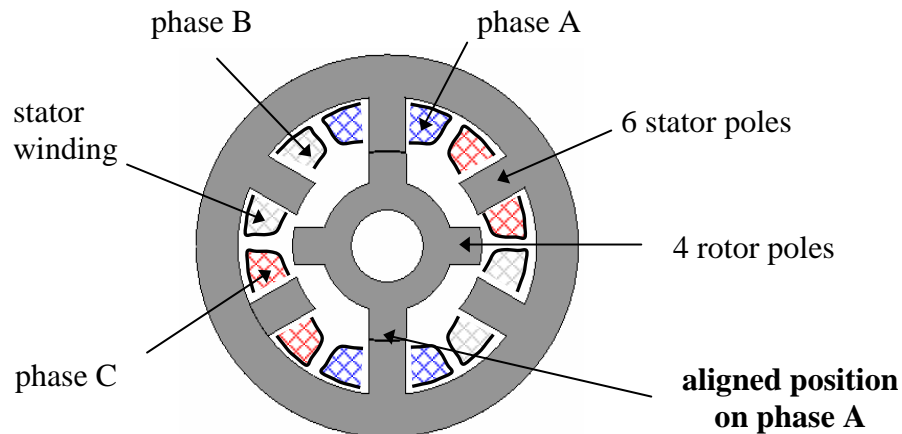


Fig.1.6 Basic structure of the SRM

The operation of the SRM is based on the tendency of the rotor poles to align with the excited pair of stator poles. Taking as origin of the movement the unaligned rotor position illustrated in Fig.1.6, a voltage is supply to phase B or phase C depending on the direction of movement when the rotor is in the position known as **turn on angle**. This makes that the rotor moves such as the rotor and the excited stator pole pairs are aligned. When the rotor is in a position known as **turn off angle**, the supplied voltage is removed from the excited coil and switch to a neighbour coil. By successively switching the supply voltage from one coil to another, the continuous movement of the rotor is assured. Some characteristic definitions used to describe the operation of the SRM are:

- **The aligned position.** This is where a pair of rotor poles is aligned with one pair of stator poles (see Fig.1.6)
- **The unaligned position.** This is where a pair of stator poles is aligned with an interpolar axis of the rotor
- **The corner position.** This is where rotor and stator poles are about to overlap
- **The turn on angle** is the position of the rotor at the time when the electrical supply is applied to the corresponding phase. This is measured from the unaligned rotor position.
- **The turn off angle** is the position of the rotor at the time when the electrical supply is removed/ reversed from the corresponding phase. This is also measured from the unaligned rotor position.

The description of the working principle of a SRM is best explained using the magnetisation characteristic. The magnetisation characteristic or flux linkage as a function of the current (Fig.1.7) is a diagram describing the magnetic flux induced in a specific configuration of magnetic circuit by a steady-state electrical current flowing through the excitation windings. One magnetisation characteristic may be drawn for any rotor position.

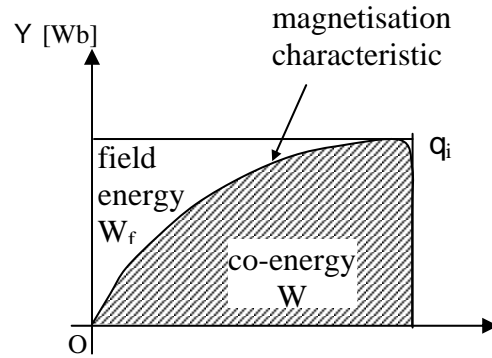


Fig.1.7 Illustration of the magnetisation characteristic, co-energy and field energy

The magnetisation curve depends on the magnetic properties of the material (permeability and saturation flux density) and on the geometry of the magnetic circuit (air gap length, etc.). It also characterises the energy stored in the magnetic field for any rotor position,  $\theta_i$ , and for any excitation current. This stored energy is denoted by  $W_f$  in Fig.1.7 and may be determined mathematically as follows:

$$W_f = - \int_0^Y i \times dY \quad (1.1)$$

The co-energy, which is complementary to the field energy has no physical significance but it helps in simplifying the calculation. It may be defined as follows:

$$W = \int_0^i Y \times di \quad (1.2)$$

The instantaneous torque may be determined by considering an infinitesimal rotation of the rotor between two positions  $q_1$  and  $q_2$ . The energy stored in the magnetic circuit in position  $q_1$  is equal to the area  $0AA'$  in Fig.1.8. During the displacement between  $q_1$  and  $q_2$ , energy is supplied to the magnetic circuit, represented by the area  $A'ABB'$ . Only a fraction of this energy is converted into mechanical energy during the actual movement. The remainder of the supplied energy remains stored in the magnetic circuit or is returned to the source if the excitation supply is removed.

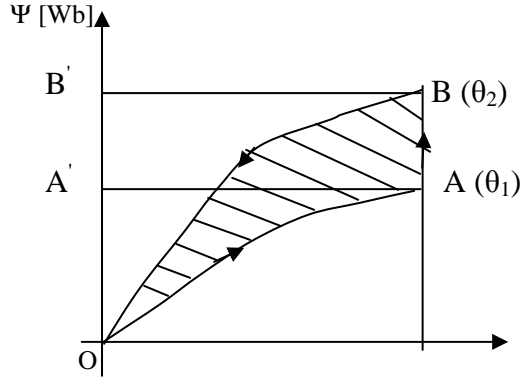


Fig.1.8 Typical energy conversion loop for a small displacement from  $\theta_1$  to  $\theta_2$

The process of conversion of the energy may be described by the following equation:

$$OAA' + A'ABB' - OBB' = OAB \quad (1.3)$$

where:  $OAA'$  is the stored energy in position  $\theta_1$ ,  $A'ABB'$  is the energy supplied from the source,  $OBB'$  is the stored energy in position  $\theta_2$  and  $OAB$ , the difference between the two, is the energy converted to mechanical energy.

The instantaneous torque developed during the rotation from  $\theta_1$  to  $\theta_2$  may be mathematically described by the following equations:

$$T = - \left[ \frac{\partial W_f}{\partial \theta} \right]_{\Psi = const} \quad (1.4)$$

and in terms of co-energy, which is complementary to the field energy:

$$T = \left[ \frac{\partial W}{\partial \theta} \right]_{i = const} \quad (1.5)$$

Ideally, the current should flow through the windings at the point when the inductance of the magnetic circuit begins to increase. This point is close to the corner position. An example of a conversion loop in an SRM is presented in Fig.1.9. Here it may be seen that the turn on angle should be selected to be after the unaligned position and the turn off angle should be selected to be before the aligned position. Selecting the turn off angle to be before the aligned position avoids a period of production of generating torque, because the inductance of the magnetic circuit begins to decrease with the increasing rotor angular position.

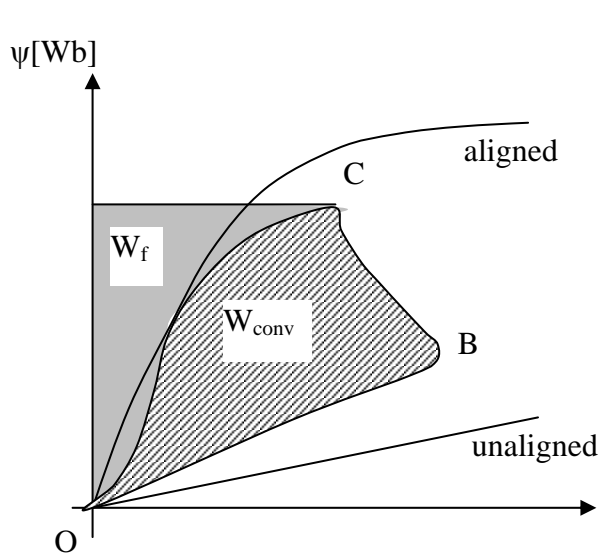


Fig. 1.9 Conversion loops for the SRM illustrating the main points used in controlling the SRM

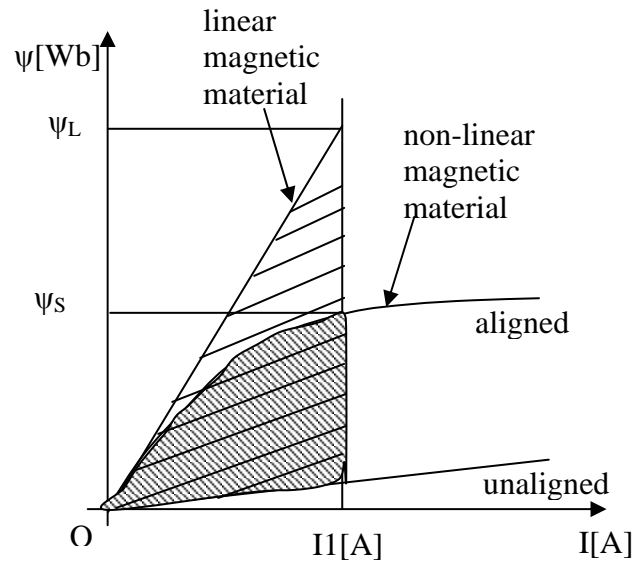


Fig. 1.10 Illustration of the energy conversion loop for SRM with linear and saturating material

The conversion efficiency may be characterised by the conversion ratio [45], defined as the ratio of the converted energy to the sum of the converted and stored energy. This relationship may be also thought of as the power factor of the machine.

$$EC = \frac{W_{conv}}{W_{conv} + W_f} \quad (1.6)$$

Magnetic saturation plays an important role in the SRM. Its influence has been discussed in various papers. Among them [46] provides an analysis that compares two SRM: one made of ideal linear material and the other made of saturating material. The ideal energy conversion loops are shown in Fig.1.10, drawn under the assumption of a constant current flowing through the windings. It was demonstrated in [46], that the machine with linear material produces more torque than that with saturating material, at the expense of a higher apparent power rating. From the loops presented in Fig. 1.10, it may be determined that the energy conversion ratio  $EC$  may be a maximum of 0.5 in the case of the linear material and greater than 0.5 in the case of the saturating material. A conversion ratio of unity may be achieved in the case of the ideal saturating material.

As the real materials used in electrical machines exhibit saturation, careful attention must be paid to this. The effect of saturation of the magnetic circuit on the produced torque is such that more torque may be produced in a machine whose magnetisation characteristics approach those of the SRM with ideal saturating material. This means that a material or magnetic circuit, which saturates at a low value of current, is desirable in the SRM.

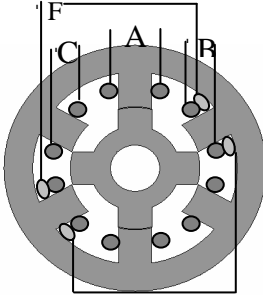
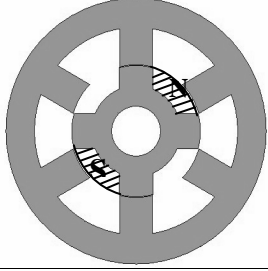
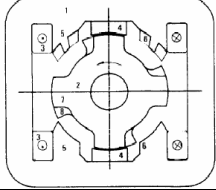
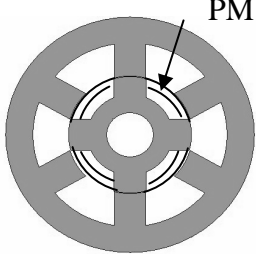
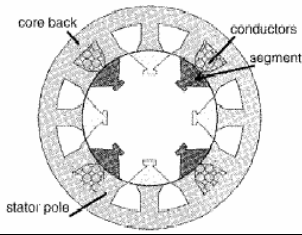
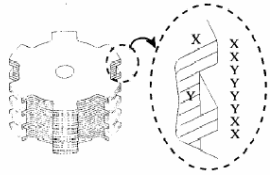
## 1.4 Variations of SRM

It is a continuous challenge to improve the performances of the SRM. This goal may be achieved by parametric optimisation or by proposing a completely new configuration. As the present work



deals with a combination of the two solutions a brief study of the design proposed so far may be of interest. In table 1.2 some variations of SRM are illustrated and their improvements are specified.

Table 1.2 Illustration of various configurations of SRM

1	SRM with DC assisted excitation [47], [117], [118]		This variation of SRM pushes the conversion loop in the region of high saturation where the energy ratio is close to 1. However, it does not use effectively the copper of the machine.
2	Hybrid type SRM [48]		Produces additional torque by the presence of the permanent magnets
3	PM-biased SRM [49], [119]		Additional torque is produced by PM
4	Screens in SRM [50], [120], [121]		Reduces the unaligned inductance but the performance depends on the diffusion time of the eddy current induced in the screen
5	SRM with segmental rotors [51], [52]		This variation of SRM utilises better the phase MMF
6	SRM with both radial and axial air gap [2]		This variation increases of the air gap surface

## 1.5 Area of application of the SRM

The area of application of the SRM is extending at present. The SRM offers some attractive features compared to other types of electrical machines. These are summarised below:

- The stator is easy to wind, and has short end windings which reduces the winding resistance turns [16], [17]
- No windings or magnets fitted on the rotor
- strong, stiff rotor construction offers potential for high speed applications
- inherent fault tolerance is caused by that the phases are decoupled electrically [16], [18], [19], [20], [21], [107]
- simple to wind stator coils cost vs. efficiency favourable relative to other motors, including BLDCM [44].
- Rugged construction of the SRM is suitable for application in harsh environments (vibration, temperature, low risk of sparks) [39], [41].

Despite the constructional advantages, the SRM has some weak points such as high torque ripple and high level of noise and vibration. Although the torque ripple and the high vibration level are often cited as main disadvantages of the SRM drive, solutions to solve these problems have been proposed [22], [108], [109], [110].

To establish the area of application of the design alternative proposed in this thesis, the Shark concept, a brief account of some recent application proposed for the SRM is given in the following paragraph. Due to the previously mentioned advantages, the applications of the SRM may become more numerous, as the unwillingness of the consumers to apply SRM drives begins to die away. The trend for SRM application may be toward niche sectors where general solutions are not desirable.

Worldwide research in SRM technology is conducted in the following subjects:

- Magnetic levitation, where linear SRM drive system is used [23]
- Automotive applications [24], [25], [26], [27], [28], [39]
- Industrial transportation [29], [30], [31]
- Wind energy, where the SRM is used as generator [32], [33]
- Pumps [34], [35], [10]
- Aerospace industry [34], [35], [36], [37], [40].

In addition to research activity, the SRM technology has also found its way to production. The latest known production applications are summarised below:

- S R Drives, now a division of Emerson Electric Co. provides SRM technology for various applications [39], [41] such as:
  - Beckman Instruments Inc, laboratory centrifuge system
  - Flameproof drive system for potentially explosive atmosphere (150kW DIAMOND Drive underground at Malby Colliery, UK)
  - BESAM sliding door operating system
  - CompAir Broomwade Limited, screw air compressors

- Maytag, washing machine
  - Smallfry, food processor
  - Air conditioning system for passenger train
  - Picanol, weaving machine
  - Ametek, Infin-A-Tek, vacuum cleaning system
  - NORDIC door ab, unit for high speed roller door
- EMOTRON [42] has developed the EMS-VVX SRM drive for ventilation systems
  - RADIO-ENERGIE [39] has developed low voltage SRM drives with power in the range 0.7-2 kW at 3000 rpm for forklifts trucks and light electric vehicles.
  - LG Electronics [43] has developed vacuum cleaner and air conditioner with SRM technology.

## 1.6 Objectives of the study

In this section, some ideas related to the Shark principle and its fundamentals are briefly reviewed, in order to define the objective of this work. As it was previously explained, the Shark principle provides a solution for further improvement of the efficiency of an electric motor. It is a design solution, that extends the conventional approach based on the radial cross-section of the motor. The Shark principle improves the magnetic circuit of a given motor by the modification of the longitudinal cross-section. In Fig.1.5, it was shown that the cylindrical air gap machine could be modified by the addition of a longitudinal geometric pattern (Shark tooth) of various shapes.

The resulting structure has a larger energy conversion area in the air gap of an electric machine, without the addition of more material. It acts by simply redistributing the existing material within the machine. Very few publications [1], [2], [3] claim, that the Shark profile provides magnetic benefits, hence the value of a detailed study of the Shark principle. Based on these considerations one objective of this study is:

**To analyse the Shark concept and to study whether it is a valid solution for improvement of the efficiency in electrical machines.**

It is also of interest to find out how a motor with Shark air gap, compares to other motor types in use. Therefore, it was decided to include a comparison of various motors, including also the motor types, including the motor with Shark air gap. This provides a useful basis on which to compare the efficiency of various types of energy conversion. So the second objective is:

**To compare various types of electric motors: Induction Motor, Switched Reluctance Motor with cylindrical air gap, Switched Reluctance Motor with Shark air gap and Brushless DC at similar working conditions**

Based on these two objectives the methodology used was as follows. To facilitate the comparative analysis, all motors were designed to be built in the same frame, for the same rated output power, achievable at similar working points defined by the (torque-speed) pair. From this point of view the initial data of the motors built and tested in this project are: Grundfos frame MG 71, output power  $P=0.55[\text{kW}]$ , rated speed  $\omega=2800 [\text{rpm}]$  and rated torque  $T=1.92 [\text{Nm}]$ .

To achieve the first objective, the SRM was selected as demonstration machine, due to its simple construction. A cylindrical air gap SRM was first designed and manufactured. Then Shark SRM was manufactured based on the geometry of the CSRSM, by modifying the shape of the air gap. In this way, the magnetic circuits of the two machines differ only in the shape of their air gaps.

The Shark structure adopted in the Shark SRM was obtained after optimisation with Finite Element Analysis. In order to ease the analysis for other ranges of Shark SRM an analytical method was also developed.

The list of the task to be achieved during this work is as following:

### **1.6.1 Parametric analysis**

The first step of the study was to make a parametric analysis of the Shark profile. The method was to analyse different Shark profiles and obtain a family of characteristics that may facilitate optimisation of the structure. The air gap length of the Shark SRM was maintained constant along the air gap region. The method included a theoretical approach followed by FEA. The FEA provides information about the field distribution, which helps in understanding the manner in which the Shark structures behaves. This step was to avoid a study of different Shark configurations using different prototypes, which was too expensive and time consuming.

### **1.6.2 Analytical tool development**

The next step was to develop an analytical tool, able to model the behaviour of a Shark structure quickly. This proved to be difficult, as the non-linearity of the machine with cylindrical air gap is emphasised by the presence of the Shark profile. The data provided by the FEA, where different configurations may be investigated, were used to verify the results of the analytical work.

### **1.6.3 Validation of the Shark principle**

Of course, any theory or simulation has to be validated by measurements on a demonstration machine. Therefore, the manufacture of a demonstration machine was a necessary part of this project. In order to prove the theory, the Shark SRM performances were compared with those of the cylindrical SRM.

### **1.6.4 Comparison with other existing motors (IM, BLDCM)**

Once the Shark SRM was analysed and compared with the CSRSM, the question of its performance in relation to the IM and BDCM arose. Therefore, four motors of different types, with the same power rating (IM, CSRSM, Shark SRM and BLDCM) were tested at defined working points.

### 1.6.5 Technological considerations

In Fig.1.5, it is shown that, due to assembling difficulties, this principle is not easy to apply in any type of electric machines. Among the existing electrical machines, the SRM with its simple configuration was selected as demonstration machine. A 3 phase 6/4 SRM, having output power of 0.55 [KW] was preferred for prototyping because of the experience gained over time at Aalborg University with SRM in this power range.

### 1.7 Outline of the thesis

The thesis is prepared in two main parts as shown in Fig1.9. The first part is dedicated to the analysis and development of the Shark structure while the second part is focused on comparison criteria, performance indicators and manufacturing considerations.

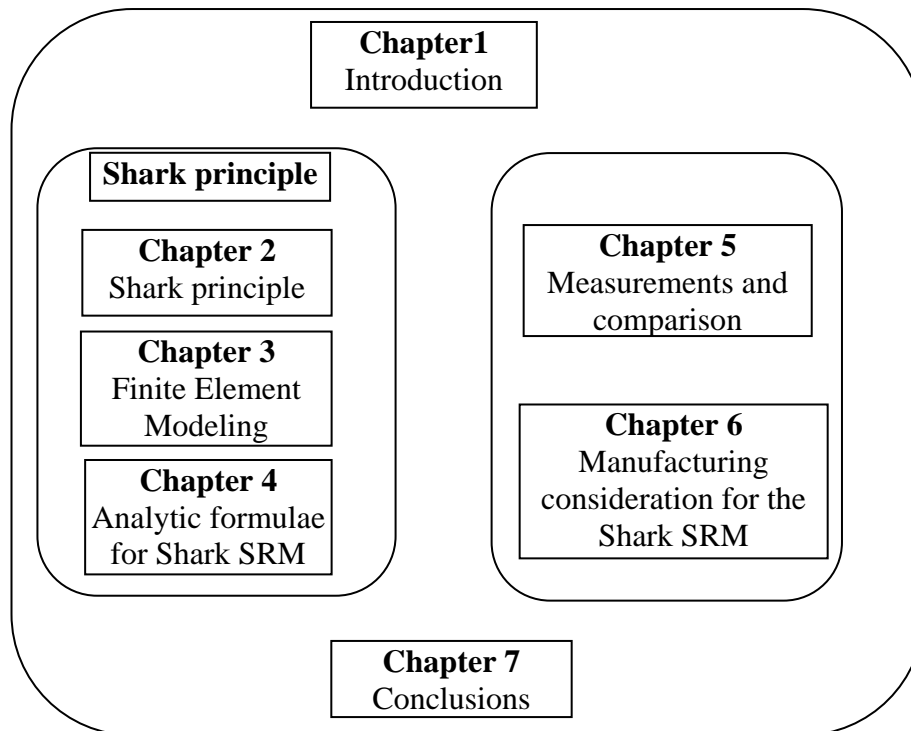


Fig 1.9 Overview of the thesis

**Chapter 1, Introduction** provides the background and terminology of the thesis. The working principle and the applications of the SRM, chosen as demonstration machine are discussed here. The chapter contains the motivation of the study, defines the objectives of this work and present the overview of this report.

**Chapter 2, Theoretical approach of the Shark concept** introduces the Shark SRM principle. A simplified linear approach leads to a preliminary assessment of the performances of the Shark concept.

**Chapter 3, Finite Element Analysis of the Shark Switched Reluctance Motor** presents the 2D Finite Element model of the axial cross-section. The data are processed in order to obtain improved the knowledge of the Shark structure behaviour. Analysis of different Shark teeth shapes is performed and the optimum configuration is selected as a compromise between the desired performance and the electrical and manufacturing constraints.

**Chapter 4, Analytic model of the Shark Switched Reluctance Motor** continues the study of the Shark concept using analytic analysis, thus avoiding the time consuming FEA. A better understanding of the structure may also be provided by studying an analytical expression where the type of dependence of the output parameters (flux, torque, axial forces) on the geometrical dimensions of the structure may be identified. Validation of the analytic formulae is performed using measurement results and FEA data. This chapter concludes on the accuracy of the analytical models and on the optimum Shark configuration to be implemented in a demonstration machine.

**Chapter 5, Measurement and comparison** The measurement performed on the four types of electrical machines (IM, CSRSM, Shark SRM, BLDCM) and the results obtained are presented and compared. Each motor is first discussed and in the end the results are combined to give a general comparison approach.

**Chapter 6, Manufacturing considerations for the Shark SRM** In this chapter are identified the particular problems generated by the assembly of a Shark structure. Some solutions are also suggested for easier methods of assembly.

**Chapter 7, Summary and conclusions.** This chapter summarises the thesis and presents suggestion for further investigations. The objectives of the study are evaluated in order to conclude this work.

**Appendix A Design data of the Induction Motor, cylindrical air gap Switched Reluctance Motor, Shark Switched Reluctance Motor and Brushless DC Motor.** Appendix A contains sections dedicated to each of the four motors considered for analysis. In each section the design data are specified.

**Appendix B Finite element analysis** This appendix contains comments and curves referring to Chapter 3.

**Appendix C Analytical models** This appendix contains comments and data referring to Chapter 4.

**Appendix D Estimation of the motor prices** In this appendix, general expression for estimating the price of a motor is provided.



## Chapter 2

# Linear analysis of the Shark-Switched Reluctance Motor

Shark – is in the present context the name of a new concept of designing electrical machines. This concept breaks the tradition of the purely cylindrical design, concentrated on the radial cross-section, and considers the machine also from the perspective of its longitudinal cross-section ( row 6 in table 2.1). The air gap shape is modified by redistributing material between the stator and the rotor bodies. The resulting configuration has the merit that it increases the area of the air gap and consequently improves the energy conversion. As shown in the previous chapter, saturation of the magnetic material plays an important role for the performances of the SRM. In the case of the Shark SRM, this phenomenon is emphasised by the specific shape of the air gap.

In order to present the way in which the Shark concept works, a linear analysis is considered initially. The first section of this chapter is dedicated to the magnetic field and energy conversion in the Shark air gap. Initially a review of the published literature concerning the Shark configuration is presented. Subsequently, various Shark profiles are presented and analysed under the assumption of linearity of the magnetic properties of the steel. Finally, the Shark profiles are evaluated based on criteria to be defined in the chapter and the Shark profile with the best magnetic properties is selected, assuming linear conditions.

### 2. 1 Shark principle

This section is dedicated to linear analysis of the Shark concept. Initially, the Shark principle is introduced and the variables that describe the geometry of the Shark air gap are defined. Then the discussion focuses on analysis of the proposed principle under the assumption of linearity of the magnetic material. The criteria used for evaluation are defined and simple expressions for the variables used to characterise each of the studied configurations are determined. The conclusions arising from the comparison of various Shark profiles are evaluated at the end of the section.

#### 2.1.1 Literature review

There are only few publications about this type of non-linear configuration of the air gap [1], [2], [4]. In [2], a single phase SRM is considered, with the air gap shape shown in row 6 of Table 2.1.



The analysis of this structure encouraged the authors to claim that the SRM with a toothed air gap exhibits an efficiency some 10 [%] bigger than that of an equivalent cylindrical air gap SRM.

In [1] the Shark concept is initially studied by the means of a simple structure, as shown in Fig.2.2. The air gap of this model has a saw-toothed profile. Measurements on this model showed that such a configuration exhibits increased air gap permeance and lower acoustic noise, compared to the model of Fig.2.1, with cylindrical air gap. The same paper also presents a prototype SRM with toothed air gap, as shown in Fig.2.3. As for the air gap shape design of the Fig.2.3 motor was not optimised, the measured results did not reach the predictions for torque production. However, the static measurement of the flux linkage characteristics indicated that for similar excitation conditions, the flux linkage is higher, than in the cylindrical air gap SRM, as long as the material does not saturate. The authors concluded that optimisation is necessary in order to reap all the benefits of adopting such a structure.

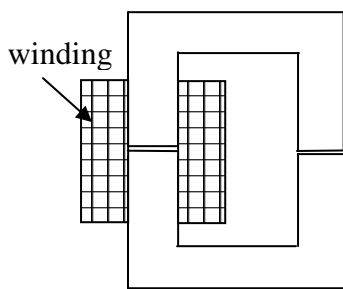


Fig. 2. 1 Cylindrical air gap structure [1]

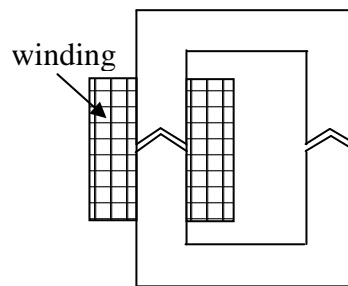


Fig. 2. 2 Simplified Shark structure [1]

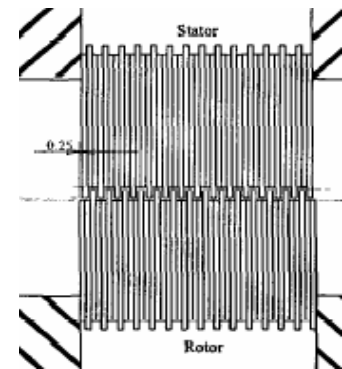


Fig. 2. 3 Toothed air gap Shark SRM [1]

Despite the improved performances measured on different Shark structures a detailed study of the Shark configuration has not yet been reported. In the present work, a step-by-step analysis is conducted. The first step consists of a simplified analysis assuming linear magnetic material properties. To introduce the subject, the Shark configuration is presented and the main geometric parameters are defined.

### 2.1.2 Shark configuration

The terms used in the analysis of the Shark SRM are defined in this section. The geometric conditions and the electromagnetic assumptions are discussed and the evaluation criteria are defined.

#### Geometric conditions

The philosophy of the Shark concept is an extension of the geometry of a cylindrical air gap SRM (CSRSM), shown in Fig.2.4. The main geometric dimensions of the CSRSM, as defined in Fig.2.4, are:  $D_s$  – stator outer diameter,  $D_{bs}$  – stator slot bottom diameter,  $D_{r1}$  – rotor diameter,  $D_{br}$  – rotor bottom diameter,  $l_{stk}$  – length of the lamination stack,  $g$  – air gap length in the aligned position and  $(g_i+g)$  – air gap length in the unaligned position.

The Shark SRM, illustrated in Fig.2.5, is obtained by redistribution of the magnetic material between the stator and the rotor bodies. This means that a certain amount of material is removed from the stator in order to shape the Shark profiles of the stator body. The same amount of material is added to the rotor in order to form the Shark profiles of the rotor body. This process is carried out keeping the main dimensions of the radial cross-section unchanged, except the rotor diameters. Whilst the original dimension  $D_{r1}$  remains unchanged, an additional dimension,  $D_{r2}$ , which helps in specifying the Shark profile, is defined. It is worth mentioning that the Shark teeth may be generated inwards or outwards on the rotor body. The second configuration is used throughout this work. Even if the air gap area were to be identical in the two cases, as the width of the poles is kept unchanged, the unaligned inductance will be slightly increased by the Shark air gap, reducing the benefit of the Shark air gap.

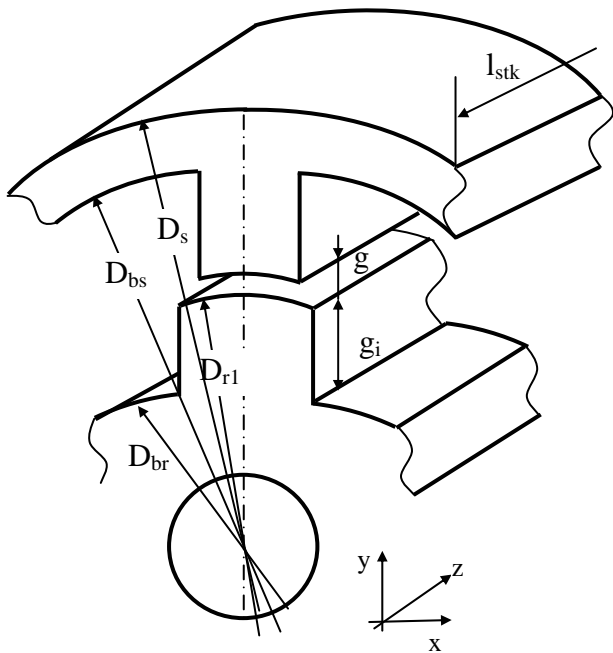


Fig.2.4 View of a CSRSM

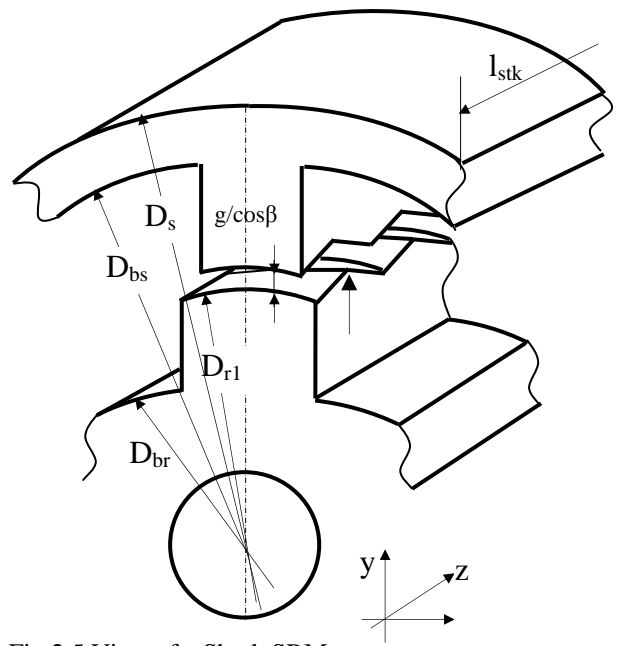


Fig.2.5 View of a Shark SRM

The main geometrical dimensions remain unchanged. This means that:

- the stack length,  $l_{stk}$ , of the Shark SRM is the same as in the equivalent CSRSM
- the stator diameter,  $D_s$ , of the Shark SRM is the same as in the equivalent CSRSM
- the air gap length,  $g$ , of the Shark SRM is the same as in the equivalent CSRSM

Under these conditions, the core volumes of the CSRSM and Shark SRM are identical, defined as:

$$V_{core} = \pi \cdot \left( \frac{D_s}{2} \right)^2 \cdot l_{stk} \quad (2.1)$$

The amount of material used in the two motors was also identical as the Shark structure is obtained simply by redistributing the iron material between stator and rotor. No material was added or removed from the machine. The excitation circuit of the two motors is assumed to comprise similar

coils, which means an equal number of turns per pole, the same conductor diameter and consequently the same quantity of copper. The geometric conditions of the analysis may be summarised as follows:

- the two motors have identical stack lengths
- the two motors have identical main dimensions (see Fig.2.4 and Fig.2.5)
- the two motors have identical lengths of the air gap
- the two motors contain the same amount of material (iron and copper)

### Methodology of the Analysis

The geometrical pattern, which is longitudinally translated to form the Shark air gap, is called Shark tooth/profile/segment and it may adopt various shapes. A study of the effect of applying these shapes was performed for the aligned rotor position in this section. The sections considered are illustrated in: Fig.2.6, Fig.2.7, Fig.2.8 and Fig.2.9. Each of these Shark profiles is defined by the following dimensions:  $l_{shk}$  – Shark tooth pitch,  $h_{shk}$  – height of the Shark profile, angle  $\beta$  and  $g$  – the air gap length. The air gap length is assumed to be constant for all Shark profiles considered. For some configurations, e.g. as the square wave, the length of the air gap may have different values in the radial and longitudinal directions, as shown in Fig.2.8. The trapezoidal version requires an additional parameter,  $l_{top}$ , expressed as a fraction  $k$  of the tooth pitch,  $l_{shk}$ .

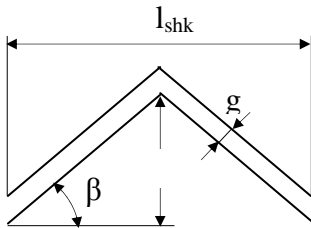


Fig. 2. 4 Saw-toothed profile showing characteristic dimensions

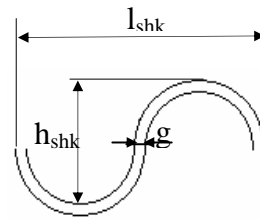


Fig. 2. 5 Elliptical profile showing characteristic dimensions

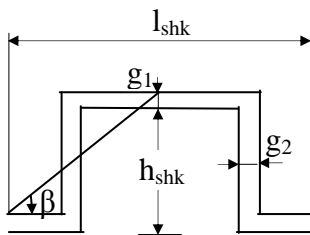


Fig. 2. 6 Square-wave profile showing characteristic dimensions

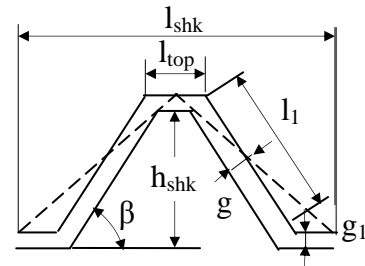


Fig. 2. 7 Trapezoidal profile showing characteristic dimensions

This study is performed using on the theory of the equivalent magnetic circuit [53]. The differential permeance of a layer of thickness  $dy$  with flux crossing the area  $l \cdot dy$ , shown in Fig.2.8 is given by the expression:

$$dG = \mu \cdot \frac{l \cdot dy}{w(y)} \quad (2.2)$$

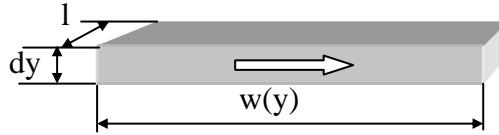


Fig. 2. 8 Illustration for differential permeance calculation

Using equation (2.2), the permeance of the magnetic circuit may be calculated in the aligned position for each of the Shark profiles considered. All these calculations are valid under specific assumptions, which are discussed in the following paragraph.

### Assumptions used in the magnetic circuit calculations

The objective of this chapter is, as stated to make a linear analysis and comparison of various Shark profiles. In order to achieve this objective some assumptions were made. First of all the iron was considered to have linear magnetic properties. This means that the BH curve is linear and no saturation is taken into account.

Secondly fringing of flux at the ends of the magnetic circuit was neglected. This admits a very simple geometry, whose parameters may be determined by the above method. These assumptions simplify expression (2.2) and facilitate calculation of the air gap permeance.

### Evaluation criteria

The comparison of the performances of the various Shark profiles was based on the following criteria:

- *inductance gain* in the aligned rotor position. This is determined as the ratio of the inductance value calculated for the Shark SRM to the same variable calculated for the CSRSM
- *energy gain*. The energy conversion in an SRM may simply be estimated by the difference of the coenergy between the aligned and the unaligned rotor positions. This quantity was determined for both Shark and cylindrical air gap SRM. The improvement of the energy conversion process in the Shark SRM may now be evaluated by observing the ratio of the energy converted in the Shark SRM during a single stroke to the energy converted in the CSRSM during a single stroke.

## 2.2 Linear analysis of various Shark profiles

The magnetic performances of various Shark profiles were analysed under the conditions and assumptions discussed in the previous section. The analysis starts with the CSRSM and continues

with the Shark SRM profiles in the following order: saw, ellipse, trapezoid and square wave and ends with conclusions.

### 2.2.1 Cylindrical air gap SRM

The magnetising inductance,  $L_0$  of the cylindrical air gap SRM in the aligned position may be determined as a function of the dimensions of the magnetic circuit:

$$L_0 = \frac{N_{ph}^2}{\left(\frac{g}{\mu \cdot A_g}\right)} = \frac{N_{ph}^2}{\left(\frac{g}{\mu \cdot (l_{stk} \cdot l_{pole})}\right)} = \frac{\mu \cdot N_{ph}^2 \cdot (l_{stk} \cdot l_{pole})}{g} \quad (2.3)$$

where  $L_0$  is the magnetising inductance of the magnetic circuit in the aligned rotor position,  $\mu$  is the permeability of the free space,  $A_g$  is the area of the air gap,  $g$  is the air gap length,  $l_{pole}$  is the length of a stator pole and  $N_{ph}$  is the number of turns per phase.

Similarly the inductance of the magnetic circuit at the unaligned rotor position may be calculated. The flux path at the unaligned rotor position has a more complex configuration. Therefore exact calculation of the unaligned inductance is complicated and must be subject of a series of approximations, which increases the uncertainty of the result. Therefore, during this simplified discussion it was assumed that the inductance of the unaligned position had the value  $L_0^u$  and may be obtained from the aligned position inductance by division with a factor  $k_L$ , whose value depends on the specific design of the radial cross-section of the SRM.

The energy of the magnetic circuit when the rotor was in the aligned position,  $W_0^a$ , is determined under the assumption of linear magnetic properties by the equation:

$$W_0^a = \frac{1}{2} \cdot L_0^a \cdot i^2 \quad (2.4)$$

where the index 0 refers to the cylindrical air gap machine, index  $a$  to the aligned position and  $i$  is the current flowing through the phase winding.

The energy converted in the CSRSM during one stroke (movement of the rotor from the unaligned to the aligned rotor position) is given by:

$$\Delta W_0 = W_0^a - W_0^u = \frac{1}{2} \cdot i^2 \cdot (L_0^a - L_0^u) \quad (2.5)$$

where  $L_0^u$  and  $W_0^u$  are the inductance and energy of the cylindrical air gap SRM in the unaligned position. Written in terms of aligned inductance,  $L_0^a$ , expression (2.5), becomes:

$$\Delta W_0 = \frac{1}{2} \cdot i^2 \cdot \left( L_0^a - \frac{L_0^a}{k_L} \right) = \frac{(k_L - 1)}{2 \cdot k_L} \cdot i^2 \quad (2.6)$$

where  $k_L = \frac{L_0^a}{L_0^u}$ .

This expression was used as reference for all following calculations in the cases of the various Shark profiles.

### 2.2.2 Saw-toothed profile

The inductance of the saw-toothed SRM in the aligned position is given by:

$$L_{saw} = \frac{N_{ph}^2}{\left( \frac{g}{\mu \cdot A_{saw}} \right)} = \frac{\mu_0 \cdot N_{ph}^2 \cdot \left( \frac{l_{stk}}{\cos \beta} \cdot l_{pol} \right)}{g} \quad (2.7)$$

where  $A_{saw}$  is the area of the saw toothed air gap and  $\beta$  is the angle which defines the geometry of the Shark profile.

This means that the inductance gain defined by the ratio of the inductance of the Shark SRM-equation (2.7), to the inductance of the CSRSM – as shown in equation (2.3) is given by:

$$k_{saw} = \frac{L_{saw}}{L_0} = \frac{1}{\cos \beta} \quad (2.8)$$

Equation (2.8) indicates that the inductance gain depends only on the angle  $\beta$ .

In order to highlight the dependence of the inductance gain on the number of Shark segments and on their height, expression (2.8) may be rewritten based on the saw-toothed geometry illustrated in Fig. 2.4 as follows:

$$k_{saw} = \frac{L_{saw}}{L_0} = \frac{\sqrt{\left(\frac{l_{shk}}{2}\right)^2 + h_{shk}^2}}{\frac{l_{shk}}{2}} = \sqrt{1 + \left(\frac{2h_{shk}}{l_{shk}}\right)^2} \quad (2.9)$$

Now the influence of the length and height of the Shark profile can be studied separately. If, for instance, the height of the Shark segment is held constant the inductance gain increases with reduction of the Shark segment pitch. The variation is shown in Fig.2.9. On the other hand, if the length of the Shark segment is held constant, then the inductance gain increases as the height of the Shark segment increases as shown in Fig.2.9.

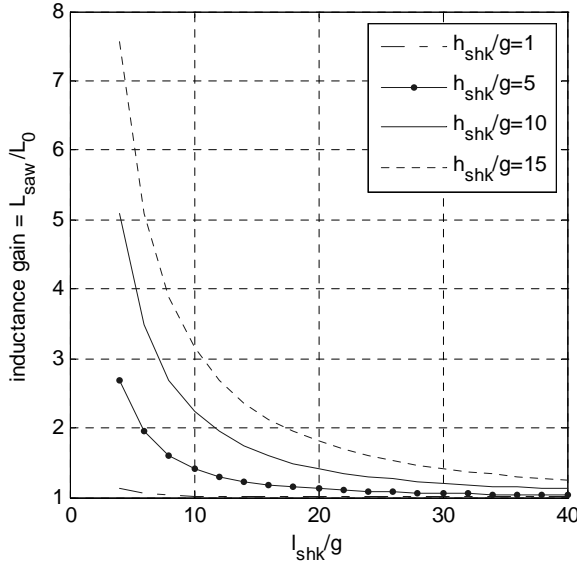


Fig.2.9 Inductance gain for the saw-toothed air gap showing the influence of the height and length of the Shark tooth

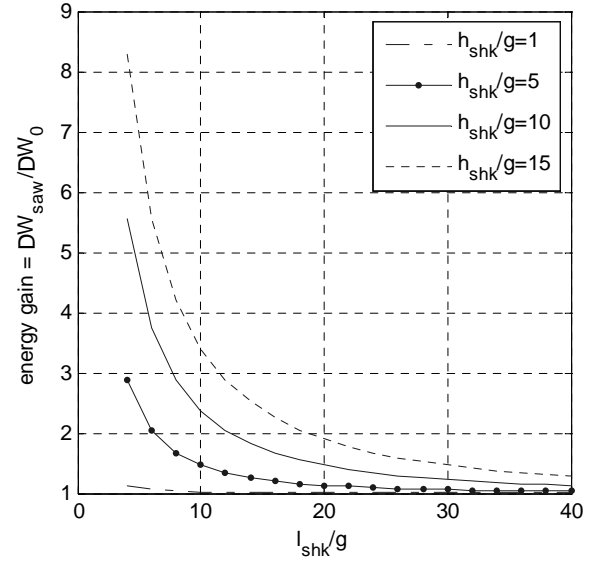


Fig.2.10 Energy gain for the saw-toothed air gap showing the influence of the height and length of the Shark tooth

The change in the energy of the saw toothed air gap may be determined as:

$$DW_{saw} = W_{saw}^a - W_{saw}^u \quad (2.10)$$

where:  $W_{saw}^a$  and  $W_{saw}^u$  are the energies of the saw toothed SRM in the aligned and unaligned position respectively.

As mentioned in the previous section, the inductance in the unaligned rotor position, was assumed to be equal for the Shark SRM and CSR. Therefore, the energy in the unaligned position is also

equal for both machines ( $W_{saw}^u = W_0^u$ ). Based on this assumption the energy converted in the Shark SRM, during movement from the unaligned to the aligned position, is given by:

$$\Delta W_{saw} = W_{saw}^a - W_0^u = \frac{(L_{saw} - L_0)}{2} \cdot i^2 \quad (2.11)$$

This expression may be written in terms of inductance gain,  $k_{saw}$  and inductance ratio  $k_L$  as follows:

$$\Delta W_{saw} = \frac{\left( L_0 \cdot k_{saw} - \frac{L_0}{k_L} \right)}{2} \cdot i^2 = \frac{L_0}{2 \cdot k_L} \cdot (k_L \cdot k_{saw} - 1) \cdot i^2 \quad (2.12)$$

From equations (2.6) and (2.12), the energy gain, defined as the ration of the change in co-energy during one stroke of the Shark SRM ( $\Delta W_{saw}$ ) to the same quantity determined for the CSRSM ( $\Delta W_0$ ), is:

$$k_{W_{saw}} = \frac{\Delta W_{saw}}{\Delta W_0} = \frac{k_L \cdot k_{saw} - 1}{k_L - 1} \quad (2.13)$$

The variation of  $k_{W_{saw}}$  with the dimensions of the Shark tooth is presented in Fig.2.10.

The equations determined suggest that the inductance gain depends on the angle  $\beta$  or on the ratio  $\frac{2 \cdot h_{sqr}}{l_{shk}}$ . This means that for a given stack length and angle  $\beta$ , the performance of the saw profile does not change with the length of the Shark segment ( $\frac{L_{saw}}{L_0} = \text{constant at constant } \beta$ ).

To be more specific, consider the Shark segments in Fig.2.13. For a given tooth pitch,  $l_{shk}$ , one or two Shark segments, having the same angle  $\beta$  might be accommodated.

The question to be answered is whether the number of the Shark segments influences the performance of the Shark configuration. According to equation (2.8), there will be no effect of the Shark segment length. Closer study reveals that not all the area of the saw-toothed air gap is effectively crossed by flux lines. The effective length of the region crossed by the flux lines may be approximated, based on the geometry of Fig. 2.11, by:

$$l_e = l_t - \delta l \quad (2.14)$$

where  $l_t$  is the length of the side of the Shark profile:



$$l_t = \frac{l_{shk}}{2 \cdot \cos \beta} \quad (2.15)$$

and  $\delta l$  is the length of the air gap which is not effectively crossed by the field lines:

$$\delta l = g \cdot \tan \beta \quad (2.16)$$

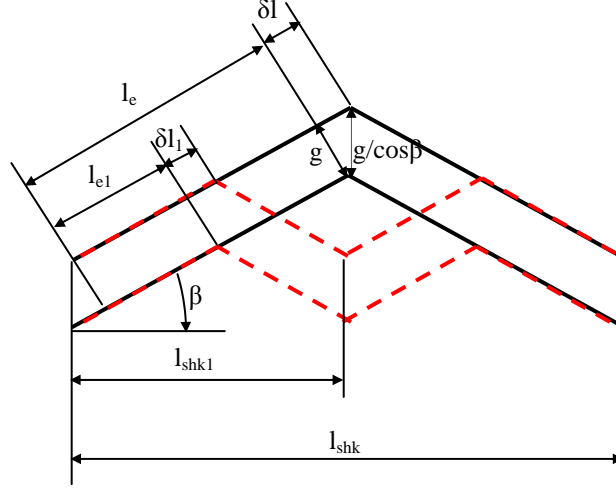


Fig.2.11 Geometry of the Shark teeth having different lengths

From equations (2.14), (2.15), (2.16) the equivalent length of the stack used in the conversion is given by:

$$l_e = \frac{l_{shk}}{2 \cdot \cos \beta} - g \cdot \tan \beta \quad (2.17)$$

Under these considerations, the total active length ( $l_e^{total}$ ) for a Shark SRM with the stack length,  $l_{stk}$  is given by:

$$\begin{aligned} l_e^{total} &= 2 \cdot n_t \cdot l_e = 2 \cdot \frac{l_{stk}}{l_{shk}} \cdot \left( \frac{l_{shk}}{2 \cdot \cos \beta} - g \cdot \tan \beta \right) \\ &= \frac{l_{stk}}{\cos \beta} - 2 \cdot \frac{l_{stk}}{l_{shk}} \cdot g \cdot \tan \beta \end{aligned} \quad (2.18)$$

Equation (2.18) suggests that the effective conversion area is dependent on the length of the Shark segment. There is a limit to the number of Shark teeth which may be built in a given stack length, for which the Shark air gap behaves similarly to the cylindrical air gap. This limit is obtained from

the condition that  $l_e^{total}$  equals the stack length,  $l_{stk}$ . The limit for  $n_t$  depends on the angle  $\beta$  as shown in Fig.2.12.

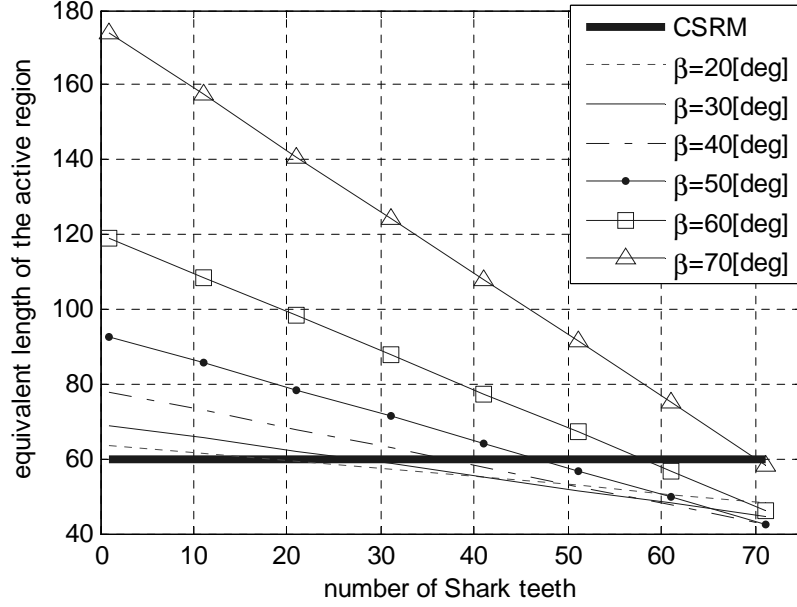


Fig.2.12 Illustration of the influence of the number of Shark teeth, with specified  $\beta$ , which may be accommodated along a given stack length, on the equivalent length of the conversion region.

### 2.2.3 Elliptical profile

The elliptical Shark profile is described by the following equation:

$$\frac{x^2}{a^2} + \frac{y^2}{b^2} = 1 \quad (2.19)$$

where  $a = \frac{l_{shk}}{2}$  and  $b = h_{shk} = \frac{l_{shk}}{2} \cdot \tan \beta$ .

The maximum inductance obtainable by using this profile is given by:

$$L_{ellipse} = \frac{N_{ph}^2}{\left( \frac{g}{\mu_0 \cdot A_{ellipse}} \right)} = \frac{\mu_0 \cdot N_{ph}^2 \cdot (l'_{stk} \cdot L_{pol})}{g} \quad (2.20)$$

where:  $A_{ellipse}$  is the area of the elliptical air gap and  $l'_{stk}$  is the equivalent length of the Shark SRM air gap.  $l'_{stk}$  may be determined from the semi perimeter of the ellipse multiplied by the number of Shark segments  $n_t$ :

$$l'_{stk} = \frac{\pi}{2} \cdot (a + b) \cdot (3 - \sqrt{4 - h_e}) \cdot n_t \quad (2.21)$$

$$\text{where } h_e = \left( \frac{a - b}{a + b} \right)^2 = \left( \frac{1 - \tan \beta}{1 + \tan \beta} \right)^2 \quad (2.22)$$

From (2.20), (2.21) and (2.22) the inductance in the aligned position becomes:

$$L_{ellipse} = \frac{\mu_0 \cdot N_{ph}^2 \cdot \left( n_t \cdot \frac{\pi}{2} \cdot (a + b) \cdot (3 - \sqrt{4 - h_e}) \cdot l_{pol} \right)}{g}$$

$$L_{ellipse} = \frac{\mu_0 \cdot N_{ph}^2 \cdot \left( n_t \cdot \frac{\pi}{2} \cdot \frac{l_{shk}}{2} \cdot (1 + \tan \beta) \cdot (3 - \sqrt{4 - h_e}) \cdot l_{pol} \right)}{g} \quad (2.23)$$

$$L_{ellipse} = \frac{\mu_0 \cdot N_{ph}^2 \cdot l_{stk}}{g} \cdot \left( \frac{\pi}{4} \cdot (1 + \tan \beta) \cdot \left( 3 - \sqrt{4 - \left( \frac{1 - \tan \beta}{1 + \tan \beta} \right)^2} \right) \right)$$

From (2.23) and (2.3) the inductance gain,  $k_{ellipse}$ , of the elliptical Shark profile is given by:

$$k_{ellipse} = \frac{L_{ellipse}}{L_0} = \frac{\pi}{4} \cdot (1 + \tan \beta) \cdot \left( 3 - \sqrt{4 - \left( \frac{1 - \tan \beta}{1 + \tan \beta} \right)^2} \right) \quad (2.24)$$

The inductance gain of the elliptical profile depends on the angle  $\beta$  only. The elliptical profile produces a higher aligned inductance compared with the saw-toothed profile for the whole range of angle  $\beta$ .

To express the inductance gain as a function of the length and the height of the Shark segment,  $\tan \beta$  is replaced by an expression in terms of  $h_{shk}$  and  $l_{shk}$ . Using this expression the variation of inductance gain with the length,  $l_{shk}$ , is presented in Fig.2.13, for different heights,  $h_{shk}$ , of the Shark profile. The variation is quite similar in shape to that in the case of the saw-toothed profile. The change of the co-energy of the elliptical toothed air gap may be determined as:

$$\Delta W_{ellipse} = W_{ellipse}^a - W_{ellipse}^u \quad (2.25)$$

where  $W_{ellipse}^a$  and  $W_{ellipse}^u$  are the co-energy of the elliptic toothed SRM – in the aligned and unaligned position.

As in the previous section, the inductance of the unaligned rotor position, was considered to be equal for the Shark SRM and the CSRSM, making the co-energy of the unaligned position also equal for both machines ( $W_{ellipse}^u = W_0^u$ ). Based on this assumption, the energy converted in the elliptical Shark SRM, during movement from the unaligned to the aligned position, is given by:

$$\Delta W_{ellipse} = W_{ellipse}^a - W_0^u = \frac{(L_{ellipse} - L_0^u)}{2} \cdot i^2 \quad (2.26)$$

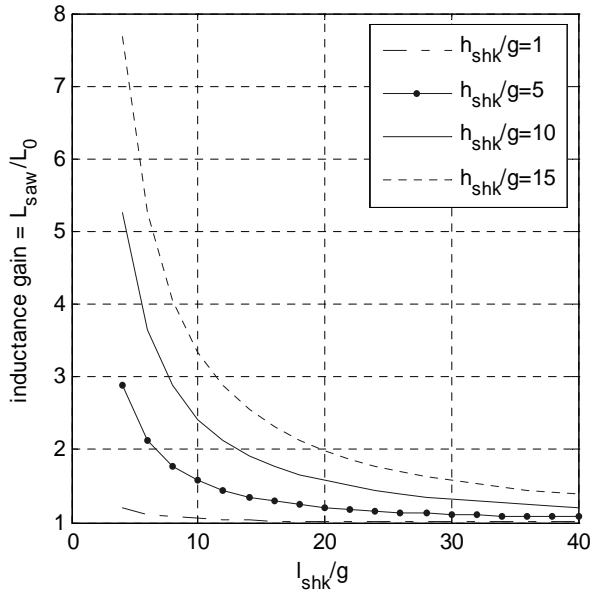


Fig.2.13 Inductance gain for the elliptical profile showing the influence of the height and length of the Shark tooth.

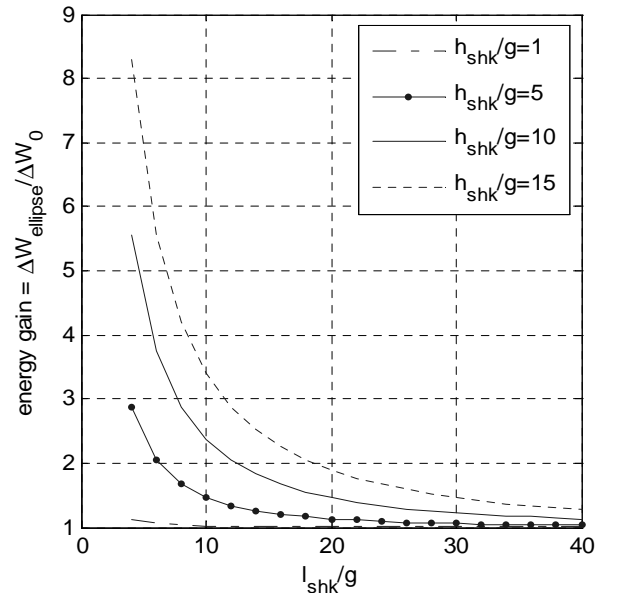


Fig.2.14 Energy gain for the elliptical profile showing the influence of the height and length of the Shark tooth.

This expression may be written in terms of inductance gain,  $k_{ellipse}$  and inductance ratio  $k_L$  as follows:

$$\Delta W_{ellipse} = \frac{\left( L_0 \cdot k_{ellipse} - \frac{L_0}{k_L} \right)}{2} \cdot i^2 = \frac{L_0}{2 \cdot k_L} \cdot (k_L \cdot k_{ellipse} - 1) \cdot i^2 \quad (2.27)$$

From equations (2.6) and (2.27) the energy gain,  $k_{Wellipse}$ , defined as the ratio of the change in co-energy during one stroke in the elliptical Shark SRM to the same variable determined for the CSRSM, is given by:

$$k_{Wellipse} = \frac{\Delta W_{ellipse}}{\Delta W_0} = \frac{k_L \cdot k_{ellipse} - 1}{k_L - 1} \quad (2.28)$$

Variation as function of the dimensions of the elliptical Shark tooth is presented in Fig2.14 and it exhibits similar features to the diagrams representing the saw-toothed profile.

#### 2.2.4 Square wave profile

The inductance of the square wave profile, illustrated in Fig.2.6 consists of two components: a radial component  $L_1$  and an axial component  $L_2$ :

$$L_{square} = L_1 + L_2 = \frac{\mu_0 \cdot N_{ph}^2 \cdot A_1}{g_1} + \frac{\mu_0 \cdot N_{ph}^2 \cdot A_2}{g_2} \quad (2.29)$$

which means that:

$$L_{square} = \frac{\mu_0 \cdot N_{ph}^2 \cdot (l_{stk} \cdot l_{pol})}{g_1} + \frac{\mu_0 \cdot N_{ph}^2 \cdot (2 \cdot n_t \cdot h_{shk} \cdot l_{pol})}{g_2} \quad (2.30)$$

Assuming that the axial and the radial air gaps are equal ( $g_1 = g_2 = g$ ) the inductance associated with the magnetic circuit of the square wave profile is given by the following expression:

$$L_{square} = \frac{\mu_0 \cdot N_{ph}^2 \cdot (l_{stk} \cdot l_{pol})}{g} \cdot \left( 1 + \frac{2 \cdot n_t \cdot h_{shk}}{l_{stk}} \right) \quad (2.31)$$

which may be expressed as follows, in terms of dimensions of the Shark profile:

$$L_{square} = L_0 \cdot \left( 1 + 1 \cdot \frac{2 \cdot \frac{l_{stk}}{l_{shk}} \cdot h_{shk}}{l_{stk}} \right) = L_0 \cdot \left( 1 + \frac{2 \cdot h_{shk}}{l_{shk}} \right) \quad (2.32)$$

This means that the inductance gain of the square wave profile is determined by:

$$k_{square} = \frac{L_{square}}{L_0} = \left( 1 + \frac{2 \times h_{shk}}{l_{shk}} \right) \quad (2.33)$$

which becomes, in terms of angle  $\beta$ :

$$k_{square} = \frac{L_{square}}{L_0} = (1 + \tan b) \quad (2.34)$$

Following the same procedure as in the cases of the saw-toothed and elliptical profiles, the energy gain may be determined as:

$$k_{Wsquare} = \frac{DW_{square}}{DW_0} = \frac{k_L \times k_{square} - 1}{k_L - 1} \quad (2.35)$$

It may be concluded that the inductance gain of the square wave air gap is proportional to the  $\tan b$  conforming to the equation (2.34).

Variations of the inductance and energy gains are presented in Fig.2.15 and Fig.2.16 respectively as function of the Shark tooth pitch

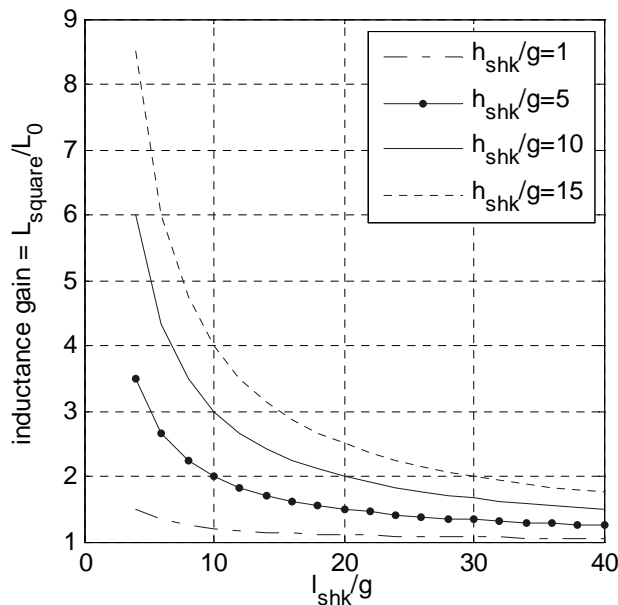


Fig.2.15 Inductance gain for the square wave profile showing the influence of height and length of the Shark tooth

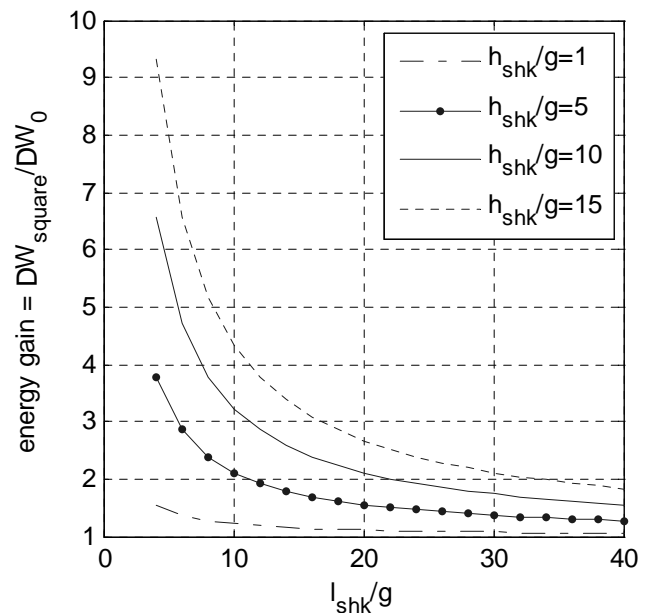


Fig.2.16 Energy gain for the square wave profile showing the influence of the height and length of the Shark tooth

### 2.2.5 Trapezoidal profile

The inductance of the Shark SRM with trapezoidal profile is given by:

$$L_{trap} = \frac{N_{ph}^2}{\left( \frac{g}{\mu_0 \cdot A_{trap}} \right)} = \frac{\mu_0 \cdot N_{ph}^2 \cdot (l'_{stk} \cdot l_{pol})}{g} \quad (2.36)$$

where:

$$l'_{stk} = 2 \cdot n_t \cdot (l_{top} + l_1) = 2 \cdot n_t \cdot \left( k \cdot l_{shk} + \sqrt{\left( \frac{l_{shk}}{2} \right)^2 \cdot (1 - 2 \cdot k)^2 + h_{shk}^2} \right) \quad (2.37)$$

$$l'_{stk} = l_{stk} \cdot \left[ 2 \cdot k + \sqrt{(1 - 2 \cdot k)^2 + \left( \frac{2 \cdot h_{shk}}{l_{shk}} \right)^2} \right]$$

$$\text{with: } l_{top} = k \cdot l_{shk} \quad k \leq 0.5 \quad (2.38)$$

From (2.36) and (2.37) the total inductance becomes:

$$L_{trap} = \frac{\mu_0 \cdot N^2 \cdot \left\{ l_{stk} \cdot \left[ 2 \cdot k + \sqrt{(1 - 2 \cdot k)^2 + \left( \frac{2 \cdot h_{shk}}{l_{shk}} \right)^2} \right] \cdot l_{pol} \right\}}{g} \quad (2.39)$$

The inductance gain for the trapezoidal profile is given by:

$$k_{trap} = \frac{L_{trap}}{L_0} = 2 \cdot k + \sqrt{(1 - 2 \cdot k)^2 + \left( \frac{2 \cdot h_{shk}}{l_{shk}} \right)^2} \quad (2.40)$$

$$\text{or } k_{trap} = \frac{L_{trap}}{L_0} = 2 \cdot k + \sqrt{(1 - 2 \cdot k)^2 + (\tan \beta)^2} \quad (2.41)$$

For  $k=0.5$ , expression (2.41) is equivalent to (2.34) for the square wave profile, and for  $k=0$ , expression (2.41) is equivalent to (2.8) for the saw-toothed profile.

The energy gain, determined as in the previous cases (2.13), (2.28), (2.35), may be expressed:

$$k_{Wtrap} = \frac{\Delta W_{trap}}{\Delta W_0} = \frac{k_L \cdot k_{trap} - 1}{k_L - 1} \quad (2.42)$$

The variation of inductance and energy gains, expressed by equations (2.40) and (2.42) is illustrated in Fig.2.17 and Fig.2.18.

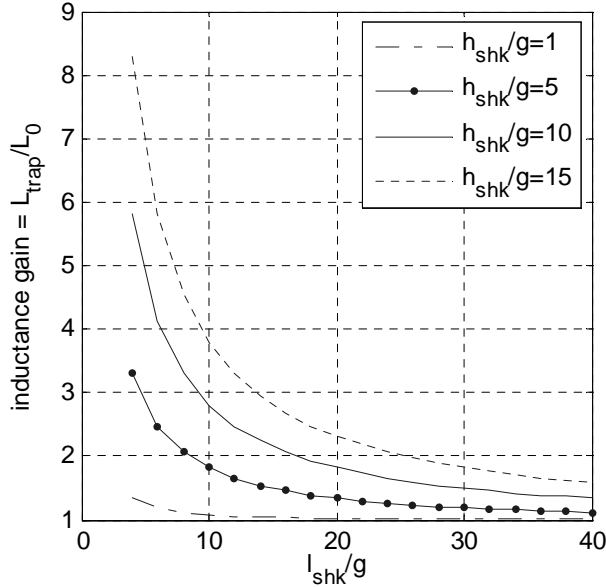


Fig.2.17 Inductance gain for the trapezoid profile showing the influence of the height and length of the Shark tooth.

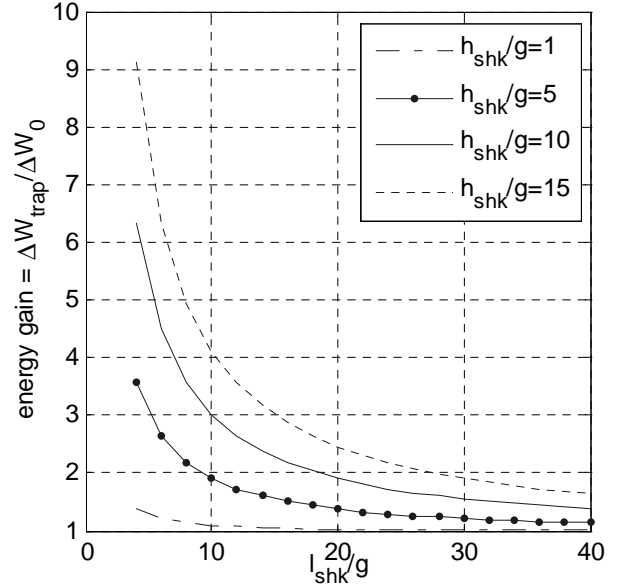


Fig.2.18 Energy gain for the trapezoid profile showing the influence of the height and length of the Shark tooth.

## 2.3 Discussion and Comparison of the analysed Shark profiles

In the linear analysis of the previous section each of the four Shark profiles was considered separately. To help the selection of the Shark structure, which has the best magnetic performance, a comparison of the results is necessary.

The expressions for the inductance gain of the Shark profiles considered are summarised in table 2.2 For each Shark profile, the expressions of the inductance gain and its value for a specified  $\beta$  (45 [degrees]) are presented. It may be observed that the SRM with trapezoidal profile is the



generalization of the saw-toothed and square wave Shark SRMs. As the dimension  $l_{top}$ , shown in Fig.2.7, varies, the inductance gain assumes values varying between those of the saw-toothed and square wave Shark SRMs. The inductance gain of the elliptical profile exceeds that of the saw-toothed profile but it is smaller than that of the square wave profile.

In Fig.2.19, the curves showing the inductance ratio variation with angle  $\beta$  are presented for the saw-toothed, square wave, elliptical and trapezoidal Shark profiles. A similar variation is observed for the energy ratio, presented in Fig.2.20

These curves show that:

- the influence of the Shark profile on the performances of the magnetic circuit increases with the angle  $\beta$
- the saw toothed and the square waved profiles represents respectively the lower and the upper limits for the inductance and energy gain
- the trapezoidal profile may be considered to be a generalisation of both the saw-toothed and the square wave profiles.

Table 2. 1 Inductance gain for saw-toothed, square-wave, ellipsoidal and trapezoidal Shark profiles

Profile type	Inductance gain in the aligned position in terms of $\beta$	Inductance gain at $\beta=45$ [deg]
Saw-toothed profile	$k_{saw} = \frac{1}{\cos \beta}$	1.41
Square wave profile	$k_{square} = (1 + \tan \beta)$	2
Ellipse profile	$k_{ellipse} = \frac{\pi}{4} \cdot (1 + \tan \beta) \cdot \left( 3 - \sqrt{4 - \left( \frac{1 - \tan \beta}{1 + \tan \beta} \right)^2} \right)$	1.57
Trapezoidal profile	$k_{trap} = 2 \cdot k + \sqrt{(1 - 2 \cdot k)^2 + (\tan \beta)^2}$ , $k = \frac{l_{top}}{l_{shk}}; k \leq 0.5$	1.41 (k=0) 1.48 (k=0.1) 1.67 (k=0.3) 2.00 (k=0.5)

According to this idealised analysis (2.13), the number of Shark teeth in a given machine does not affect the performances of the Shark configuration if the ratio of the Shark tooth height to its length remains constant ( $\beta = \text{const.}$ ). This is contradicted by equation (2.18), which shows that if there are many Shark profiles much active area of the air gap is lost. This is due to the fact that the flux density is not uniformly distributed along the Shark air gap. This subject will be discussed in chapter 3 as it may be decisive in choice of Shark profile for further considerations.

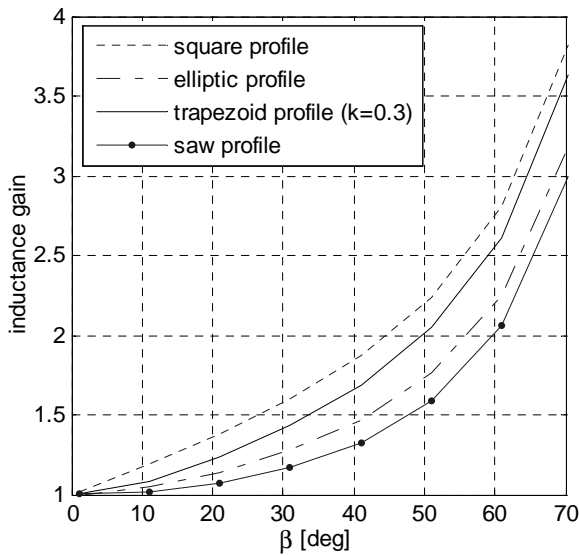


Fig.2.19 Comparison of inductance gain variation as a function of angle  $\beta$  for various Shark profiles

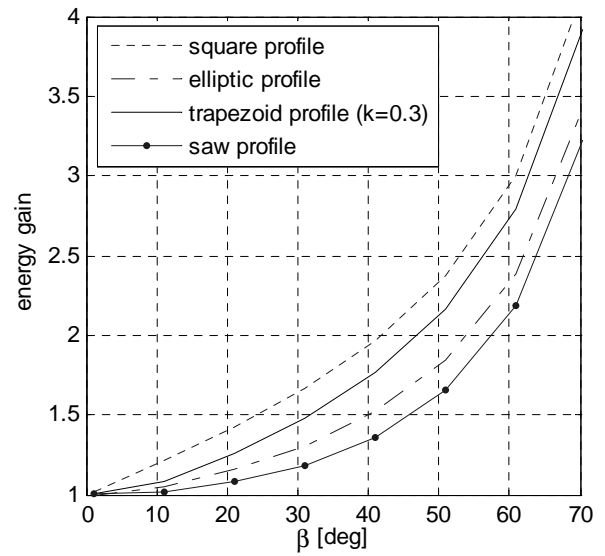


Fig.2.20 Comparison of energy gain variation as a function of angle  $\beta$  for various Shark profiles

The influence of the length and height of the Shark tooth on the magnetic performances of the Shark SRM is illustrated in Fig.2.21 and Fig.2.22. It may be observed that the inductance and energy gains decrease with the length of the Shark profile provided that the height,  $h_{shk}$ , remains constant. Again the trapezoidal profile behaves as a generalisation of the saw toothed and square-wave profile.

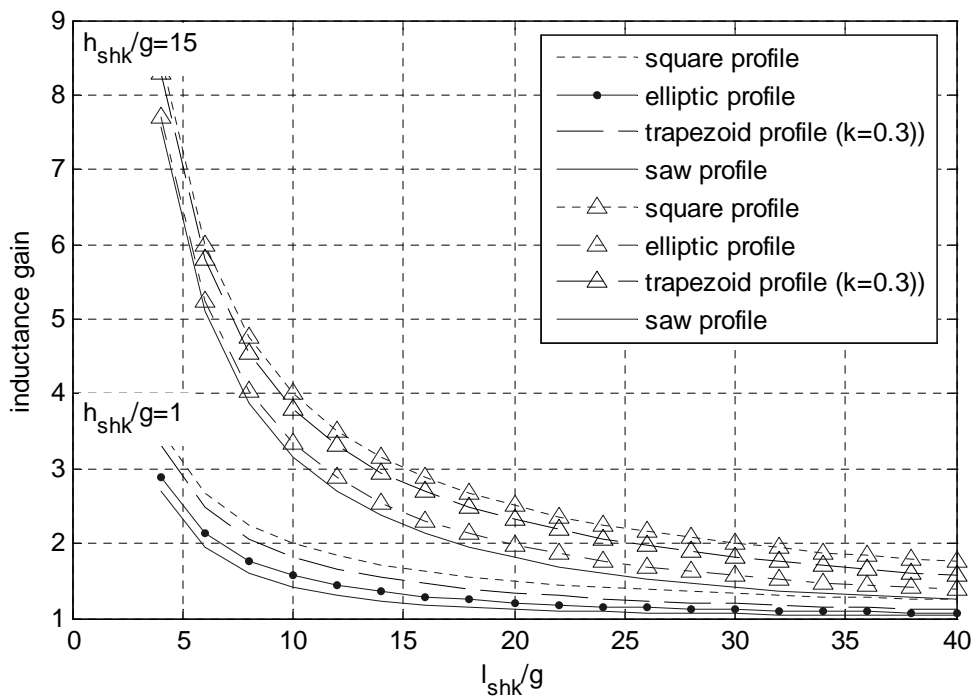


Fig.2.21 Illustration of the inductance gain as a function of the length and height of the Shark profile

If the length,  $l_{shk}$ , of the Shark profile remains constant then the inductance and the energy gains both increases with the increasing height,  $h_{shk}$ , of the profiles.

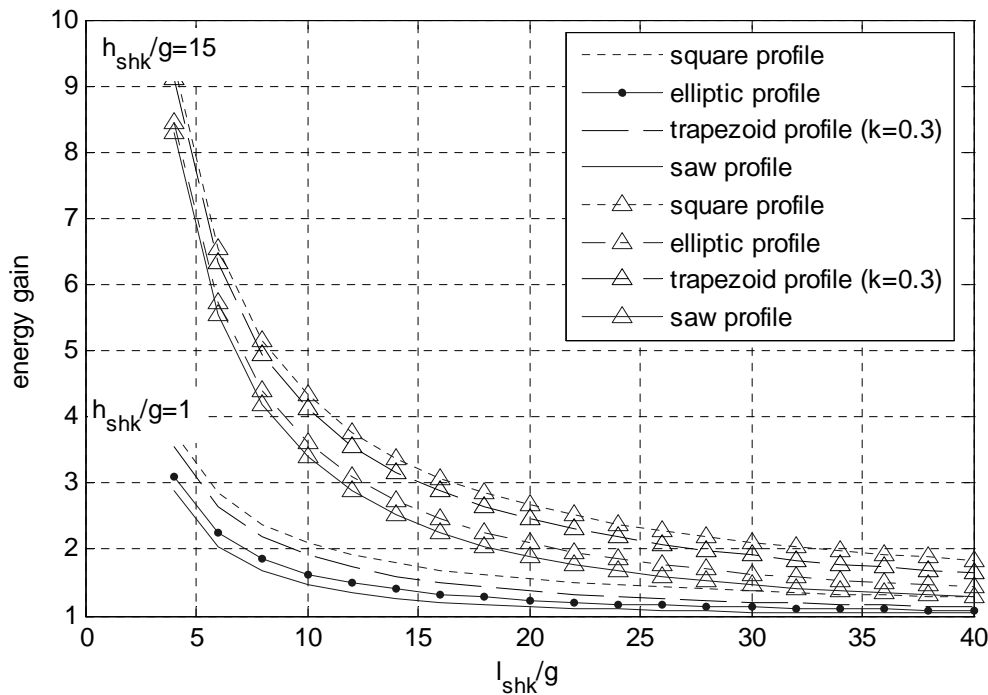


Fig.2.22 Illustration of the energy gain variation as a function of the length and height of the Shark profile

According to this linearised analysis the square wave profile exhibits the best magnetic performances compared to the other shapes of Shark teeth analysed. The best performances of the square wave profile are obtained for large  $\beta$ , which is equivalent to a large ratio of the height to the length of the profile. This may be seen in Fig.2.19, Fig.2.20, Fig.2.21 and Fig.2.22. This means that the optimum Shark configuration comprises a square wave air gap whose teeth are as high and narrow as possible. However, when selecting these dimensions there will be some limitations.

The height of the Shark teeth is limited as the presence of the Shark teeth reduces the available winding area. In this project, the height  $h_{shk}$  of the Shark profile was limited to about 20 [%] of the height of the stator pole. For the SRM, with the dimensions given in Appendix B1, this limit is 4.5 [mm]. The length of the Shark tooth is limited by the lamination thickness. The shortest square wave Shark tooth that could be built has the length  $l_{shk} = 3 \cdot l_{lam}$ , where  $l_{lam}$  is the thickness of the lamination as shown in Fig.2.23.

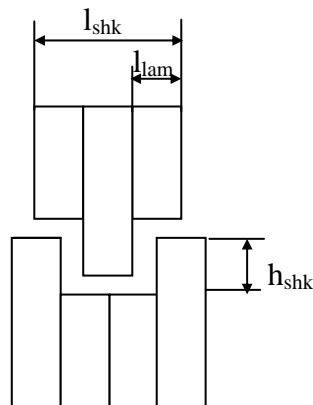


Fig.2.23 Illustration of the minimum length square wave Shark profile

## 2.4 Summary and conclusion

A linear analysis of various Shark profiles was presented in this chapter. The analysis used the method of the equivalent magnetic circuit assuming linear magnetic properties of the iron and complete absence of fringing flux. The profiles selected for analysis were: saw-toothed, square wave, trapezoidal and elliptical. For each of them, the inductance gain and the energy gain were taken as criteria for evaluation. While the inductance in the unaligned position was considered to be identical for the Shark and the cylindrical air gap machines, the inductance of the circuit in the aligned position was considered to be a useful indicator of the performance of the Shark profiles. It was calculated for each case. The energy gain was selected as an indicator for the capability of the Shark machine to produce torque.

Comparison of the performances of the four Shark shapes showed that:

- The square wave profile exhibits the best capability for improvement of the energy conversion
- The saw-toothed profile exhibits the lowest inductance gain and energy gain
- The trapezoidal profile is a generalisation of the saw-toothed and square wave profiles
- The inductance gain and the energy gain exhibit similar dependences on the values of geometrical parameters of the Shark profiles
- The inductance gain and the energy gain decrease with decreasing angle  $\beta$
- The inductance gain and the energy gain decrease with the length of the Shark tooth, assuming that its height remains constant
- The inductance gain and the energy gain increase in proportion with the height of the Shark tooth, assuming that its length remains constant.

By these results the first objective of the chapter was reached. This further allowed selection of the Shark profile providing the best magnetic performance. It was decided that assuming linear magnetic properties of the iron, the square-wave Shark profile having a height of 20 % of the stator pole height and the length equal to 3 times the lamination thickness offers the best magnetic performance. This conclusion was drawn assuming uniform distribution of the air gap magnetic flux density.



## Chapter 3

# Finite Element modelling of Shark Switched Reluctance Motor

In the preceding section, discussion was limited to linear analysis of the magnetic circuit of various configurations of Shark SRM – that is, saturation of the iron material has not been taken into account. However, saturation plays an important role in the process of energy conversion in the SRM. Therefore, the analysis of the magnetic capabilities of the Shark SRM is extended in this section to include the non-linear regions of the magnetisation characteristics, and the considerations from chapter 2 are amended to reflect the real field distribution in Shark structures.

Traditionally, analytical methods represent the first step in designing and analysing electrical machines, Finite Element Analysis (FEA) being rather used as optimisation tool. However, no analytical method, describing the magnetic circuit of the Shark SRM, is available. Therefore, throughout this work, FEA is used to provide the basic data about the various configurations of Shark SRM and the Cylindrical air gap SRM (CSRSM), which is considered as reference machine. By analysing different Shark geometries, the optimum Shark configuration – that is the optimum shape and the optimum dimensions- is selected to be applied and tested in a demonstration machine.

This chapter examines the influence of the Shark air gap dimensions on the magnetic performance of the Shark SRM. The performance is assessed by studying the flux linkage characteristics and flux linkage gain. Initially, the objectives are defined. Then, a brief review of the FEA and Finite Element Model (FEM) is considered. The discussion follows with the question of whether a Shark structure, with inherent 3D flux flow, might be studied using a two-dimensional (2D) FEM.

The FEM of CSRSM and Shark SRM are described for both the aligned and unaligned rotor positions and the results of the computations are used to analyse the magnetic capabilities of the Shark SRM. At the end of the chapter, the optimum shape of Shark air gap and its dimensions are determined.

### 3.1 Objectives and methodology

The main attractive feature of the Shark structure resides in the improvement of the energy conversion due to the larger air gap area, created by the particular geometry of the Shark air gap. This increase in air gap area is achieved by redistributing the iron material between stator and rotor (see description in chapter 2). This causes the field patterns in the Shark SRMs to change relative to those in CSRMs. Consequently, the flux linkage induced in Shark structures will also change. In chapter 2 the air gap flux density was assumed to be evenly distributed. In this chapter, this assumption will be investigated and amended if necessary.

The linear analysis of chapter 2, showed that any Shark SRM produces more flux linkage in the aligned rotor position than its CSRMs counterpart does. It also showed that this improvement is strongly dependent on the dimensions of the Shark teeth and on the excitation current.

Therefore, a parametric analysis of various Shark SRMs is necessary in order to reveal the influence of each Shark tooth dimension on the performances of the Shark SRM. Further, the phenomenon of local saturation is emphasised in Shark configurations. It is believed that the regions with local saturation have different locations in various Shark profiles, and their influence on the performances of the Shark structures is analysed in this chapter.

The objectives of this chapter may be summarised as following:

- To amend the results of chapter 2, if necessary
- To extend the linear analysis from chapter 2 to include saturation condition
  - To document the influence of Shark tooth dimensions on the magnetic performance of the Shark structure
  - To analyse the mechanism of saturation in various Shark profiles and to document its effect on the performance of the Shark structures
- To compare various Shark profiles and to determine the optimum shape and dimensions to be applied in a demonstration machine

In order to assure that these objectives are accomplished, the method used in this chapter is as follow:

- Finite element solutions are obtained for various Shark profiles (saw-toothed, square-wave, trapezoidal), having different dimensions
- The analysis is performed so as to identify the influence of each dimension of the Shark profile on the performances of the Shark SRM. That is:
  - variable angle  $\beta$  (or height  $h_{shk}$ ) and constant Shark tooth pitch,  $l_{shk}$ ,
  - variable tooth pitch,  $l_{shk}$  and constant angle  $\beta$
  - variable angle  $\beta$  (or tooth pitch  $l_{shk}$ ) and constant height of the Shark tooth,  $h_{shk}$
- The results are compared and the optimum shape of the air gap is determined

### 3.2 Solving the magnetic field by the means of the Finite Element Analysis

In this section general aspects of finite element modelling such as mesh generation and flux linkage calculation are reviewed.

The FEA is a powerful tool for engineering applications. First developed in 1942 by R. Courant [55], it is an indispensable design tool, especially now, when the concept of virtual prototyping is actual. The tradition of electrical machine design indicates it more as an optimisation tool, but it may be used also in the preliminary phase of the design process, as it is the case in this study.

Its principle is "Divide et impera". A complicated problem is broken into small regions, where the wanted solution may be much more easily determined. Despite the time consumption, which is much reduced on the latest computers, the results are valuable for a new system about which no knowledge is available. Reducing the time to progress from idea to final product, FEA provides a powerful tool in various application areas as: structural analysis, thermal analysis and heat transfer, frequency analysis, fluid flow, motion simulation, electrostatics, electromagnetics. There is a variety of software package for FEA dedicated to the electromagnetic field. Among them Opera – Vector Fields software, [54] is used throughout this work.

To create a FEM, requires an amount of a priori knowledge about the field pattern, in order to decide whether a Cartesian or an Axisymmetric model has to be built. A Cartesian model (xy) may be useful if the field is confined in a plane, without rotational symmetry whilst an axisymmetric model (rz) may be made if the field in a cross-section of the problem preserves the same pattern in cross-section located at different positions along one of the axes.

For an electric motor, the Cartesian model description is used. Other aspects of using FEA are related to the type of elements, mesh density and air gap discretisation. The *type of elements*, the *order of the interpolation function* and the *mesh size* are important for the accuracy of the solution [55], [58], [101]. The *air gap* requires special care when the mesh is generated for rotating electrical machines. As a solution of the field may be needed at different rotor positions, it is important to keep unchanged the mesh in the air gap so that the solutions for different positions have an identical mesh error. Therefore, the air gap is typically split into at least 3 layers, which allows the use of mesh sliding technique [55] – that is the two outer layers are attached to the stator and to the rotor body respectively while the inner layer(s) are allowed to slide with a step determined by the size of the mesh. The multi-layer air gap is also important in force and torque calculation by Maxwell stresses method, as the solution is strongly affected by the air gap mesh error.

**Calculation of the flux linkage.** Once the field solutions are obtained, the flux linkage may be calculated mainly by two methods: the magnetic vector potential and the energy method. In a 2D solution, the first method gives the flux linkage as results of [55]:

$$\Psi = -N \cdot \int_{x=a}^{x=b} \frac{dA_z}{dx} \cdot dx = N \cdot (A_z(a) - A_z(b)) \quad (3.1)$$



where  $N$  is the number of turns per phase,  $A_z$  is the magnetic vector potential defined at the coordinates ( $x=a$  and  $x=b$ ) shown in Fig. 3.1.

For a coil with uniform turns density, the mean flux linkage in terms of the vector potential is [39]:

$$\Psi = \frac{N}{A_{coil}^a} \cdot \int_{A_{coil}^a} A_z(a) \cdot dx \cdot dz - \frac{N}{A_{coil}^b} \cdot \int_{A_{coil}^b} A_z(b) \cdot dx \cdot dz \quad (3.2)$$

where  $A_{coil}^{a,b}$  are the cross-sections of the conductors located at  $x=a,b$ .

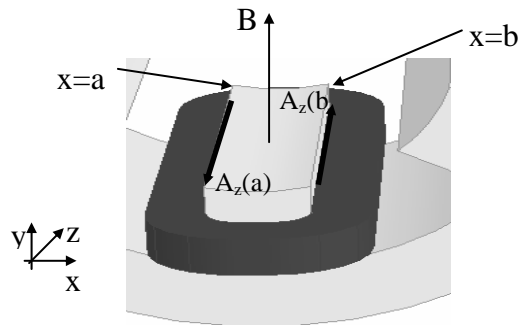


Fig.3.1 Illustration of the magnetic circuit used to describe the flux linkage calculation by method of magnetic vector potential.

The energy method considers that the magnetic energy is obtained by integration of the field solution over the whole volume of the problem. In a 2D solution this integral is reduced to a surface integral.

$$W = \frac{1}{2} \cdot \int B \cdot H \cdot dV \quad (3.3)$$

where  $W$  is the magnetic energy stored in the magnetic circuit,  $B$  and  $H$  are the flux density and the field strength in the volume  $dV$ . In this chapter the method of magnetic vector potential is used.

### 3.3 Two-dimensional Finite Element Analysis of the Shark Switched Reluctance Motor

In this section, the question of whether 2D FEA may useful be used to model the Shark structure is discussed initially. Then the FEM of CSRSM and Shark SRM are described, and the CSRSM is used to highlight the differences between finite element models of axial and radial cross-section of the motor. The details of the Shark SRM are discussed and solutions for generation of an economic mesh are provided. A study of the error distribution in the air gap is used to assess the mesh of the models.

### 3.3.1 Why two dimensional Finite Element Analysis?

The choice between 2D and 3D FEA is the first decision to make when performing FEA. Whether an electrical machine can be analysed in two-dimensions is decided based on the a priori knowledge of the flux flow in the machine. Generally, a 3D flow exists in any electrical machine. It is caused by (1) 3D end effect [57] or (2) by the particular geometry of the magnetic circuit (claw machine [59], transverse flux machine [60], Shark machine [1]). In the first situation, the flux flow within the machine is preponderant 2D. The third component of the field occurs only at the end of the stack in the axial cross-section. According to [57] the 3D effects are: the anisotropy of the laminations, the end winding flux and the fringing flux. The magnitude of the 3D effects in an SRM depends on the machine dimensions (short or long stack), on the rotor position (aligned, intermediate or unaligned) and on the saturation level.

In a cylindrical air gap SRM, shown in Fig. 3.3 a), the flux flows in the lamination plane. This is the situation where a 2D FEA might be substituted for the 3D version.

When the 3D field is caused by geometries of the magnetic circuit, such that shown in Fig.3.3 b), 2D FEA can be seldom used without losing significant information. Due to the modified air gap geometry, the flux lines in the Shark SRM have an intrinsic 3D pattern.

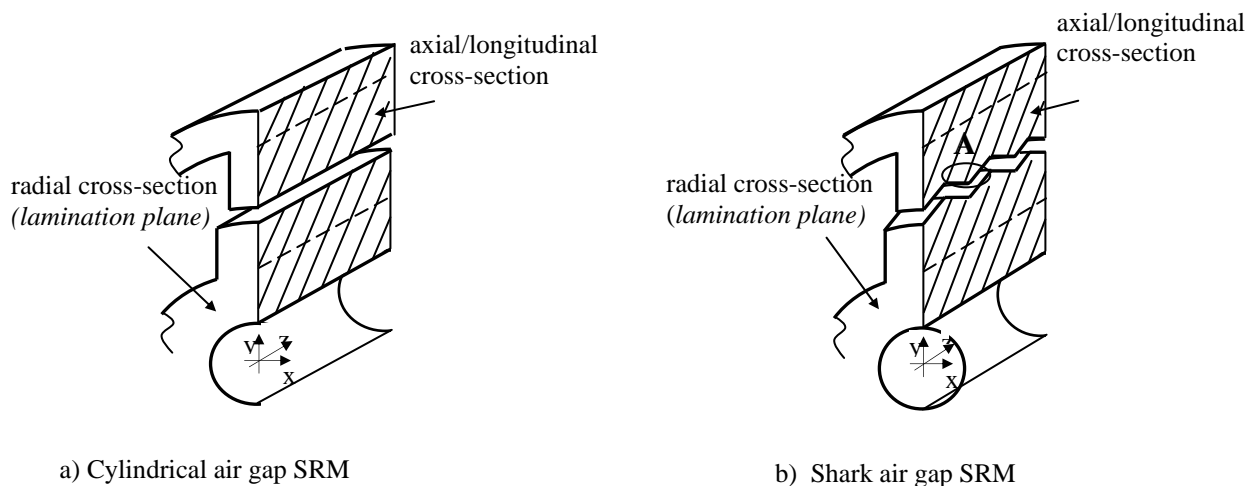


Fig.3.3 Illustration of cylindrical air gap and Shark air gap SRM

The field lines follow paths such as these shown in Fig. 3.4. In region 2 (called Shark tooth), the flux lines leave the lamination plane (plane  $xy$ ), which determined the 3D feature of the field. Thus, a 2D FEM of the radial cross-section ( $xy$ ) of a Shark SRM will not account for the main flux flowing in the machine. Attention is drawn to the axial/longitudinal cross-section ( $yz$ ) because it may be considered that the flux lines are more or less parallel to the axial cross-section (plane  $yz$ ), as drawn in Fig.3.4

*This means that the axial cross-section contains alone most of the information about the Shark profile and it may be used to make a 2D FEM of the Shark SRM. The flux fringing in the radial cross-section (Fig.3.3) is not accounted in the 2D axial model but the resulting data contain the essential information about the magnetic field in the Shark configuration.*

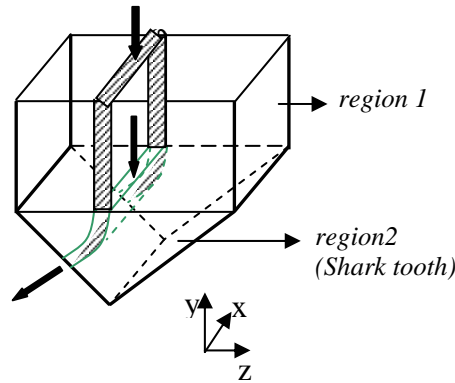


Fig.3.4 Expansion of region A from Fig. 3.3 and illustration of the flux lines in Shark SRM.

The drawback of using the 2D axial model is that only the aligned rotor position can be modelled. For the unaligned rotor position, a partial model might be conceived and this will be discussed further in this sub-section.

### 3.3.2 Model of the cylindrical air gap Switched Reluctance Motor

The finite element model of the CSRSM is described in this sub-section. Initially, the geometric model of the CSRSM is described for both axial and radial cross-sections, then the results are compared such as to highlight the properties of each of the considered models.

#### a) Geometric description of the two-dimensional models

The CSRSM considered in this sub-section has the dimensions given in Appendix A.2 The FEM of the axial and radial cross-sections, for both aligned and unaligned rotor position are illustrated in Fig. 3.5 and Fig. 3.6 (aligned position) and Fig. 3.7 and Fig. 3.8 (unaligned position).

The FEM of the *radial cross-section* considers the lamination plane. The air gap of the FEM consists of four air gap layers so as to allow the mesh to slide (see section 3.2). By solving this model for various rotor positions, the flux linkage characteristics of the CSRSM may be calculated.

The model of the *axial cross-section*, illustrated in Fig.3.6 and Fig.3.8 consists of lamination stack, winding regions and air gap regions. This has the disadvantage that it does not include the region of the back iron. In order to account for the missing region, the FEA model may be combined with yoke reluctance, as shown in Fig. 3.6. This reluctance may be readily calculated analytically.

Furthermore, to allow the return of the flux lines, a region of infinite permeability is created all around the regions of cut AA'. The infinite permeability region extends far from the winding regions such to keep the field lines unaffected by the boundary of the problem.

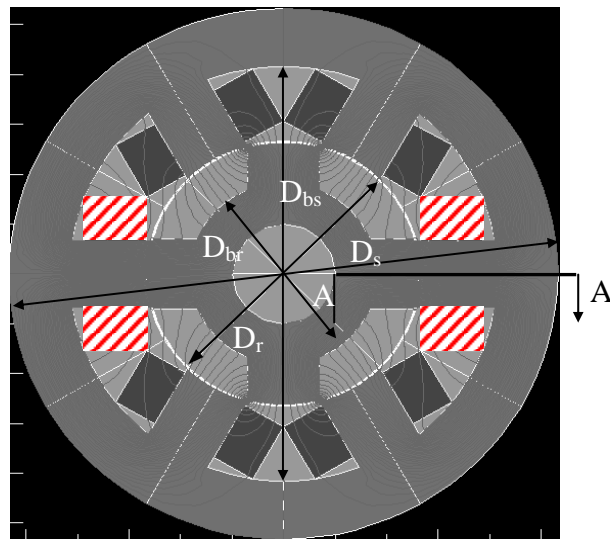


Fig. 3.5 2D FEM of radial cross-section of cylindrical air gap SRM – aligned position

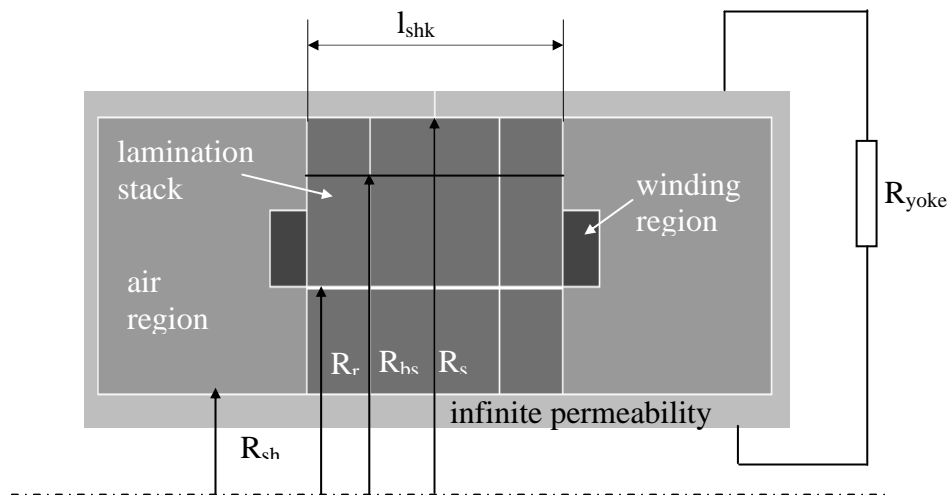


Fig. 3.6 2D FEM of axial cross-section  $A-A'$  of cylindrical SRM – aligned position

With some limitations, the 2D FEM of the *axial cross-section* of the unaligned rotor position might be created in a similar way as that of the aligned position. The limitations concern the geometry of the radial cross-section of the motor (Fig. 3.7). If the distance between the stator pole face and the rotor interpolar face is shorter than the distance between the corners of the stator and rotor poles, the unaligned position might be described by 2D FEM of the axial cross-section. The only difference between the FEM of the aligned and unaligned rotor position would be the length of the air gap, as shown in Fig.3.7 and Fig. 3.8 However, this model cannot provide valuable data because it accounts for only a fraction of the flux linkage at the unaligned position.

If the previous condition is not satisfied, the axial 2D model cannot to be modelled at all.

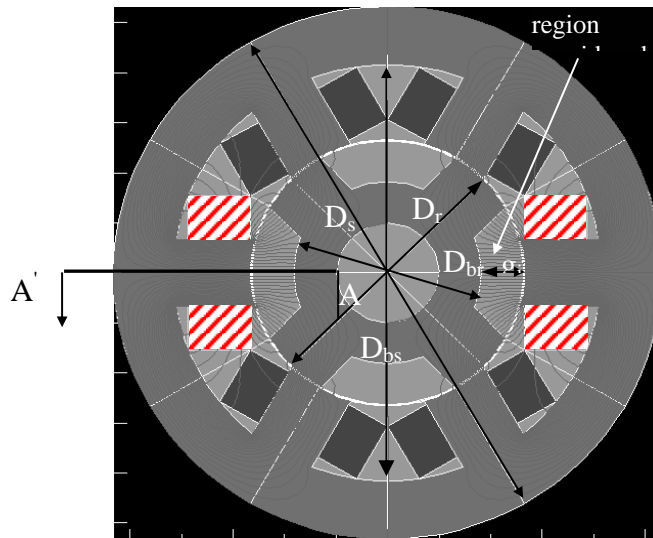


Fig. 3.7 2D FEM of radial cross-section of cylindrical air gap SRM – unaligned position

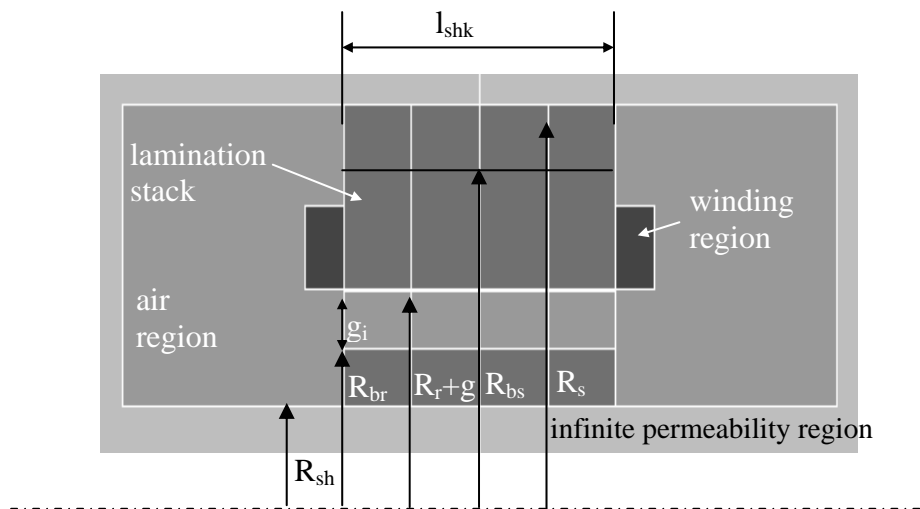


Fig.3.8 2D FEM of axial cross-section A-A' of cylindrical SRM – unaligned position

### b) Results obtained for the cylindrical air gap Switched Reluctance Motor

The results obtained from FEA of the models described in Fig. 3.5, Fig. 3.6, Fig.3.7 and Fig.3.8 are presented in Fig.3.9. The flux linkage calculated from the radial model exceeds that obtained from FEA of the axial model for both the aligned and unaligned rotor position.

For the flux linkage characteristic in the aligned rotor position this difference is explained by the fringe flux (at low current) and by the reluctance of the yoke regions (at high current).

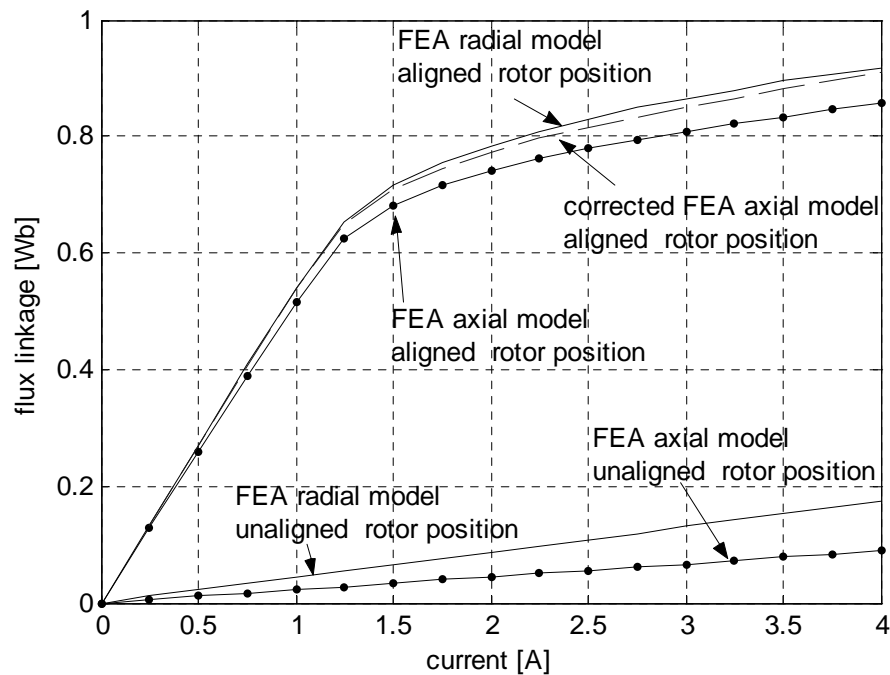


Fig. 3.9 Flux linkage for the conventional SRM in aligned and unaligned rotor position. Results from FEA of the radial and axial cross-sections

The magnetisation characteristic, corrected for the yoke region is very closed to that obtained from the radial model, as shown in Fig. 3.9

The axial model of the unaligned position cannot be used to calculate the total flux linkage because it accounts only for the flux lines that leave the face of the stator pole and enter the interpolar region of the rotor pole. Hence, a big difference is obtained between the characteristics obtained from the 2D FEM of axial and the radial cross-sections. This means that the unaligned rotor position cannot be analysed by 2D FEM of the axial cross-section.

*Conclusion* The aligned rotor position of the Shark SRM may be analysed by 2D FEM of the axial cross-section of the motor, whilst the unaligned position cannot be analysed by 2D FEM. Therefore in order to analyse the unaligned rotor position 3D FEA or an analytical model is required.

### 3.3.3 Model of the Shark Switched Reluctance Motor

In the preceding sub-section, the 2D FEM of the CSRSM was discussed. Now, the FEM of the Shark SRM is presented and discussed. As shown in sub-section 3.3.1, Shark SRM may be analysed by using 2D FEM of the axial cross-section. The model is similar to that described for the CSRSM. The only difference is that the air gap is shaped with one of the Shark profiles illustrated in Fig. 3.10 In this sub-section, only the saw-toothed and the square-wave air gaps are discussed, the trapezoidal air gap SRM (Fig.3.10 c), which is a generalisation of the first two shapes, being detailed in Appendix. B.5.

The Shark profiles are defined by geometrical parameters such as angle  $\beta$ , Shark tooth pitch,  $l_{shk}$ , height,  $h_{shk}$ , and air gap length,  $g$ . The air gap length of the saw-toothed profile  $g$ , is defined as the shortest distance across the air gap. The square-wave profile may be built having two different air gap lengths  $g_1$  as radial air gap and  $g_2$  as axial air gap, but they are considered equal throughout this work. The same is valid for the trapezoidal profile.

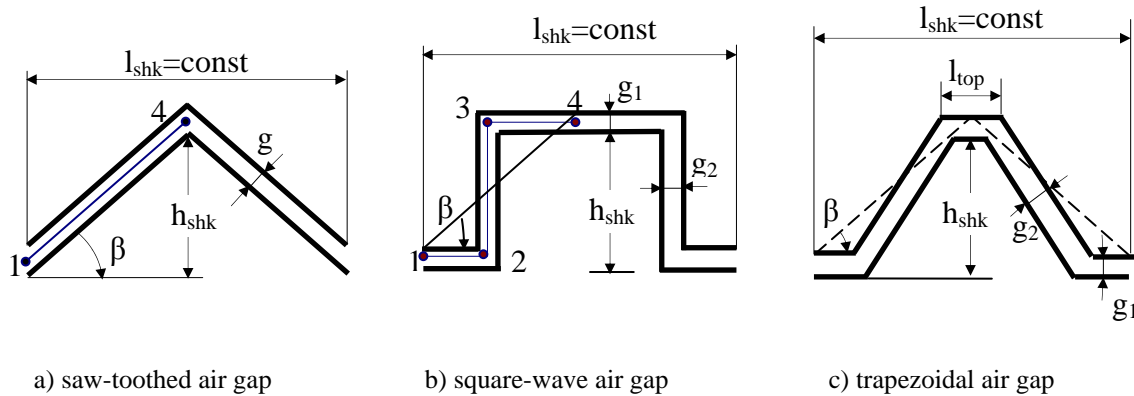


Fig. 3.10 Illustration of various shapes of Shark air gaps

### a) Mesh generation

Compared to the 2D FEM of the CSRSM, the FEM of the Shark SRM presents two special problems. One is that the Shark segment might be somewhat higher than it is long. This means that when a fine mesh is wanted in the air gap, a fine mesh will be generated also in regions far from the region of interest.

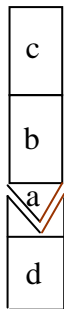


Fig. 3.11 Illustration of the Shark segment division

Another problem is that any Shark segment presents sharp corners – that is in Fig.3.10 points 1 and 4 for the saw-toothed air gap and points 2 and 3 for the square-wave air gap. This means that the error of the finite element solution in the air gap regions surrounding these corners [54] is greater than in the rest of the air gap. This error is strongly linked to the size of the elements surrounding the point and it is only weakly linked to the average size of the elements over the whole problem [54]. To reduce this error the mesh in the air gap and in the regions surrounding it, must be fine, whilst that of the other regions may be coarse such as to keep down the total number of element and to save computation time.

The first problem may be solved if the Shark segment on the stator side is divided into two or more regions and the Shark segment on the rotor side into two or more regions as shown in Fig. 3.11. In this way, a fine mesh may be generated in the Shark tooth and in the air gap, whilst a coarse mesh may be defined in the regions far from the air gap – that is regions b, c and d in Fig. 3.11.

The second problem may be solved as shown in Fig. 3.12, by biasing the mesh of the air gap towards the corners such as to reduce the size of the elements in these regions. After several trials (see recommendation from [54]), it was observed that the error in the few elements surrounding the

vertices of the Shark teeth could not be reduced below a certain value. Therefore, it was concluded that reducing the mesh size further in the whole air gap offers no benefit. It was more significant to add new points around the vertices of the Shark tooth. In this way, the size of the elements around corners may be controlled without a major increase in the total number of elements.

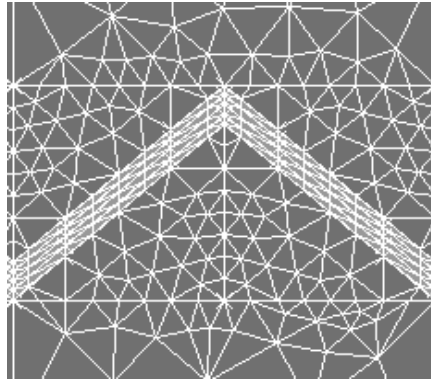


Fig. 3.12 Illustration of the mesh generated in saw-toothed air gap SRM

### b) Error distribution

A correct analysis is determined by finite element models with small local error in the air gap regions. Therefore, the error distribution in the air gap was checked for each of the studied profiles. Data necessary for analysis were read at various locations across and along the air gap. These locations are defined in Appendix B.1. The result was that the maximum local error was less than 5[%] of the local flux density. The maximum error was read in elements surrounding the sharp corners of the Shark profiles. This is illustrated by the distribution of the local error along saw-toothed and square-wave Shark profile from Appendix B.2. The comparison of the average air gap flux density obtained with and without accounting for the mesh error, shows that there are no substantial differences (Appendix.B.2). Thus the model was considered satisfactory.

## 3.4 Analysis of the Shark air gap Switched Reluctance Motor

In this section, various Shark air gap SRM are analysed using the finite element solution obtained from the discussed FEMs. The main dimensions of the analysed Shark SRM are given in Appendix A.2. The flux linkage of the aligned rotor position, the flux linkage gain and the air gap flux density distribution are considered as variables of interest for this analysis. The data in the air gap are read between points 1-4 in each of the four layers, shown in Appendix B.1. However, in this section only the average values of the air gap flux density are used, the details of the air gap flux density distribution in each of the air gap layer can be found in Appendix B.2.

Based on the described FEM, finite element solutions for different configurations of Shark profiles were calculated and used to study the dependence of the magnetic behaviour of the Shark SRM on the dimensions of the Shark tooth. The FEA solutions are also compared with the data from chapter 2, and used to amend some of the results.

Three situations are studied in this section:



- 1) variable angle  $\beta$  (or height  $h_{shk}$ ) at Shark tooth pitch,  $l_{shk}$ , constant
- 2) variable tooth pitch,  $l_{shk}$  at angle,  $\beta$ , constant
- 3) variable angle  $\beta$  (or tooth pitch,  $l_{shk}$ ) at height of the Shark tooth,  $h_{shk}$ , constant

### 3.4.1 Influence of the height, $h_{shk}$ at length of the Shark tooth, $l_{shk}$ , constant

The influence of the angle  $\beta$  on the magnetic behaviour of the Shark SRM, having tooth pitch constant is documented in this sub-section. The configurations to be studied are illustrated in Fig. 3.14. The lengths,  $l_t$  and  $l_e$  have been defined in chapter 2 as being the length of one side of the Shark tooth, and the active region on one side of the Shark tooth respectively. Points 1 and 4 from Fig. 3.14 a) and 1, 2, 3 and 4 from Fig. 3.14 b) are used to define the lines along which data from FEA are read. A detailed illustration may be found in Appendix B.1.

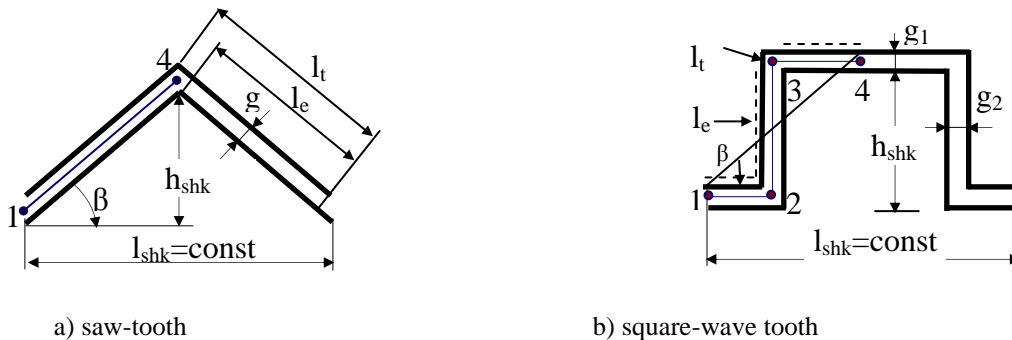


Fig. 3.14 Shark teeth analysed

The field patterns of the two Shark air gaps are illustrated in Fig.3.15. These show that the flux lines curve around the corners of the Shark profiles, and cross the air gap perpendicularly. Therefore, the regions around the vertices of the Shark air gap are crossed by fewer flux lines than the rest of the air gap is. This confirms the prediction from chapter 2, where  $l_e$  was defined and calculated for various Shark SRM showing that the effective length of the air gap region is less than the ideal length of the Shark air gap region. This observation will be used later in this sub-section.

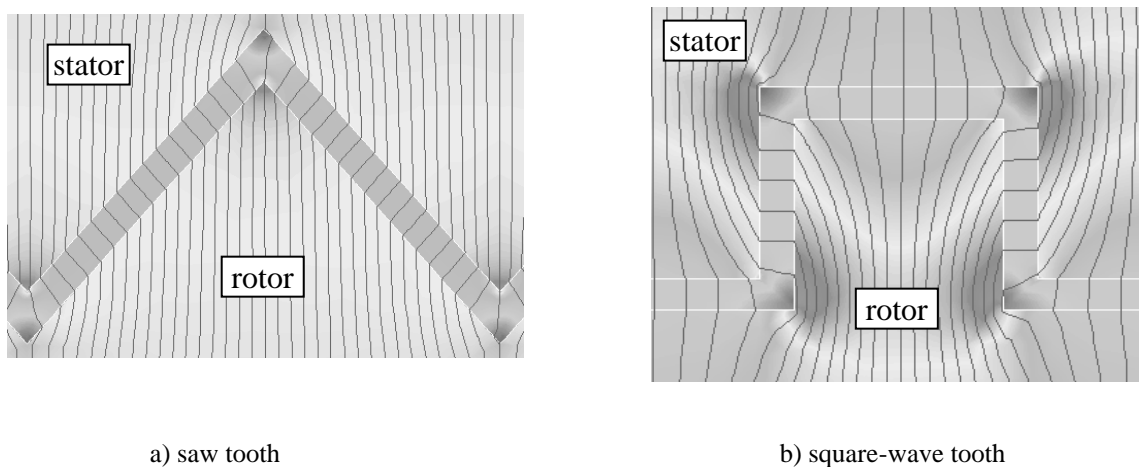


Fig. 3.15 Illustration of the field pattern in saw-toothed and square-wave air gap

This analysis considers as evaluation indicators the flux linkage characteristics and the flux linkage gain. The air gap flux density distribution is used to support the explanations.

### (a) Static flux linkage and flux linkage gain

The static flux linkage characteristics, calculated for saw-toothed and square-wave air gap SRM, having constant tooth pitch and different angles  $\beta$ , are shown in Fig. 3.16 and Fig. 3.17.

From their analysis, it results that, at all current values, the Shark SRM with saw toothed air gap ( $\beta \neq 0$  in Fig. 3.16) produces more flux linkage than the CSRSM ( $\beta = 0$  in Fig. 3.16). Keeping the Shark tooth pitch constant, more flux linkage may be obtained by increasing  $\beta$  or the height of the Shark tooth, as it may be seen in Fig. 3.14.

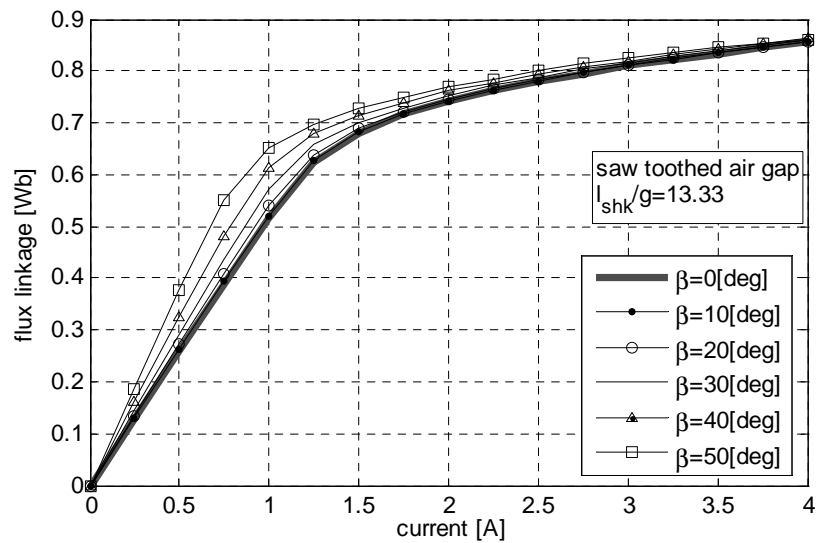


Fig. 3.16 Magnetisation characteristics for saw-toothed air gap SRM with constant tooth pitch,  $l_{shk}$ , and variable angle  $\beta$

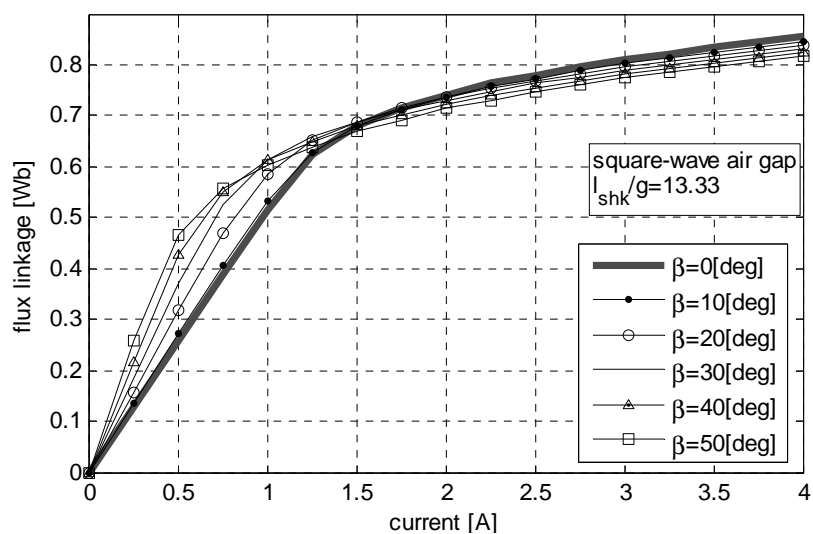


Fig. 3.17 Magnetisation characteristics for square-wave air gap SRM with tooth pitch,  $l_{shk}$ , constant and angle  $\beta$ , variable

In the case of the square-wave air gap SRM ( $\beta \neq 0$  in Fig. 3.17) it can be observed that at low current (e.g.  $i=0.5$  [A]) the Shark SRM produces more flux linkage than the corresponding CSRSM ( $\beta = 0$  in Fig. 3.17). The flux linkage produced by any Shark SRM, having square-wave air gap, may be improved by increasing the angle  $\beta$ . On the other hand, at high current (e.g.  $i=3$ [A]) the flux linkage of the CSRSM exceeds the flux linkage of the Shark SRM. The magnetisation characteristics of the SRM with square-wave air gap cross over the magnetisation characteristic of the CSRSM and, less flux linkage is induced in the magnetic circuit by increasing  $\beta$ .

The current value, at which the crossing between the characteristics of Shark SRM and the CSRSM occurs, decreases as  $\beta$  increases. This may be explained by the influence of the saturation in the Shark teeth.

From Fig. 3.16 and Fig. 3.17 it may be observed that the saw-toothed and the square-wave air gap SRMs exhibit different magnetic behaviour, when the excitation conditions are identical. Two facts may be noted:

*O1: The difference between the two Shark air gaps consists in that the flux linkage characteristic of the square-wave air gap SRM crosses over the characteristic of the CSRSM, whilst the flux linkage characteristic of the saw-toothed air gap SRM does not.*

The improvement of the flux linkage is assessed by the flux linkage gain, which is calculated, at any current, by the ratio of the flux linkage at  $\beta \neq 0$  to the flux linkage at  $\beta = 0$ . The flux linkage gain is calculated for all the configurations studied and it is plotted for saw-toothed and square-wave air gap in Fig. 3.18 and Fig. 3.19 respectively.

From these figures it results that the flux linkage gain decreases with the increase in excitation current and that at low currents the flux linkage gain of the square-wave air gap SRM exceeds that of the corresponding saw-toothed air gap SRM. These results conform to the predictions made in chapter 2.

*O2: It can also be observed that the flux linkage gain of the square-wave air gap falls quicker with the increase in current, than the flux linkage gain of the saw-toothed air gap does.*

The observations *O1* and *O2* are related and they may be explained by the field pattern in each Shark configuration, illustrated in Fig. 3.15. Their examination shows that at a given current, the iron material of the Shark tooth is worked at an increased flux density compared the rest of the iron regions of the magnetic circuit. This means that more magnetomotive force (MMF) drops across these regions and consequently the flux density in the air gap decreases. The field pattern in saw-toothed and square-wave air gap with identical excitation, show that the regions with increased flux density are located at the tip of the saw tooth, but at the root of the square-wave tooth. Their different location is the only difference between the two shapes and therefore it may be claimed that it causes the different behaviour of the two Shark SRMs. The flux density distribution in the air gap may be used to explain the influence of these local saturation regions on the flux linkage value.

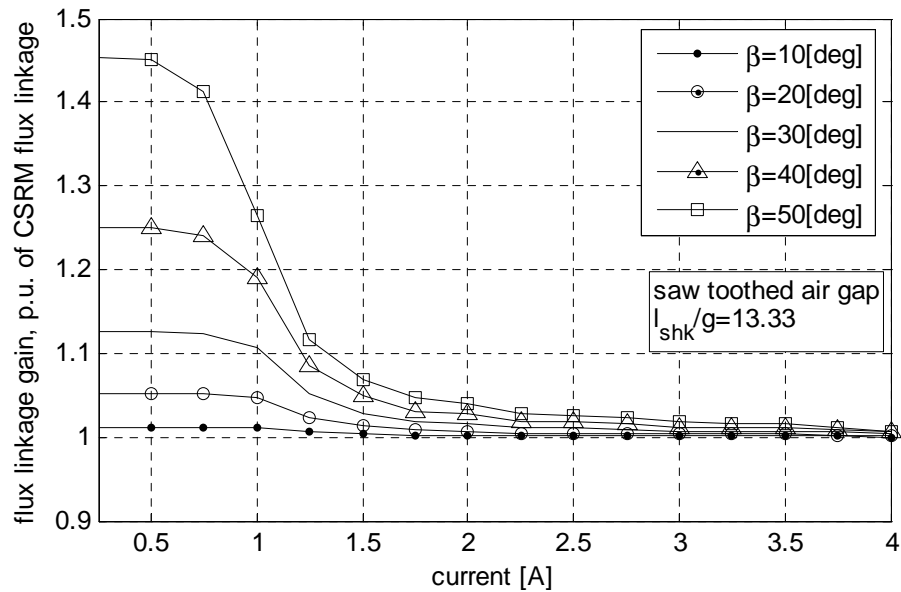


Fig. 3.18 Flux linkage gain calculated for saw-toothed air gap SRM

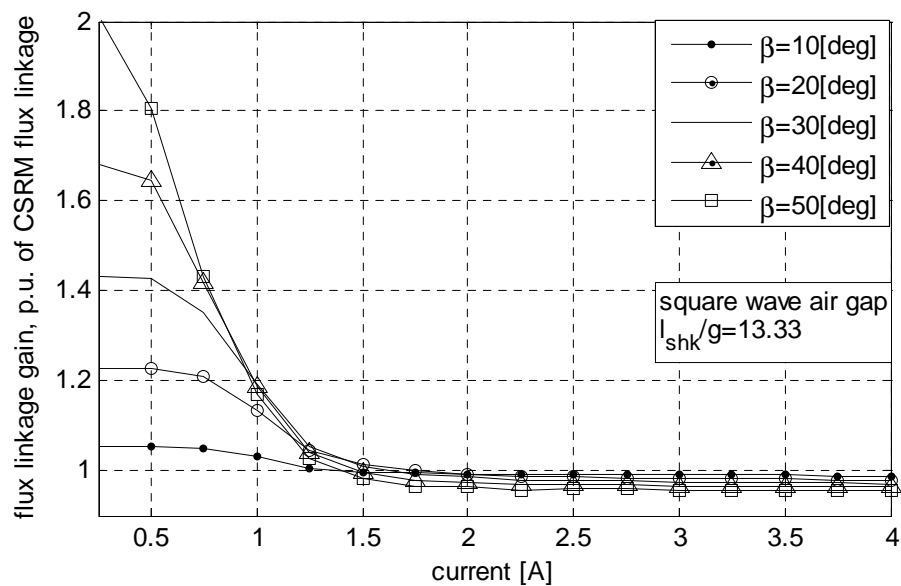


Fig. 3.19 Flux linkage gain for square-wave air gap SRM

**(b) Air gap flux density distribution**

In this sub-section, the magnetisation characteristics are explained using the distribution of the air gap flux density. The influence of the location of the regions with increased flux density is also discussed. The discussion considers the situations where low and high current is fed into the windings of the SRMs.

At low current, the flux linkage values from Fig.3.16 and Fig. 3.17 are determined by both the air gap flux density and the surface of the air gap crossed by the flux lines (proportional to the length  $l_e^{total}$ , defined in chapter2). To identify the influence of each of these two elements, on the flux

linkage value, consider two Shark configurations, having identical tooth pitch and two different angles,  $\beta$ , given in Table 3.1. The ratio of the corresponding flux linkages may be approximated by:

$$\frac{\psi^{(1)}}{\psi^{(2)}} \approx \frac{B_g^{(1)}}{B_g^{(2)}} \cdot \frac{l_e^{total(1)}}{l_e^{total(2)}} \quad (3.4)$$

$\underbrace{\hspace{1.5cm}}_{\text{flux densities ratio}} \cdot \underbrace{\hspace{1.5cm}}_{\text{air gap region lengths ratio}}$

where indexes 1 and 2 refer to two different tooth pitches,  $\psi$  is the flux linkage,  $B_g$  is the average air gap flux density and  $l_e^{total}$  is the total length of the Shark teeth which is uniformly crossed by the flux lines (see chapter 2).

Each factor from equation (3.4) may be calculated. From finite element solutions, the air gap flux density distribution is obtained for any wanted Shark configuration as illustrated in Fig.3.20. The flux density in the saw-toothed air gap drops around the vertices of the Shark profile (points 1 and 4), this drop being more significant at bigger angles  $\beta$ . From these data, an equivalent flux density corresponding to a uniform distributed field may be calculated. For the considered configurations, the equivalent flux densities are given in Table 3.1.

The equivalent length of the two configurations may be determined using equation (2.18) from chapter 2. The calculated values are given also in Table 3.1. It results that increasing the angle,  $\beta$ , it is obtained a longer equivalent lamination stack, but a smaller average air gap flux density.

Table 3.1 Calculated active length of the saw-toothed Shark profile and air gap flux density for 2 different Shark SRMs, having tooth pitch constant,  $l_{shk}/g = 13.33$

$\beta$	$l_e^{total}$ [mm]	$B_g$ [T]
10	59	0.56
40	70	0.54

From these data, the flux linkage ratio of the two configurations may be calculated as shown in equation (3.5)

$$\frac{\psi^{(1)}}{\psi^{(2)}} \approx \frac{0.56}{0.54} \cdot \frac{59}{70} = 1.03 \cdot 0.84 = 0.86 \quad (3.5)$$

$\underbrace{\hspace{1.5cm}}_{\text{flux density ratio}} \cdot \underbrace{\hspace{1.5cm}}_{\text{length ratio}}$

The result indicates that the configuration with smaller angle  $\beta$  produces less flux linkage.

Extensive calculations indicated that this result may be generalised to any magnetic circuit having saw-toothed air gap, assuming that the iron is not saturated.

Combining all these data, it may be concluded that at low current, the flux linkage of a saw-toothed air gap SRM is improved due to the increase in the air gap area. The air gap flux density is smaller in Shark configuration with bigger angle  $\beta$ . This may be seen as an advantage if radial force or noise production is considered.

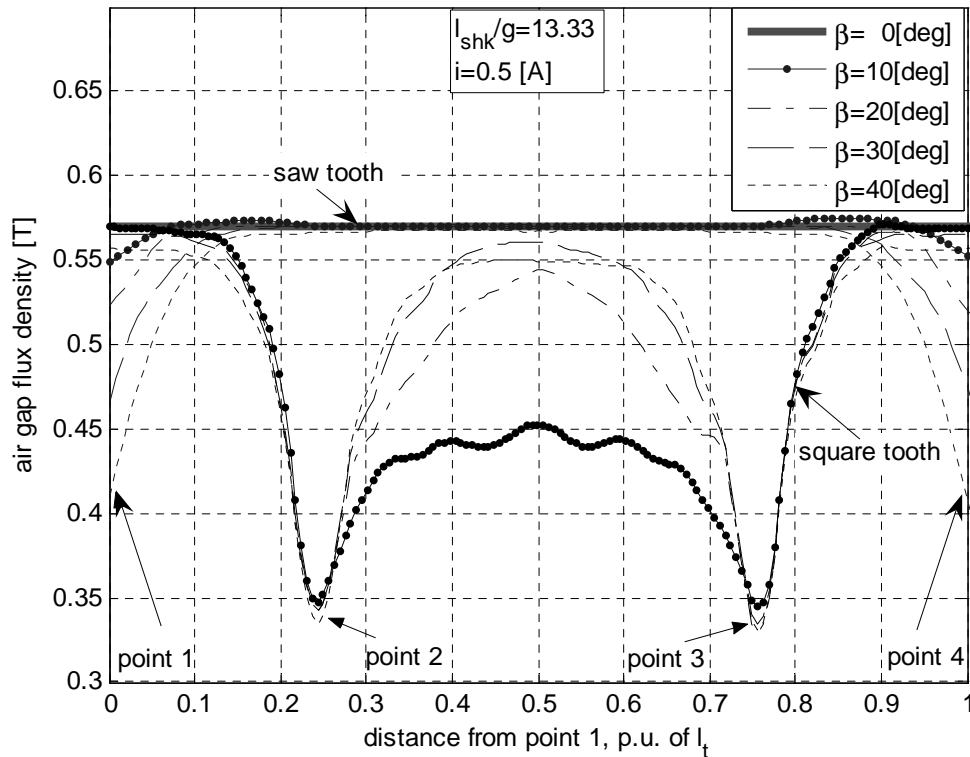


Fig. 3.20 Average flux density distribution in saw toothed and square wave air gap, at  $i=0.5$  [A].

The square wave tooth offers the advantage of a longer air gap region. The sum of lengths between points 1-2 and 3-4 is equal to the Shark tooth pitch,  $l_{shk}$ . As it may be seen from Fig. 3.20, the flux density along these faces of the Shark air gap is only slightly smaller than the flux density in the CSRSM (4 % point less). Thus, the improvement of the flux linkage of the square-wave air gap SRM is mainly due to the contribution of the lateral sides of the Shark tooth (region between points 2 and 3 and 4 and 1 in Fig. 3.20).

The square-wave air gap exhibits quite an opposite behaviour compared to that of the saw-toothed air gap, because here the air gap flux density increases with increasing angle  $\beta$ . *This combined with the increase in the air gap area makes that the flux linkage of the square-wave air gap exceeds the flux linkage of the corresponding saw-toothed air gap.*

*At high current, the air gap flux density distribution is shown in Fig. 3.21 for both saw-toothed and square-wave SRMs.*

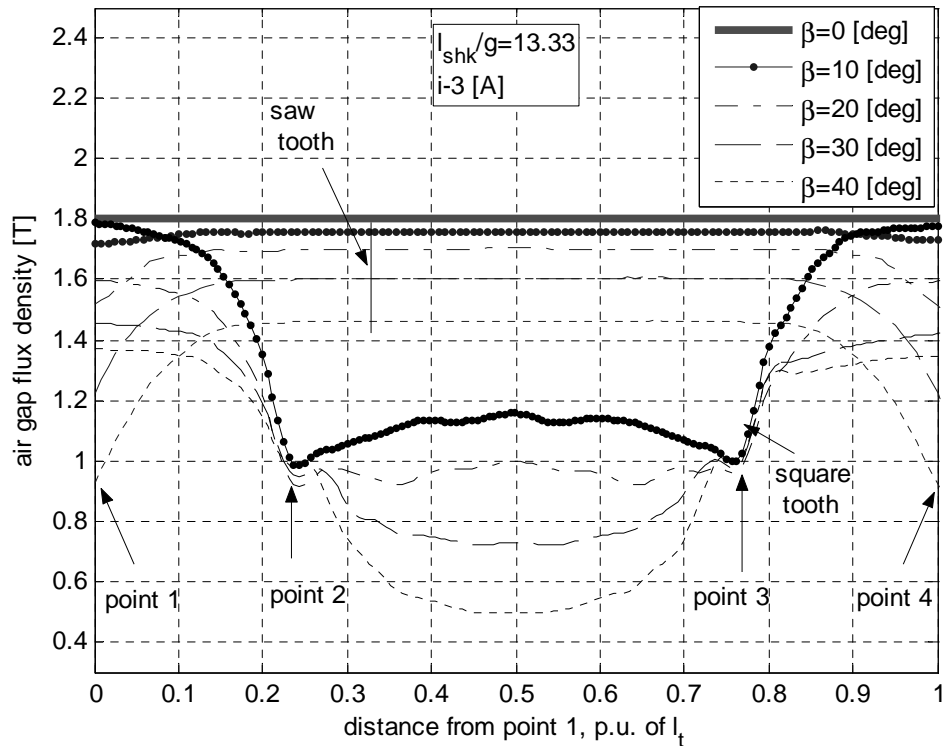


Fig. 3.21 Average flux density distribution in saw toothed and square wave air gap, at  $i=3$  [A]

In the saw-toothed air gap machine, the finite element solutions verify that the relationship between the average air gap flux density in the CSRSM,  $B_g(0^\circ)$ , and the average flux density in the Shark SRM,  $B_g(\beta)$ , is given by equation (3.6).

$$\frac{B_g(\beta)}{B_g(0^\circ)} = \cos\left(\beta \cdot \frac{\pi}{180}\right) \quad (3.6)$$

This relationship was verified for different saw-toothed air gap SRMs and the results are summarised in Table 3.2. This, together with the fact that the ratio of the lengths of the air gap regions of Shark SRM and CSRSM is  $1/\cos(\beta)$ , explains why the flux linkage characteristic of the saw air gap SRM (which is proportional to the air gap flux density and to the air gap area) does not cross over the characteristic of the CSRSM (Fig. 3.16).

Table 3.2 Illustration of the relationship between the flux density in the saw-toothed air gap,  $B_g(\beta)$  and that in the corresponding cylindrical air gap,  $B_{g0}$ . Verification of equation (3.6)

$\beta$ [deg]	$\beta=0$	$\beta=10$	$\beta=20$	$\beta=30$	$\beta=40$	$\beta=45$
$B_g(0^\circ) \cdot \cos\beta$ [T]	1.79	1.76	1.68	1.55	1.37	1.26
$B_{g(\beta)}$ [T]	1.79	1.74	1.68	1.55	1.38	1.27

In the square-wave air gap SRM, the air gap flux density along the lateral sides of the air gap- that is between points 2 and 3- drops as  $\beta$  is increased (Fig. 3.21). This is because of the increased flux density in the region of the root of the Shark tooth. The field patterns, illustrated in Fig. 3.22, show that, *at low current*, the flux lines are uniformly distributed along the Shark tooth, except at the regions of the vertices (see also Fig.3.19).

*At high currents* there are more flux lines crossing the radial air gap,  $g_1$ . This is because the saturated regions located at the root of the Shark tooth causes the flux lines, which cross the axial air gap, to see an equivalent air gap consisting of the mechanical air gap,  $g$ , and twice the height of the saturated region. Simultaneously the flux lines crossing the radial air gap,  $g_2$ , see an equivalent air gap consisting of mechanical air gap,  $g$  and only once the height of the saturated region. Therefore, at high currents, the square-wave air gap SRM produces less flux linkage than the CSRSM does.

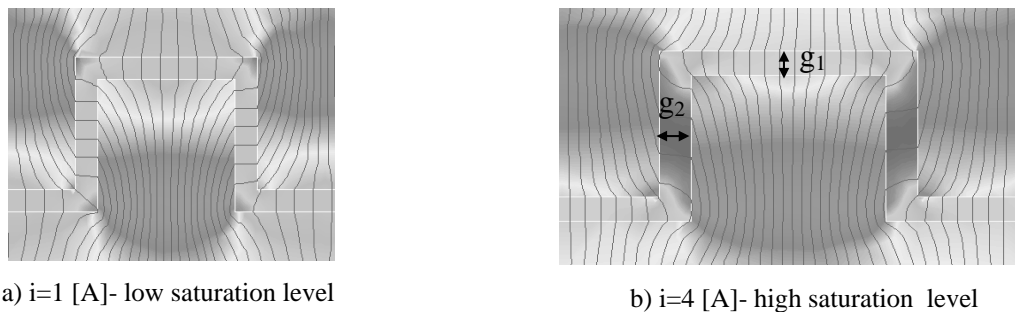


Fig. 3.22 Field patterns in a square-wave SRM at different current values ( $l_{shk}/g=13.34$ ,  $\beta=40$  [deg])

### (c) Amendment of the results of chapter 2

If the flux linkage gain,  $k^{FEA}$ , calculated by finite element analysis for low current is compared with the flux linkage gain,  $k^{linear}$ , determined in chapter 2 (see Table 3.3), it may be noticed that for the saw toothed air gap, the agreement between these two values is good at small values of  $\beta$ . At greater values of  $\beta$ , the difference between the two values is greater. This difference increases which increasing angle  $\beta$ . For the square-wave air gap SRM, the flux linkage gain calculated by the two methods shows disagreement at all  $\beta$ .

Table 3.3 Differences between the linear and FEA results.

$i=0.5$ [A]	factor	saw toothed air gap	square-wave air gap
$\beta=10$ [deg]	$k^{FEA}$	1.01	1.05
	$k^{linear}$	1.015	1.18
$\beta=20$ [deg]	$k^{FEA}$	1.052	1.23
	$k^{linear}$	1.064	1.36
$\beta=30$ [deg]	$k^{FEA}$	1.13	1.43
	$k^{linear}$	1.15	1.58
$\beta=40$ [deg]	$k^{FEA}$	1.25	1.65
	$k^{linear}$	1.3	1.84



These differences are explained by that in chapter 2, the air gap flux density was assumed uniformly distributed, and this is not the case as it may be seen from the finite element solutions shown in Fig. 3.15, Fig.3.20 and 3.21.

To verify this claim, the following considerations were made. The flux linkage of the Shark tooth was estimated first using the real distribution obtained from FEA (Fig. 3.20). Then the flux linkage of the Shark tooth was calculated assuming uniform distribution of the air gap flux density. Their ratio, *ratio 1* is then compared with the ratio  $k^{FEA}/k^{linear}$ , determined with data from Table 3.1 and called *ratio 2*. The results are given in Table 3.4 and they show a perfect match.

Table 3.4 Flux linkage gain ratio

	ratio 1	ratio 2
$\beta=10$ [deg], $i=0.5$ [A]	0.99	0.99
$\beta=20$ [deg], $i=0.5$ [A]	0.99	0.98
$\beta=30$ [deg], $i=0.5$ [A]	0.98	0.97
$\beta=40$ [deg], $i=0.5$ [A]	0.96	0.96

The differences for the square wave tooth are also due to the assumption of uniformly distributed air gap flux density made in chapter 2. Because the reasons are similar to those presented for the saw-toothed air gap, they are not discussed in this section.

#### (d) Summary

In this sub-section, it was shown that for a constant tooth pitch and variable angle,  $\beta$ , the saw toothed air gap produces, at all current values, more flux linkage than the CSRSM. This improvement is due to the increase in air gap area. The flux density in the air gap is lower than in the corresponding CSRSM. This may be a benefit if the radial force or the noise is considered.

For identical geometrical conditions, the square-wave air gap produces, at low current, more flux linkage than the CSRSM (Fig. 3.16 and Fig. 3.17, Table 3.3). Increasing the excitation current, the benefits of the square-wave air gap SRM are lost due to the local saturation of the regions of increased flux density, located at the root of the square teeth (Fig. 3.16 and Fig. 3.17).

### 3.4.2 Influence of the Shark tooth pitch, $l_{shk}$ , for constant angle, $\beta$

The influence of the Shark tooth pitch, on the behaviour of the Shark SRM is documented in this sub-section. The structures to be studied are illustrated in Fig. 3.23.

The relation between the geometrical variables is  $\tan \beta = \frac{2 \cdot h_{shk}}{l_{shk}}$ , which means that for constant  $\beta$ , a change in the tooth pitch causes a corresponding change of the height of the Shark tooth. The geometrical dimensions in Fig. 3.23 have the same meaning as in the preceding sub-section and the analysis follows the same method.

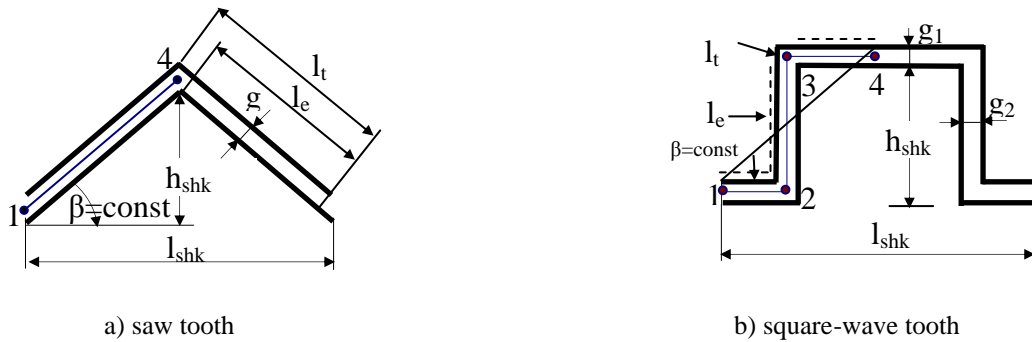
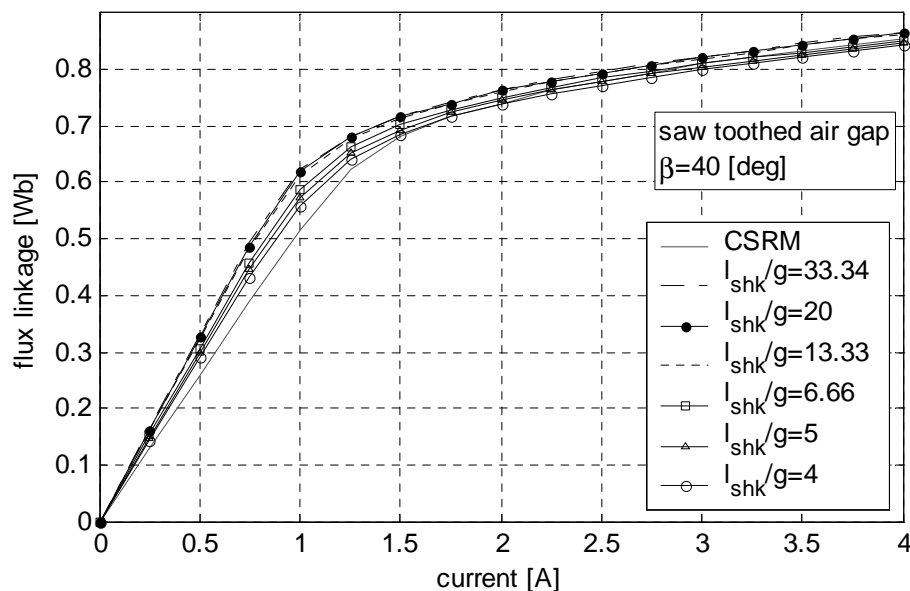


Fig. 3.23 Shark teeth analysed

### (a) Flux linkage characteristics and flux linkage gain

The flux linkage characteristics calculated using FEA for saw-toothed and square-wave air gap SRM, having angle  $\beta$  constant, are shown in Fig. 3.24 and Fig. 3.26 respectively.


 Fig. 3.24 Magnetisation characteristics of saw-toothed air gap SRM with constant  $\beta$  and variable tooth pitch.

From Fig.3.24, it may be observed that the flux linkage characteristics of any saw-toothed Shark SRM, having  $l_{shk}/g$  bigger than 13.33, are almost identical. This can be seen better in the corresponding flux linkage gain characteristics shown in Fig. 3.25.

The flux linkage curves of the Shark air gaps, having  $l_{shk}/g$  smaller than 13.33 (Fig. 3.24) are distinct from each other as shown also by the corresponding flux linkage gain from Fig.3.25.

These observations indicate that for a constant angle,  $\beta$ , there is a critical tooth pitch,  $l_c$ , which determines the transition between different behaviours of the saw-toothed air gap SRM. This critical value may be determined from the condition that the active region of the air gap ( $l_e$ )

represents 90% of the total length of the Shark tooth ( $l_t$ ). This is confirmed by the finite element solutions calculated for different Shark configurations. For data corresponding to the magnetisation characteristics from Fig. 3.24, this is illustrated in Table 3.5.

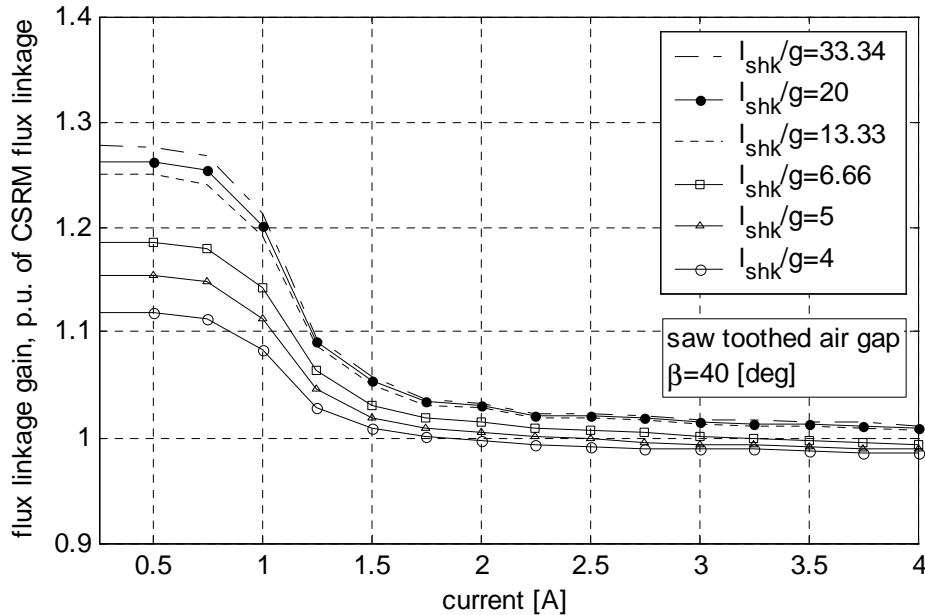


Fig. 3.25 Flux linkage gain calculated for saw-toothed air gap SRM

To obtain these results, equation (2.18), from chapter 2 was used. This equation describes the relationship between  $l_c$  and  $l_t$ . In [58], this equation was also used to set the geometrical limitations of the analytical model of Shark SRM.

Table 3.5 Determination of the critical tooth pitch for a saw-toothed air gap SRM, having angle  $\beta = 40$  [degree]

$l_{shk}/g$ [p.u]	33.34	20	13.33	6.66	5	4
$l_c/l_t$ [%] <sup>4</sup>	96	94	90	81	74	67

For the square-wave air gap SRM, the influence of the Shark tooth pitch is more obvious. Unlike the saw toothed air gap SRM, the magnetisation characteristics of the square-wave air gap SRM are distinct for any value of the Shark tooth pitch (Fig. 3.25). For tooth pitch longer than a critical length,  $l_c$ , the flux linkage of the Shark SRM may be improved by reducing the tooth pitch. Increasing the current, the magnetisation characteristics of the square-wave Shark SRM cross over that of the CSRSM and less flux linkage is produced by decreasing the tooth pitch.

For Shark tooth pitch shorter than the critical length,  $l_c$ , the flux linkage of the Shark SRM decreases as the tooth pitch is reduced when low current is supplied to the excitation windings. This is shown in Fig. 3.27 for  $l_{shk}/g$ , of 13.33, 6.66 and 5. As the current is increased the magnetisation characteristics of the Shark SRM cross over the characteristic of the CSRSM. However, the tendency observed at low current is now maintained for large currents – that is the

<sup>4</sup>  $l_c$  is calculated by equation (2.18), chapter 2

$l_t$  is calculated by equation (2.15), chapter 2

flux linkage decreases as the tooth pitch decreases. The origin of this behaviour is, as shown for the saw-toothed air gap, the extent of the overlap between the sides of stator and rotor Shark teeth. The length,  $l_e$ , of the Shark teeth regions effectively used by the flux lines depends, at a specified angle, on the length of the Shark pitch (equation 2.40, chapter 2).

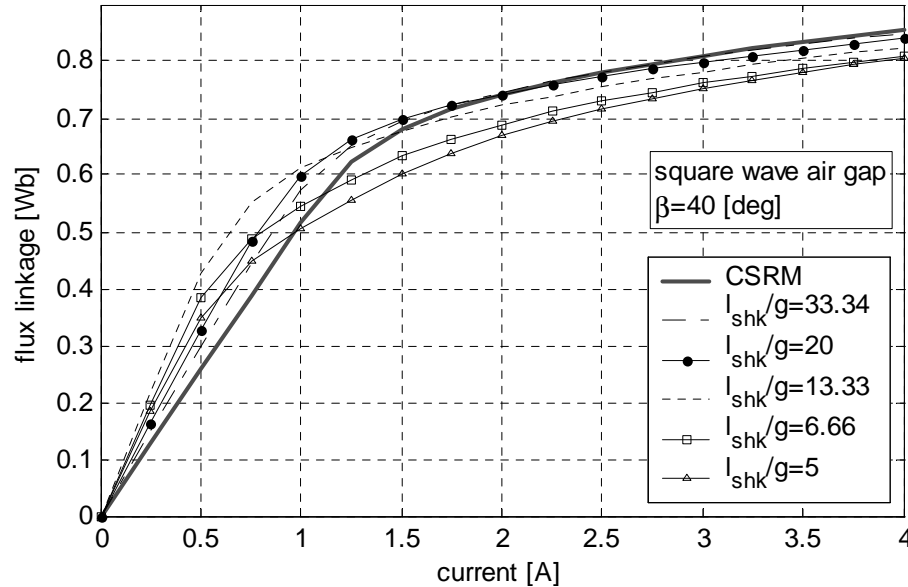


Fig. 3.26 Magnetisation characteristics of square-wave air gap SRM with constant  $\beta$  and variable tooth pitch.

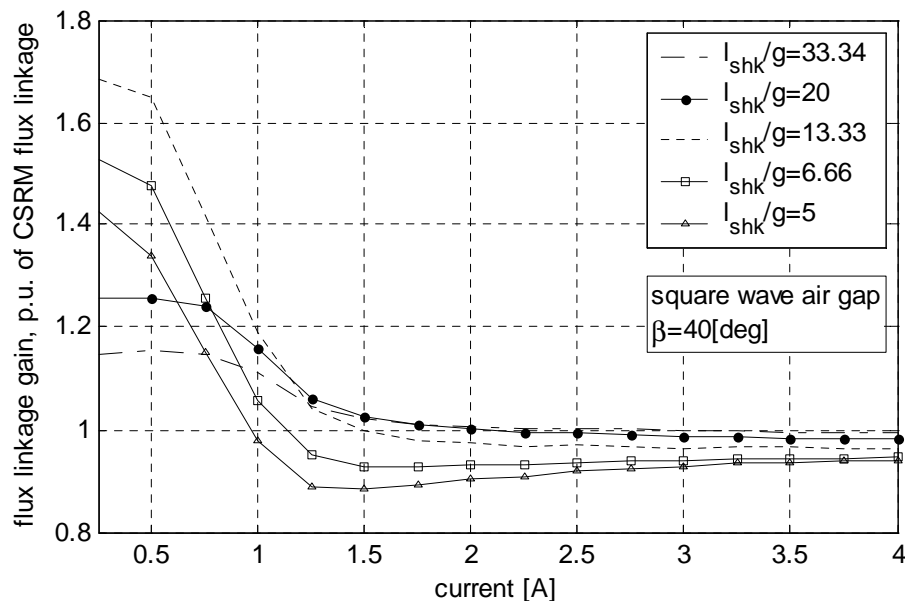


Fig. 3.27 Flux linkage gain calculated for square-wave air gap SRM

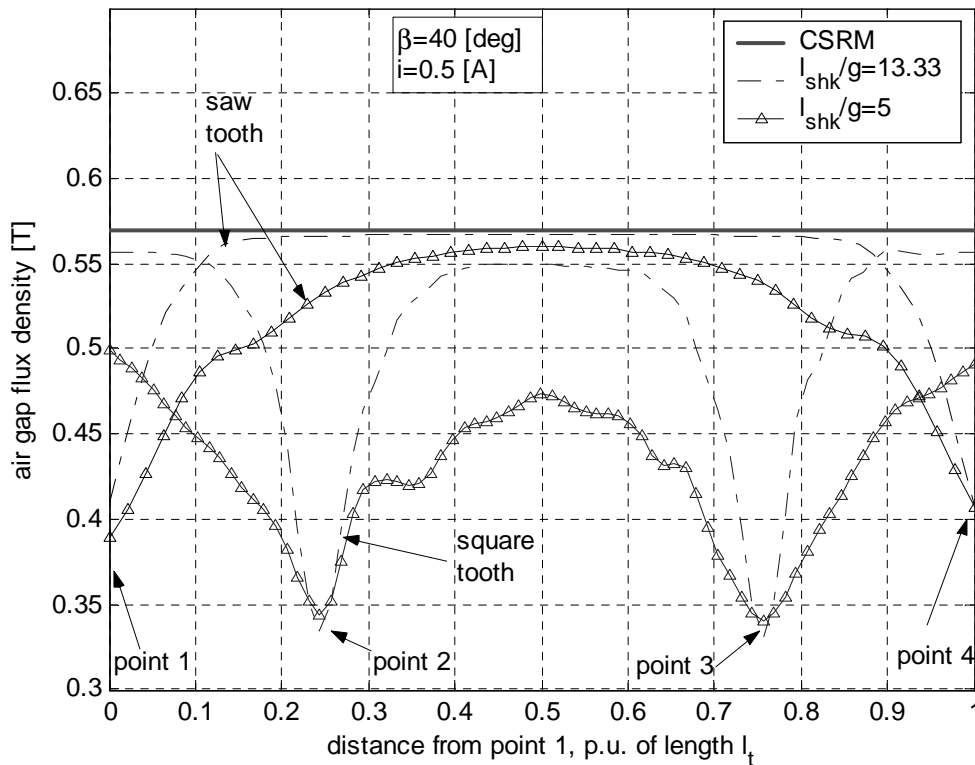
If length,  $l_e$ , is calculated and expressed in percent of the total length,  $l_t$ , then the data of Table 3.6 are obtained. From these data and from the characteristics shown in Fig.3.26 and Fig.3.27, the ratio  $l_{shk}/g$  of 13.33 is identified as critical value, for  $\beta=40$  [degree]. This corresponds 84 % of the air gap area is effectively used by the flux lines.

Table 3.6 Determination of the critical tooth pitch for a square-wave air gap SRM, having  $\beta$  constant

$l_{shk}/g$ [p.u.]	33.34	20	13.33	11	6.66	5
$l_e/l_t$ [%] <sup>5</sup>	93	89	84	80	67	56

### (b) Flux density distribution

The distribution of the air gap flux density provides the background for this discussion. In both the saw toothed and the square-wave air gap, the air gap flux density drops in the vicinity of the corners –that is points 1 and 4 in saw toothed air gap and points 2 and 3 in square-wave air gap in Fig. 3.28. It can be observed that the extent of these regions is bigger at smaller Shark tooth pitch, which means that the area of the air gap crossed effectively by the flux lines is reduced by applying a shorter tooth pitch. The influence of the Shark tooth pitch at constant  $\beta$  is more significant in the square-wave air gap SRM than it is in the saw-toothed SRM. This can be seen in Fig. 3.28.

Fig. 3.28 Average flux linkage distribution in saw-toothed and square wave air gap, at  $i=0.5$  [A]

At high current, the discussion of sub-section 3.4.1 is valid for the saw-toothed air gap. This discussion is supported by the field patterns shown in Fig. 3.22 at low and high current for the square-wave air gap. In the case of the square-wave air gap SRM, the flux density along the lateral face of the tooth is smaller for a shorter tooth pitch (Fig. 3.29). This is explained by that there is less material in the Shark teeth of the Shark SRM with shorter tooth pitch. Therefore, the iron will carry

<sup>5</sup>  $l_e$  is calculated by equation (2.43), chapter 2

$l_t$  is calculated by equation (2.40), chapter 2

a higher flux density than the rest of the iron regions and the saturation region will be located at the root of the tooth. The reduced permeability of the iron in these regions causes the equivalent air gap seen by the flux lines is equal to the mechanical air gap,  $g$ , plus twice the saturation regions of the root of the tooth.

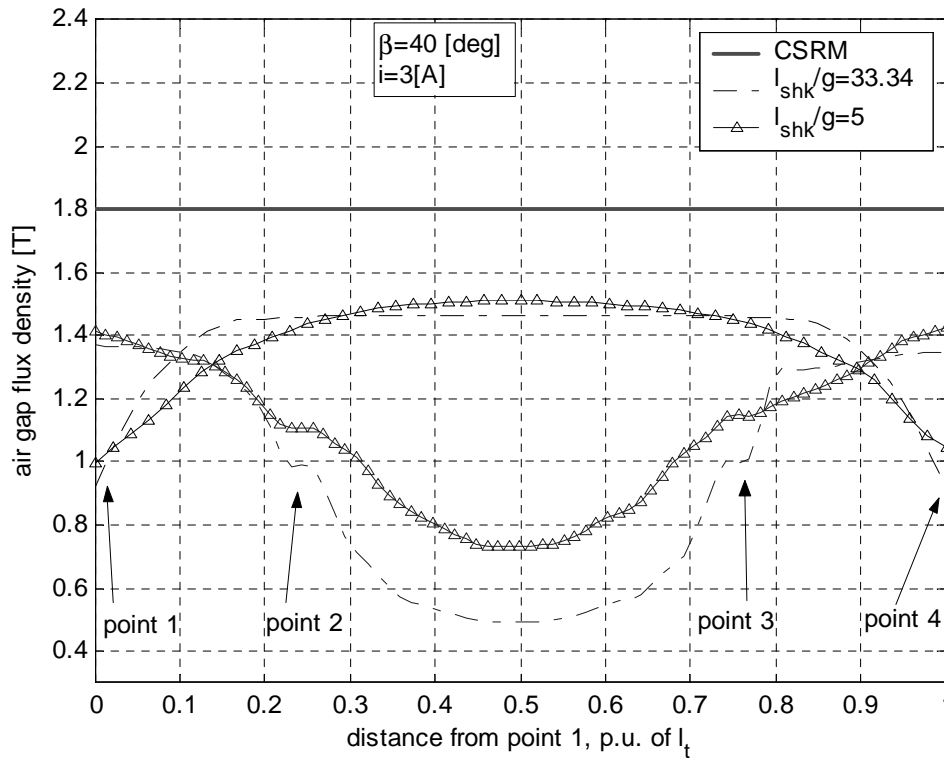


Fig. 3.29 Average flux linkage distribution in saw-toothed and square-wave air gap, at  $i=3$  [A]

### 3.4.3 Influence of the Shark tooth pitch, $l_{shk}$ , at height of the Shark tooth, for constant $h_{shk}$

The influence of the Shark tooth pitch on the magnetic behaviour of the Shark SRM is discussed in this sub-section. The Shark configurations to be discussed are illustrated in Fig. 3.30. The height of the Shark tooth,  $h_{shk}$ , is held constant whilst the Shark tooth pitch,  $l_{shk}$  is varied.

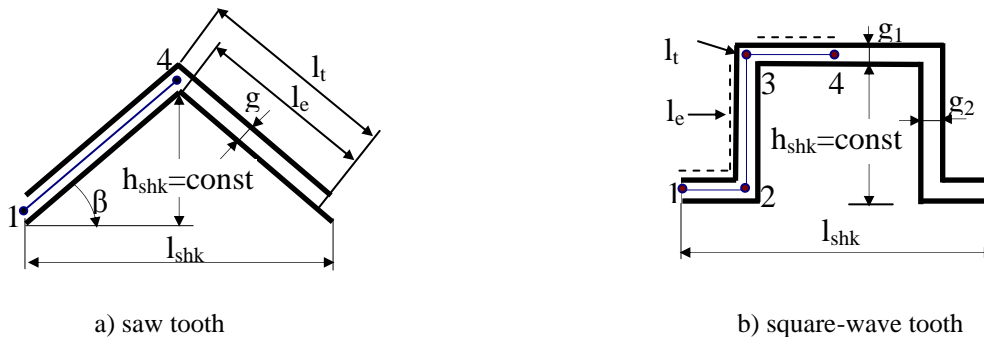


Fig. 3.30 Analysed Shark air gaps

Finite element solutions were obtained for different combinations of height and Shark tooth pitch, for both the saw toothed and the square-wave air gap SRM. From these, only one ( $h_{shk}/h_{pol}=0.23$ ) is

considered as example here. The analysis considers the flux linkage characteristics, the flux linkage gain and the air gap flux density.

### (a) Static flux linkage and flux linkage gain

In Fig. 3.31 and Fig.3.32, the flux linkage characteristics are shown for saw toothed air gap and square-wave air gap respectively. The results reveal that at any current value, the saw toothed air gap SRM produces more flux linkage than the CSRSM and that more flux linkage is produced by reducing the Shark tooth pitch.

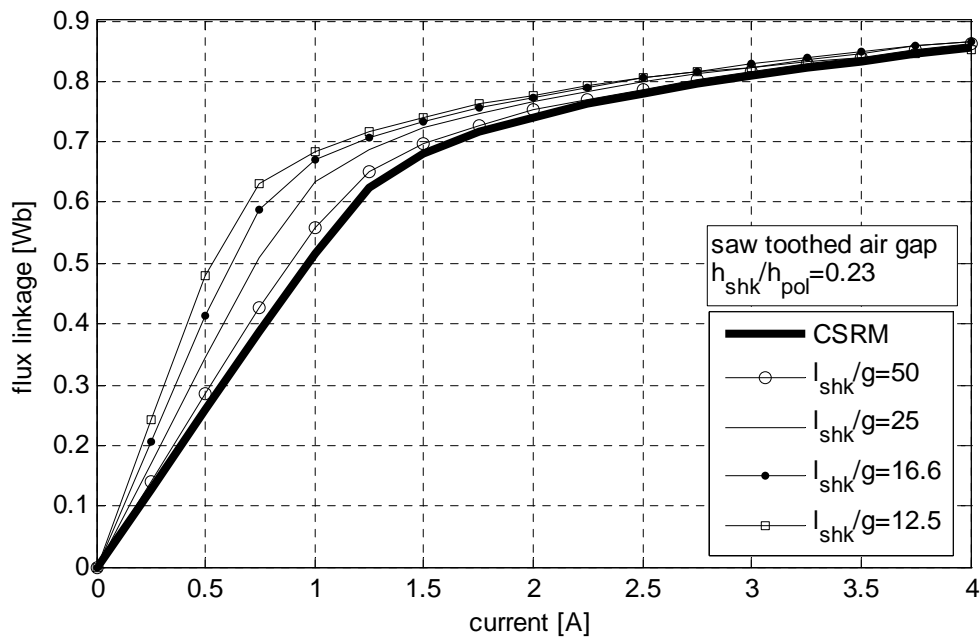


Fig. 3.31 Magnetisation characteristics of saw-toothed air gap SRM, having tooth height constant

The magnetisation characteristics of the square-wave air gap, shown in Fig. 3.32, indicate that at low current, more flux linkage is produced in the Shark SRM with square-wave air gap than in the corresponding CSRSM. The Shark characteristics cross over that of the CSRSM and, at high current, the square-wave air gap SRM produces less flux linkage than the CSRSM.

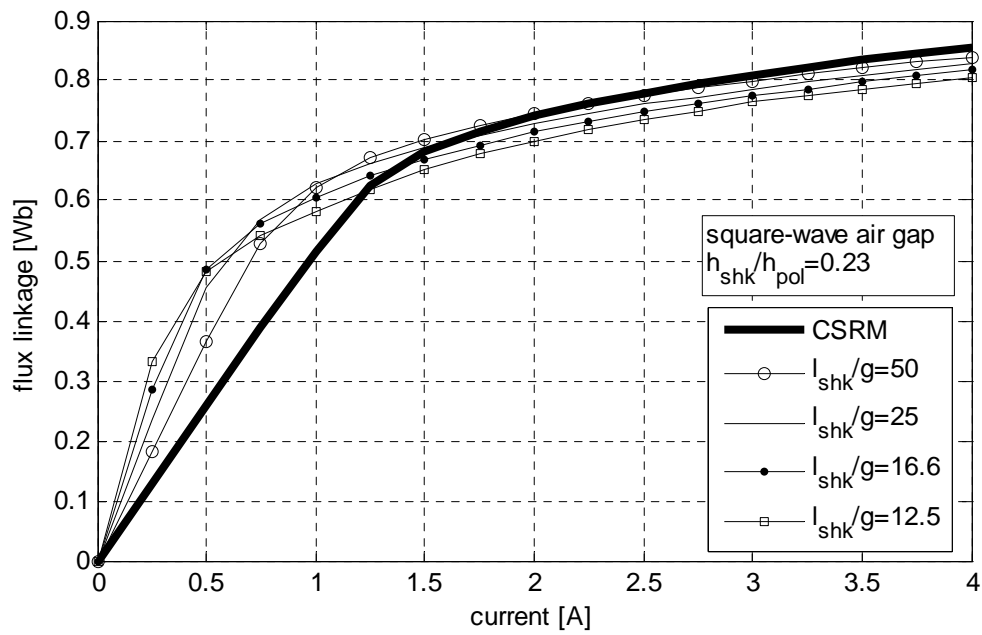


Fig. 3.32 Magnetisation characteristics of square-wave air gap SRM, at constant tooth height

The flux linkage gain is a measure of the performance improvement determined by the Shark air gap. The flux linkage gains of saw-toothed and square-wave air gaps are represented in Fig.3.33 and Fig. 3.34 respectively.

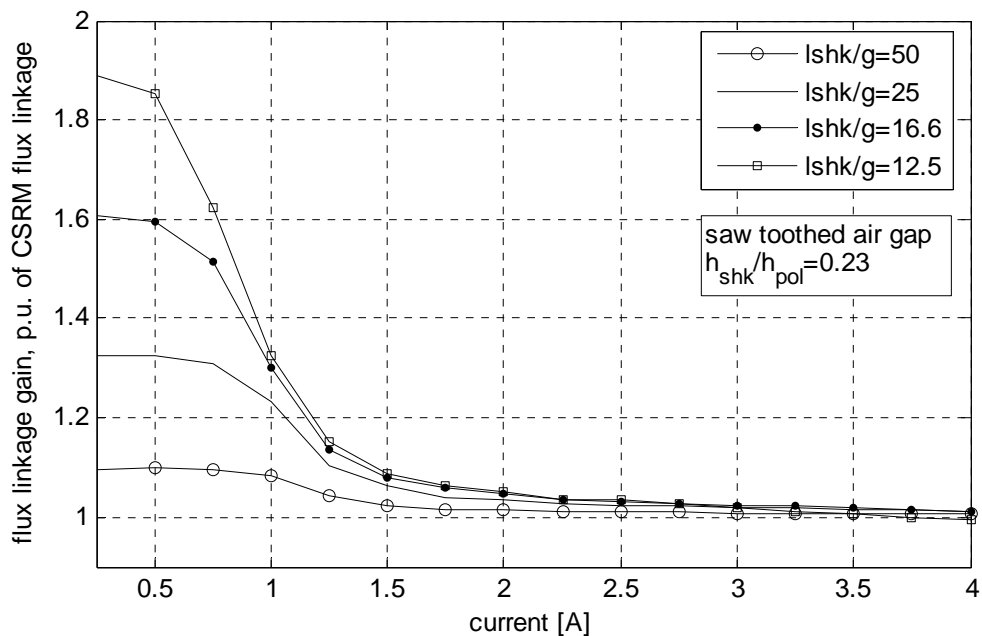


Fig.3.33 Flux linkage gain calculated for the saw-toothed air gap SRM, at constant tooth height

From these figures, it appears that the flux linkage gain falls as the current increases. At low current, the flux linkage gain of a square-wave air gap is bigger than that of a corresponding saw-toothed air gap.



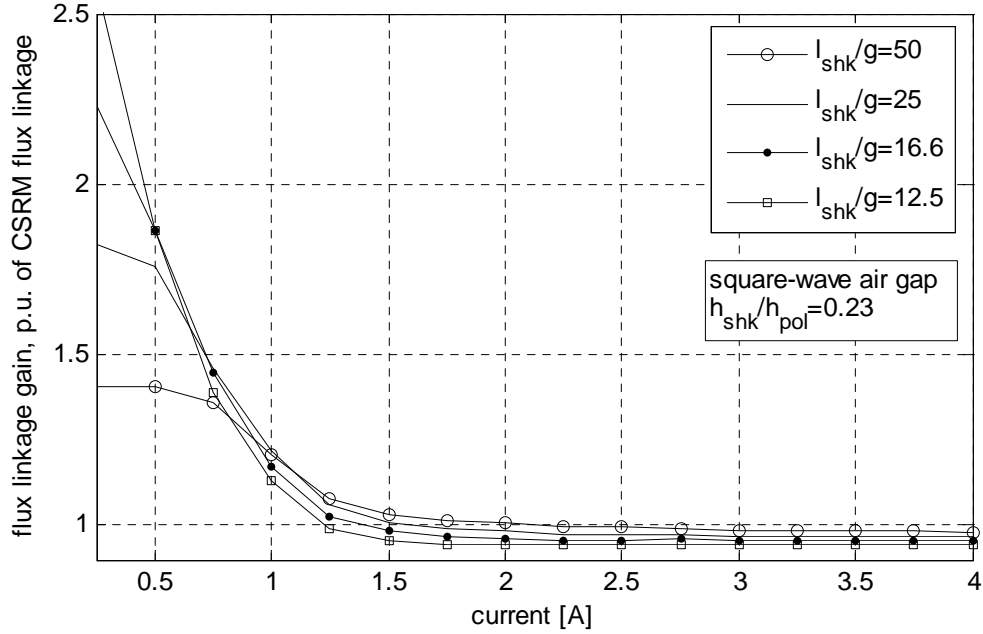


Fig.3.34 Flux linkage gain calculated for the square-wave air gap SRM, having tooth height constant

### (b) Air gap flux density distribution

The air gap flux density distribution is shown in Fig. 3.35 and Fig. 3.36 for the saw-toothed and square-wave air gaps at low and high current.

At low current, it may be observed that the air gap flux density is smaller in configurations with shorter tooth pitch. However, the flux linkage of the Shark SRM with short tooth pitch is better than that of the Shark SRM with a long tooth pitch.

As in the preceding section, the explanation is found in the fact that among the factors, which determine the flux linkage, it is the area of the air gap region, which is proportional to the equivalent length of the Shark stack and is mainly affected by the Shark profile. This is explained by the following considerations.

For the saw-toothed air gap SRM, equation 2.18 from chapter 2 may be expressed as function of the height,  $h_{shk}$ , and Shark tooth pitch,  $l_{shk}$ :

$$l_e^{total} = 2 \times \frac{l_{stk}}{l_{shk}} \times \left( \sqrt{l_{shk}^2 + h_{shk}^2} - g \times \frac{2 \times h_{shk}}{l_{shk}} \right) \quad (3.7)$$

where  $l_e^{total}$  is the total length of the active air gap region, and  $l_{stk}$  is the stack length of the Shark SRM.

This expression shows that the length of the air gap region effectively crossed by the flux lines (of a configuration with constant height) increases as the Shark tooth pitch decreases.

The same tendency may be identified for the square-wave air gap if equation 2.42 is written in terms of Shark height,  $h_{shk}$ , and tooth pitch,  $l_{shk}$ :

$$l_e^{total} = l_{stk} \cdot \left( 1 + \frac{2 \cdot h_{shk}}{l_{shk}} \right) - 4 \cdot g \cdot \frac{l_{stk}}{l_{shk}} \quad (3.8)$$

The average flux densities used in calculations are those shown in Fig.3.35. The results are given in Table 3.7.

Table 3.7 Calculated active air gap length and air gap flux density for 2 different Shark SRMs, having  $h_{shk}$  constant

Shark tooth pitch, $l_{shk}/g$		saw-toothed air gap	square-wave air gap
50	$l_e^{total}$ [mm]	65.1	83.2
13.33		105.2	147.2
50	$B_g$ [T]	0.56	0.53
13.33		0.51	0.41

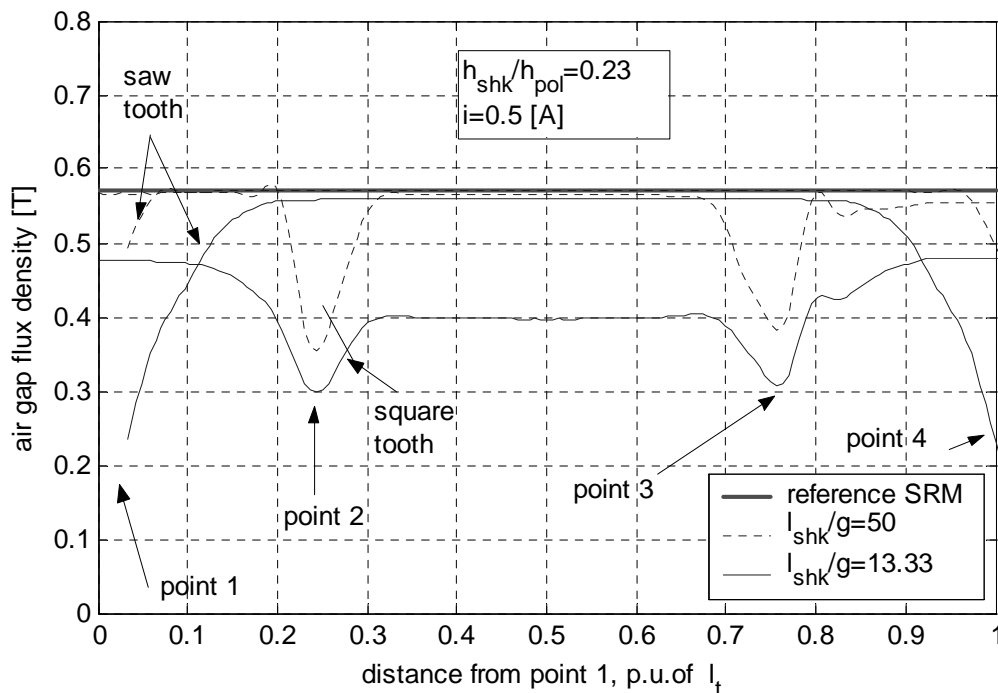


Fig. 3.35 Average flux linkage distribution in saw toothed and square wave air gap, at  $i=0.5$  [A]

With these data the ratio of the flux linkage produced by the two configurations may be approximated by equation (3.4), which becomes:

- *saw toothed air gap:*

$$\frac{\psi^{(1)}}{\psi^{(2)}} \approx \frac{0.56}{0.51} \cdot \frac{65.1}{123.2} = 1.09 \cdot 0.62 = 0.68 \quad (3.9)$$

$\frac{\text{flux density}}{\text{ratio}} \quad \text{length ratio}$

- square-wave air gap

$$\frac{\psi^{(1)}}{\psi^{(2)}} \approx \frac{0.53}{0.41} \cdot \frac{83.2}{147.2} = 1.29 \cdot 0.56 = 0.71 \quad (3.10)$$

$\frac{\text{flux density}}{\text{ratio}} \quad \text{length ratio}$

At low current, the flux density ratio of the two configurations is more than unity while that of the equivalent length of the active region is less than unity and the resulting ratio of the flux linkages is less than unity. This indicates that the resulting flux linkage is determined in a bigger part by the increase in the length of the active region,  $l_e^{total}$ .

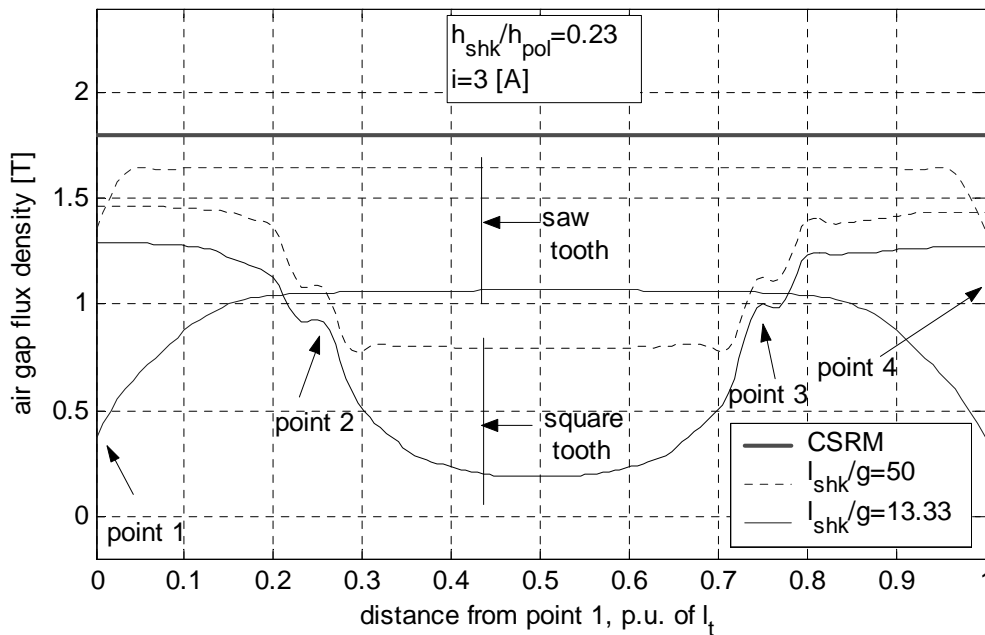


Fig. 3.36 Average flux linkage distribution in saw toothed and square wave air gap, at  $i=3$  [A]

At high current, the discussion from sub-section 3.4.1 is valid for the saw toothed air gap. In the case of the square-wave air gap SRM, the flux density along the lateral face of the tooth is smaller in a configuration with a shorter tooth pitch (Fig. 3.29). This is explained by that there is less material in the Shark teeth of a Shark SRM with shorter tooth pitch. Therefore, their iron material will have a higher flux density than the rest of the iron regions and the saturation region is located at the root of the tooth. The reduced permeability of the iron in these regions makes that the equivalent air gap seen by flux lines is equal to the mechanical air gap plus twice the saturation

regions at the root of the tooth. This discussion is supported by the field patterns shown in Fig. 3.22 at low and high current for a specified configuration of the air gap.

### 3.5 Selection of the optimum Shark air gap

The analysis of various Shark profiles has underlined that the shape of the Shark tooth plays an important role in the magnetic performance of the Shark SRM. Therefore, one of the objectives of this chapter is to identify the shape of Shark tooth producing the best magnetic performance. Another objective is to determine the optimum dimensions of the selected Shark profile to be implemented in a demonstration machine.

To fulfil these objectives, the following evaluation criteria are used: the magnetisation characteristics of various Shark profiles, and the energy gain at different excitation currents. The energy gain is defined as the ratio of the co-energy change between unaligned and aligned rotor positions of the Shark SRM to that of the corresponding CSRSM. This ratio is used because it reflects the improvement of the torque capability of a Shark SRM.

#### (a) Flux linkage characteristics

The flux linkage characteristics of a saw-toothed and a square-wave air gap SRM are plotted in Fig. 3.37. Analysing this picture, three regions may be discerned.

**Region R1** – is the region characterised by the linearity of the magnetic properties of the iron. In this region, the magnetic circuit of the square-wave air gap SRM produces more flux linkage than both the saw-toothed air gap SRM and the CSRSM. Their flux linkage values are as follows:

$$\Psi_{square} > \Psi_{saw} > \Psi_{CSRSM} \quad (3.11)$$

In this region, the FEA revealed that the conversion area has the main influence on the magnetic performance (see the discussions from section 3.4).

**Region R2** is that region of the magnetisation characteristics, where the iron of the Shark teeth begins to exhibit increased reluctance. Because the flux is compressed in the narrower sections of the Shark teeth, the flux density in these regions is higher. At this higher flux density, a significant proportion of the source mmf is used in driving the flux through iron. Therefore, the flux density in the air gap will be smaller and the flux linkage gain begins to decrease.

The square-wave profile is the most sensitive to increased flux density because the iron sections in its teeth are narrower than those in the saw-toothed air gap SRM. It was shown in section 3.4.1 that the shape of the Shark tooth makes that the saturation regions occurs in different locations – that is at the tip of the Shark tooth in the saw tooth and at the root of the square-wave tooth. Therefore, the magnetisation characteristic of the square-wave air gap SRM crosses over that of the saw-toothed air gap SRM. The flux linkage values in this zone become ranked as follows:

$$\Psi_{saw} > \Psi_{square} > \Psi_{CSRSM} \quad (3.12)$$

**Region R3** is that region of the magnetisation characteristic, where the flux linkage characteristic of the square-wave toothed air gap crosses over and becomes less than the magnetisation characteristic of the CSRSM. The values of the flux linkage are now ranked as follows:

$$\Psi_{saw} > \Psi_{CSRSM} > \Psi_{square} \quad (3.13)$$

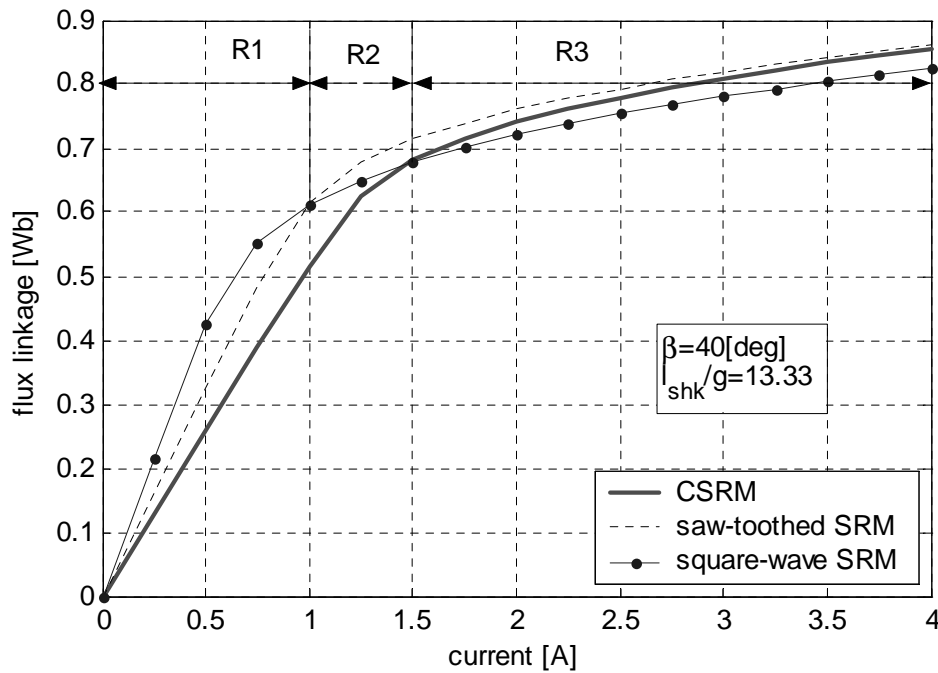


Fig. 3.37 Magnetization curves of various Shark profiles having angle  $\beta$ , constant.

The magnetisation characteristics of the aligned rotor position, shown in Fig.3.37, indicate that the relative performances of the considered Shark profiles depend upon current value. Based on these characteristics, it may be concluded that the Shark profile that may be effective at working points characterised by non-saturated iron may not be as effective assuming working conditions when iron is saturated.

As in the SRM, saturation plays an important role, it may be concluded that the saw-toothed air gap is preferred to the square-wave air gap. However, the flux linkage characteristic cannot be used alone in selection of the optimum Shark profile. Therefore the energy ratio was defined and used in the present evaluation.

### (b) Energy ratio

The second criterion for selection is the change of co-energy during a single stroke. The determination of this variable requires also the magnetisation curves of the Shark SRM in the unaligned rotor position (chapter 2). In section 3.2, it was shown that is impossible to make a 2D FEM of the axial cross-section of the Shark SRM in the unaligned rotor position. Therefore, the unaligned magnetisation curves of the Shark SRM were assumed to be identical to that of the

CSRM. This decision is not far from the real situation, where only a slight increase of the unaligned flux linkage of the Shark SRM is expected. This matter will be addressed in chapters 4 and 5.

The co-energy change through a single stroke is an indicator of the torque capability of the motor. Therefore the ratio of the co-energy change (called energy gain) is calculated and plotted in Fig. 3.38. These result reveal that the energy gain depends on the current level, saturation and the shape of the Shark teeth:

At all current levels, the energy gain increases with the increase in  $\beta$ .

For each current value, and tooth pitch, there is a critical angle  $\beta$ , where the energy gain of the square-wave air gap SRM becomes smaller than that of the saw-toothed air gap SRM. This suggests that the selection of the optimum shape and its dimensions has to be made a function of the current value.

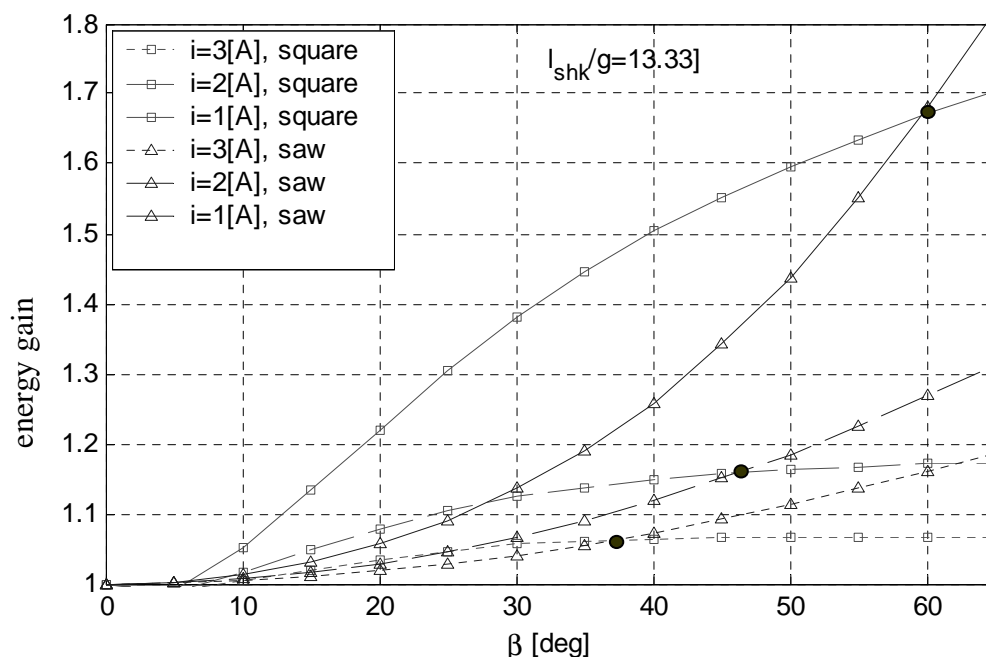


Fig. 3.38 Energy gain at different  $\beta$  and tooth pitch,  $l_{shk}$ , constant

### (c) Selection of the Shark configuration to be implemented in a demonstration machine

#### *Selection of the shape of the Shark profile*

Based on the flux linkage characteristic (Fig. 3.37) it may be considered that for a maximum current,  $i = 3$  [A], the saw-toothed air gap SRM may provide better performances than the square-wave air gap SRM. This is because in the aligned rotor position, its flux linkage does not become smaller than that of the CSRM.

#### *Selection of the dimensions of the Shark profile*

In section 3.4.2 it was shown that the optimum length of the saw-toothed profiles is  $\frac{l_{shk}}{g} = 13.33$

(Fig. 3.24).

The optimum angle  $\beta$  of the profile may be determined based on the energy gain curves calculated for Shark air gaps having  $\frac{l_{shk}}{g} = 13.33$  and presented in Fig. 3.38. It results that a saw-toothed air gap having big angle  $\beta$  may produce more torque than the corresponding cylindrical air gap.

However, the value of the angle  $\beta$  is limited by manufacturing considerations such as time, number and difficulty of the operations. Therefore the final configuration was selected to be a saw profile with  $\beta = 45$  [deg] and a tooth pitch  $l_{shk} = 13.33 \cdot 0.3 \cong 4$  [mm]. This means that there will be 15 Shark teeth, to be accommodated along the 60 [mm] long lamination stack.

### 3.5 Summary and Conclusions

In this chapter, various air gap shapes (saw, square, trapezoid) were analysed using FEA. The decision to use 2D FEA was motivated by the fact that the axial cross-section of the Shark SRM carries the main information about the magnetic field improvement in a Shark structure.

The analysis indicated that the magnetic behaviour of the various Shark profiles differs according the shape and dimensions. The main conclusions that may be drawn from the calculated magnetisation characteristics are that:

- the saw-toothed air gap SRM produces more flux linkage than the CSRSM at any value of the excitation current,
- the square-wave air gap SRM produces more flux linkage than the CSRSM and than the saw-toothed air gap SRM at low current,
- the square-wave air gap SRM produces less flux linkage than the CSRSM at high current,
- the Shark SRM with trapezoidal teeth is the generalisation of the saw-toothed and square-wave geometries. Its magnetisation characteristic has values between the characteristics of the saw and square wave air gap SRM (Appendix B.5). Its shape is affected by the value of the parameter  $l_{top}$ , which defines the geometry of the Shark tooth. For  $l_{top} / l_{shk} = 0.5$ , the trapezoid tooth takes the shape of the square-wave tooth, whilst for  $l_{top} / l_{shk} = 0$ , it has the shape of the saw tooth.

The flux linkage gain produced by the Shark air gap has different values according to the shape of the Shark tooth and to its specific dimensions. Some observations have been made:

- the flux linkage gain calculated by FEA, for the linear region of the magnetisation characteristic, differs from the value determined by analytical method. The difference is caused by that, in the analytical method a uniform distribution of the air gap flux density was assumed and this is not the case in the Shark structures
- the flux linkage gain calculated at high current has different values depending on the Shark geometry (this was explained by the different location of the saturation regions in the Shark tooth):

- in the saw toothed geometry, the flux linkage gain approaches unity at high saturation
- in the square wave geometry, the flux linkage gain becomes less than unity at high saturation

In this chapter, the flux density in the air gap was analysed for various conditions such as: constant tooth pitch, constant height of the Shark tooth, constant angle  $\beta$  while the other parameters were varied. The results shown that the region of local increased flux density has different locations:

- at the tip of the Shark tooth in the saw profile
- at the root of the Shark tooth in the square wave profile

The analysis revealed also the possibilities to improve the performance of the Shark structure. These possibilities are summarised in Table 3.8.

Table 3.8 Possibilities to improve the magnetisation characteristic of various Shark profiles

	Saw toothed profile	square wave profile	trapezoidal profile
$l_{shk} = const$	$\uparrow h_{shk}$ or $\uparrow \beta$	$\uparrow h_{shk}$ or $\uparrow \beta$	$\uparrow h_{shk}$ or $\uparrow \beta$
$\beta = const$	$\downarrow l_{shk}$	$\downarrow l_{shk}$	$\downarrow l_{shk}$
$h_{shk} = const$	$\downarrow l_{shk}$ or $\uparrow \beta$	$\downarrow l_{shk}$ or $\uparrow \beta$	$\downarrow l_{shk}$ or $\uparrow \beta$

For Shark teeth having tooth pitch constant:

- **saw profile:** flux linkage increases as the height of the tooth increases
- **square wave profile:** at low current the flux linkage increases with the increase in height but at high current the flux linkage decreases as the height of the tooth increases

For Shark teeth having  $l_{shk} / h_{shk} = \text{constant}$ :

- **saw profile:** the flux linkage is, at all current values, bigger than that of the CSRSM as long as the active region of the air gap is not smaller than 90% of the total air gap area.
- **square wave profile:** The flux linkage, at low current, increases by increasing the tooth pitch, as long as the active region of the air gap is not smaller than 85% of the total air gap area.

For the condition  $h_{shk} = \text{constant}$ :

- **saw profile:** the flux linkage increases as the length,  $l_{shk}$ , increases
- **square wave profile:** at low current the flux linkage increases with the decrease of the length,  $l_{shk}$ . At high current the flux linkage decreases as the length,  $l_{shk}$ , decreases.

The optimum Shark configuration was selected to be a saw profile with  $\beta = 45$  [deg] and a tooth pitch  $l_{shk} = 13.33 \cdot 0.3 \cong 4$  [mm].





## Chapter 4

# Analytical modelling of the Shark Switched Reluctance Motor

The Shark structure obtained by redistributing the iron material, requires an optimisation procedure, to ensure that the maximum benefit is obtained from the resulting machine. In the previous chapter, FEA was used to seek the optimum Shark configuration. However, this method proved to be time consuming. If the results are to be obtained more quickly, an analytical or a combined analytical-numerical model has to be developed, which is quicker in operation.

Several analytical models of the Shark structure were studied during this project. However, only the most convenient and reliable model is analysed and validated by using data from FEA and only one configuration will be verified by using data from measurements on the demonstration machine.

In this chapter, the definition of the objectives is followed by a brief summary of the analytical methods previously used to model cylindrical air gap SRMs. Then, the proposed analytical models of the Shark SRM in aligned and unaligned rotor positions are described, and their limitations and verification are discussed. The influence of the available winding area on the ideal energy conversion loop is also discussed. Subsequently, the forces produced in the machine are studied. Attention is focused on axial and radial forces, as these two may have a detrimental impact on the machine. They may produce vibration of the parts of the machine, leading to malfunction or eventual failure. Summary and conclusions end this chapter.

### 4.1 Motivation and Objective

Most of the effort put into the development of analytical models of cylindrical air gap Switched Reluctance Motors (CSRMs) are motivated by the need to obtain the wanted results more quickly. Various analytical models, describing the static and dynamic performance of the cylindrical air gap SRM, may be found in the literature [40], [66], [67], [68], [69], [70], [71], [72]. However, no analytical model of the Shark air gap SRM has yet been proposed. Probably, the increased difficulty of assembly, consequent upon the Shark structure, has been perceived as an impediment to its promotion. Advances in manufacturing technology may open new possibilities for application of Shark structures. Therefore, it was considered that developing an analytical model of Shark air gap SRM that is quick and easily applied might help the understanding and the promotion of this concept.

Generally, the difficulties of making an analytical model of the CSRMs are caused by two factors. One factor is that, in the aligned rotor position, the non-linear magnetic properties of the iron

material are pronounced. The non-linear character of the magnetic material is emphasised in the Shark SRM by the shape of the Shark teeth. The second factor is that in the unaligned rotor position, although the iron paths do not exhibit saturation, the calculations are complicated as the field lines cannot be exactly described by simple mathematical expressions [67], [68]. Furthermore, their mathematical description might vary for different SRM configurations [67].

Analytical models of CSRSM has been long discussed and several models have been proposed and verified [40], [62], [63], [64], [65], [66], [67], [68]. Therefore, it is not in the scope of this work to propose a new model of the magnetisation characteristics of a cylindrical air gap SRM. The scope of this chapter is restricted to propose a method that describes the flux linkage of the Shark SRM by extending existing models of CSRSM. This means that the Shark air gap must be described mathematically so as to match the existing models.

In chapter 3, it was shown that, in the aligned rotor position, the saturation problem is exacerbated by the geometry of the Shark teeth, which add new regions of local saturation. Therefore, the development of an analytical model of the Shark SRM must focus on the consideration of these regions, located at the tip of the saw-toothed profile or at the root of the square wave profile. In this chapter, only the model of the saw-toothed air gap is presented, as the model of square-wave air gap SRM is similar.

Based on these considerations the objectives of this study may be defined as:

- To develop and validate an analytical model of the Shark SRM in the aligned rotor position
- To develop and validate an analytical model of the Shark SRM in the unaligned rotor position
- To analyse and optimise the structure of the Shark SRM and to compare the results with those provided by FEA from chapter 3

Due to the special shape of the air gap, the force produced in the Shark SRM has different components compared to those produced in CSRSM. It is believed and it will be demonstrated, that at saturation the radial force component is smaller in the Shark structure than it is in the CSRSM; this is seen as an advantage from vibration and noise production considerations. However, this reduction is obtained by producing an axial component of force, which may cause malfunctioning of the machine. Therefore,

- To calculate and to analyse the influence of the Shark teeth dimensions on the forces produced in the Shark SRM is of interest.

#### • Requirements of the simulation models

The requirements of the simulation model of the Shark SRM must be formulated precisely to ensure that the outcome of the modelling process is useful to the design and optimisation of any Shark air gap SRM. In the formulation of the objective, it is required that two models should be developed: one of the aligned rotor position of the Shark SRM and one of the unaligned rotor position of the Shark SRM, the characteristics at intermediate rotor positions being derived from these two. The overall requirements of these two models are listed below:

- To provide the flux linkage characteristic as output variable
- To make use of the models already established for cylindrical air gap SRM
- To account for the influence of the Shark air gap in non-saturating and saturating conditions.

## 4.2 Analytical calculation -overview

In this section, an overview of the methods previously used in literature to estimate analytically the characteristics of the SRM is presented. Different approaches have been reported but most of them consider the method of the Magnetic Equivalent Circuit (MEC) [25], [63], [66], [67], [68]. Attempts to use exponential functions to account for the magnetic saturation of the iron paths are also reported [62], [71].

The model proposed in [62] is actually a combination of MEC and analytical functions. The flux linkage in the aligned position is determined by using only two points of the magnetisation characteristic (at the knee point and at the maximum current of the flux linkage characteristic), whose coordinates are determined from the MEC. The magnetisation characteristics are then obtained by piecewise first- and second order functions for linear and saturation regions. The magnetisation curves at intermediate rotor positions are obtained by considering that the SRM behaves almost linearly with respect to the rotor position over a substantial range of rotor angles, [69], [70].

A similar representation is used in [65] where the concept of *gage curve* is also considered for an ultra-fast analytical model of the SRM. The authors claim that the proposed model is the simplest model that accounts for both bulk and local saturation.

Consideration of local saturation in intermediate rotor positions in modelling of the flux linkage curves is reported in [63]. In this approach the MEC is updated at each rotor position accounting for local saturation in the approaching stator and rotor poles.

The unaligned rotor position raises difficulties in calculations, even though the magnetic circuit is not saturated. The field lines cannot be described by simple mathematical expressions. Moreover, it is difficult to conceive a model whose validity applies to a large range of SRM. An example is given in references [67] and [68]. While both models are developed based on simple geometrical characterisation of the field lines in the air gap of the machine, the applicability of the model proposed in [67] does not extend to single and two phase SRM, where the model proposed in [64] is suitable. There are also other alternatives for unaligned inductance calculation as is the method presented in [64] or the FEA, where the dual energy method proves to be very accurate [62].

## 4.3 Magnetisation characteristic of the Shark Switched Reluctance Motor in the aligned rotor position

In this section, analytical modelling of the magnetisation characteristics of the Shark SRM in the aligned rotor position is discussed. Two approaches such as the use of the Langevin function or the

use of the MEC were tried. The approach using the Langevin function is based on a purely mathematical description of the magnetisation curves and it uses initially a curve-fitting algorithm, which requires a data table compiled for a large dimensional range of Shark profiles. All data may be obtained from FEA.

The second approach uses a magnetic equivalent circuit (MEC) of the motor. The purpose is to transform the Shark SRM into an equivalent conventional SRM, having similar magnetic behaviour, i.e. identical flux linkage assuming identical excitation, then solve the MEC of this equivalent motor.

Because the use of MEC proved to be simple and reliable, this approach is the only presented in this section. However, the method using the Langevin function is described in Appendix C.1.

In this section, the assumptions are initially specified; subsequently the proposed model is described, verified and its limitations are discussed. To verify the model, various configurations of SRMs were considered – that is different numbers of stator and rotor poles and different pole arcs. The magnetisation characteristics, calculated for Shark air gaps, having different dimensions, are compared to those resulting from FEA. For one configuration of CSRSM and Shark SRM, the model is also checked by using the data from measurement on a demonstration machine.

### **4.3.1 Equivalent cylindrical air gap Switched Reluctance Motor approach**

In acknowledgement of the need to meet researchers who have developed analytical models of cylindrical air gap SRM, Dr. Corda, from University of Leeds, UK, was contacted. This resulted in a three months stay at University of Leeds, where a complete model of the Shark SRM in aligned and unaligned rotor positions was developed [61].

This proposed simulation model is introduced here by specifying first the methodology. Then two modelling possibilities are discussed and the basic dimensions of the demonstrator model were calculated. Subsequently, the elements of the MEC are expressed as a function of the dimensions of the Shark profile. The design constraints are established by referring to the results provided by FEA and discussed previously in section 3.4.2. Finally, the proposed analytical model is verified by comparing its results to those provided by FEA or measurement, where available.

#### **(a) Methodology**

The idea of this approach is to simulate the magnetisation characteristics of the Shark SRM in aligned rotor position by determining an *equivalent cylindrical air gap* SRM, having identical flux linkage characteristic. This approach makes it possible to use existing knowledge of modelling cylindrical air gap SRMs allowing attention to be focused on modelling the Shark configuration. The steps involved in the development of the simulation model are as follows:

- Identify the most appropriate approach of calculating the equivalent CSRSM
- Calculate the main dimensions of the CSRSM equivalent to the Shark SRM
- Specify the design constraints

- Present, discuss and verify the results

**(b) Selection of the modelling approach for determining the CSRМ, equivalent to a specified Shark SRМ**

A Shark SRМ having saw-toothed air gap, whose magnetisation characteristic will be modelled, is illustrated in Fig.4.1. To calculate the wanted characteristic, this structure will be transformed into a cylindrical air gap SRМ, producing identical flux linkage. Thus, the flux linkage of the Shark SRМ may be calculated by using existing simulation models of the flux linkage produced by the equivalent CSRМ. The equivalent CSRМ is illustrated in Fig.4.2. The dimensions affected by the presence of the Shark profiles are the equivalent air gap length,  $g'$ , and the equivalent stack length,  $l_{stk}'$ . Additional details of the Shark air gap are illustrated in Fig.4.3. It should be noted that the diameter at the bottom of the rotor Shark tooth is equal to the rotor diameter,  $D_{r1}$ . This is an important observation because the area of the air-gap. Region is directly proportional to this diameter.

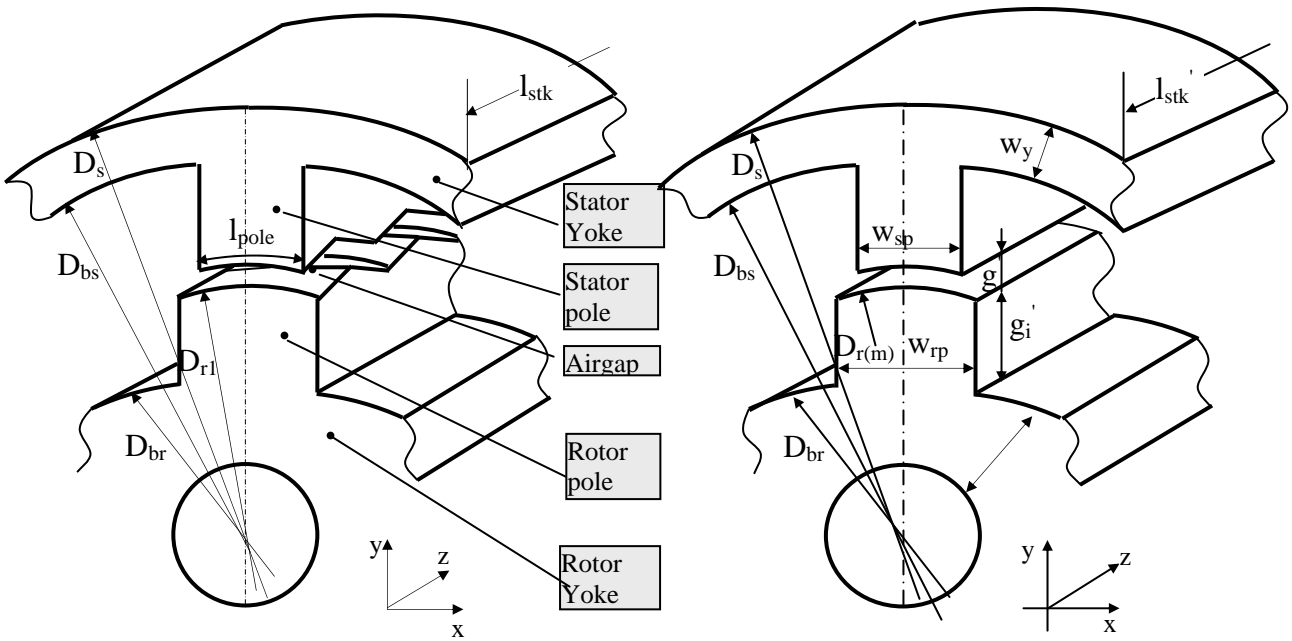


Fig.4.1 Shark SRМ, having saw-toothed air gap.

Fig.4.2 CSRМ, equivalent to the Shark SRМ from Fig. 4.1.

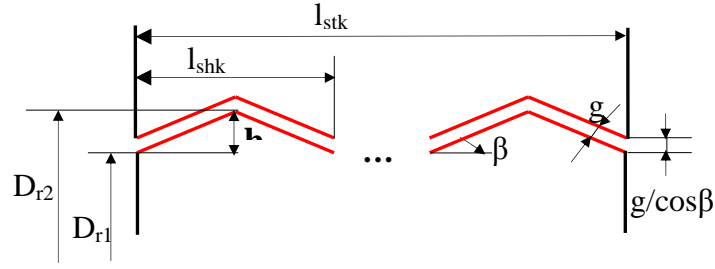


Fig.4.3 Illustration of the Shark air gap

To determine the main dimensions of the equivalent CSRSM, two conditions are used. These conditions are defined such as to ensure that the behaviour of the two structures is identical in non-saturated and saturated conditions. These conditions are:

- *Condition 1*, which demands that the air gap reluctances in the Shark SRM and in the equivalent CSRSM are identical
- *Condition 2*, which demands that the iron reluctances in the Shark SRM and in the equivalent CSRSM are identical.

In the following paragraphs each of the conditions mentioned above is discussed.

#### *Condition 1*

Assuming no fringing and uniform distribution of the field in the air gap, the reluctance,  $\mathfrak{R}_g$ , of the air gap region of the Shark SRM (Fig.4.1 and Fig.4.3) is given by [53]:

$$\mathfrak{R}_g = \frac{g}{\mu_0 \cdot \left( l_{pole} \cdot \frac{l_{stk}}{\cos \beta} \right)} = \frac{g \cdot \cos \beta}{\mu_0 \cdot (l_{pole} \cdot l_{stk})} \quad (4.1)$$

where  $g$  is the air gap length (the shortest distance across the air gap),  $l_{stk}$  is the length of the lamination stack,  $\beta$  is the angle which define the shape of the Shark profile and  $l_{pole}$  is the width of the pole as illustrated in Fig.4.1.

Equation (4.1), suggests that there are two possibilities to determine a cylindrical air gap SRM, which behaves similarly to a specified Shark SRM. These two models are called *model a* and *b* and are obtained as described below.

*Model a* may be determined from the term  $e1$  of equation (4.1). The equivalent SRM is thus a cylindrical air gap SRM, having the air gap length equal to the air gap length of the Shark SRM,  $g$ , and the equivalent stack length,  $l'_{stk}$ , given by:

$$l'_{stk} = \frac{l_{stk}}{\cos \beta} \quad (4.2)$$

where  $l_{stk}$  is the real stack length of the Shark SRM and  $\beta$  is the angle which define the shape of the Shark profile

*Model b* may be determined from the term  $e_2$  of equation (4.1). The equivalent SRM becomes in this case, a cylindrical air gap SRM, having the stack length, equal to the stack length of the Shark SRM,  $l_{stk}$ , but a shorter equivalent air gap length,  $g'$ , given by:

$$g' = g \cdot \cos \beta \quad (4.3)$$

where  $g$  is the real air gap length of the Shark SRM and  $\beta$  is the angle that defines the shape of the Shark profile.

These two models indicate that the Shark SRM may be regarded as equivalent to a cylindrical air gap SRM, having a longer stack length, given by equation (4.2), and the same air gap length as the Shark SRM or alternatively to a cylindrical air gap SRM, having a shorter air gap length, given by equation (4.3), and the same stack length as the Shark SRM.

However, the two models would behave differently in saturated conditions. The different behaviours are determined by the way they account for the presence of the Shark profile. To evaluate them and to select the model that best conforms to the physical phenomena, the flux density distribution along the axial cross-section of the machine might be relevant.

In chapter 3, it was showed that in the aligned rotor position of a saw-toothed Shark SRM, the iron regions located at the tip of the Shark teeth are worked at a higher flux density than the flux density in the rest of the magnetic circuit. Based on this observation, the saturation regions in both the CSRSM and the Shark SRM are sketched in Fig.4.4 and Fig.4.5. It may be observed that the magnetic circuit of the Shark SRM may be divided into two regions: one with bulk saturation and the other with local saturation. Only region of local saturation is affected by the presence of the Shark teeth.

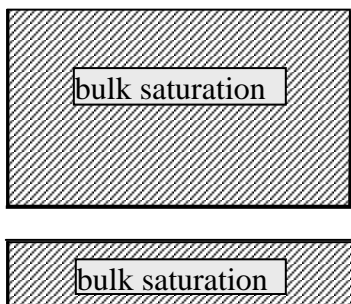


Fig.4.4 Bulk saturation regions in CSRSM

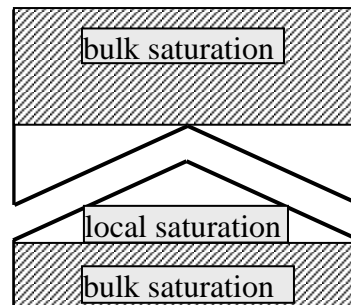


Fig.4.5 Bulk and local saturation regions in Shark SRM



Considering an equivalent cylindrical SRM with the dimensions modified according to *model a* ( $g$  and  $l'_{stk}$ ), appropriate results would be provided at low currents (no saturation of the iron material), where the drop of MMF may be considered as being entirely across the air gap. At high current (where the iron material becomes saturated), the flux linkage estimated by applying *model a* would be greater than that in the real Shark machine. This is because a longer stack, according to equation (4.2), is assigned to the regions of bulk saturation of the stator and rotor poles and yoke regions as well. Unfortunately, this is not conforming to the physical structure, where only the regions neighbouring the air gap are affected by the Shark teeth. Thus, it may be concluded that the magnetisation characteristics of the Shark SRM cannot be modelled by using *model a*.

In *model b* ( $g'$  and  $l_{stk}$ ), the stack length of the equivalent machine is equal to the stack length of the real Shark machine. This fulfils the considerations regarding the length of the regions of bulk saturation. The effect of the Shark profile on the air gap region is considered in this model by the means of the air gap length,  $g'$ , calculated by equation (4.3).

To ensure that the equivalent CSRSM provides identical flux linkage also in saturating condition, an additional condition will be formulated below.

*Condition 2*

The second condition ensures that the iron regions of the magnetic circuit have identical reluctances. This is important when the iron material is worked at increased flux density and saturation.

According to *Condition 1*, *model b* considers the rotor diameter at the crown of the poles of the equivalent SRM to be equal to the rotor diameter at the crown of the poles in the reference machine  $D_{r1}$ , as it is showed in Fig.4.2. This means that the mean flux paths in the stator poles of the equivalent model are longer than those in the Shark SRM, whose air gap is characterised by  $D_{r1}$  and  $D_{r2}$ , as it is showed in Fig.4.3. To account for the redistribution of the iron material, a mean air gap diameter is defined based on the diameters at points G<sub>1</sub> and G<sub>2</sub>, which are illustrated in Fig.4.6.

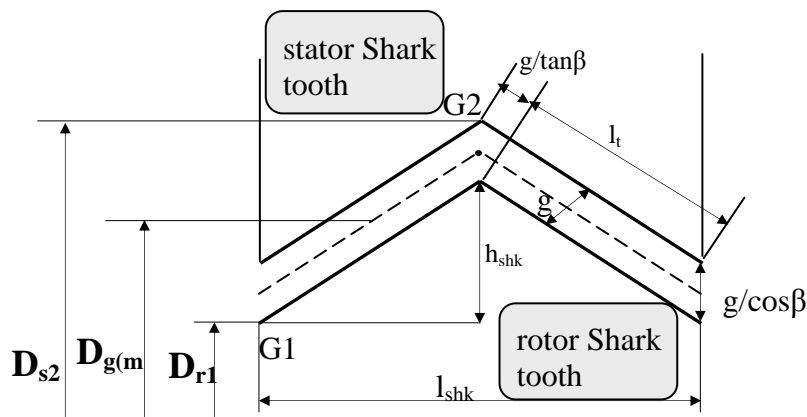


Fig.4.6 Illustration of the Shark segment

These points are located as follows:

- Point G1, at the root of the rotor Shark segment, is described by the diameter  $D_{r1}$
- Point G2, at the root of the stator Shark segment, is described by the diameter  $D_{s2}$ , defined in terms of rotor original diameter  $D_{r1}$  and the dimensions of the Shark tooth by equation (4.4).

$$D_{s2} = D_{r1} + 2 \cdot h_{shk} + 2 \cdot \frac{g}{\cos \beta} \quad (4.4)$$

The mean air gap diameter  $D_{g(m)}$  may be defined by:

$$D_{g(m)} = \frac{D_{r1} + D_{s2}}{2} = D_{r1} + h_{shk} + \frac{g}{\cos \beta} \quad (4.5)$$

where:  $D_{r1}$  and  $D_{s2}$  are defined above,  $h_{shk}$  is the height of the Shark tooth,  $g$  is the air gap length of the original machine and  $\beta$  defines the Shape of the Shark tooth.

The mean stator diameter may be obtained by adding the equivalent air gap length,  $g'$ , calculated by equation (4.3), to the mean air gap diameter calculated by equation (4.5).

$$D_{s(m)} = D_{g(m)} + 2 \cdot \frac{g'}{2} = D_{g(m)} + g \cdot \cos \beta \quad (4.6)$$

The mean rotor diameter may be obtained by subtracting the equivalent air gap length, calculated by equation (4.3), from the mean air gap diameter calculated by equation (4.5).

$$D_{r(m)} = D_{g(m)} - 2 \cdot \frac{g'}{2} = D_{g(m)} - g \cdot \cos \beta \quad (4.7)$$

The diameters calculated by equations (4.5), (4.6) and (4.7) and the air gap length calculated by equation (4.3) ensures that the resulting CSRSM is equivalent to the specified Shark SRM.

### **(c) Solution of the MEC of the equivalent cylindrical air gap Switched Reluctance Motor**

The simulation model used in this work has been reported in [68] and [61]. Each element of the magnetic circuit is described separately, assuming that:

- The field lines are uniformly distributed in the lamination plane
- The conductors are uniformly distributed
- There is no flux leakage – that is all flux passes from stator to the rotor and back

- The flux is linked with all the turns

To support the calculations, the magnetic circuit of a 6/4 CSRSM in the aligned rotor position is illustrated in Fig.4.1. It consists of two stator poles, two rotor poles, two air gaps - due to the symmetry around the x-axis, two stator yokes and two rotor bodies - due to the symmetry around y-axis. For a general configuration  $N_s/N_r$ , the magnetic circuit consists of  $N_s/ph$  ( $N_s$  is the number of stator poles and  $ph$  is the number of phases) elementary patterns, having the same components as illustrated for the 6/4 SRM. The dimensions of each components of the magnetic circuit may be determined for a general configuration of SRM. Then the solution of the MEC may be calculated at different current values.

Each component of the magnetic circuit is described in the following paragraphs. All the dimensions referred to in the following equations are related to Fig.4.1 and Fig.4.2.

- Stator poles

The stator pole of the equivalent machine has the width  $w_{sp}$  determined from the stator equivalent diameter  $D_{s(m)}$  and the stator pole angle,  $\beta_s$ , of the original machine:

$$w_{sp} = 2 \cdot \frac{D_{s(m)}}{2} \cdot \sin \frac{\beta_s}{2} \quad (4.8)$$

The cross-section area of the stator pole  $A_{sp}$  may be obtained as:

$$A_{sp} = w_{sp} \cdot l_{stk} \quad (4.9)$$

The length of the flux path will be  $l_{sp}$ , equal to:

$$l_{sp} = \frac{(D_{bs} - D_{s(m)})}{2} \cdot \frac{N_s}{ph} \quad (4.10)$$

- Rotor poles

The width of the rotor pole  $w_{rp}$  is given by:

$$w_{rp} = 2 \cdot \frac{D_{r(m)}}{2} \cdot \sin \frac{\beta_r}{2} \quad (4.11)$$

Then the cross-section  $A_{rp}$  will be:

$$A_{rp} = w_{rp} \cdot l_{stk} \quad (4.12)$$

and the length of the flux path  $l_{rp}$  :

$$l_{rp} = \frac{(D_{r(m)} - D_{br})}{2} \cdot \frac{N_s}{ph} \quad (4.13)$$

○ Air gap regions

The equivalent width  $w_g$  and the air gap cross-section,  $A_g$ , are determined using the mean air gap diameter,  $D_{g(m)}$ . The fringe flux is also included in the model by using the Carter coefficient [72], [78]. The Carter coefficient may be determined by equations (4.15) and (4.16), provided that  $\beta_s < \beta_r$ .

The equivalent width of the flux region in the air gap is obtained by:

$$w_g = 2 \cdot \frac{D_{r(m)}}{2} \cdot \sin \frac{\beta_s}{2} + (1 - \sigma) \cdot i \quad (4.14)$$

where:

$$i = \frac{D_{r(m)}}{2} \cdot \frac{\beta_r - \beta_s}{2} \quad (4.15)$$

$$\sigma = \frac{2}{\pi} \cdot \left[ a \tan \left( \frac{i}{g} \right) - \frac{g}{2 \cdot i} \cdot \log \left( 1 + \left( \frac{i}{g} \right)^2 \right) \right] \quad (4.16)$$

These equations are justified by the fact that the regions of fringe flux may be considered equivalent to a slot opposing a pole with the width equal to  $i$  given by equation (4.15), according to Carter [72], [78], [79].

The active air gap area may be obtained as a function of the mean air gap diameter and of the length of the lamination stack by:

$$A_g = w_g \cdot l_{stk} \quad (4.17)$$

The length of the flux path across the air gap,  $l_g$ , is twice the equivalent air gap length,  $g \cdot \cos \beta$ , because of the symmetry with respect to the x-axis:

$$l_g = 2 \cdot g \cdot \cos \beta \quad (4.18)$$

○ Stator yoke

The yoke cross-section  $A_{sy}$  is not affected by the presence of the Shark teeth in the machine:

$$w_{sy} = \frac{(D_s - D_{bs})}{2} \quad (4.19)$$

$$A_{sy} = w_{sy} \cdot l_{stk} \quad (4.20)$$

and the general expression for the length of the flux path through the stator yoke,  $l_{sy}$ , may be approximated by:

$$l_{sy} = 2 \cdot \pi \cdot \frac{(D_s - D_{bs})}{2} \cdot \frac{ph}{N_s} \quad (4.21)$$

○ Rotor yoke

The cross-section,  $A_{ry}$ , of the rotor yoke may be determined by:

$$w_{ry} = \frac{(D_{br} - D_{shaft})}{2} \quad (4.22)$$

$$A_{ry} = w_{ry} \cdot l_{stk} \quad (4.23)$$

while the length,  $l_{ry}$ , of magnetic circuit may be approximated by:

$$l_{ry} = 2 \cdot \pi \cdot \frac{(D_{br} + D_{sh})}{2} \cdot \frac{ph}{N_s} \quad (4.24)$$

The expressions (4.19) – (4.24) show that the stator and rotor yoke considered in the model are not affected by the presence of the Shark profile, which is conforming to *Condition2*.

The method used to solve the MEC is the same as that presented in [61] and [68]. To avoid iterative calculation for a single working point, the MEC has been solved assuming known the flux linkage. The flux densities in each section of the MEC may be calculated and the field intensities may be determined from the B-H curve of the magnetic material. The current, corresponding to the considered flux, may be obtained from the total MMF calculated as following:

$$MMF = \frac{B_g}{\mu_0} \cdot l_g + H_{sp} \cdot l_{sp} + H_{rp} \cdot l_{rp} + H_{sy} \cdot l_{sy} + H_{ry} \cdot l_{ry} = N_{ph} \cdot i \quad (4.25)$$

where:  $B_g$  is the flux density in the air gap,  $H_{sp}$ ,  $H_{rp}$ ,  $H_{sy}$ ,  $H_{ry}$  are the field intensities in the stator poles, rotor poles, stator yoke and rotor yoke respectively, and  $l_g$ ,  $l_{sp}$ ,  $l_{rp}$ ,  $l_{sy}$ ,  $l_{ry}$  are the estimated lengths of the air gap, stator and rotor poles, stator and rotor yokes respectively,  $N_{ph}$  is the number of turns in series per phase,  $i$  is the current flowing through the phase winding and  $\mu_0$  is the magnetic permeability of the free space. From equation (4.25), the current value corresponding to the specified flux linkage is readily obtained knowing the number of turns per phase  $N_{ph}$ .

### 4.3.2 Limitations of the model

The model presented above, provides reliable results for a limited range of dimensions of the Shark profile. These limits are set by two conditions, which are discussed in this sub-section.

*The first condition* emerges from the analysis of the field pattern in the air gap of a Shark tooth, which is illustrated in Fig.4.7 and Fig. 4.8. The field pattern in the Shark air gap, having short tooth pitch, proves to be different from that in a Shark air gap, having longer tooth pitch. It may be appreciated from the two illustrations that the equivalent air gap in the configuration with short Shark tooth pitch is longer than  $g$ .

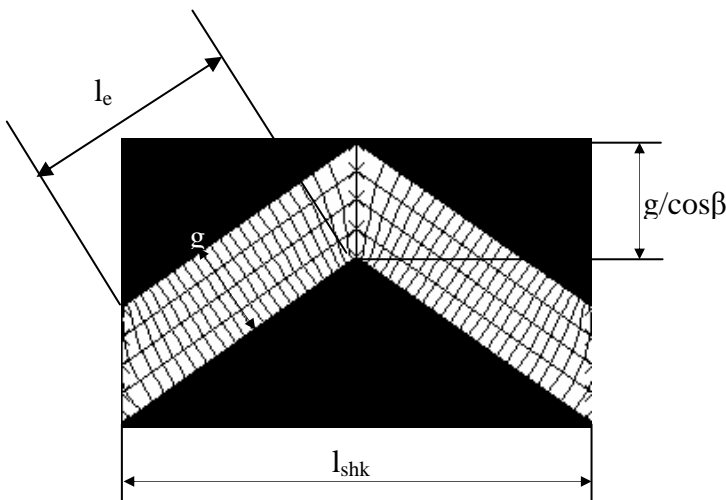


Fig. 4.7 Illustration of the field pattern in the Shark air gap, having  $l_{shk} > 2g$  and  $\beta = 35$  [degree]. The length of the field line across the air gap is equal to  $g$

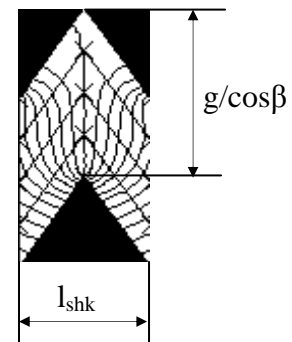


Fig. 4.8 Illustration of the field pattern in the Shark air gap, having  $l_{shk} < 2g$  and  $\beta = 65$  [degree]. The length of the field line across the air gap is approximately  $g/\cos\beta$

Due to these changes in the field pattern the viability of the present model is limited to the case where the sides of the stator and rotor Shark teeth overlap, provided uniform distribution of the air gap flux density. This condition was determined in chapter 2, and it is remembered here:

$$l_e \geq 0$$

$$l_e = \frac{l_{shk}}{2 \cdot \cos \beta} - g \cdot \tan \beta \geq 0 \quad (4.27)$$

where:  $l_e$  is the length of the overlapped sides,  $l_{shk}$  is the Shark tooth pitch,  $\beta$  defines the shape of the Shark tooth and  $g$  is the air gap length of the specified Shark SRM.

After simplification, condition (4.27) becomes:

$$\sin \beta \leq \frac{l_{shk}}{2 \cdot g} \quad (4.28)$$

As  $\sin \beta$  is always less or equal to unity, it results that if  $l_{shk} > 2 \cdot g$  then the inequality is satisfied for any angle  $\beta$ . Consequently, there is no limitation of the model. However, if  $l_{shk} < 2 \cdot g$ , then the upper limit of the angle  $\beta$  is given by:

$$\beta_{lim} \cong a \sin \left( \frac{l_{shk}}{2 \cdot g} \right) \quad (4.29)$$

For  $\beta > \beta_{lim}$ , the air gap length used in calculation has to be considered equal to  $g$  and not to the equivalent value,  $g'$ , as it is given by equation (4.3).

A stronger formulation of the condition (4.27), which assures that the air gap area is effectively crossed by the field lines, has been derived based on the data from section 3.3.2:

$$\frac{2 \cdot n_t \cdot l_e}{14 \cdot 2 \cdot 4} > 0.9 \cdot \frac{l_{stk}}{\cos \beta} \quad (4.30)$$

$\frac{2 \cdot n_t \cdot l_e}{14 \cdot 2 \cdot 4}$  effective length of the airgap region  
 $\frac{l_{stk}}{\cos \beta}$  ideal length of the airgap region

where  $n_t$  is the number of Shark profiles accommodated along a specified stack length,  $l_{stk}$ .

The second condition emerges from considerations regarding the available winding area. Because the Shark teeth are oriented outward from the rotor body, the available winding area will be reduced in the Shark SRM compared with that in the reference CSR. If the same number of turns is to be accommodated in the slot, then a higher fill factor must be considered. Therefore, it is necessary to consider an upper limit for the height of the Shark teeth. This limit is calculated using equations from Appendix C.2 and the results are illustrated in Fig.4.9 for a 6/4 SRM with the dimensions given in Appendix A.2. The reduction of the winding area, caused by the Shark teeth, might be compensated by rearranging the winding in the slot, if the height of the Shark teeth were limited to a maximum  $k_w=22$  [%] of the stator pole height.

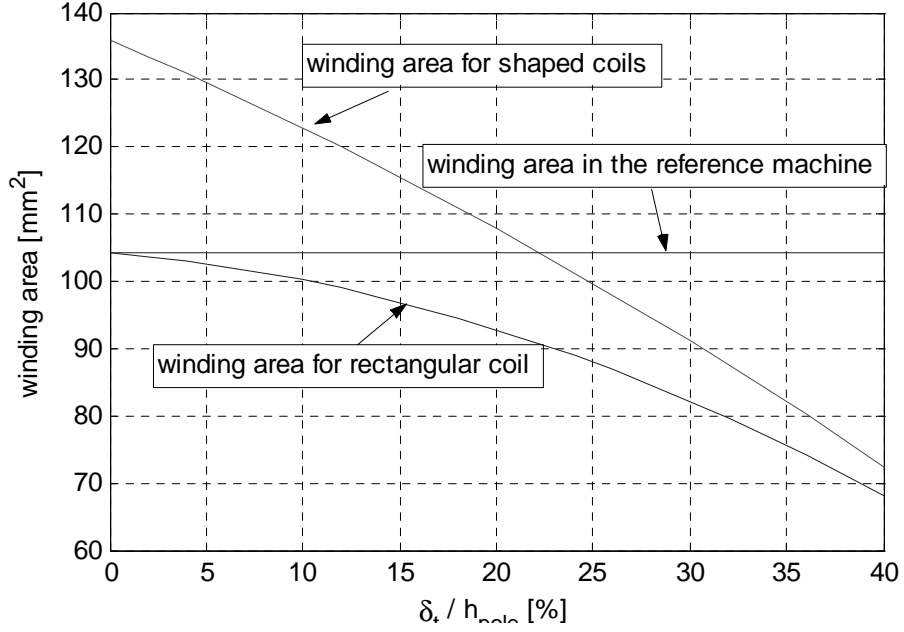


Fig. 4.9 Illustration of the limitation of the height of the Shark tooth

This condition is expressed by:

$$h_{shk} \leq k_w \cdot h_{pole} \quad (4.30)$$

where:

$$h_{shk} = \frac{l_{shk}}{2} \cdot \tan \beta \quad (4.31)$$

and

$$h_{pole} = \frac{(D_{bs} - D_{s(m)})}{2} \quad (4.32)$$

Equations (4.30)-(4.32) provide the expression of the maximum angle allowed for a specified Shark segment:

$$\beta \leq a \tan \left( \frac{2 \cdot k_w \cdot (D_{bs} - (D_{r1} + 2 \cdot g + 2 \cdot k \cdot h_{pole}))}{l_{shk}} \right) \quad (4.33)$$



### 4.3.3 Validation of the simulation model of the Shark SRM in aligned rotor position

The proposed model is verified for various configurations of CSRSM, having cylindrical and different Shark air gaps. The results of the analytical model are compared with the results from FEA. In this sub-section only the results obtained for the 6/4 SRM are presented, the results obtained for a 12/8 SRM being illustrated in Appendix C.3.

- **Cylindrical air gap SRM**

The curves plotted in Fig.4.10 show good agreement between the flux linkage calculated analytically and the results from FEA.

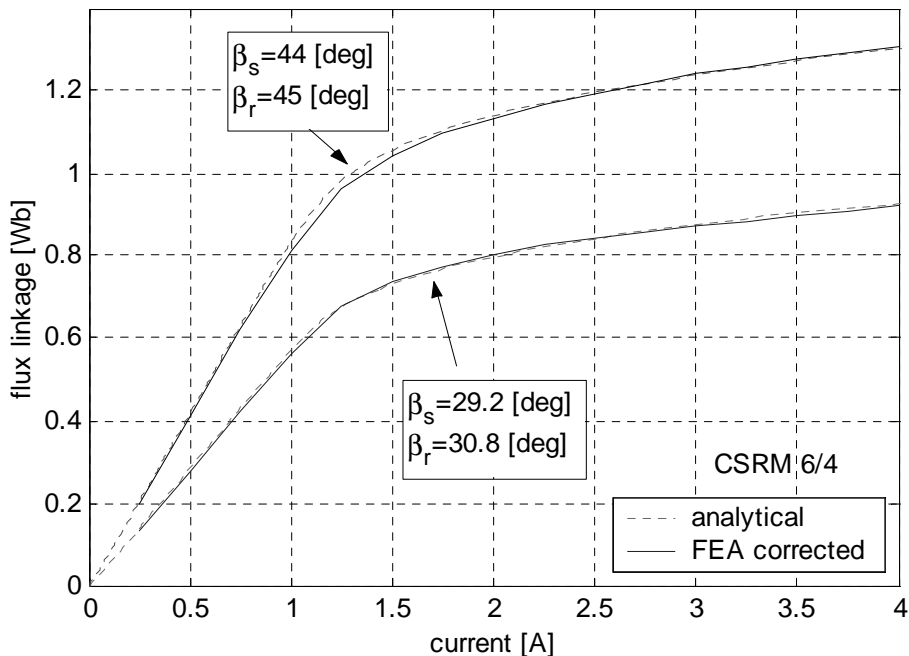


Fig.4.10 Magnetisation characteristic in the aligned position of the cylindrical air gap SRM 6/4, having the dimensions given in Appendix A.2.

- **Shark SRM**

The comparison of the flux linkage calculated with the model presented in this section with the results from FEA, has showed that the proposed analytical model does not account properly for the influence of the saw-toothed Shark air gap. This is because it was considered that the width of the stator and rotor poles depends on the dimensions of the Shark profile – that is equations (4.6) and (4.7). Therefore, some changes have been made:

- the average air gap diameter was replaced by the initial air gap diameter of the CSRSM

- the air gap length was written such as to account for the non-uniform distribution of the flux density in the air gap:  $g' = g \cdot \cos \beta - 2 \cdot n_t \cdot g \cdot \tan \beta$

With these observations, the results from Fig.4.11 and Fig.4.12 have been obtained. In Fig.4.11, how the model accounts for the effect of the angle beta is verified, whilst in Fig.4.12, how the model accounts for the effect of the Shark tooth pitch is illustrated. In both cases, the agreement is good.

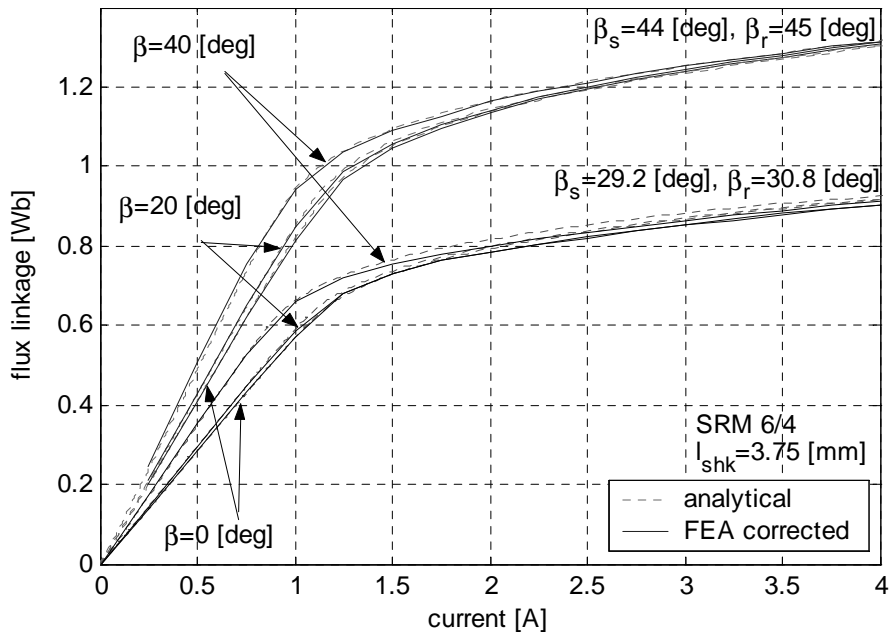


Fig. 4.11 Magnetisation characteristics calculated analytically and by FEA for the Shark SRM in the aligned rotor position, having different angle beta

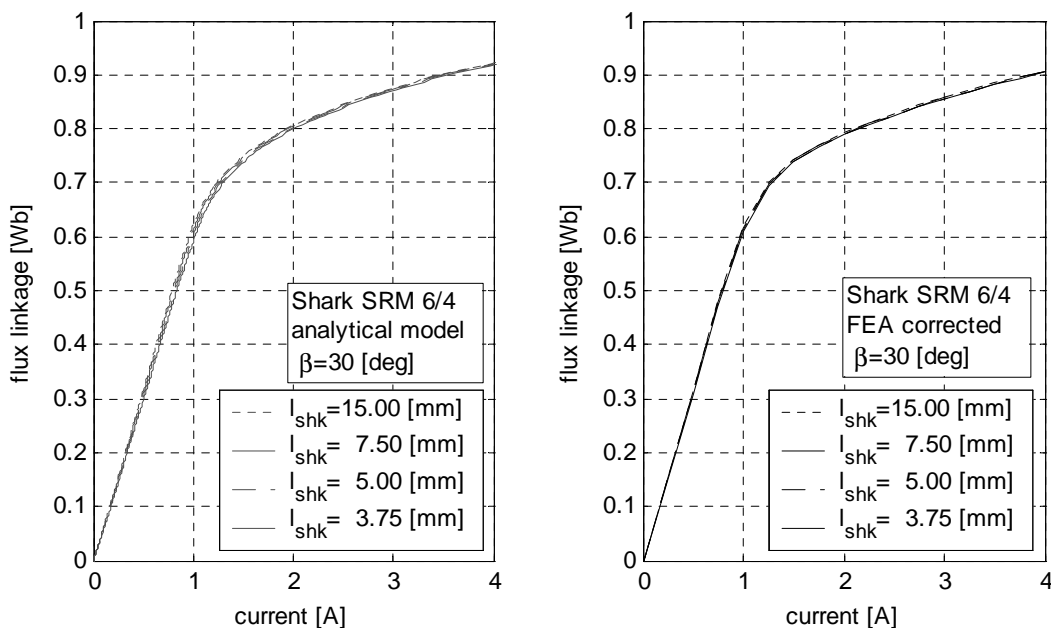


Fig. 4.12 Magnetisation characteristics calculated analytically and by FEA for the Shark SRM in the aligned rotor position, having different Shark tooth pitch.

#### 4.4 Magnetisation characteristic of the Shark Switched Reluctance Motor in the unaligned rotor position

The analytical model of the magnetic circuit of the Shark SRM in the unaligned rotor position is presented and discussed in this section. The model is developed by using the approach reported in [68], where the field paths are approximated by circular arcs and straight lines, described mathematically by simple expressions. These expressions are then adapted to account for the influence of the Shark air gap.

##### (a) General description of the analytical model

The model is described by the geometry and notation of Fig.4.13. The radial cross-section of the SRM presents two symmetry axes, therefore only part of the machine is represented. In Fig.4.13, the section of a 6/4 SRM is illustrated but the model is described for a general configuration  $N_s/N_r$  of SRM.

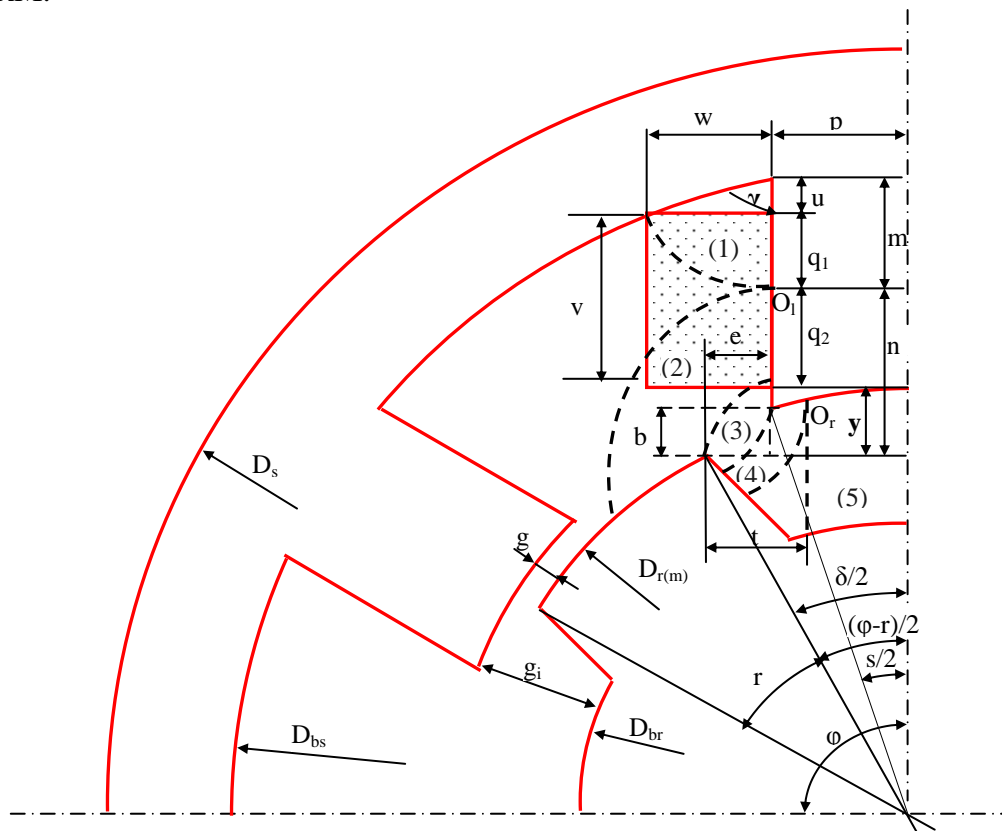


Fig.4.13 Flux paths through the air in the unaligned position of a cylindrical air gap SRM

From the configuration presented, it may be suggested that there are three dimensions, that affect the value of the unaligned inductance<sup>6</sup> significantly:

- the clearance,  $e$ , between stator and rotor poles
- the distance,  $g_i$ , from the stator pole surface to the rotor interpolar surface
- the rotor diameter,  $D_{r(m)}$ , which combined with the stack length defines the area of the air gap.

The supposed equipotential lines are divided into five groups as shown in Fig.4.13:

- Flux lines which leave the stator pole side and enter the stator back iron (region 1)
- Flux lines which leave the stator pole side and enter the rotor pole face (region 2)
- Flux lines which leave the stator pole side and enter the rotor pole side (region 3)
- Flux lines which leave the stator pole face and enter the rotor pole side (region 4)
- Flux lines which leave the stator pole face and enter the rotor interpolar region (region 5)

The transition from one region to another is defined by two points  $O_l$  and  $O_r$ . Point  $O_l$  defines the transition between region 1 and region 2 and point  $O_r$  defines the transition between region 4 and region 5. The location of the point  $O_l$  may be specified analytically based on the conditions that the lengths of the flux lines starting from point  $O_l$  are equal. The ratio of the length of these lines is equal to the ratio of the amp-turns linked by them. This leads to:

$$\frac{l_1}{l_2} = \frac{\left(\frac{1}{2} \cdot \gamma \cdot m^2\right)}{\left(w \cdot v + \frac{1}{2} \cdot w \cdot u\right)} \bigg/ \frac{\left(w \cdot v - \frac{\pi}{4} \cdot n^2\right)}{(w \cdot v)} = 1 \quad (4.34)$$

which together with  $n + m = v + u + y$ , makes possible to locate the point  $O_l$ , by determining the length,  $n$ , from  $O_l$  to the rotor interpolar face:

$$n(O_l) = \frac{-b + \sqrt{b^2 - 4 \cdot a \cdot c}}{2 \cdot a}, \quad (4.35)$$

where  $a, b, c$  are expressed as function of the dimensions shown in Fig.4.13:

$$a = \frac{\gamma}{2} + \frac{\pi}{4} \cdot \left(v + \frac{1}{2} \cdot u\right) \quad (4.36)$$

$$b = -\gamma \cdot v \cdot (v + u + y) \quad (4.37)$$

<sup>6</sup> here the inductance is preferred to the flux linkage, because the inductance of the magnetic circuit in unaligned rotor position is constant

$$c = \frac{1}{2} \cdot \gamma \cdot (v + u + y)^2 - w \cdot v \cdot \left( v + \frac{1}{2} \cdot u \right). \quad (4.38)$$

The location of the point  $O_r$ , may be determined from the condition that the length of the circular arc  $O_r O_1$  is equal to the length of the segment  $O_r O_2$ . This condition makes that:

$$t = \frac{2 \cdot g_i}{\pi - (\phi - r)} \quad (4.39)$$

Having defined the location of points  $O_1$  and  $O_r$ , the geometrical description of the field pattern is completely defined and the inductance of each field path represented in Fig. 4.13 may be calculated.

### (b) Method of modelling

The idea of the proposed approach is to describe the unaligned inductance of a Shark SRM by using the existing model of the unaligned inductance of a CSRSM [68]. To do this the following method was adopted; initially, the model of the CSRSM is described and discussed. The deduction of the expressions used to estimate the inductances of the magnetic circuits corresponding to the five regions, is not detailed here as it can be found in [68]. Then each component of the total inductance is corrected such as to account for the dimensions of the Shark profile. No empirical parameters is used in this model.

### (c) Analytical model of the cylindrical air gap SRM in the unaligned rotor position

Since the magnetic circuit of the CSRSM in the unaligned rotor position is symmetrical with respect to the pole axis, the flux linkage of one pole,  $\Psi_{CSRSM}$  may be written as a function of the flux linkage of the five flux paths,  $\Psi_j$ ,  $j = \overline{1,5}$ , illustrated in Fig.4.13:

$$\Psi_{CSRSM} = 2 \cdot \sum_{j=1}^5 \Psi_j \quad (4.40)$$

where 2 is due to the symmetry with respect to the pole axis.

The inductance of one phase may be determined by:

$$L_{CSRSM} = \left( \frac{N_s}{ph} \right) \cdot \frac{\Psi_{CSRSM}}{i} \quad (4.41)$$

because there are  $\left(\frac{N_s}{ph}\right)$  poles per phase.

Combining equations (4.40) and (4.41) it results that:

$$L_{CSRМ} = 2 \times \frac{N_s}{ph} \times \sum_{j=1}^5 L_j \quad (4.42)$$

where:  $L_j = \frac{Y_j}{i}$ ,  $j = \overline{1,5}$

The phase inductance may be written, in terms of normalised permeance of the five flux paths, as:

$$L_{CSRМ} = N_{ph}^2 \times \mu_0 \times l_f \times \left( \sum_{j=1}^5 P_j' \right)_{CSRМ} \quad (4.43)$$

or

$$L_{CSRМ} = N_{ph}^2 \times \mu_0 \times l_{stk} \times P_{CSRМ}' \quad (4.44)$$

where  $l_f$  is the effective core length, accounting for the end flux. Its expression will be discussed later in this section.  $P_j'$ ,  $j = \overline{1,5}$  are the normalised permeances of the flux paths illustrated in Fig.4.13 and  $P_{CSRМ}'$  is the total normalised permeance of the magnetic circuit of the CSRМ in the unaligned rotor position. Equation (4.44) expresses the inductance of the unaligned rotor position by defining a total equivalent normalised permeance such as the resulting expression is related to the stack length,  $l_{stk}$ . In  $P_{CSRМ}'$ , the end effects are included.

#### (d) Calculation of the normalised permeance

Equation (4.42) may be expressed in terms of permeance,  $P_j$ ,  $j = \overline{1,5}$  by:

$$L_{CSRМ} = 2 \times \frac{N_{turns}^2}{N_s / ph} \times \left[ \sum_{j=1}^5 P_j \right]_{CSRМ} \quad (4.45)$$

By comparing equation (4.43) and (4.45), it may be found that:

$$P'_j = \frac{2 \times P_j}{m_0 \times \mu_f \times \left( \frac{N_s}{ph} \right)} \quad (4.46)$$

where  $N_s$  is the number of stator poles and  $ph$  is the number of phase of the motor.

In terms of inductance, the normalised permeance becomes:

$$P'_j = \frac{L_j}{m_0 \times \mu_f \times \left( \frac{N_{turns}^2}{2 \times \left( \frac{N_s}{ph} \right)} \right)} \quad (4.47)$$

The total normalised inductance may be calculated as:

$$P'_{CSR M} = \frac{l_f}{l_{stk}} \times \left[ \sum_{j=1}^5 P_j \right]_{CSR M} \quad (4.48)$$

#### (e) Calculation of the components of the phase inductance

The permeance of each flux path and the corresponding contribution to the phase inductance may be calculated as reported in [64].

Component  $L_1$  is determined by considering that the number of turns,  $N$ , linked by the flux path, is given by the relation (4.49).

$$\frac{N}{N_{turns}} = \frac{\frac{1}{2} \times g \times (q + u)}{w \times u + \frac{1}{2} \times w \times u} \quad (4.49)$$

where  $N_{turns}$  is the number of turns in series per pole.

The resulting expression for the inductance of the region 1 is:

$$L_1 = m_0 \times \mu_f \times \left( \frac{N}{2} \right)^2 \times \frac{g \times m^4}{4 \times w^2 \times (2 \times w + u)^2} \quad (4.50)$$

The dimension  $l_f$  is the equivalent length of the machine that accounts for the core end fringing flux and will be discussed later on this section.

Component  $L_2$  is expressed by equation (4.51).

$$L_2 = \mu_0 \cdot l_f \cdot \left(\frac{N}{2}\right)^2 \cdot \frac{2}{\pi} \left( \log\left(\frac{n}{e}\right) + \frac{2 \cdot y \cdot (n - e)}{w \cdot v} + \frac{(2 \cdot y^2 - \pi \cdot w \cdot v)}{4 \cdot (w \cdot v)^2} \cdot (n^2 - e^2) - \frac{\pi \cdot y^2 \cdot (n^3 - e^3)}{6 \cdot (w \cdot v)^2} + \frac{\pi \cdot (n^4 - e^4)}{64 \cdot (w \cdot v)^2} \right) \quad (4.51)$$

Component  $L_3$  may be expressed by:

$$L_3 = \mu_0 \cdot l_f \cdot \left(\frac{N}{2}\right)^2 \cdot \frac{2}{(\phi - r)} \cdot \log\left(\frac{2 \cdot \tan(\phi - r) + \pi - (\phi - r)}{2 \cdot \tan(\phi - r) + \pi - 2 \cdot (\phi - r)}\right) \quad (4.52)$$

Components  $L_4$  and  $L_5$  may be calculated by:

$$L_4 = \mu_0 \cdot l_f \cdot \left(\frac{N}{2}\right)^2 \cdot \frac{2}{\pi - (\phi - r)} \cdot \log\left(\frac{2 \cdot g_i}{e \cdot [\pi - (\phi - r)]}\right) \quad (4.53)$$

$$L_5 = \mu_0 \cdot l_f \cdot \left(\frac{N}{2}\right)^2 \cdot \frac{p + e}{g_i} - \frac{2}{\pi - (\phi - r)} \quad (4.54)$$

The equivalent length of the machine that accounts for the fringing flux at the core end is determined based on considerations from [68] and [72]. A detailed description of the calculation applied to the SRM is given in [68], where the length  $l_f$  is determined by:

$$l_f = l_{stk} + 2 \cdot n \cdot (1 - \sigma) \quad (4.55)$$

where  $n$  is defined in Fig.4.13.

In order to determine the coefficient  $\sigma$ , a fictitious uniform air gap,  $g_f$ , is defined. For simplicity, the method of [68] was adopted. It resulted in:

$$g_f = \frac{1}{5} \cdot \left[ \frac{\pi}{2} \cdot n + \frac{\pi}{2} \cdot e + \left( \frac{\pi}{2} - \frac{\phi - r}{2} \right) \cdot e + g_i + g_i \right] \quad (4.56)$$



**(f) Calculation of the phase inductance for the Shark SRM**

The above equations were used to calculate the components of the phase inductance in the Shark SRM but each of them was corrected to account for the presence of the Shark profile. To do this, the influence of the Shark profile on each region has to be identified and described:

- Region 1 has no Shark teeth
- Region 2 has Shark teeth on the rotor surface
- Region 3 has Shark teeth on both stator and rotor surface
- Region 4 has Shark teeth on the stator surface
- Region 5 has Shark teeth on the stator surface

The presence of the Shark teeth affects the flux path used to calculate the each inductance component as it is illustrated in Table 4.1. Therefore, the inductances associated to regions 1÷5 in a Shark SRM may be expressed by combining the inductance of the regions 1÷5 in the CSRSM and the inductance of the Shark teeth regions calculated separately. This component is called  $L_{ktooth}$ , where k denominates the region k, where the Shark teeth are located.

The resulting expressions for the tooth region inductances and for the resulting inductances of the flux paths are given in Table 4.1, row 4.

The inductance of the path 3 in the Shark SRM is determined by modifying the equivalent length,  $l_f$ , by accounting for the dimensions of the Shark profile:

$$l_{fShark} = \frac{l_{stk}}{\cos \beta} + 2 \cdot n \cdot (1 - \sigma) \quad (4.57)$$

Table 4.1 Calculation of the path inductances of the Shark SRM by using the model of the CSRSM

Path 1	Path 2	Path 3	Path 4	Path 5
no influence	Shark teeth on the rotor pole	Shark teeth on both stator and rotor	Shark profiles on the stator pole	Shark profiles on the stator pole
<p>The diagram shows a cross-section of a Shark Switched Reluctance Motor. It features a stator with four poles and a rotor with two poles. Five magnetic flux paths are indicated by dashed lines: (1) is a path through the stator pole; (2) is a path through the rotor pole; (3) is a path through both stator and rotor poles; (4) is a path through the stator pole and the air gap; (5) is a path through the stator pole and the air gap. The centers of the stator and rotor poles are labeled O1 and Or, respectively.</p>				
$L_{1Shark} = L_{1CSRSM}$	$L_{2Shark} = L_{2CSRSM} + L_{2tooth}$	$L_{3Shark} = L_{3CSRSM} \cdot \frac{l_{fShark}}{l_f}$	$L_{4Shark} = L_{4CSRSM} - L_{4tooth}$	$L_{5Shark} = L_{5CSRSM} - L_{5tooth}$
-	$L_{2tooth} \cong \frac{4 \cdot \mu_0 \cdot n_t \cdot q_2}{\tan \beta}$	-	$L_{2tooth} \cong \frac{4 \cdot \mu_0 \cdot n_t \cdot (t - e)}{\tan \beta}$	$L_{2tooth} \cong \frac{4 \cdot \mu_0 \cdot n_t \cdot (p + e - t)}{\tan \beta}$



**(g) Results**

The magnetisation characteristics for the unaligned position are presented for both the CSRSM and the Shark SRM in Fig 4.14. In terms of inductance, for the reference SRM the measured unaligned inductance was  $L_0=58.7$  [mH] and the calculated value was  $L_0=60.9$  [mH]. In the case of the Shark SRM the measured value was of  $L_0=62.5$  [mH] while the calculated inductance  $L_0=66.5$ [mH] as it may be verified in Fig. 4.14.

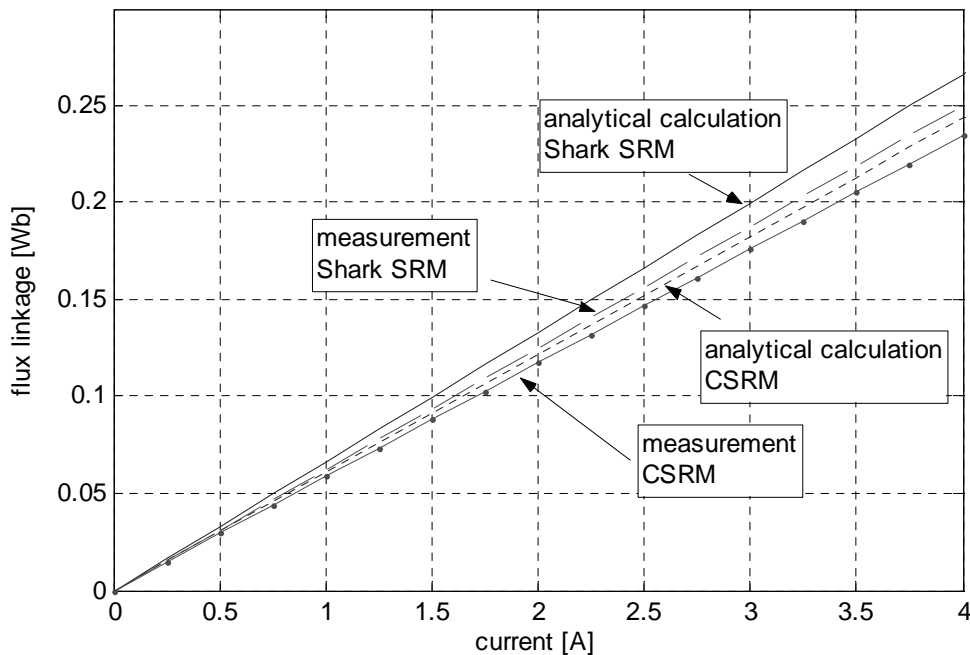


Fig.4.14 Comparison of the calculated magnetization characteristics in the unaligned position with those measured on the demonstration machines for both reference and Shark SRM.

The ratios of each path permeance to the total permeance are given for CSRSM and Shark SRM in Appendix C.5. These results indicate that the flux lines are concentrated in regions 3 and 5.

## 4.5 Energy conversion and optimum Shark configuration

In this section, the performance of the saw-toothed Shark SRM is analysed for different dimensions of the Shark profile. The models presented in the previous sections are used to calculate the necessary magnetisation characteristics. The objective function for this analysis is the *energy gain*,  $k_W$ , which is defined as the ratio of the energy change in the two considered motors. Its mathematical expression is given by:

$$k_W = \frac{\Delta W_{Shark}}{\Delta W_{reference}} \Big|_{i=const} \quad (4.58)$$

where

$$\Delta W_{reference/Shark} = (W_{\max} - W_{\min})|_{i=const} \quad (4.59)$$

$$\text{with: } W|_j = \int_{i=0}^{i_{\max}} \lambda(i, \theta)|_j \cdot di, \quad j = \min, \max \quad (4.60)$$

where  $\lambda(i, \theta)$  is the flux linkage as a function of current and rotor position.

The analysis was performed for two cases:

- a) The number of turns per phase was maintained constant for both the CSRSM and the Shark SRM. This condition can be satisfied as long as the conditions expressed by the equations (4.27) and (4.33) are satisfied.
  - b) The number of turns per phase was changed to fill the available winding area
- a) *Identical number of turns in CSRSM and Shark SRM.*

The energy gain calculated analytically for different Shark configurations is presented in Fig.4.15. The envelope represents the dependence of the Shark tooth pitch on the angle  $\beta$ , expressed by the conditions given by equations (4.26) for the upper limit and (4.33) for the lower limit. The results illustrated were obtained for SRMs with main dimensions from Appendix A.2. The results were obtained for different values of the Shark tooth pitch, limited as expressed by equations (4.27) and (4.33). The results indicate that the optimum Shark configuration is given by the set of parameters ( $l_{shk}$  5 [mm],  $\beta=50$  [deg]).

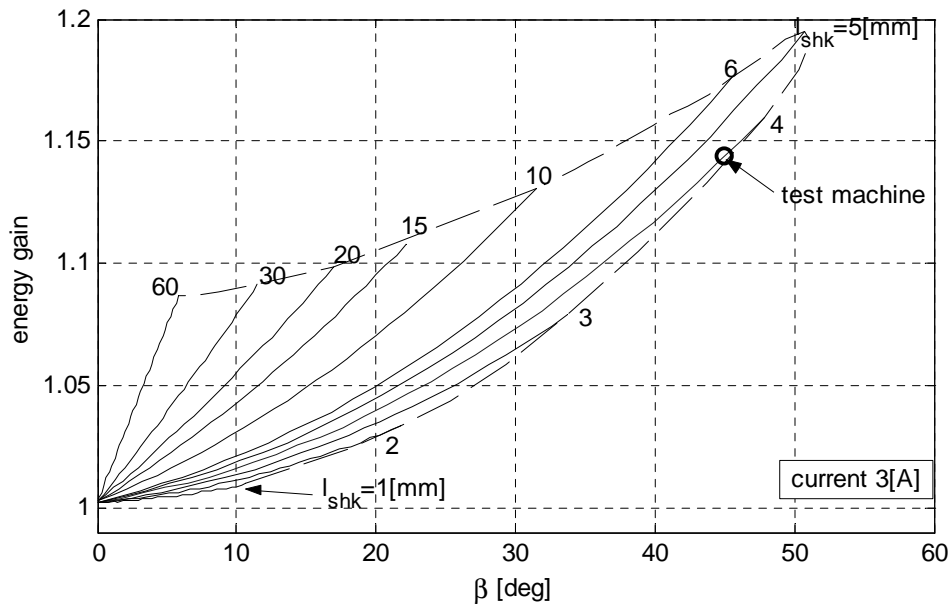


Fig.4.15 Energy gain as a function of  $\beta$  and tooth pitch for Shark SRM, having constant number of turns per pole  $N_{\text{turns}}$  and high current

The energy gain at a lower current i.e 1 [A] is illustrated in Fig.4.16. By comparing the energy gain from Fig.4.15 to that from Fig.4.16, it may be observed that the energy gain at lower current exceeds that at higher current. This means that the use of the Shark air gap is more beneficial when the iron of the magnetic circuit is not saturated. It may also be observed that the optimum configuration of Shark air gap is obtained again for Shark tooth pitch,  $l_{shk}$ , of 5 [mm] and angle,  $\beta = 50$  [deg].

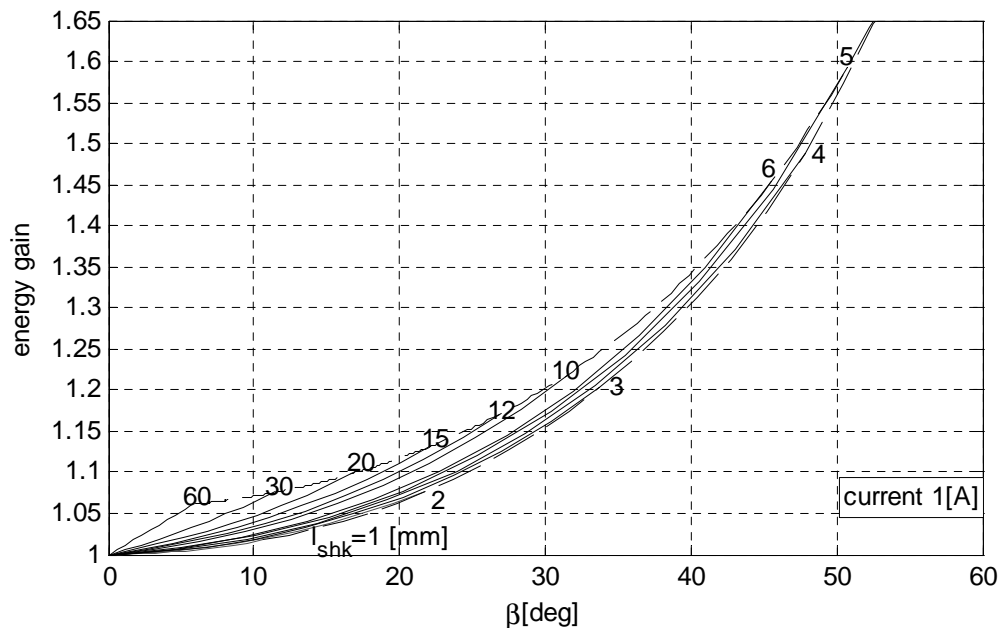


Fig.4.16 Energy gain as a function of  $\beta$  and tooth pitch for Shark SRM, having constant number of turns per pole  $N_{turns}$  and low current

b) *Number of turns modified accordingly to the available winding area.*

When the number of turns is not considered constant but variable conforming to the available winding area, the family of energy gain characteristics are modified as shown in Fig.4.17.

It could be seen that the energy gain is reduced compared to that represented in Fig.4.15. The energy gain reaches its maximum for a Shark tooth pitch of 4 [mm] and an angle  $\beta$  of 47.5 [degree].

This time the diagrams plotted for a maximum current of 3 [A] indicate that the optimum configuration the Shark profile is length  $l_{shk} = 4$  [mm] and angle  $\beta = 47.5$  [deg]. The gain in the co-energy variation is substantially reduced due to the reduction of the phase MMF. If the excitation conditions were preserved, the reduction of the number of turns requires a higher current to flow through the winding. This will consequently affect the resistive losses and the performance of the machine.

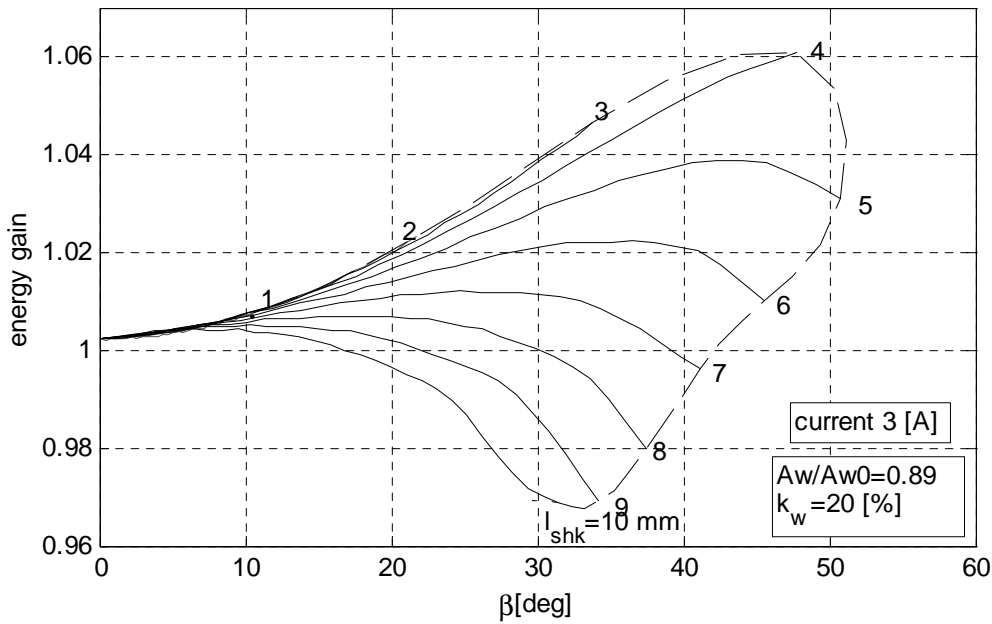


Fig.4.17 Energy gain characteristics for the different  $\beta$  and  $l_{shk}$  of Shark segment, when the number of turns per pole varies proportional to the available winding area for  $k_w=20$  [%].

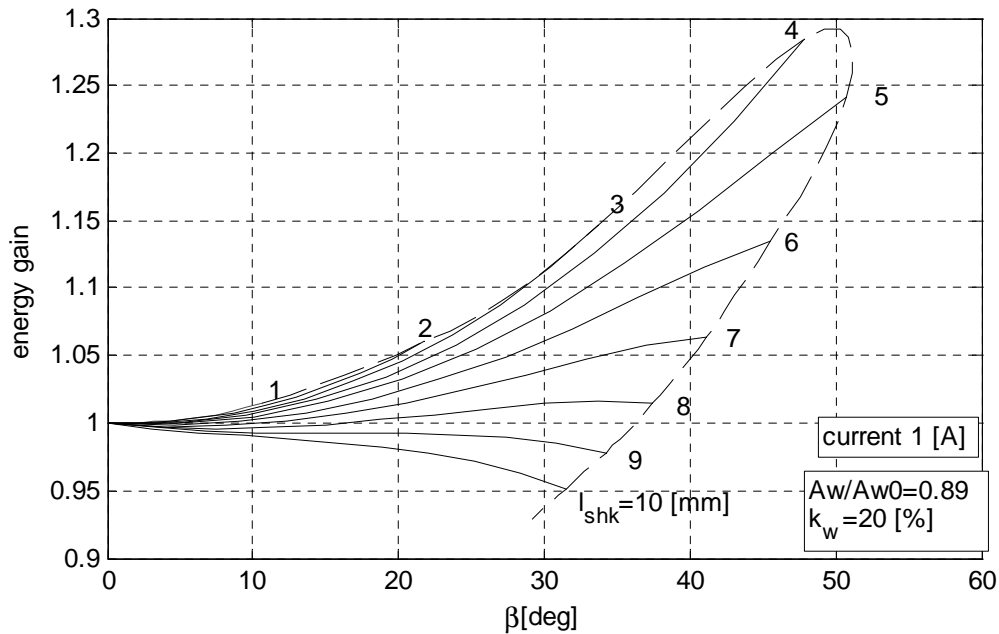


Fig.4.18 Energy gain characteristics for the different  $\beta$  and  $l_{shk}$  of Shark segment, when the number of turns per pole varies proportional to the available winding area for  $k_w=20$  [%],  $i=1$  [A]

It may be concluded that the optimum Shark configuration lies in a narrow dimensional range (tooth pitch of 4 to 5 [mm], and angle of 47 to 50 [degree].), regardless of the winding layout. For the prototype a saw profile with angle  $\beta$  of 45 [deg] and tooth pitch  $l_{shk}$  of 4[mm] was selected.

## 4.6 Analytical calculation of the static force in Shark Switched Reluctance Motor

Generally, three forces are produced in any electrical machine. These are:

- Tangential force, which acts tangentially to the rotor in the direction of movement. This force produces the torque of the machine.
- Radial force, acts radially. This force may cause vibration of the lamination stack and is usually larger than the tangential force. Therefore, several methods to reduce the radial force are reported [75], [76], [77], [108], [109], [110].
- Axial force, acts oriented along the lamination stack. It is generally very small and is often be neglected in cylindrical air gap machines.

In the Shark SRM, the relative values components of force change amplitude with respect to those in the CSRSM. This change depends on the shape and dimensions of the Shark teeth. It will be shown that these changes are important for the vibration of the machine and for the mechanical layout of the assembly.

Therefore, in this section, an analytical method to calculate the components of the force produced in a Shark SRM, having saw-toothed air gap is presented and discussed. This method uses the method of virtual work and the models of the magnetisation curves, determined in the previous sections of this chapter.

Initially, the components of force are illustrated for both CSRSM and Shark SRM having axially symmetrical and unsymmetrical air gap. Then, the methodology of the calculations, highlighting two different approaches, is specified. Subsequently, the calculations are presented and discussed and the data obtained FEA of the specified models are used to verify the analytical model for force calculation.

### 4.6.1 Force distribution in cylindrical and Shark air gap Switched Reluctance Motors

Prior to the final selection of the analytical model, the components of force in CSRSM and Shark SRM and the relationship between them are identified. To do this, the axial cross-section of the machine is considered, because, as shown in chapter 3, this is the cross-section relevant for the Shark SRM, when 2D modelling is performed.

In a CSRSM, a radial force,  $f_r^{(c)}$  and a tangential force,  $f_t^{(c)}$  are produced. The axial force is very low and it may be neglected. This is illustrated in Fig.4.19 a). On the other hand, in a Shark SRM, a force is produced perpendicular to each side of the Shark tooth as illustrated in Fig.4.19 b). These forces are termed  $f_n^{(1)}$  and  $f_n^{(2)}$ . Each normal component  $f_n^{(i)}$  has itself two components; one component acts along the lamination stack and is termed axial force,  $f_a^{(1)}$ ,  $f_a^{(2)}$ ; the second component acts radially to the motor and is termed radial force,  $f_r^{(1)}$ ,  $f_r^{(2)}$ . The axial components



$f_a^{(1)}$  and  $f_a^{(2)}$  act in opposite directions. Therefore, if the air gap is axially symmetrical, there is no resultant axial force.

On the other hand, if the air gap were axially unsymmetrical, as shown in Fig. 4.19 c), the forces produced on the two sides of the Shark tooth are no longer equal. This is because the air gap flux density on the two sides is not equal, as the corresponding magnetic circuits have different air gap lengths. A resultant force will be produced that will be axially oriented, in the direction such as to increase the initial axial displacement,  $\delta$ . If axial movement of the rotor were not prevented, the rotor would physically contact the stator and would not be able to rotate.

The components of force produced in a Shark SRM may be determined as a function of the normal force and the angle  $\beta$ , defining the geometry of the Shark tooth:

- radial component:

$$f_r^{(1)} = f_n^{(1)} \cdot \cos \beta \quad (4.61)$$

- axial component:

$$f_a^{(1)} = f_n^{(1)} \cdot \sin \beta \quad (4.62)$$

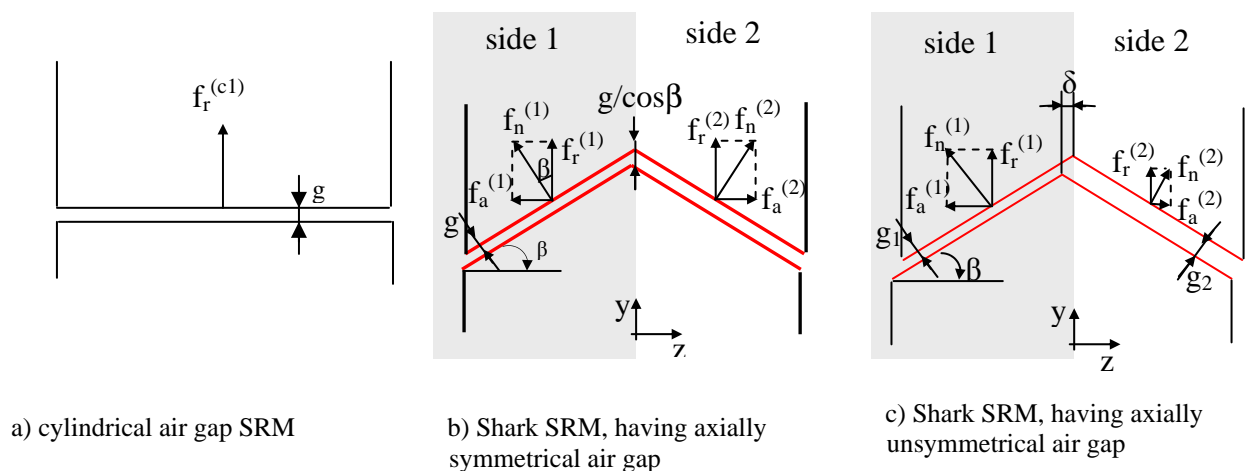


Fig.4.19 Illustration of the forces produced in the axial cross-section of a CSRSM and Shark SRM.

Imagining a CSRSM, equivalent to the half Shark tooth (e.g. side 1 in Fig.4.19), it may be written that:

$$f_r^{(c1)} = f_n^{(1)} \quad (4.63)$$

where:  $f_r^{(c1)}$  is the radial force and  $f_n^{(1)}$  is the force produced in the axial cross-section of the Shark SRM.

The axial component of the force produced in the equivalent CSRМ is:

$$f_a^{(c1)} = 0 \quad (4.64)$$

The tangential component of the equivalent CSRМ is identical to that of the corresponding Shark SRМ.

#### 4.6.2 Method for calculating the forces in a Shark SRМ

The analytical model for calculating the forces in a Shark SRМ is based on the idea of transforming a specified Shark SRМ into an equivalent CSRМ. The method used to perform the transformation was discussed in section. 4.2. Now, it will be shown how this method may be applied to the Shark SRМ with axially unsymmetrical air gap.

From Fig.4.20 it may be seen that the Shark tooth with axially unsymmetrical air gap has different air gap lengths on its sides. If the maximum axial displacement of the rotor,  $\delta_{\max}$  is:

$$\delta_{\max} = \frac{g}{\sin \beta} \quad (4.65)$$

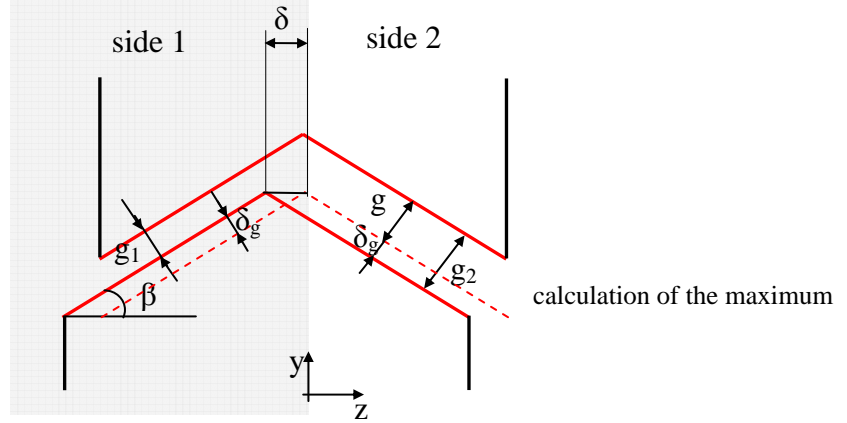
then, the actual displacement may be written as a ratio  $k_{\delta}$  of  $\delta_{\max}$  :

$$\delta = k_{\delta} \cdot \delta_{\max} \quad (4.66)$$

Using these equations, the air gap lengths on each side of the Shark tooth may be calculated by:

$$g_1 = g - \delta_g = g - \delta \cdot \sin \beta \quad (4.67)$$

$$g_2 = g + \delta_g = g + \delta \cdot \sin \beta \quad (4.68)$$

Fig.4.20 Illustration of the displacement  $\delta_{\max}$ 


Assuming uniform distribution of the field lines, the Shark SRM, having axially unsymmetrical air gap may be considered equivalent to two Shark SRM, having stack length equal to half the stack length of the specified machine and the air gap lengths defined by equations (4.67) and (4.68).

Following this transformation, each half machine may be analysed separately, using the analytical model presented in section 4.2. This model provides the magnetisation characteristics for each of the two Shark SRMs as a function of rotor position and current.

The force may be calculated by the method of virtual work. That is to determine the ratio of co-energy change caused by an infinitesimal displacement.

Another method is to perform all calculations on the equivalent Shark SRMs. It means that the components of the force may be obtained directly by the variation of the co-energy with respect to the corresponding coordinate:

- The normal force in the axial cross-section of the Shark SRM with uniform air gap may be determined from the change of co-energy with respect to the air gap length:

$$f_n^{(i)} = \frac{\partial W_i}{\partial g_i}, \quad i = 1, 2 \quad (4.69)$$

- The axial force may be determined by the change in the co-energy with respect to the coordinate  $z$ :

$$f_a^{(i)} = \frac{\partial W_i}{\partial z_i}, \quad i = 1, 2 \quad (4.70)$$

- The radial force may be determined from the change of the co-energy with respect to the coordinate  $y$ :

$$f_r^{(i)} = \frac{\partial W_i}{\partial y_i}, \quad i = 1, 2 \quad (4.71)$$

or direct from axial force:

$$f_r^{(i)} = \frac{f_a^{(i)}}{\tan \beta}, \quad i = 1, 2 \quad (4.72)$$

or by:

- axial component:  $f_a^{(i)} = f_r^{(ci)} \cdot \sin \beta, \quad i = 1, 2$
- radial component:  $f_r^{(i)} = f_r^{(ci)} \cdot \cos \beta, \quad i = 1, 2$

The calculated forces were compared to those determined by FEA and the results were satisfactory. However, this subject is not discussed in here as it is outside the scope of this chapter. Here, the intention is to provide only a general overview of the forces produced in Shark SRM.

#### 4.6.2 Study of the forces produced in a Shark SRM

The redistribution of iron between the stator and rotor bodies, caused by the Shark shape, makes the components of the forces different, compared to those arising in CSRSM.

The radial force, produced in an SRM, excites vibration of the mechanical assembly, especially the stator and rotor yokes. Axial force may cause difficulties in the mechanical assembly and may excite vibration of the mechanical structure along the longitudinal axis as well.

Axial vibration is very small in a CSRSM without skew [40]. Although, the CSRSM is normally designed without skew, there are examples of skewed CSRSM [80]. In Shark SRM, with an axially unsymmetrical air gap, this axial vibration may be excited by the resultant axial force.

The amplitude of these forces may change with the dimensions of the Shark profile. Therefore, in this section, this influence is studied by using the models described in the previous section. The radial and axial components of force are studied as functions of: the excitation current, the axial displacement of the rotor stack with respect to the stator stack and the dimensions of the Shark profile – that is the angle  $\beta$  and the Shark tooth pitch,  $l_{shk}$ .

##### a) Study of the radial force

In this subsection, the normal and radial forces produced in a Shark SRM are studied with symmetrical ( $k_{\mathcal{S}} = 0$ ) and unsymmetrical ( $k_{\mathcal{S}} \neq 0$ ) air gap. The study includes the effect of the dimensions of the Shark profile, on the force components mentioned.

By radial force is understood the force that acts perpendicularly to the axis of the machine. Here, the sum of the forces produced on each side of the Shark profile is considered.

By normal force is understood the force that acts perpendicular to one side of the Shark profile – that is  $f_n^{(1)}$  or  $f_n^{(2)}$  in Fig.4.19. However, because the total force produces the effects mentioned above, this will be used in the following paragraphs. The resulting force is determined for the Shark SRM formed by all sides 1 of the initial machine.

Initially, the case of the axially symmetrical air gap is considered. The symmetry of the air gap makes that the forces produced by the two equivalent Shark SRMs are equal. Therefore, only one component of the normal and radial forces is illustrated for the case in point.

The normal force and the corresponding radial component are illustrated for a Shark SRM with low excitation current in Fig.4.21 and Fig.4.22 and for high current in Fig.4.23 and Fig.4.24.

From Fig.4.21, it may be seen that the normal force increases by increasing the angle  $\beta$ . It may also be seen that the Shark tooth pitch,  $l_{shk}$ , has no significant effect on the normal force. The total radial force illustrated in Fig.4.22, is not much affected by the dimensions of the Shark air gap. It may be seen that the change in its amplitude is of maximum 1.7 [N], which represent 3.7 % of the radial force of the corresponding CSRMs. This means that, at low current, application of the Shark air gap does not significantly reduce the total radial force.

If the iron regions of the Shark SRM are saturated, the effect of the Shark air gap on the normal force is substantial. This is illustrated in Fig.4.23 and Fig.4.24. For identical mechanical conditions (symmetrical air gap, identical Shark profiles) but at high current, the normal force decreases for increasing the angle  $\beta$  and by increasing the tooth pitch,  $l_{shk}$ . The corresponding radial force, which is illustrated in Fig. 4.24, decreases by increasing the angle,  $\beta$ , and the tooth pitch,  $l_{shk}$ .

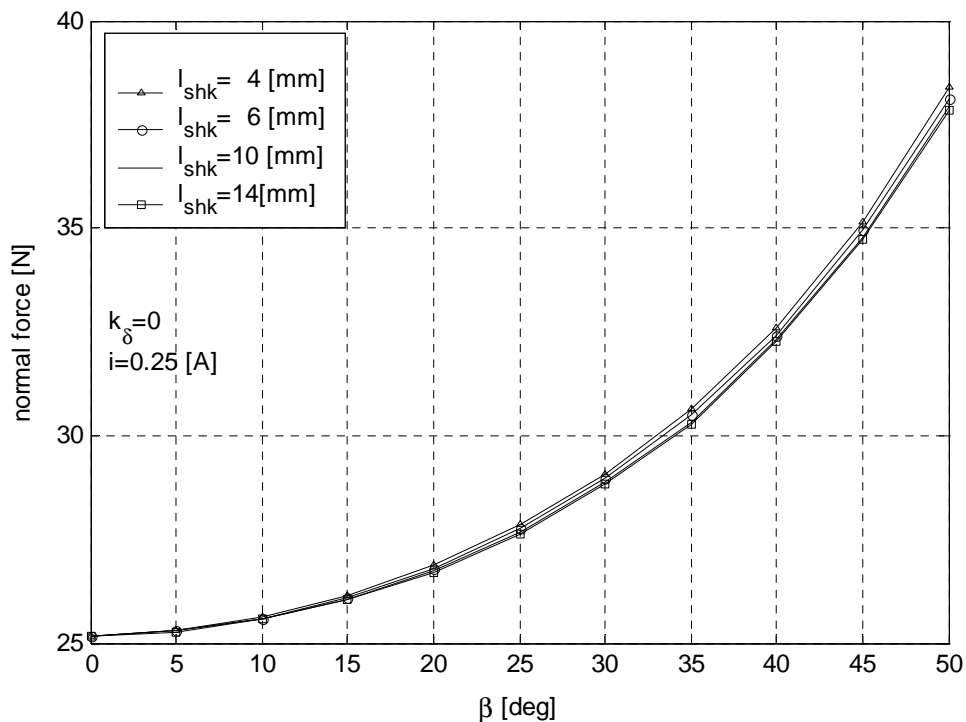


Fig.4.21 Normal force in the Shark SRM with axially symmetrical air gap and low current

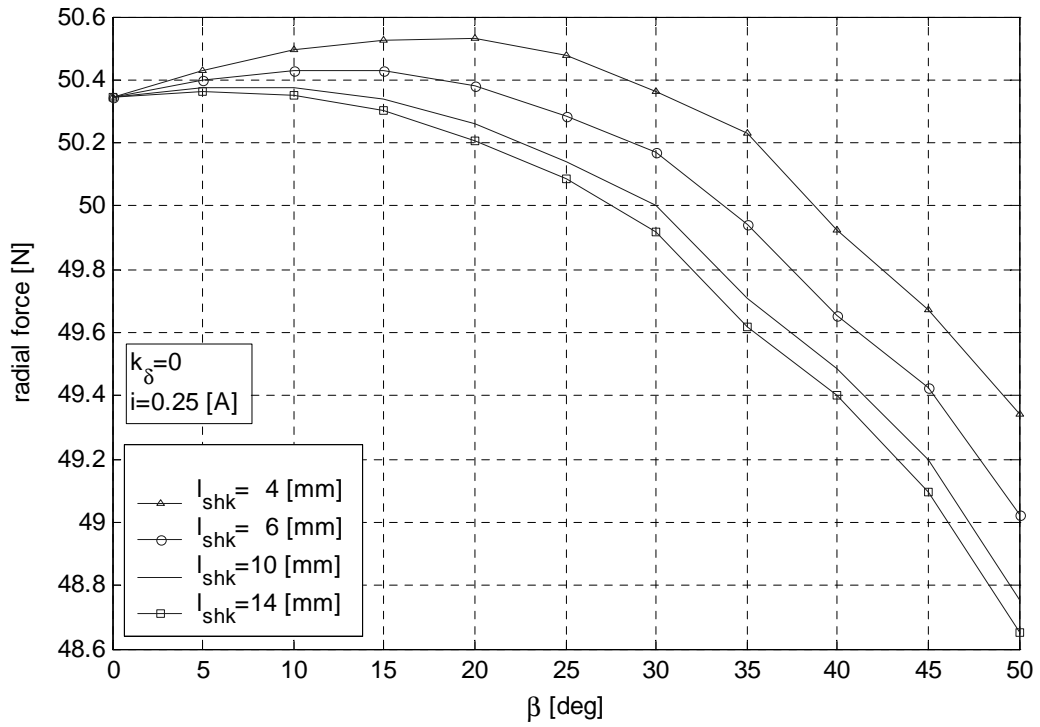


Fig.4.22 Radial force in the Shark SRM with axially symmetrical air gap and low current

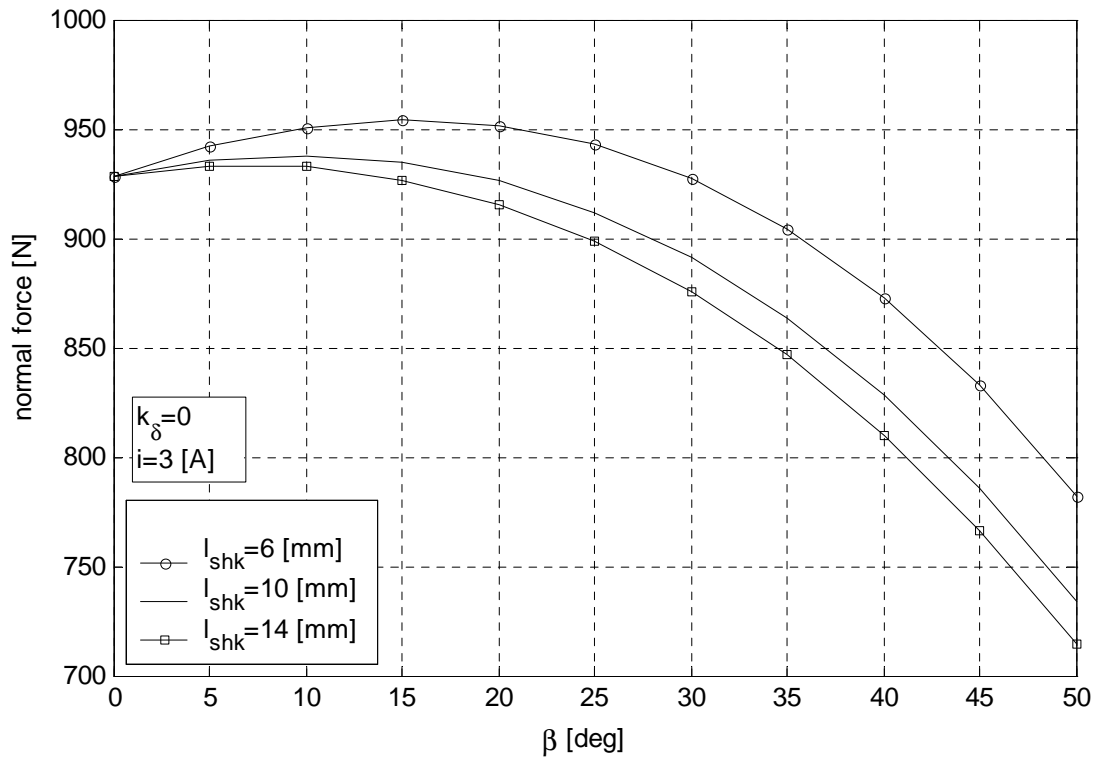


Fig.4.23 Normal force in the Shark SRM with axially symmetrical air gap and high current

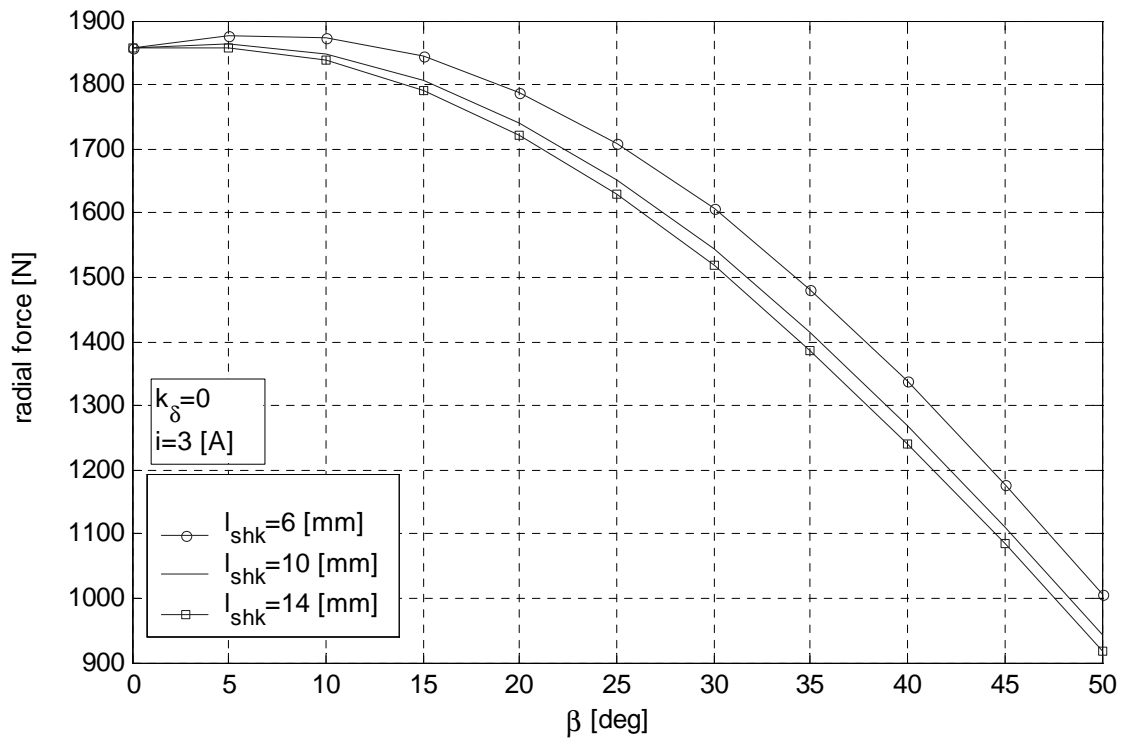


Fig.4.24 Radial force in the Shark SRM with axially symmetrical air gap and high current

Because, the reduction in the radial force that might be obtained at high current is of interest, only this situation is explored further if the air gap were axially unsymmetrical. The total radial force of the Shark air gap, having tooth pitch constant decreases by decreasing the angle  $\beta$ , as shown in Fig.4.25. For a specified tooth pitch, the increase in axial displacement determines the increase in the total radial force only for a limited range of angles  $\beta$ . By increasing  $\beta$ , the total radial force is affected only by the tooth pitch.

The components of the radial force produced on each side of the Shark profile are illustrated in Fig.4.26 and Fig.4.27. It may be observed that the total radial force of side 1,  $F_r^{(1)}$ , having a shorter air gap, increases compared to the corresponding value of the Shark SRM with symmetric air gap ( $k_\delta = 0$ ). On the other hand, the total radial force corresponding to the side 2,  $F_r^{(2)}$ , having longer air gap is smaller than that of the Shark SRM having symmetrical air gap ( $k_\delta = 0$ ).

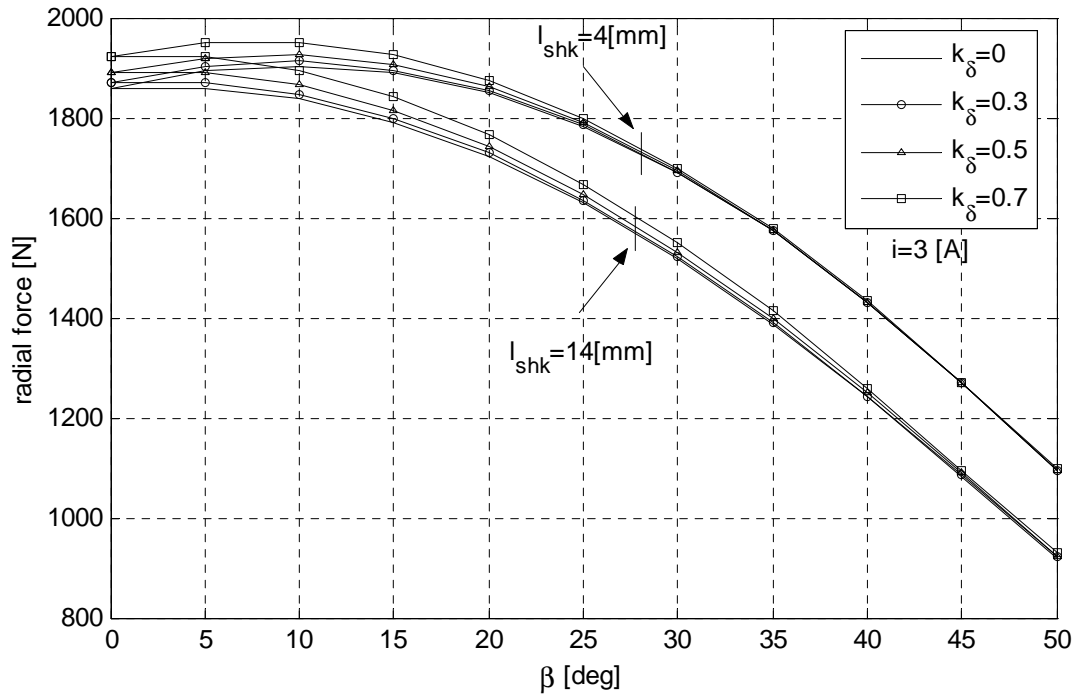


Fig.4.25 Total radial force in the Shark SRM with axially unsymmetrical air gap

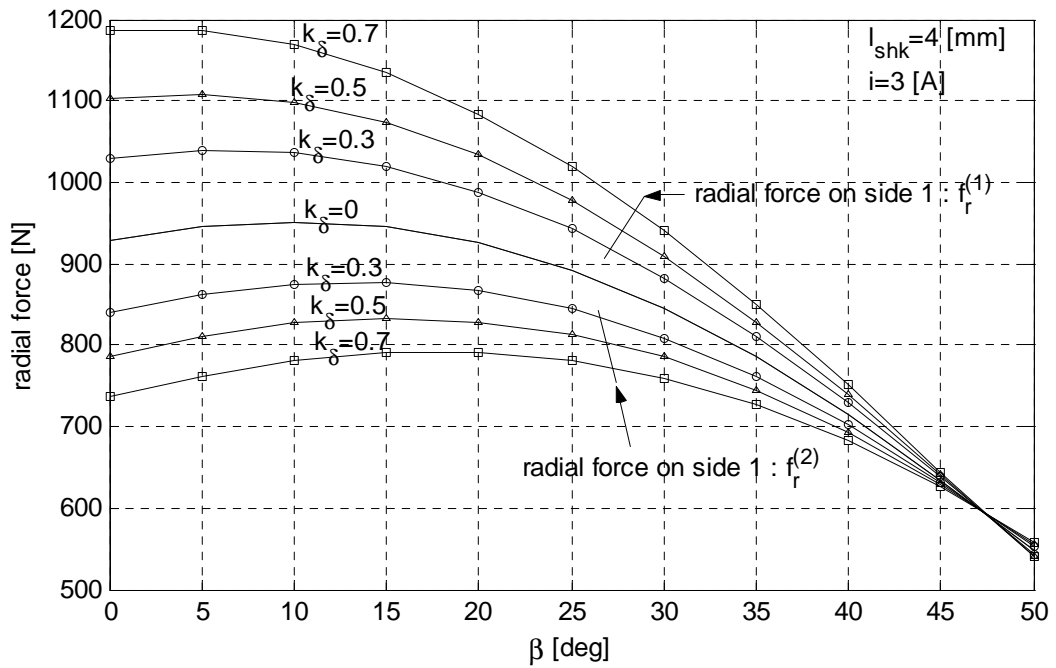


Fig.4.26 Radial force produced on each side of the Shark profile



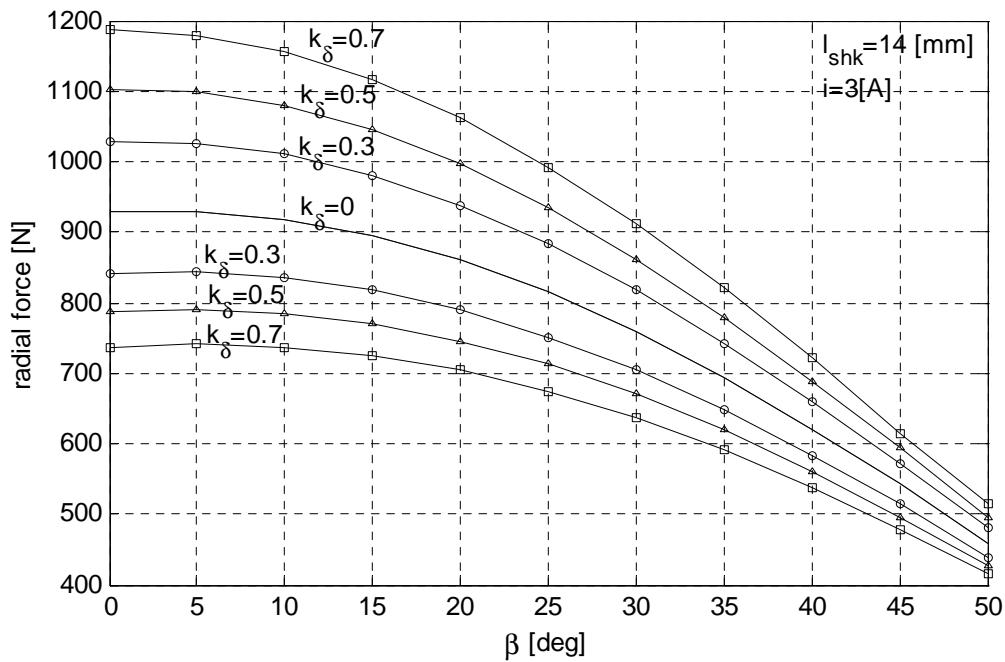


Fig.4.27 Radial force produced on each side of the Shark profile as a function of the angle  $\beta$  of the Shark profile

The analysis of the curves plotted in Fig.4.26 and Fig.4.27 shows that:

- A Shark profile having a large angle  $\beta$  and long Shark tooth pitch is beneficial if the radial force were of main concern
- The difference in the magnitude of the normal components produces a moment that tends to rotate each segment as shown in the drawing associated with . The magnitude of this moment is given by:

$$\tau = (f_r^{(1)} - f_r^{(2)}) \cdot \frac{l_{shk}}{4} \quad (4.76)$$

#### b) Study of the axial force

If the air gap in a Shark SRM is axially unsymmetrical, this generates unsymmetrical forces on the sides of the Shark profiles. The resultant axial force differs from zero and this may cause difficulties in the mechanical assembly. Therefore, it is interesting and useful to know the effect of the dimensions of the Shark profile on the amplitude of the axial force.

The axial force may be also determined by using the models presented in the previous section. As for the radial forces, the axial forces are analysed using the same methods as was used for the radial forces for various configurations of Shark SRMs at low and high current.

For low excitation current and axial displacement specified by  $k_\delta = 0.5$ , the axial forces acting in both directions and the total axial force are represented in Fig.4.28. It may be observed that the

Shark tooth pitch has no significant influence on the amplitude of these forces. On the other hand, the increase in angle  $\beta$  determines a substantial increase in the total axial forces produces on the two sides of the Shark teeth. Consequently, the resulting total axial force increases by increasing the angle  $\beta$ .

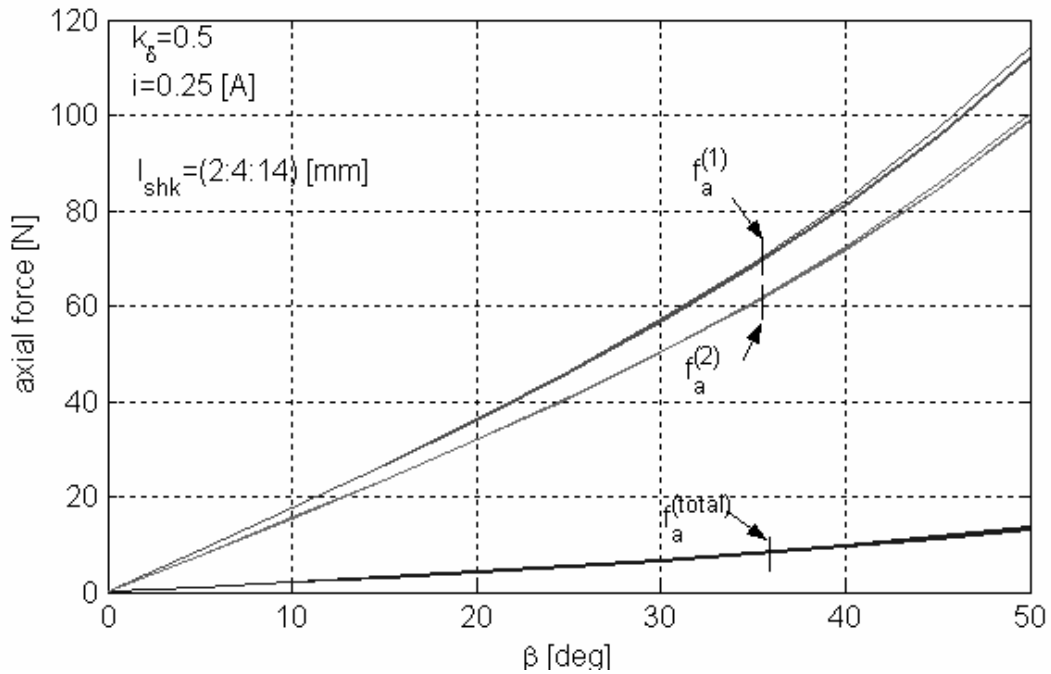


Fig.4.28 Total axial force produced on each side of the Shark teeth and total resultant axial force in Shark SRM having, axially unsymmetrical air gap,  $k_\delta = 0.5$ , and low current

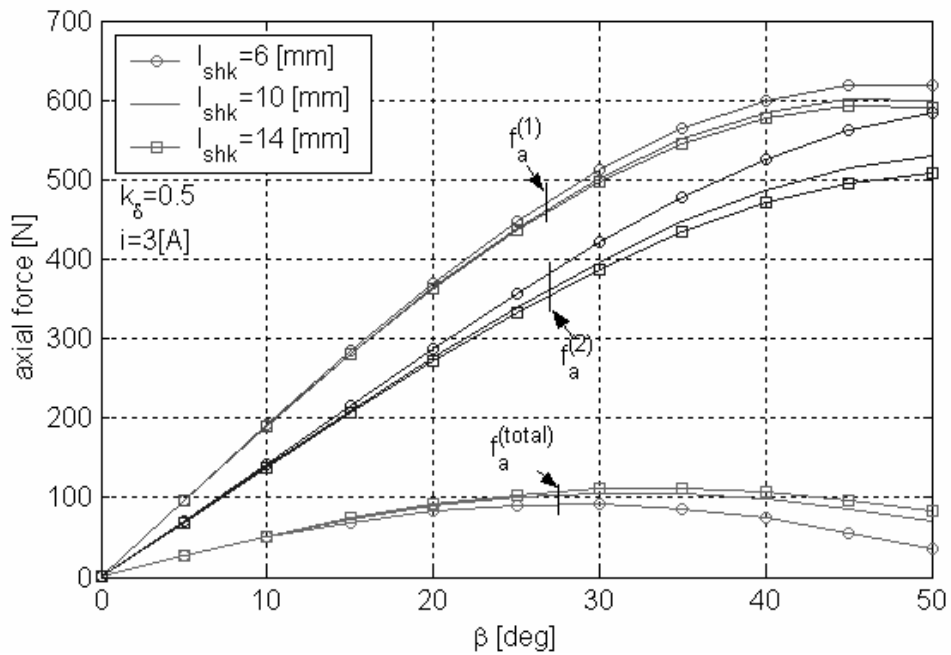


Fig.4.29 Total axial force produced on each side of the Shark teeth and total resultant axial force in Shark SRM having, axially unsymmetrical air gap,  $k_\delta = 0.5$ , and high current

For high current, the same forces are represented for various Shark configurations in Fig.4.29. The total axial force corresponding to each side of the Shark teeth increases by increasing the angle  $\beta$ . However, by increasing the angle  $\beta$ , the resultant axial force increases to a maximum value, afterwards, starting to decrease.

The influence of the axial displacement on the axial force is illustrated in Fig.4.30. It can be observed that the amplitude of the resultant axial force would be greater if the axial displacement were to be increased.

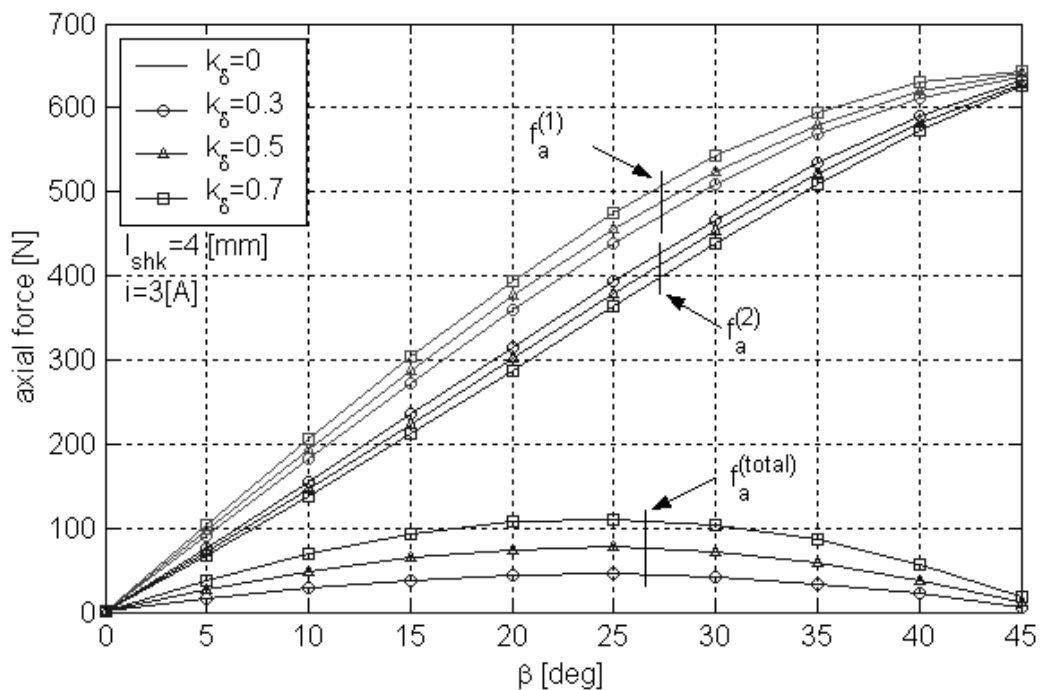


Fig. 4.30 Resultant axial force at different displacements

The relations between the radial and the axial total forces, produced on each side of the Shark teeth is illustrated in Appendix C.6.

## 4.7 Summary and conclusions

In this chapter, models of the aligned and unaligned magnetisation characteristics of the Shark SRM have been presented. Two approaches have been discussed. One is an adaptation of the Langevin function to model the magnetisation characteristic of the CSRSM and Shark SRM. This approach was shown to have important drawbacks because it requires a large amount of data from FEA in order to calculate the coefficients of the modified Langevin function.

The second approach is characterised by simplicity. The key idea is to reduce the Shark SRM to an equivalent cylindrical SRM, whose characteristics can be determined by making use of one of the existing modelling methods. The equivalent CSRSM was derived from considerations regarding the

saturation mechanisms in the Shark profiles, which were identified in chapter 3. In the proposed model, the main air gap dimensions of the equivalent CSRSM are calculated based on the dimensions of the Shark SRM and of the Shark profile. The transformation was made based on the condition of equal air gap reluctances. The redistribution of magnetic material inside the Shark machine was accounted for by the means of the average stator and rotor diameters.

The validation of the model was made by comparison of the calculated data with data determined by a numerical method (FEA) for a large range of Shark profile configurations.

The evaluation criterion was the magnetisation characteristics in both aligned and unaligned positions. For a single case, that of the demonstration machine, the experimental results were used to verify the model when it was applied in both cases of the cylindrical air gap SRM and Shark SRM.

Comparison between the data obtained by analytical calculations, measurements or FEA corrected for the yoke regions indicated good agreement. The analytical model was checked for cylindrical and for Shark SRM with various configurations.

The modelled magnetisation characteristics were then used to analyse and optimise the configuration of the Shark SRM. It was shown that when the reduction of the winding area is taken into consideration, the optimum configuration of the Shark SRM with the main dimensions given in Appendix A.2 is obtained for the saw-toothed profile having the tooth pitch  $l_{shk} = 4 [mm]$  and the angle  $\beta = 45 [deg]$ .

Using the proposed model of the Shark SRM, the forces produced in the axial cross-section of the motor have been calculated. The variation of these forces as a function of the dimensions of the Shark profile was studied.

It was concluded that the Shark profiles reduce the radial component of the force, which may be expected to contribute to reduced vibration level. Calculation of the vibration is beyond the scope of this project. On the other hand, in a Shark SRM, having axially unsymmetrical air gap, a resultant axial force is produced if the air gap is axially unsymmetrical. This may cause difficulties for assembly of the machine and even axial vibration of the rotor stack. In the worst case the rotor will rub on the stator.

It may be concluded that by the redistribution of the mass between the stator and the rotor body the Shark SRM provides improvement of the magnetic circuit. Its capability of producing flux is improved. The components of the force are redistributed, in the sense that the radial force is reduced at the expense of the appearance of new axial force.



## Chapter 5

# Measurement and comparison of different motor types

In this chapter, the Shark concept is tested experimentally. The CSRSM and the Shark SRM, having the dimensions given in Appendices A.2 and A.3 and the Shark profile defined in chapter 3 and 4, were tested in static and steady-state conditions. The results of the static test have already been used in the previous chapters to verify the flux linkage characteristics calculated by FEA or by an analytical method. Here the results of the steady-state tests are used to evaluate output coefficients such as efficiency, power factor.

Additionally, various motor technologies are compared by using the mentioned output coefficients. Therefore, an Induction Motor (IM), a BrushLess DC Motor (BLDCM), a cylindrical air gap SRM (CSRSM) and its Shark counterpart were all tested at similar operating points. In an attempt to ensure valid similarity between the different motor types, similar geometrical and electromagnetical conditions were selected.

This chapter is organised as follows. The objectives are specified initially. Then the method, the test arrangements and the specifications of the motors to be tested are defined. Subsequently, the results of the measurements are presented for each motor separately. The relative evaluation of their performances is discussed, according to criteria to be defined. A summary and conclusions are presented at the end of this chapter.

### 5.1 Objectives and methodology

The aim of this chapter is to assess the relative steady-state performances of the mentioned electric motors, operating at working points, which will be specified.

To compare various types of electric motors, an appropriate approach assuring similar test conditions is required. Therefore, a review of existing methods is presented initially. Subsequently, the methodology selected in this project will be defined. Then the results of the steady-state test are presented for each motor, followed by a general comparison of the considered motors.

In the previous chapters, the static characteristics (flux linkage and torque) of various Shark air gap SRMs, have been obtained by using FEA and analytical models. All these calculations have been verified by comparing them with those measured on the test machines (a CSRSM and a Shark SRM). Therefore, the results of the static measurement will not be discussed in this chapter.

### 5.1.1 Existing approaches for comparison

The comparison of various electric motors may be designed mainly in two ways: by using the output equation or by calculating output coefficients of interest from variables measured on the test machine.

The output equation is generally used in preliminary design of electric motors and expresses the output or the electromagnetic power as a function of the main dimensions, efficiency and power factor of the motor. It was first developed for induction motors supplied with sinusoidal voltage. Subsequently, this has been extended to account for effects of the non-sinusoidal current and electromotive force (EMF) waveforms [92], [99], as to enable comparison of different motor technologies such as IM, SRM and BLDCM, by a unique equation.

The second method uses experimental data to compare electric motors. In this case the input variables (voltages, currents) and output variables (torque, speed) of the motor are measured at specified operating points. Subsequently the coefficients of interest and the loss distribution are calculated. Because by this method, data are collected directly from the test machines, these results are not affected by empiric factors as the results of the output equation are. Therefore, **the method of direct measurement on the specified motors was preferred in this work.**

To reach the objectives of the chapter a basis for comparison of various motor technologies must be defined. Generally, the comparison may be performed by two methods. These methods are defined based on that an electric motor is a device that makes use of a certain volume/mass of material with magnetic properties to convert the electrical energy (supplied into it through a certain volume/amount of conducting material) into mechanical energy:

- One method of comparing different motor technologies [97] is to impose constraints on the amount of different materials (i.e. same copper mass or same iron mass) used to build the motor and then evaluate the efficiency of the energy conversion process in each motor. By this method, the capability of the magnetic circuit to make use of a certain amount of material may be assessed (Fig.5.1, Approach 1).
- Another approach [93], illustrated in Fig.5.1. Approach 2, is to design motors capable of delivering a specified output power at a specified working point and to evaluate the volumes/masses of iron and copper used by each motor to produce the required power.

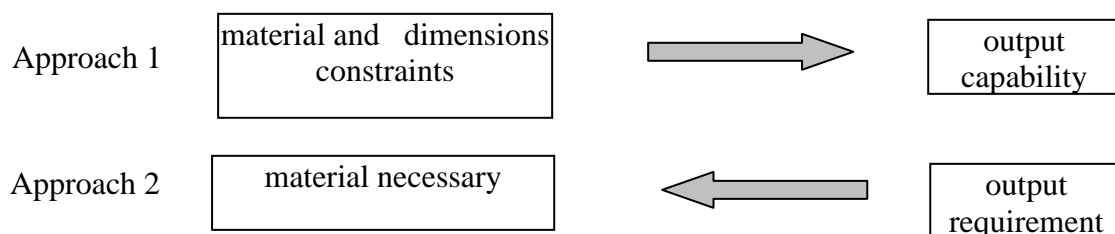


Fig. 5.1 Basic methodologies to compare different technologies of electric motors.

In this work direct measurement were performed such as to acquire data necessary for calculating the output coefficient of interest. The conditions of comparison were defined by combining

geometrical (specific to Approach 1) and electromagnetic (specific to Approach 2) constraints. These constraints are discussed in the next section.

### 5.1.2 Methodology of comparison

In this section, the constraints and the criteria for comparison of various electric motors are discussed. The elements approached are: *initial constraints*, *comparison criteria*, and *methodology* of the analysis have to be defined.

#### *Initial constraints*

Defining the *initial constraints* ensures that the data are collected in identical or similar conditions for each motor. These constraints fall into two categories:

- Geometrical constraints
- Electromechanical constraints

*The geometrical constraints*, are specified mainly by the volume of the frame, accommodating the motor. Initially, it was decided that all four motors were to be built into a Grundfos standard frame MG71 (Fig. 5.2.a). This is an advantage for the IM because it is designed for this frame. However, due to assembly difficulties, the Shark SRM was eventually assembled into a special Aluminium frame (Fig. 5.2. b), which alters the similitude of the cooling conditions.

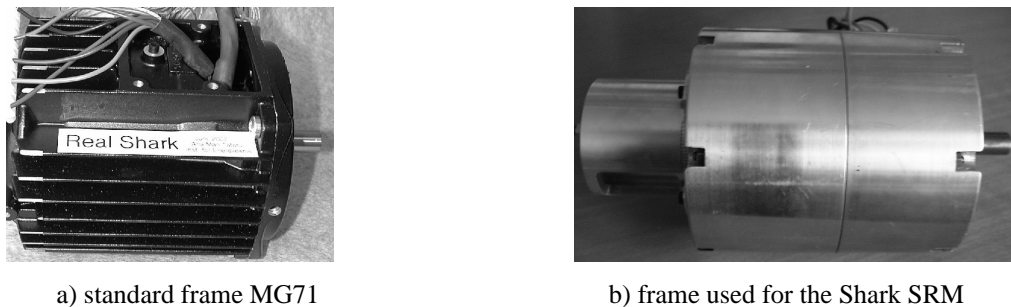


Fig. 5.2 Types of frames used to accommodate the studied motors.

The lamination stack has identical lengths in IM, CSRSM and Shark SRM (Table 1, row 7). This condition ensures identical electromagnetic volumes<sup>7</sup> for the three motors. The BLDCM was, however, designed with a shorter stack length as shown in Table 1, row 7.

The air gap length is identical in IM, CSRSM and Shark SRM (Table 1, row6). It is, however, longer in BLDCM but this has no significant influence on the motor performances, since the magnetisation of the BLDCM is produced by surface mounted permanent magnets.

*The electromechanical constraints* refer to the designed output variables such as rated output power, speed and torque. The specifications of the motors to be compared are given in Table 5.1, rows 1, 2, 3. All but the BLDCM are designed for an output power of 550 [W] attainable at 2800 [rpm] and  $T=1.9$  [Nm].

<sup>7</sup> volume determined by the length of the lamination stack and the stator outer diameter



Table 5.1 Specifications and geometric constraints for the motors used in comparison

Row	Parameter name	Parameter symbol	Unit	IM	CSR	Shark SRM	BLDCM
<i>specifications</i>							
1	output power	$P_m$	[W]	550	550	550	268
2	shaft torque	$T_{sh}$	[Nm]	1.85	1.9	1.9	1.1
3	speed	$\omega$	[rpm]	2822	2800	2800	2250
<i>geometric constraints</i>							
4	frame			MG71	MG71	-	MG71
5	stator diameter,	$D_s$	[mm]	106.5	106.5	106.5	106.5
6	air gap	$g$	[mm]	0.3	0.3	0.3	0.5
7	stack length	$l_{stk}$	[mm]	60	60	60	40
8	total length with winding overhang						

### Comparison criteria

Definition of the *comparison criteria* is a controversial topic, due to different operation principles of the motors. Furthermore, their specification is dependent on application. Furthermore, it is important to know the phenomena, which cause that an output coefficient has a certain value. Knowing the correlation between different components of the losses, allows the improvement of the design with regard to the efficiency of the motor. Various criteria to evaluate various motor technologies are proposed in [94] and [95].

In this project, the steady-state output coefficients, determined from measured data and used to compare the different motor types are: efficiency, electric and magnetic loadings, power factor, torque-weight ratio and torque-current square characteristic.

## 5.2 Experimental arrangements

*Steady-state* tests are made on all four machines. The goal of the steady-state test is to provide all the data necessary to calculate efficiency, power factor and losses of the tested motors.

The steady-state measurements are performed using the arrangement illustrated in Fig.5.3. It consists of two main units: the load system and the tested system. The load system consists of the load machine (PM motor) and the control unit. Details may be found in [82] and [83]. Facilities for data acquisition (GPIB and analog output transducers which are fed to an A/D converter) are included so that all the results of the measurement are available for storage. The tested system consists of the tested machine and its control unit.

The acquired variables, such as phase voltages and currents, speed and shaft torque, are illustrated in Fig.5.4 by points 3, 4 and 5 as to acquire only the input and output variables of the electric motor.

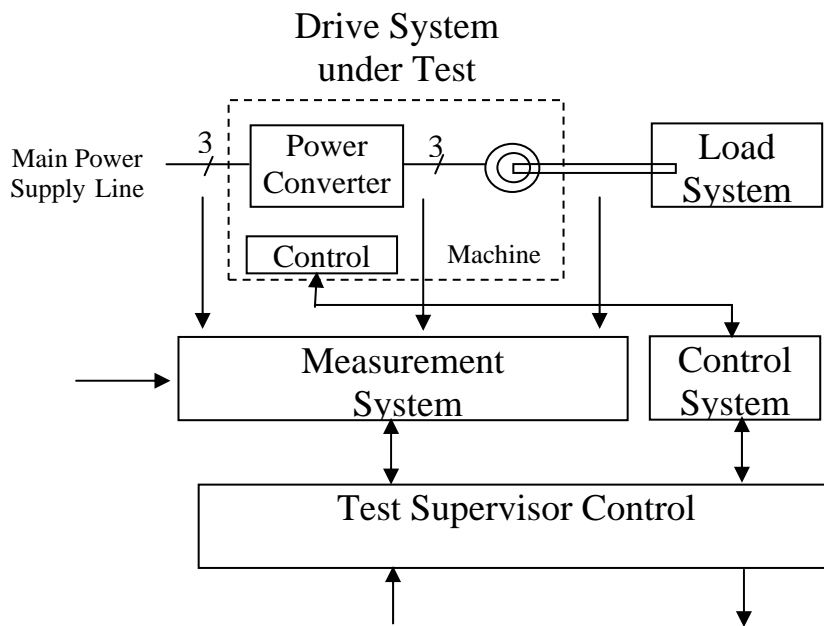


Fig.5.3 Configuration of the test system [82]

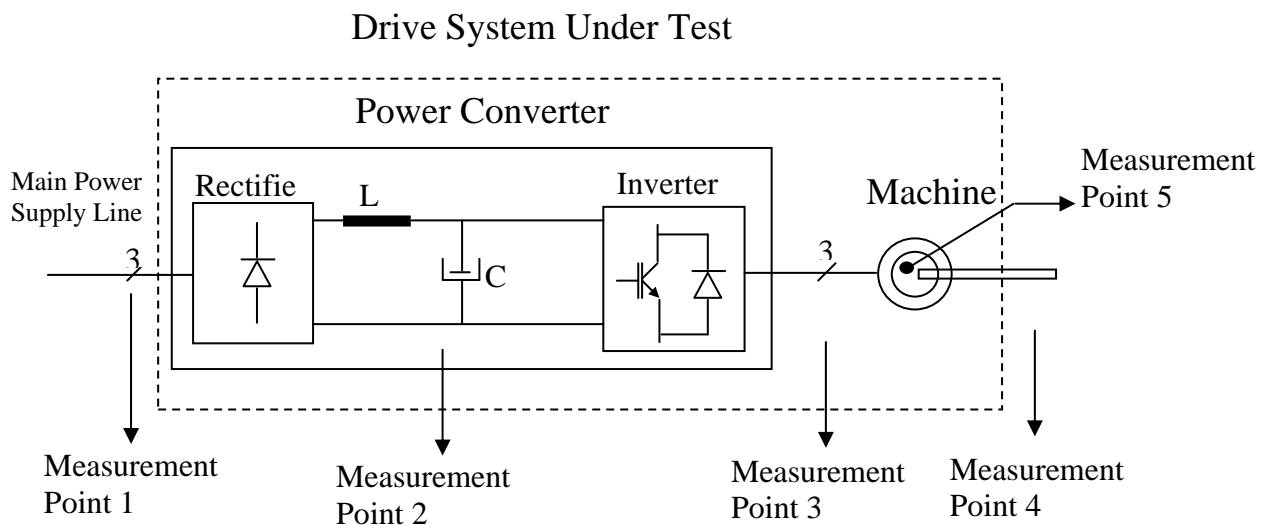


Fig.5.4 Measurement points in the test system [82], for evaluation of the Power Converter and of the electric Machine.

### 5.3 Results of the steady-state tests

The measurements procedure is the following: the motor was run at full load for one hour until warm. Then measurements were made successively at 1.9 [Nm] and speed of 500, 1000, 1500, 2000, 2500 and 2800 [rpm]. The procedure was repeated for load torque down to 0.5 [Nm], such as to provide data at the working points shown in Fig.5.5. This procedure was followed for CSRSM, Shark SRM and BLDCM, whilst the IM was tested only at rated voltage. The test points for the IM, CSRSM, Shark SRM and BLDCM are shown in Fig.5.5. Because of the voltage limitation of the controller used to control the BLDCM, this could not be tested at 2800 [rpm] and 1.9 [Nm].

Therefore, all the data used in this chapter for the BLDCM operating at this point are obtained by extrapolation of the measured data.

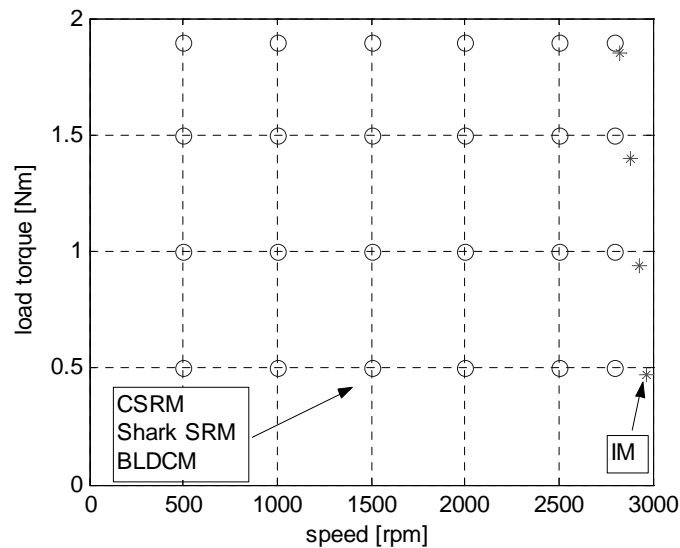


Fig.5.5 Example of the test points for IM, CSR, Shark SRM and BLDCM

### 5.3.1 Measurements on the Induction Motor (IM)

The measurements on the IM, having the dimensions given in Appendix A.1, are made according to the procedure B from IEEE Std. 112 (measurement and loss segregation) [102]. This method indicates as necessary, tests at no-load and at different loadings.

Initially, the core losses were determined by a test at no-load and rated voltage. The measured values are given in Table 5.2. Knowing the friction and windage losses,  $P_{fw}$  (provided by Grundfos and given in Table 5.2), the core losses were calculated by:

$$P_{core} = P_0 - P_{fw} - 3 \cdot R_{s0} \cdot I_0^2 \quad (5.2)$$

where  $P_0$  is the input power,  $I_0$  is the no-load current,  $R_0$  is the measured phase resistance,  $P_{fw}$  is the friction and windage loss and  $P_{core}$  is the core loss.

Table 5.2 No-load measured data for core loss determination

$P_0$ [W]	$I_0$ [A]	$R_0$ [ohm]	$P_{fw}$ [W]	$P_{core}$ [W]
50.79	0.76	14.11	7.6	17.93

The efficiency was then calculated from the experimental data at 25, 50, 75, 100, 125 and 150 [%] of the rated torque. The characteristic obtained is shown in Fig.5.6.

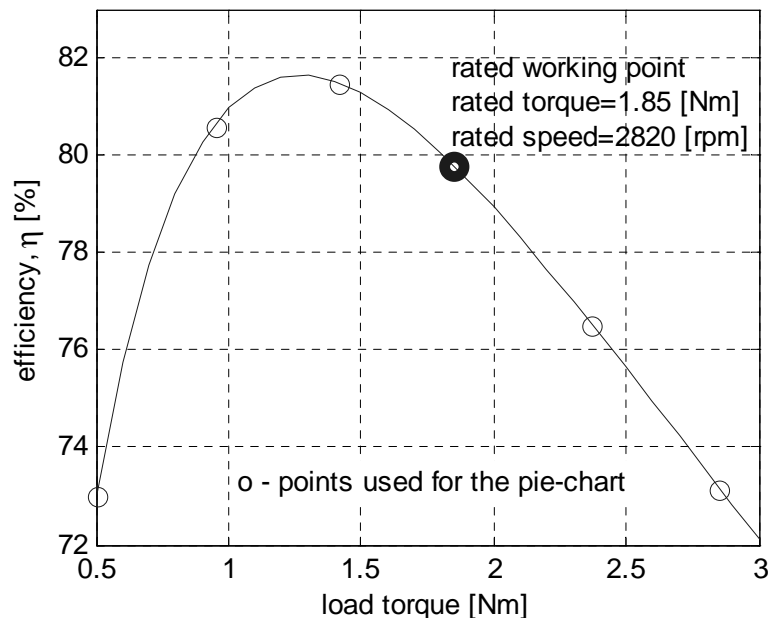


Fig.5.6 Measured efficiency of IM, supplied with rated sinusoidal voltage.

The loss distributions at all test points of the IM are presented in Fig.5.7. It may be noticed that the contribution of core loss to the total loss decreases by increasing the load torque whilst the contribution of the copper loss to the total loss increases by increasing the load torque. The most substantial change is exhibited by the rotor copper loss.

Because the measurements are made with nominal voltage, the efficiency at reduced load is low since the magnetisation current cannot be controlled. In [96] it was shown that at reduced load there is an excess of magnetisation, corresponding to a large magnetisation current. Therefore, an adequate control strategy may significantly improve the performance<sup>8</sup> of the machine.

The loss distribution for the IM supplied with rated voltage, operating at various load torque is shown in Fig.5.8.

<sup>8</sup> For a 4 poles 2.2[kW] IM tested in [96], the gain in efficiency was about 20 % point at 14 % of the rated torque and about 10 % point at load torque of 28 % from the rated torque.

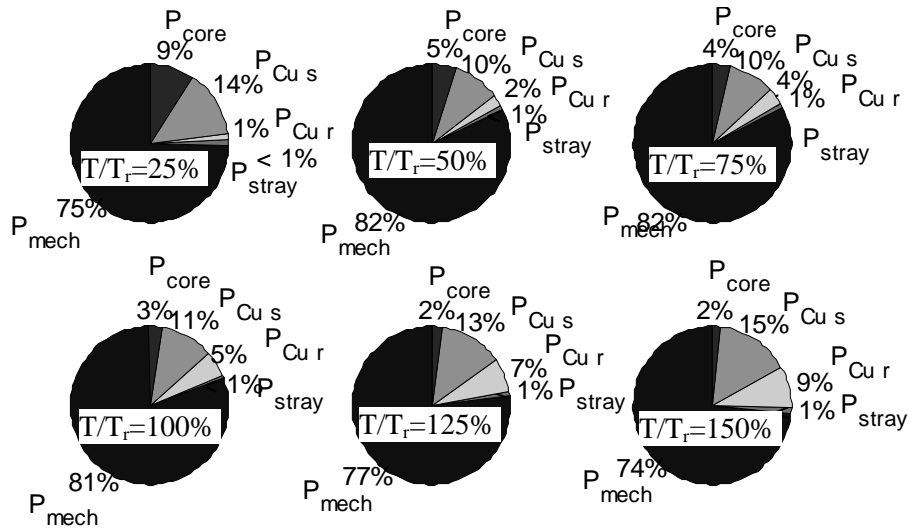


Fig.5.7 Measured loss distribution for IM supplied with sinusoidal rated voltage.

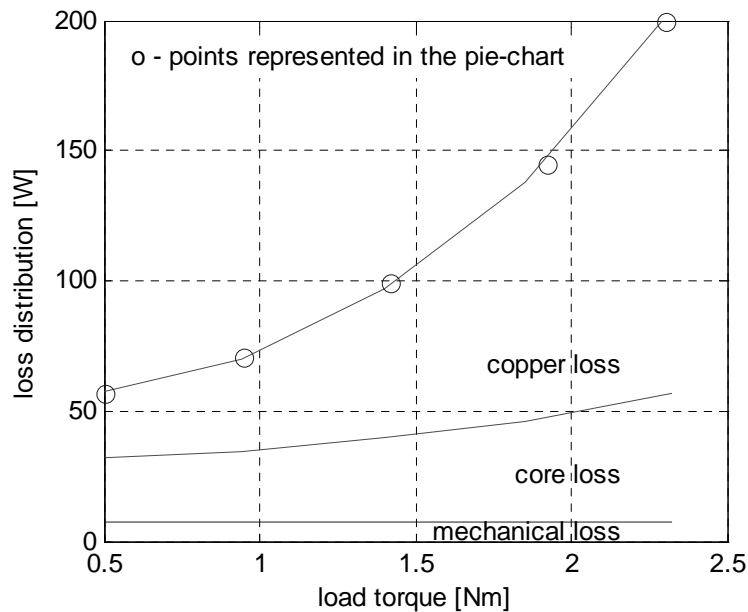


Fig.5.8 Mechanical, core and copper losses measured for the IM at rated speed 2820 [rpm]

### 5.3.2 Measurements on the Cylindrical air gap SRM (CSRSM)

The CSRSM is designed for rated power of 550 [W] at 2800 [rpm] and load full load torque, 1.9 [Nm]. The design data may be found in Appendix A.2. The steady-state tests were performed at operating points, specified in Fig.5.5.

Extensive research on SRM control [40], [103], [104], [105] indicates that the efficiency of the SRM is strongly dependent on control parameters such as turn on angle  $\alpha_{on}$ , turn off angle  $\alpha_{off}$  and duty cycle D. Therefore, the results presented in this section are obtained by using control parameters, that produce the optimum efficiency of the tested CSRSM.

The search procedure was based on the idea that the duty cycle in SRM is similar to the modulation index in a scalar controlled IM. This is proportional to the speed [40], [103]. Furthermore, the turn on angle, may play the primary role in controlling the torque whilst the turn off angle, may depend almost linearly upon the speed [40], [103].

To determine the optimum combination of control parameters, for a specified duty cycle, the turn on and turn off angles, which produce the required shaft torque, were found. The resulting control characteristics of the duty cycle and turn on and turn off angles are presented in Fig.5.9 and Fig.5.10 and Fig.5.11. The results have confirmed the control characteristics predicted by [40] and [103].

The duty cycle, illustrated in Fig.5.9 varies almost linearly with speed and is independent of the load torque.

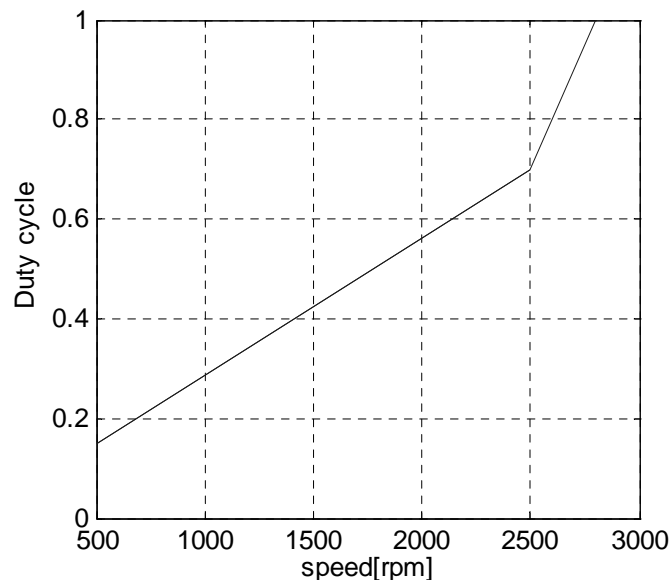
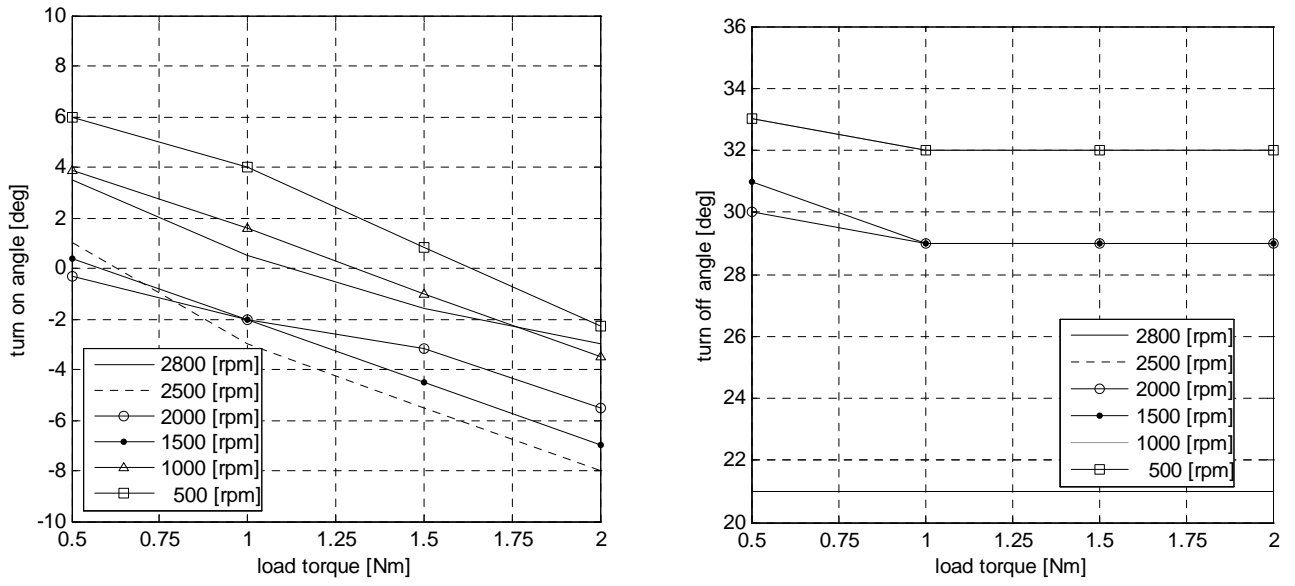


Fig.5.9 Duty cycle for the tested CSR

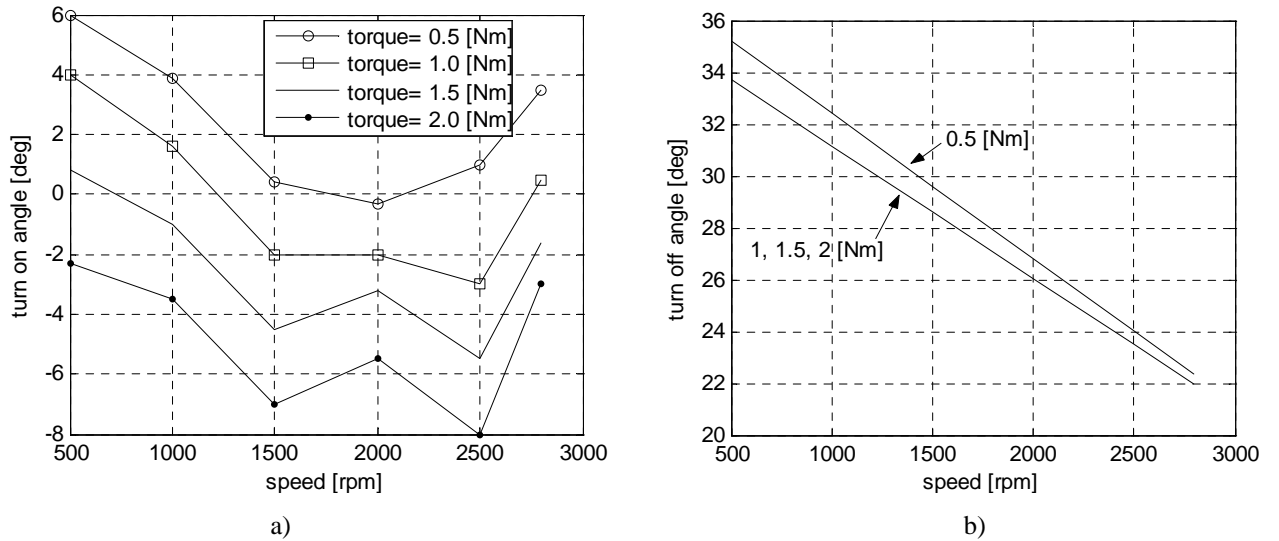
The turn off angle, illustrated in Fig.5.10 b and Fig.5.11 b is almost independent of the load torque, and decreases for increasing operational speed. This is because at increased speed the phase must be disconnected earlier to avoid or reduce the negative torque produced when the rotor passes beyond the aligned position and the inductance variation has a negative slope.

The resulting turn on angles are illustrated as a function of the load torque and speed in Fig.5.10 a and Fig.5.11 a, respectively. At a specified speed, the phase voltage is applied earlier to the phase winding in order to produce more torque. This is seen in that the best turn on angle decreases for increasing the load torque.



a) b)

Fig.5.10 Variation of the optimum turn on and commutation angles of CSRMs as a function of load torque



a) b)

Fig.5.11 Optimum turn on and turn off angles of CSRMs as a function of speed

The efficiency characteristics measured on the CSRMs are shown in Fig.5.12. They present a flat shape over a wide range of load torque as seen in Fig.5.12 a. In Fig.5.12 b, it may be observed that the efficiency is improved for increasing operation speed.

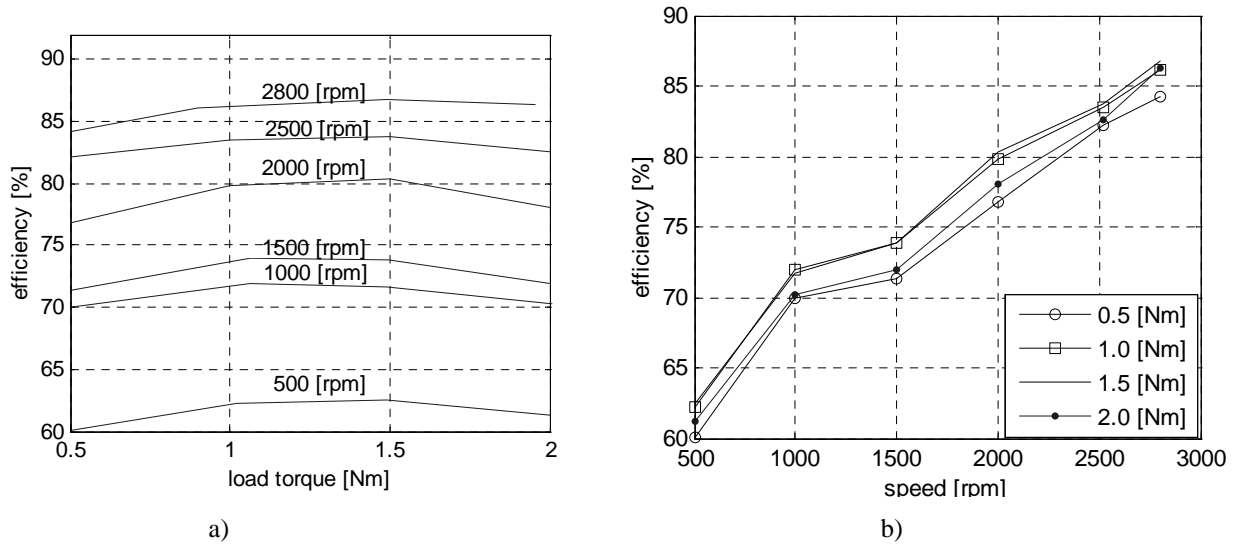


Fig.5.12 Measured efficiency as a function of the load torque for the CSR. a) Efficiency vs. torque at different speed values. b) Efficiency vs. speed at different torque values.

The loss distribution depends on the load torque, as illustrated in Fig.5.13, for 500 and 2800 [rpm]. In both cases the contribution of copper loss to the total loss increases for increasing load torque and the proportion of core loss in the total loss decreases for increasing load torque. Operation at increased speed makes the core losses become a larger proportion of the total loss.

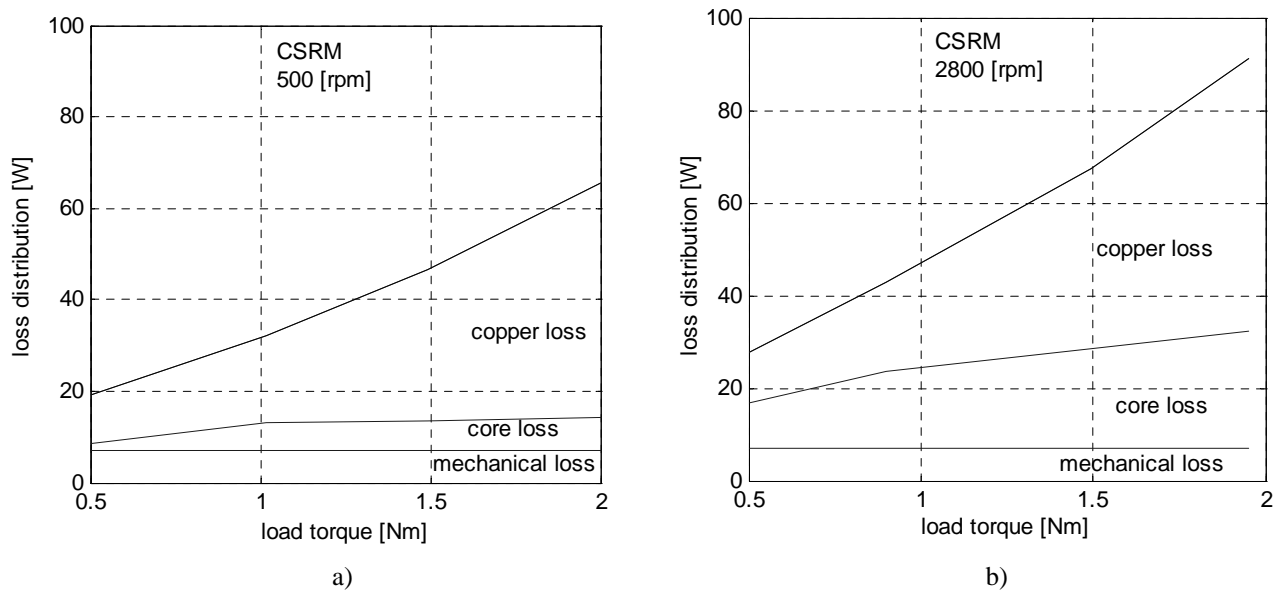


Fig.5.13 Loss distribution as a function of the load torque of the CSR at 500 and 2800 [rpm]

### 5.3.3 Measurements on the SHARK air gap Switched Reluctance Motor (Shark SRM)

The optimisation procedure employed for the CSR was also applied to the Shark SRM. To ensure a valid the basis of comparison, the control parameters of the Shark SRM were determined by maintaining the duty cycle and the turn off angles of the CSR and finding the optimum turn on angle. The results of this procedure are illustrated in Fig.5.14.



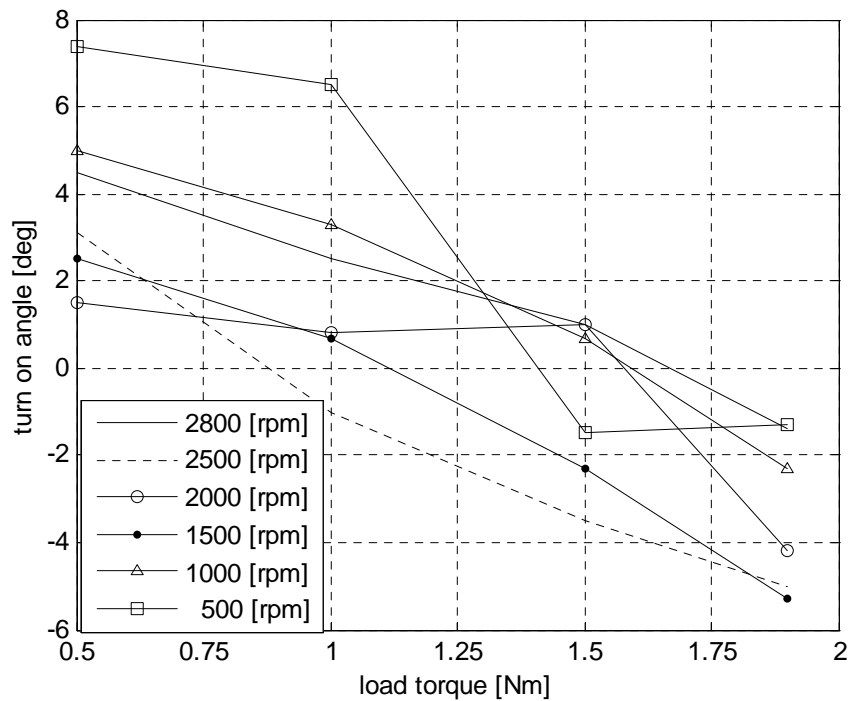


Fig.5.14 Turn on angle as a function of the load torque at different speed values.

Comparing Fig.5.10 and Fig.5.14, for the Shark SRM, the phase voltage has to be applied later than it is for the CSRSM. This is a direct consequence of the improvement of the flux linkage provided by the Shark air gap. The delayed in turn on angle determines a reduction of the RMS current, as it will be discussed in section 5.4.

With these control parameters, the measured efficiency characteristics are given in Fig. 5.15. They present a flat shape over a wide range of the load torque (Fig.5.15 a) and the efficiency improves with increasing operational speed (Fig.5.15 b).

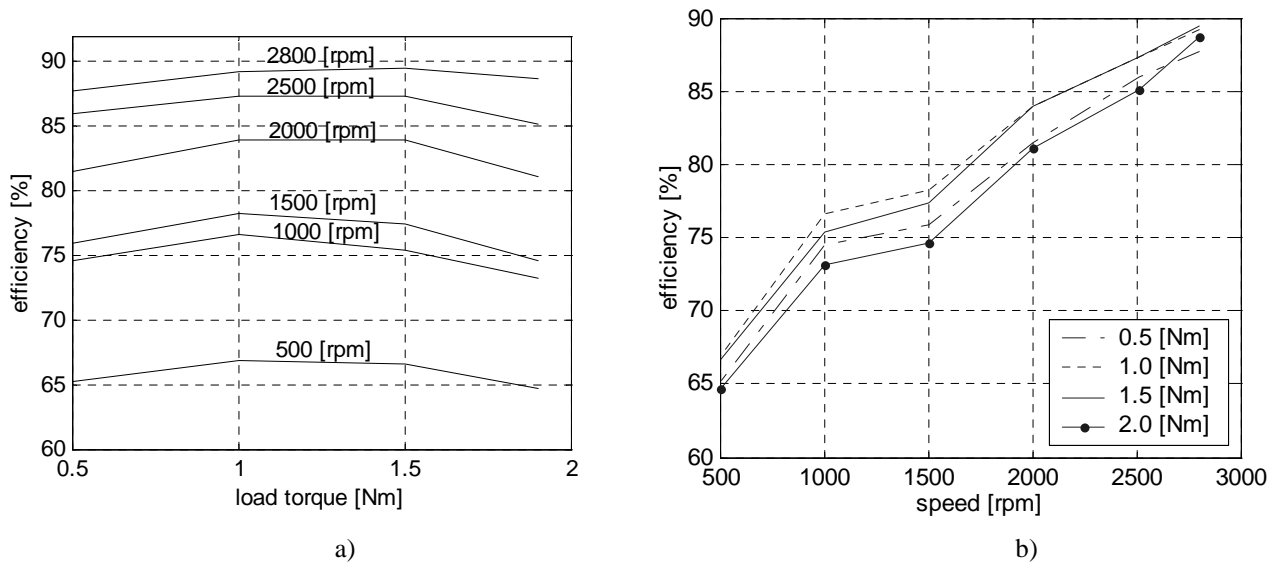


Fig.5.15 Measured efficiency for the Shark SRM. a) Efficiency as a function of torque at different speed values. b) Efficiency as a function of speed at different torque values.

At rated speed ( $\omega=2800$  [rpm]) the loss characteristics of the Shark SRM as a function of load torque are presented in Fig.5.16. As in the CSRSM, the contribution of copper loss to the total loss increases with the increase in load, whilst that of the core loss decreases with the increase in load.

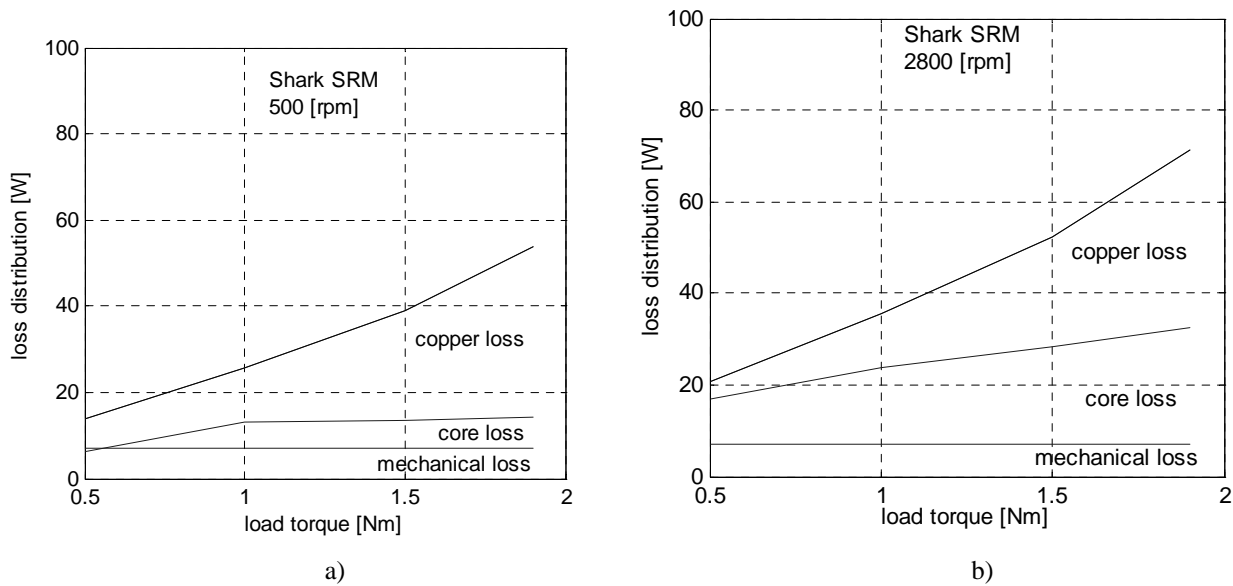


Fig. 5.16 Loss distribution in Shark SRM at 500 and 2800 [rpm]

### 5.3.4 Measurements on the brushless DC motor (BLDCM)

The measurements on the BLDCM were performed applying a controller kit from Agile Systems, whose features are given in Appendix D.1. A ring of permanent magnets was installed outside the motor frame in order to provide the position signals for commutation of the phases. Measurements were taken at different speed and load torque values. The measured efficiency characteristics are

shown in Fig.5.17. The efficiency increases with operational speed up to the rated speed of 2250 [rpm]. Increasing further the speed, the efficiency decreases.

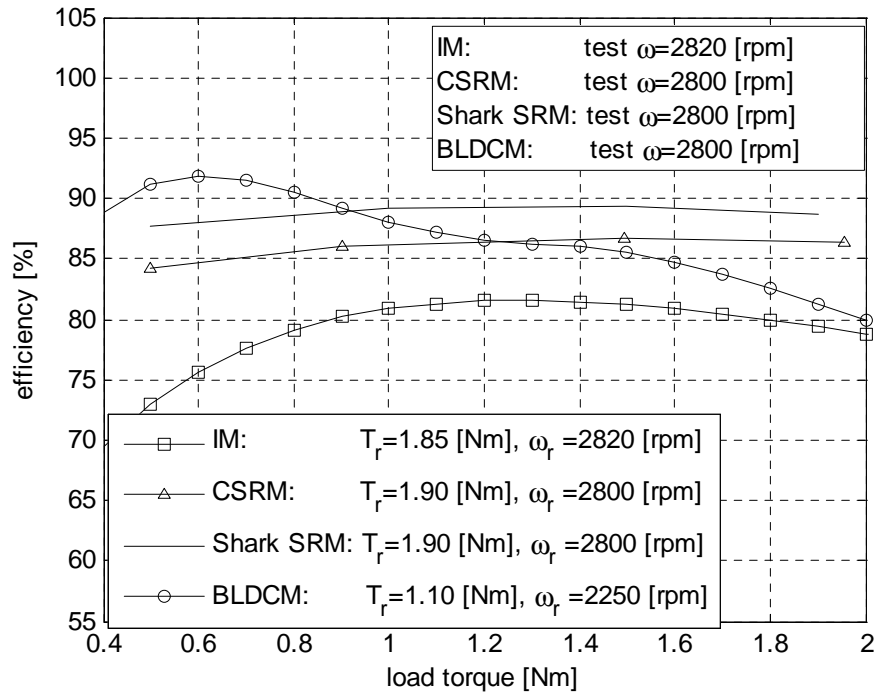


Fig.5.17 Efficiency characteristic at rated speed of 2250 [rpm]

The loss distribution at rated speed is shown in Fig.5.18. It should be noted that the core loss makes the largest contribution to the total loss.

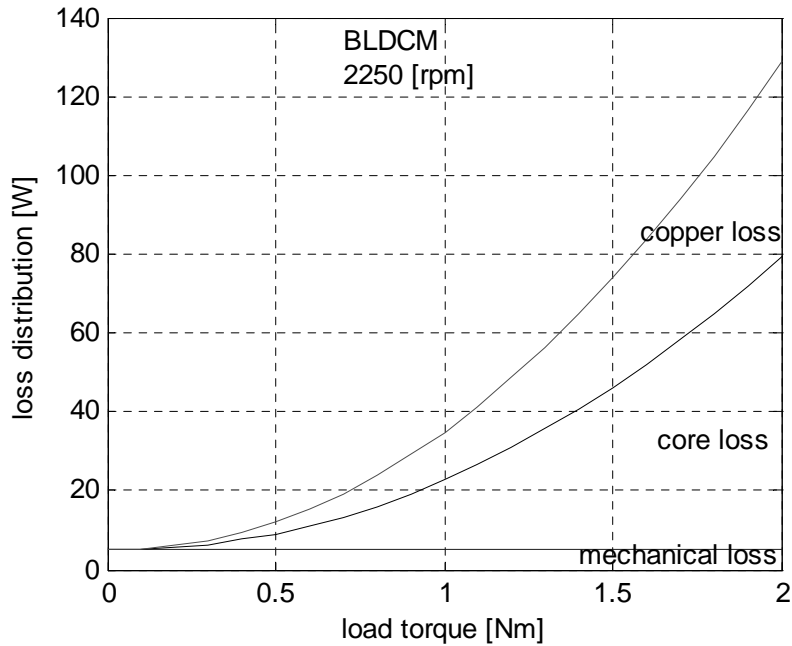


Fig.5.18 Loss distribution in [W] at 2250 [rpm]

### 5.3.5 Summary

In this section the results of the tests made on an Induction Motor, a cylindrical air gap SRM, a Shark SRM and a permanent magnet brushless DC motor have been presented. The motors dimensions are given in Appendices A.1, A.2, A.3 and A.4. All the four motors were tested at operating points, specified in Fig.5.5.

Because the efficiency of an SRM is strongly dependent on the control parameters, the data for the CSRSM and the Shark SRM were processed for that combination of control parameters, which provided the optimum efficiency. The procedure used to determine the optimum control parameters was inspired by the discussions from references [40] and [103].

The results indicated that at rated load torque and rated speed the IM has an efficiency of 79.8 %, the CSRSM of 86 %, the Shark SRM of 88 % and the BLDCM of 90 %. The rated torque and speed of the IM, CSRSM and Shark SRM were 1.9 [Nm] and 2800 [rpm] and those of the BLDCM were 1,1 [Nm] and 2250 [rpm].

## 5.4. Comparison of the motors

In this section, the four motors, whose test results have been presented in the previous section, are compared. The comparison considers the size and the steady-state performances.

### 5.4.1 Size comparison

The geometrical constraints determine a particular material distribution within the magnetic circuit of the four motors and affect the magnetic capabilities of the circuit.

In Table 5.3, the main dimensions of the radial cross-section and the stack length are specified for the all motors used in comparison. It may be observed that:

- Air gaps of the IM, CSRSM and Shark SRM are identical. The BLDCM has a longer air gap but this does not make much difference because of the use of permanent magnets –Table 3, row 5
- The width of the stator yoke of the IM and SRM are similarly, and they are both larger than that of the BLDCM, Table3, row 8. This is because the BLDCM has 8 poles compared to only 2 poles in IM and SRM – row 4
- Stack lengths of IM, SRM and Shark SRM are identical, whilst the stack length of the BLDCM is about 30% point shorter than in the other 3 motors, row 11.
- Assuming that the coefficient from equation (5.1) are identical for the considered machines, it may be concluded that the BLDCM was design for a rated output power of about 50 % of that of the IM and CSRSM.

These geometrical dimensions determine the mass distribution, which is shown in Table 5. 4 and illustrated graphically in Fig.5.19. The materials used are valuable indicators of the cost of the

motor. Knowledge of the mass distribution allows estimation of the relative prices of the motors. Following the procedure from Appendix D.1, the CSRSM was the cheapest motor, from the material cost point of view, while the IM was the most expensive. If the BLDCM were to be built with the required stack length, then this one would be the most expensive one.

Table 5.3 Geometrical dimensions of the radial cross-section and the stack length

row	Parameter name	Parameter symbol	Unit	IM	SRM	Shark SRM	BLDCM
1	phase number	phase	-	3	3	3	3
2	number of stator poles	$N_s$	-		6	6	15
3	number of rotor poles	$N_r$	-		4	4	8
4	number of poles	$p$	-	2	2	2	8
5	<b>air gap length</b>	<b><math>g</math></b>	[mm]	0.30	0.30	0.30	0.50
6	stator outer diameter	$D_s$	[mm]	106.50	106.50	106.50	106.50
7	rotor diameter	$D_r$	[mm]	54.40	52.60	52.60	53.40
8	stator yoke width	$S_{yoke}$	[mm]	13.65	11.65	11.65	5.00
9	rotor yoke width	$R_{yoke}$	[mm]	4.95	8.20	8.20	14.70
10	shaft diameter	$D_{sh}$	[mm]	20.00	20.00	20.00	20.00
11	stack length	$l_{stk}$	[mm]	60.00	60.00	60.00	40.00

The following observations may be made for the data in Table 5.4 and Fig.5.19:

- SRM uses the smaller amount of copper. Compared to the IM, which has the identical length of the lamination stack, the difference is due to the longer end winding in the IM, Table 4, row 1.
- BLDCM uses of a smaller amount of iron as its stack is 33% shorter than the stack of the IM and SRM. The SRM uses slightly less iron compared to the IM. This is due to the fact that more iron is cut off in order to create the stator and rotor poles, Table 4, row 3
- The smallest amount of active material, used to produce the required MMF, is in the SRM, Table 4, row 5

Table 5.4 Distribution of the mass in IM, CSRSM, Shark SRM and BLDCM

row	Parameter name	Parameter symbol	Unit	IM	CSRSM	Shark SRM	BLDCM
1	copper mass	$m_{Cu}$	[Kg]	0.959	0.479	0.479	0.787
2	aluminium mass	$m_{Al}$	[Kg]	0.221	-	-	-
3	iron mass	$m_{Fe}$	[Kg]	2.810	2.587	2.587	1.654
4	permanent magnet mass	$m_{PM}$	[Kg]	-	-	-	0.110
5	total material used for excitation (1+3+4)	$m_{exc}^9$	[Kg]	1.178	0.479	0.479	0.897
6	total mass (2+5)	$m_{total}$	[Kg]	3.988	3.066	3.066	2.552

<sup>9</sup>  $m_{excitation}$  is the total mass of the materials used to produce the mmf required for magnetization of the iron regions. It consists of  $m_{PM}$ ,  $m_{Cu}$  and  $m_{Al}$ .

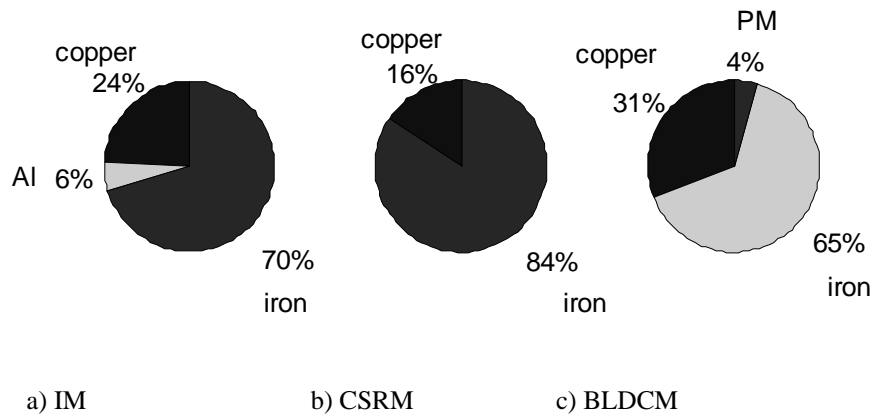


Fig.5.19 Mass distribution a) IM, b) SRM, c) BLDCM

### 5.4.2 Steady-state comparison

Integral to any comparison of the four motors, the electromagnetic differences between them must be mentioned. One of them is that the motors are not wound for the same voltage, which affect the phase current and consequently the copper loss. This may be seen in Table 5.5, rows 3, 4 and 5.

Another difference is that the BLDCM is actually designed for a smaller rated power than the other motors. However, it can be operated at similar operating points as the other motors due to its overload capability. Thus, the comparison may be performed at similar working points as shown in Table 5, rows 1 and 2. However, this is unfair for the BLDCM.

The output coefficients, which are compared in this section are:

- a. Efficiency
- b. Loss distribution
- c. Power factor
- d. Electric and magnetic loadings
- e. Torque per current square

Table 5.5 Geometrical, electrical and magnetic variables of the IM, CSRМ, Shark SRM, BLDCM.

row	Parameter name	Parameter symbol	Unit	IM	CSRМ	Shark SRM	BLDCM
1	torque	T	[Nm]	1.856	1.9	1.9	1.9
2	speed	$\omega$	[rpm]	2822	2800	2800	2800
3	turns per phase	$N_{ph}$		420.00	556.00	556.00	225.00
4	current	$I_{rms}$	[A]	1.25	1.32	1.14	4.00
5	phase resistance	$R_{ph}$	[ $\Omega$ ]	13.7	11	11	1
6	magnetomotive force	MMF	[A turns]	525.00	778.00	634.00	900.00
7	magnets magnetomotive force	pm MMF	[A turns]	-	-	-	1338.00
8	total magnetomotive force	total MMF	[A turns]	525.00	778.00	634.00	2238.00
9	rotor diameter	$D_{sg}$	[mm]	56.00	55.20	55.2	54.40
10	electric loading	$A_1$	[A/mm]	18.40	28.30	23.00	32.20
11	magnetic loading	$B_g$	[T]	0.28 (0.79)	0.14	0.24	0.57
12		$B_g \cdot A_1$	[TA/mm]	5.20	4.00	5.50	18.40
13	power factor	pf	-	0.82	0.45	0.50	0.90
14	output power	$P_{out}$	[W]	548	558	558	558
15	stator conductive loss	$P_{Cu(s)}$	[W]	73.3	58	40	50
16	rotor conductive loss	$P_{Al(r)}$	[W]	35.3	-	-	-
17	total conductive loss	$P_{Cu(t)}$	[W]	108.6	58	40	50
18	electromagnetic power	$P_{em}$	[W]	607.7	588.4	586.3	630
19	core loss	$P_{Fe}$	[W]	17.93	25.39	23.3	116
20	friction and windage loss	$P_{fw}$	[W]	6.7	5	5	6
21	input power	$P_{in}$	[W]	681	646.4	626.3	680
22	total loss	$\Delta P$	[W]	133	92	82	121
23	efficiency	$\eta$	[%]	80.5	86.4	88	82

### a. Efficiency

The efficiency expresses the capability of the electric motor to convert the electrical energy into mechanical energy. The efficiency may be calculated by the ratio of output power,  $P_{out}$ , to input power,  $P_{in}$ :

$$\eta = \frac{P_{out}}{P_{in}} \quad (5.3)$$

The efficiencies, calculated from the measured input and output power for each of the 4 motors, are shown in Fig.5.20 as a function of the load torque. The test speed is 2800 [rpm] for all the motors except the IM.

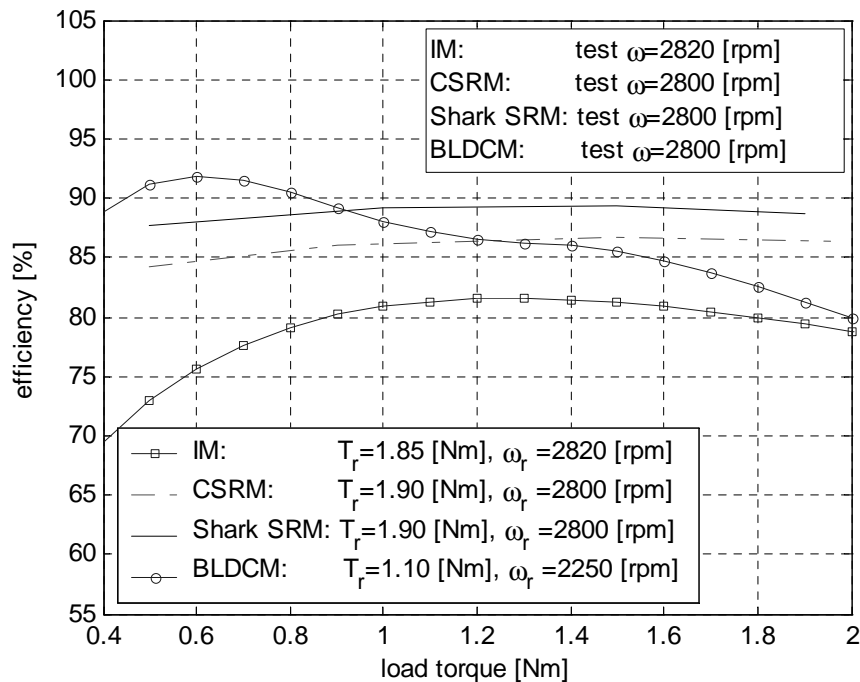


Fig.5.20 Measured efficiencies of IM, CSRМ, Shark SRM and BLDCM, as a function of load torque at 2800 [rpm].

The comparison may be unfair for the IM and BLDCM because the IM is tested at nominal voltage, without any control strategy whilst the BLDCM was designed for a different rated power.

The CSRМ and the Shark SRM may be directly compared as their dimensions are similar<sup>10</sup> and the control parameters were determined in similar manner. The control strategy and the optimum control parameters have been discussed in sections 5.3.2 and 5.3.3.

The IM, having the main dimensions identical to those of the CSRМ, is supplied with rated sinusoidal voltage. As shown in [96], the control strategy improves substantially the efficiency, at reduced load, of the IM. However at load torque bigger than about 70 % of the rated torque, the control strategy has no influence. Therefore at such load torque the measured efficiency of the IM can be directly compared with those of the CSRМ and Shark SRM. This means that, at the rated working point the IM may be directly compared to the CSRМ and Shark SRM, keeping in mind that the motors are not wound for identical voltages.

From Fig.5.20, it can be seen that the efficiency of the Shark SRM is 2 to 3 % point bigger than that of the CSRМ. This indicates that the Shark air gap has a substantial influence on the energy conversion, provided that the only difference between the two motors is the shape of the air gap. The improvement of the efficiency is more significant at reduced load, where the iron core of the machine is not saturated. This conforms to the conclusions drawn in chapters 3 and 4. The

<sup>10</sup> as shown in chapters 2, 3 and 4, there is only the air gap shape, which is different in the two SRMs



efficiency improvement is illustrated in Fig.5.21. It can be noticed that the general tendency is that the efficiency improvement decreases by increasing the load torque and/or the speed.

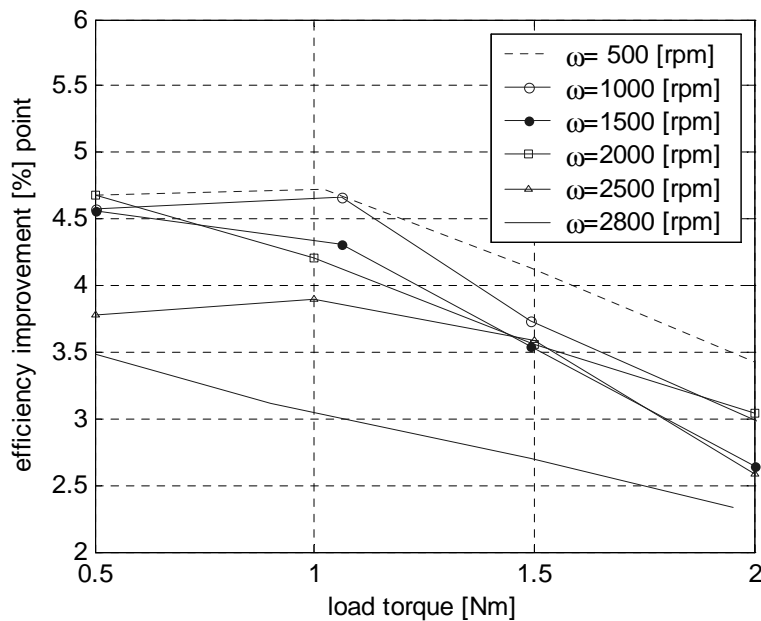


Fig.5.21 Efficiency improvement in Shark SRM as a function of the load torque, at different speed

The measured efficiency of the standard IM is the smallest compared to the other three motors. As already mentioned the absence of any control strategy makes a big difference at low load, but almost no difference at load of above 70 % of the rated torque [92].

### b. Loss distribution

Although, it provides valuable information about the conversion process, the efficiency does not say anything about where the lost power goes. In this section, the origin of the losses in the four motors tested is identified, then the copper loss is analysed.

The nature of loss in an electric motor is *electrical*, *magnetic* and *mechanical*. The *electric or conductive loss* is due to the heating effect of current flowing through stator and/or rotor windings. This loss component depends on the total resistance of the conductor material and on the square of the rms value of the current.

The *magnetic loss*, named also iron or core loss is the power lost due to changing magnetisation of the iron regions. The magnetic loss is due to eddy currents, which may find paths through the iron, and to hysteresis, which is specific in any material with magnetic properties.

The *mechanical loss* is produced by bearing friction, loss in the ventilation system, and any other source of friction or air movement in the motor.

During the conversion of the electrical energy into mechanical energy all these losses are dissipated as heat. In Fig. 5.22 a simplified diagram of the conversion processes is presented.

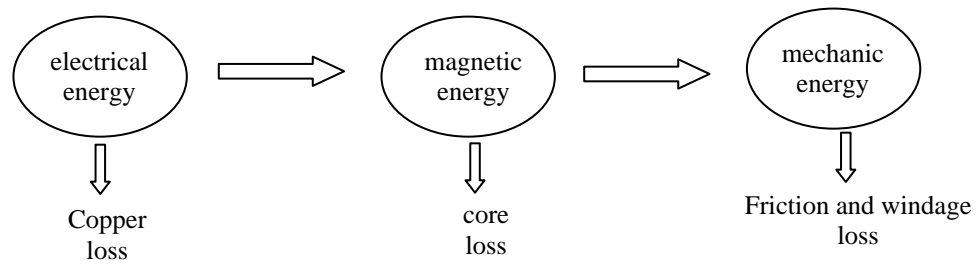


Fig.5.22 Conversion chain in electric motors

The following discussion considers only the rated working points. In Table 5.5, the input, output and loss power are given. It may be observed that the CSRSM uses less electric power to produce the required output, than the IM. Moreover, the energy conversion is improved in the Shark SRM as less copper loss is produced.

The analysis of the losses, calculated in Table 5.5, shows that:

- The copper loss in the IM has the biggest value compared to the SRM. Copper losses occur in both stator coils and rotor bars in the IM whilst in the SRM there is power loss only on the stator side.
- The iron losses are not much bigger in CSRSM and Shark SRM (about 4% point of those in IM) compared to the IM. This is remarkably as the SRM has non- sinusoidal magnetic flux flowing through the iron regions. However the unipolar flux waveforms are an advantage for the SRM.

#### *Copper loss*

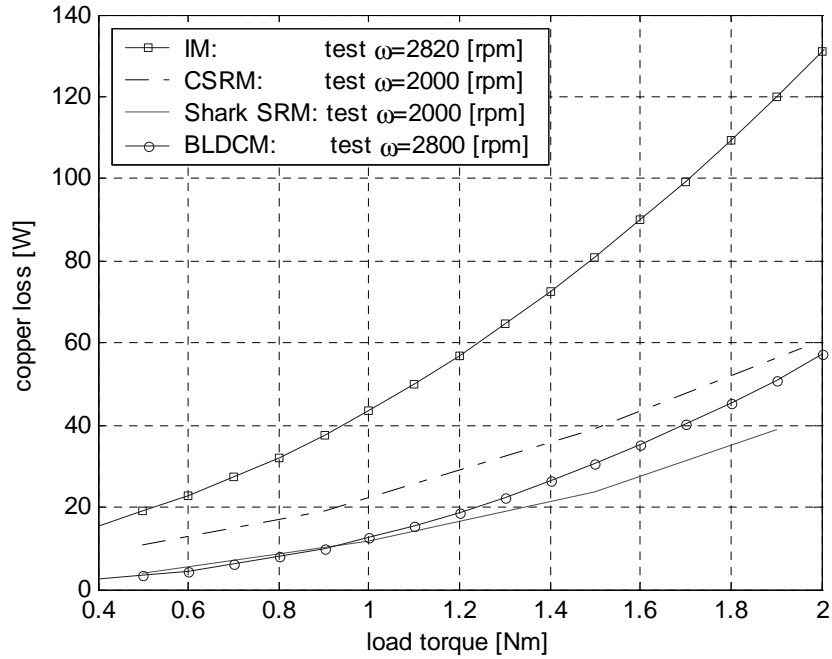
The copper loss depends on the resistance of the coil and on the current flowing through the conductors according to the expression:

$$P_{Cu} = ph \cdot R_{ph} \cdot I_{rms}^2 \quad (5.4)$$

where:  $ph$  is the number of phases;  $R_{ph}$  is the phase resistance and  $I_{rms}$  is the phase rms current.

The data in Table 5.5, show that in order to deliver similar output power, the CSRSM needs more current than the IM, but this may be due to the fact that they are not wound for same voltage. The current required by the Shark SRM to produce the rated torque is lower than that required by the CSRSM to produce the same torque. This is exclusively due to the improvement of the magnetic circuit provided by the Shark air gap.

The influence of the load on the copper loss is presented in Fig.5.23. In the IM the copper loss has the highest gradient with respect to the load torque. It is important to notice the reduced copper loss in the Shark SRM compared to the CSRSM. The copper loss of the BLDCM is bigger or equal to that of the Shark SRM, but again, the BLDCM is wound for a lower voltage than the Shark SRM is.


 Fig.5.23 Copper loss variation with load torque at rated speed  $\omega=2800$  [rpm]

The effect of the Shark air gap on the stator current is reduced by increasing the load torque. If at low load the current required by the Shark SRM is 59 [%] of that of the CSRSM, at rated the Shark SRM needs a current of 81 [%] of that in the CSRSM.

Table 5.6 Reduction of the excitation current in Shark SRM at 2800 [rpm] and different load torque

row	T/T <sub>r</sub>	0.26	0.47	0.78	1
1	I <sub>Shark SRM</sub>	0.36	0.63	0.89	1.14
2	I <sub>CSRSM</sub>	0.6	0.8	1.14	1.4
3	I <sub>Shark SRM</sub> /I <sub>CSRSM</sub> [%]	59	77	78	81

### c. Electric and magnetic loadings

The torque produced by an electric motor may be expressed function of the air gap diameter, stack length, electric and magnetic loading. The last two variables are defined in relation to the air gap circumferential length and they indicate how much load (electric and magnetic) is in the air gap. In this section these two variables are defined for each of the considered machine.

The electric loading in IM represents the total RMS current ( $N_{ph} \cdot I_{rms}$ ) per unit length of periphery of the machine. In a  $ph$ -phase machine, having  $N_{ph}$  turns in series per phase, there are  $ph \cdot N_{ph}$  turns carrying a current  $I_{rms}$ . As each turn has two sides, the total MMF around the air gap is  $2 \cdot ph \cdot N_{ph} \cdot I_{rms}$ . The armature electric loading is then defined by:

$$A_1 = \frac{2 \cdot ph \cdot N_{ph} \cdot I_{rms}}{\pi \cdot D_r} \quad (5.5)$$

where  $D_r$  is the rotor outside diameter.

The magnetic loading, represents the average magnetic flux density,  $\bar{B}$ , over the surface of the air gap. If the flux density is assumed sinusoidal distributed, the fundamental flux per pole,  $\Phi_{pole}$ , is given by:

$$\Phi_{pole} = \bar{B} \cdot \frac{l_{stk} \cdot \pi \cdot D_r}{2 \cdot p} \cdot N_{ph} \quad (5.6)$$

For comparison purposes the electric and magnetic loadings must be defined also for the SRM and BLDCM. In the BLDCM there is no difficulty in defining these parameters as the stator is similar to the stator of an IM

To define the electric and magnetic loadings of the SRM, in a similar manner as it is done for the IM, the notion of time average flux linkage<sup>11</sup> was introduced by Harris [91]. Using this variable the electric loading may be defined in the SRM according to equation (5.5). This suggests that the total MMF is considered to produce the average shaft torque. The time averaged phase flux linkage helps in defining the average flux density in the air gap, which is produced by the total MMF considered in equation (5.5). The equation which expresses this idea is:

$$m \cdot \bar{\psi}_{ph} = \bar{B} \cdot l_{stk} \cdot \pi \cdot D_r \cdot N_{ph} \quad (5.7)$$

It must be noticed that the average flux linkage  $\bar{\psi}_{ph}$  is multiplied by the number of phases  $ph$ . In this way the total flux linkage produced by all  $ph$  phases is taken into account. This total flux is produced for the pole pair specific to the SRM configuration. Equation (5.7) suggests that the average flux density in the air gap of a SRM is produced by each phase separately and not by the contribution of the all  $ph$  phases together as in the IM.

The magnetic loading directly influences the core loss and the magnetising current. Thus, it has an important effect on the power factor. It is limited by saturation and losses in the teeth. The electric loading affects the copper losses and the armature reaction in the IM. The electric and magnetic loadings for the tested motors are given in Table 5.5, rows 11 and 12.

The SRM does not use the air gap area efficiently, compared to the IM and BLDCM. The electric loading in the CSRSM is bigger than that in the IM or BLDCM. The Shark SRM improves the utilisation of the air gap, as for the same air gap diameter, the current necessary to magnetise the magnetic circuit is smaller than in the CSRSM.

<sup>11</sup> average flux linkage is about half the peak flux linkage during a stroke because of the approximately triangular shape of the flux linkage with respect to the rotor position.

#### d. Power factor

The power factor is influenced by both the nature of the load (resistive, inductive or capacitive) and the shape of the voltage and current waveforms supplied to the motor terminals. The load is inductive in all four motors, but the voltage and current wave shapes are different:

- The IM is supplied by sinusoidal currents
- The CSRSM and Shark SRM the voltage supply has a square wave shape whilst the current shape depends on the speed and load torque
- The BLDCM is supplied by square wave voltage.

Bearing these observations in mind, it may be observed, from the measured power factor characteristics illustrated in Fig.5.24 that:

- The Shark air gap has an improved power factor compared to the SRM. This is because the Shark SRM is equivalent to a motor with the same stack length but a shorter air gap length (see chapter 4). The equivalent shorter air gap reduces the reluctance of the magnetic circuit and consequently less magnetisation current is required. The amount of the improvement may be determined from:

$$PF = \frac{P_{mean / phase}}{U_{rms} \cdot I_{rms}} \quad (5.8)$$

providing that the power produced per phase and the rms voltage are identical in CSRSM and Shark SRM. As the current required by the Shark SRM to produce 1.9 [Nm] was 81 [%] of that required by the CSRSM to produce the same torque, it may be concluded that the power factor of the Shark SRM would be 1.23 times bigger than that of the corresponding CSRSM. This may be seen in Fig.5.24.

- The power factor of the BLDCM is greater than that of the IM, due to the permanent magnets, which are the main source for magnetisation of the magnetic circuit.

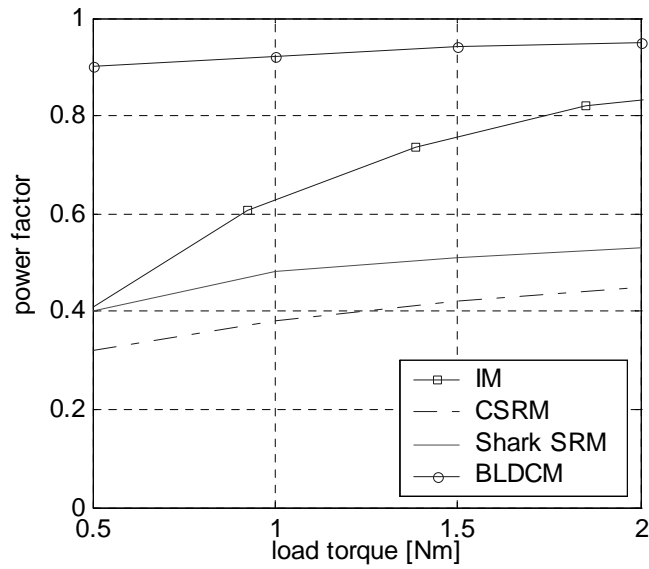


Fig.5.24 Power factor characteristics for the IM at  $\omega = 2820$ [rpm] CSRSM, Shark SRM, BLDCM at ( $\omega = 2800$ [rpm])

**e. Torque-current square**

Torque as a function of the square of the current expresses the capability of the magnetic circuit to produce torque at a specified current value. The capability of the SRM to produce torque is improved by the Shark configuration of the air gap. The curves shown in Fig. 5.25 are strongly influenced by that the four motors are not wound for the same voltage.

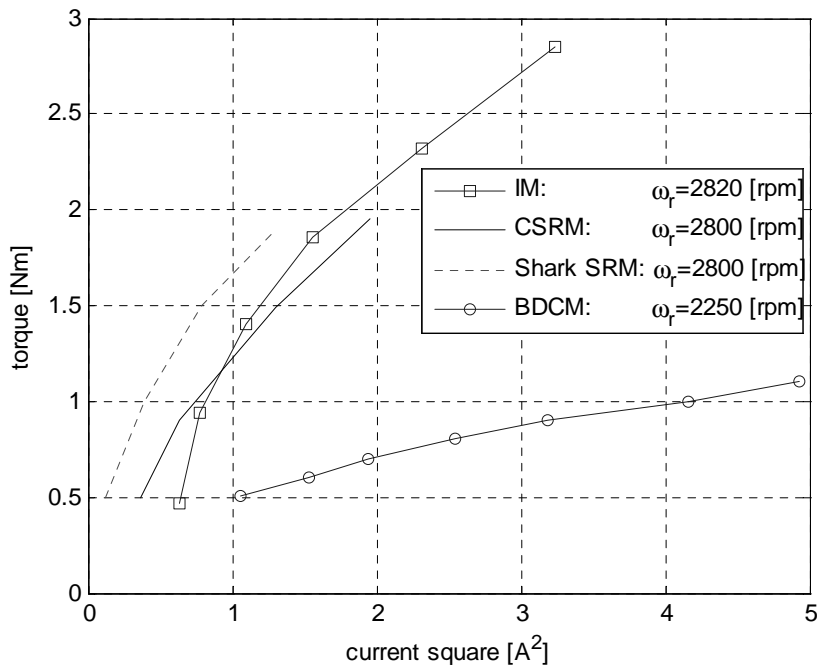


Fig.5.25 Torque vs. current square characteristic at  $\omega= 2800$  [rpm] for CSRSM and Shark SRM and at  $\omega=2822$  [rpm] for the IM

### f. Specific torque

The torque to weight ratio provides the basis for estimation of the relative cost of different motor technologies. The following ratios are defined:

- Torque per unit iron mass  $T/m_{\text{iron}}$
- Torque per unit copper mass  $T/m_{\text{Cu}}$
- Torque per active mass  $T/m_{\text{active}}$

From the data presented in Table 5.6—rows 1, 2 and 3, it may be seen that in order to produce the same output power, at a specified working point, the CSRSM needs less material per unit mechanical torque.

Table 5.6 Torque to volume and torque to weight ratios for IM, CSRSM, Shark SRM and BLDCM

row	Parameter name	Parameter symbol	Unit	IM	CSRSM	SharkSRM	BLDCM
1	torque per iron mass	$T/m_{\text{iron}}$	[Nm/Kg]	0.65	0.73	1.05	1.15
2	torque per copper mass	$T/m_{\text{Cu}}$	[Nm/Kg]	1.93	3.97	5.71	2.40
3	torque per active mass	$T/m_{\text{active}}$	[Nm/Kg]	0.47	0.62	0.87	0.74

### g. Annual energy consumption

The annual energy consumption was calculated for three load profiles, illustrated in Fig.5.26 [96]. The corresponding energy consumed over a year is illustrated in Fig.5.27. The figures show that the Shark SRM is the best of all the motors considered. It should be borne in mind that this comparison is unfair for the BLDCM, as this was designed for a different rated point than that of the IM and CSRSM.

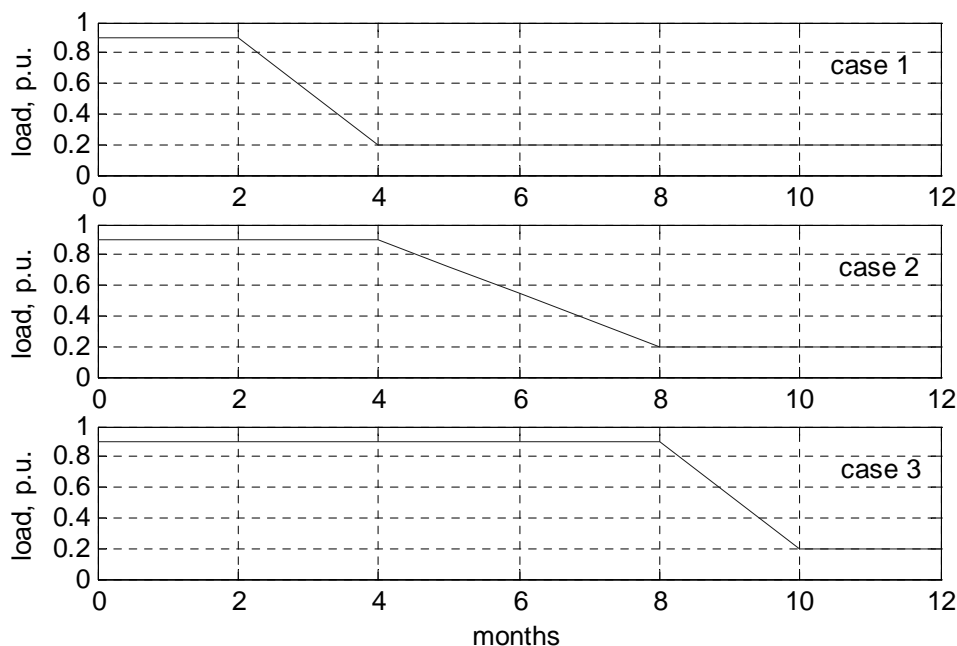


Fig.5.26 Three annual load profiles used to calculate the annual energy consumption.

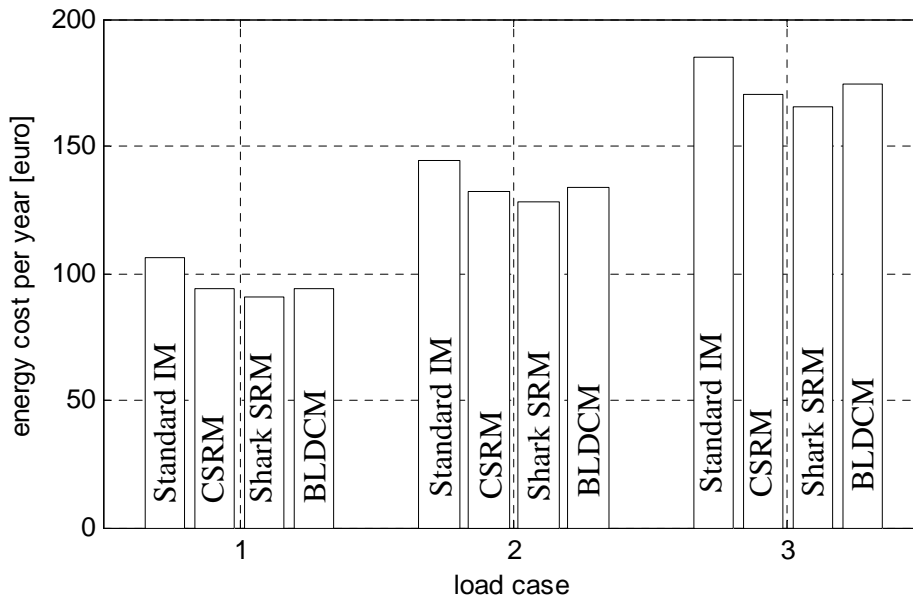


Fig.5.27 Annual energy cost for the 0.55[kW] motor in three cases of load profiles

## Summary and conclusions

In this chapter, the results of the measurements conducted on four different motor types have been presented and discussed. An IM, a CSRМ, a Shark SRM and a BLDCM were tested in static and steady-state conditions. The steady-state tests were performed at operating points specified by torque-speed values. All the measured data were used to calculate some output parameters, which were thought to highlight the differences between the different motor technologies.

Initially, the comparison of the motors involved, a size comparison, which has showed that the IM, CSRМ and the Shark SRM have identical stack and air gap lengths ensuring equals electromagnetic volumes. The BLDCM has, however, a smaller electromagnetic volume and a longer air gap but this difference does not significantly affect its performance due to the use of permanent magnets.

Subsequently, the efficiency, electric and magnetic loadings, power factor and specific output have been compared. The comparison of the CSRМ with the Shark SRM indicated that applying the Shark air gap improves the efficiency and power factor of the CSRМ. This performance is obtained as less RMS current is necessary to produce a specified torque because the energy conversion loop is larger due to the higher flux linkage induced in the magnetic circuit of the Shark SRM.

The CSRМ and the Shark SRM have also been compared with an IM and a BLDCM. Some essential differences such as coils designed for different voltages, optimisation for different working points and absence of any control of the IM may make this comparison unfair for some of the motors. However, an interesting conclusion may be drawn regarding the Shark SRM. This is that the proposed concept is viable and may be applied to substantially improve the performance of a cylindrical air gap motor.



Finally, the annual energy consumption was determined for each of the motor considered. The Shark SRM was found to be the best among them, provided the differences mentioned above were applied.

## Chapter 6

# Manufacturing considerations for the Shark Switched Reluctance Motor

The manufacturing of electric motors falls generally into two categories: manufacturing for prototyping and industrial manufacturing. These two aspects differ in that closer tolerances and more complicated assembly technologies may be used for prototyping. In industrial manufacturing, the focus is on simple and low cost assembly operations.

In this chapter, manufacturing the Shark SRM is discussed. The experience gained during the assembly of the saw-toothed air gap SRM suggested solutions for simple assembly of Shark SRMs.

This chapter is organised to underline the peculiarities of assembly raised by Shark structures. Initially, the constructional differences between the cylindrical and the Shark air gap SRMs are identified. Then, each difference is discussed and specific solutions proposed. The manufacturing problems, which were identified, are: forming the Shark air gap, assembly of stator and rotor, coil insertion, axial alignment of stator and rotor lamination stacks.

### 6.1 Motivation and objective

The Shark concept is intended to provide a more efficient substitute for more usual electric motors. Thus, the Shark SRM has to compete not only in the area of magnetic capabilities but also on that of manufacturing. As the process of manufacturing the saw-toothed air gap machine revealed specific problems, it was considered necessary to present and discuss them and to suggest possible solutions.

The assembly of a Shark SRM raises generally four problems, which may be identified by examining the cylindrical air gap and saw-toothed air gap SRMs from Fig.6.1:

- (a) The special air gap geometry of the Shark SRM demands a time consuming forming process because different laminations are necessary to build one machine. This is as opposed to the cylindrical air gap SRM, where a single type of lamination suffices.
- (b) For most SRM configurations, the Shark air gap geometry makes the direct insertion of the rotor stack into the stator stack impossible. An onerous assembly procedure, consisting of

simultaneous forming of stator and rotor stacks, was used to assemble the Shark SRM used in this project. It will be shown that an easier assembly method may be possible for specific Shark SRM configurations.

- (c) The coils cannot be directly inserted into slots as is the case in the cylindrical air gap SRM.
- (d) The alignment of stator and rotor stacks along the longitudinal axis of the machine requires special attention. In chapter 4, it was shown that a slight misalignment along the longitudinal axis, produces an unbalanced electromagnetic force acting on the axial direction. This force tends to increase the initial unbalance and if the axial displacement of the motor is not prevented, this force may impede the mechanical rotation of the rotor. As this was experienced during the assembly of the demonstration machine, the solution used to solve this problem is discussed in this chapter.

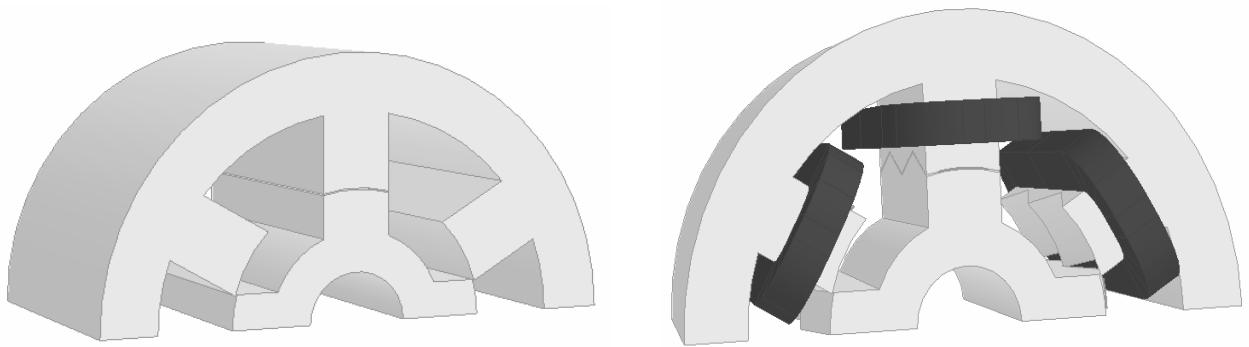


Fig.6.1 Schematics of the CSR and Shark SRM illustrating the differences between the cylindrical and saw-toothed air gap SRMs

## 6.2 Cutting of lamination and of lamination stack for Shark Switched Reluctance Motor

To cut the laminations for electrical machines, shearing or advanced machining processes such as electroerosive, laser beam or water jet machining [111], [112] may be used. The most appropriate method was selected as a function of the efficiency of operation-to-cost ratio. Each cutting technology has advantages and disadvantages associated with using it for Shark SRM. Therefore, the process of forming the air gap of the Shark SRM is investigated in this section.

The framework of the discussion is set by the thickness of the lamination sheet, hardness and by the quality of cutting (tolerance). The features of the material used in electrical machines are determined by:

- the thickness of the lamination sheet, which is generally in the range 0.15 to 1 mm

- the hardness of the material (hard silicon steel), which is generally in the range 65-80Rb<sup>6.1</sup> [113]

The requirements for the quality of the surface are defined by:

- the tolerances at the surface level. This requirement has impact on the air gap symmetry.
- the quality of the surface –that is absence of burrs. This requirement assures that the insulation of the lamination is not damaged by the penetration by burrs in the insulation layer.

### 6.2.1 Shearing process

During the shearing process, the lamination part is made by removing a blank from a large sheet of material. This is, the sheet is cut by subjecting it to the shear process between a die and a punch as shown in Fig.6.2 Among various shearing operations, *punching* and *blanking* are used to cut laminations for electrical machines. During the punching operation, the lamination is the part that is removed from the large sheet of material. In the blanking operation, the slug is removed and the remaining material is the lamination part.

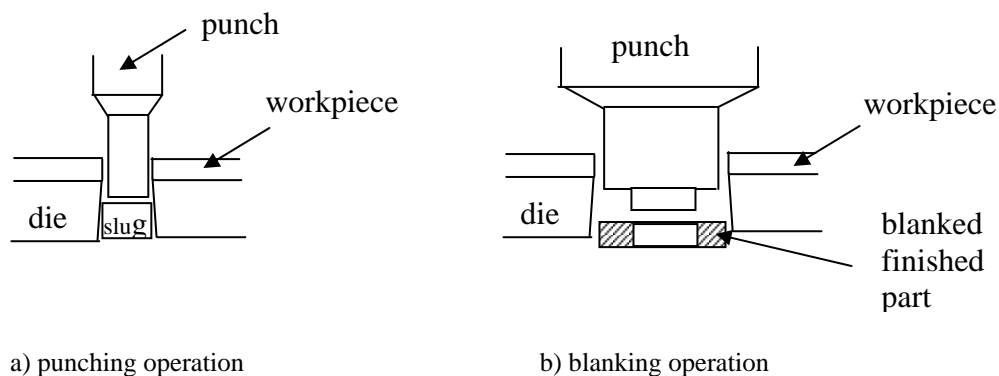


Fig.6.2 Shearing operations.

The shearing process, illustrated in Fig.6.3, starts with the formation of cracks at the top and bottom edges of the metal sheet. When these cracks meet, the separation of the blank is complete. An examination of the resulted surface reveals:

- Some roughness appears at the surface of the cracks during shearing. In [103] it is shown that the clearance between the punch and the die affects the quality of the surface of the cut edge. For large clearances, material tends to be pulled into the clearance zone causing a much rougher surface than is the case when the narrow clearance is small. The punching speed also affects the quality of the surface by determining the ratio of the burnished surface

<sup>6.1</sup> the hardness of the material is determined by Brinell, Vickers, Rockwell test by measuring the depth of an indentation left by an indenter of a specified shape, with a specific force applied for a specific time [103].

to the rough area (see Fig.6.6 b). At higher speed, the heat generated is confined to a smaller zone and the rough area is reduced.

- b) Burrs form at the bottom edge of the work piece, in the direction of movement of the punch. The burrs, may penetrate the inter-lamination insulation and, reduce the effect of the insulation layer against the interlamination eddy currents. Due to pressing of the lamination stack, during assembly, burrs establish metal-to metal contact at lamination edges. In this way the eddy currents may flow between laminations.
- c) Stresses are created in the material during sheering due to distortion of the crystal structure. Magnetic experiments [106] indicated that such stresses may affect the magnetic properties of the lamination at some distance from the cut edge often said to be equal to the lamination thickness. This results in reduced permeability. In order to eliminate the stresses from the material the finished lamination may be annealed.

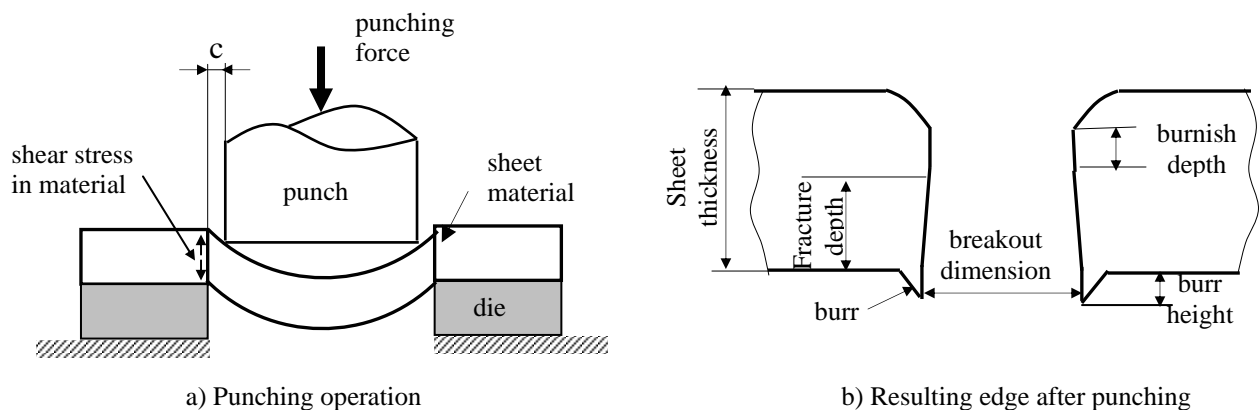


Fig.6.3 Illustration of the punching operation

From the above discussion it seems that the punching operation may be successfully used to cut straight edges on thin steel sheets if appropriate clearance, punching speed and force are used. However, the saw-toothed air gap SRM, requires that the edge of the lamination is cut at a specific angle and this seems to be difficult by using shearing process.

### 6.2.2 Electroerosive Machining

Electroerosive machining utilises electric current, accompanied by a cooling liquid to remove a certain amount of material from the workpiece. Electroerosive machining falls into two categories [112]:

- Electrical-Discharge Machining (EDM)
- Electro-Chemical Machining (ECM)

EDM uses a wire electrode to cut shapes in conducting materials. The workpiece is formed by slowly moving a wire along a prescribed contour as shown in Fig.6.4 a. The cutting process is based on the discharge electrical sparks between the wire and the metal surface [111].

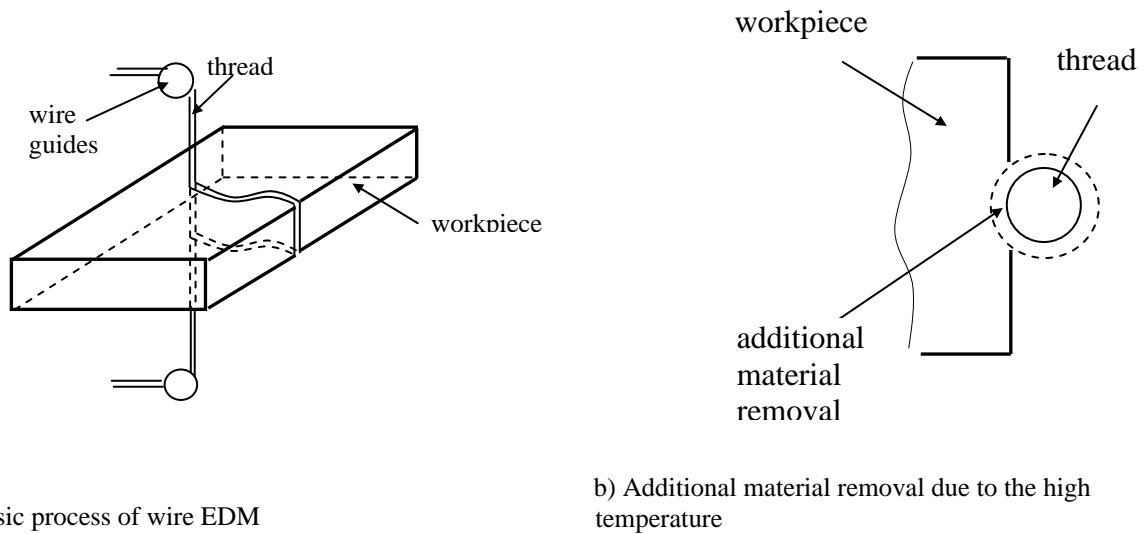


Fig.6.4 Schematic illustration of the wire Electrical-Discharge Machining process.

The surface of the metal is eroded at the point of contact with the wire. Due to the high temperature between the electrode and the surface, the metal melts leaving a slight gap, shown in Fig.6.4 b.

The machine has the possibility of cutting various profiles at different angles within  $\pm 30$  [deg]. If a different angle, outside this range were wanted, a new accessory tool is necessary. Because stacks with various lengths may be cut by EDM, this technique may be used to produce the stack of the saw toothed air gap SRM.

However, there are also disadvantages. The most noticeable of these is the effect that the EDM has on the surface condition of the material. The high temperature between the electrode and the workpiece causes the surface layer of the metal to melt and resolidify [112]. The layer underneath the working surface is also affected. If the temperature of this second layer does not reach such high levels as the surface, an alteration of the properties does occur [112] and as it was shown in the previous section, the temperature affects the magnetic properties of the steel. However, a detailed study of these effects is not in the scope of this work.

### 6.2.3 Laser-Beam Machining

In Laser Beam Machining (LBM), the source of energy is a laser, which focuses optical energy on the surface of the workpiece. The high energy density melts and evaporates portions of the workpiece in a controlled manner. As in the EDM, the high temperature affects the surface properties of the workpiece.

### 6.2.4 Water-Jet Machining

Water Jet Machining (WJM) is widely used for cutting materials such as plastic, fabric or paper due to the absence of the heat. To cut harder materials such as metal, abrasive particles are added to the

water before it enters the cutting zone. This technology is called Abrasive Water Jet Machining. The jet of water and abrasive particles is directed to the surface of the workpiece through an orifice of 0.05 to 1 mm in diameter at a rate of 0.5 to 25 liters per minute [115]. The concentrated force makes a clean cut with practically no rags or burrs. The absence of heat represents the main advantage.

### 6.2.5 Summary of cutting technologies

From the previous discussions it may be concluded that:

- all technologies, that were discussed, are capable of cutting metal sheet with straight edge.
  - The punching operation produces burrs (undesirable for laminations used in electrical machines), affects the structure of the material due to the heat and to the shearing process. The quality of the surface may be controlled by the clearance  $c$  and the punching speed.
  - the EDM and LBM have the advantage of leaving a cleaner surface free of burrs due to the cutting being made by local contact between the workpiece and the electrode. They present the disadvantage of high temperatures developed at the surface of the metal, which affect the structure of the superficial layer. Consequently, the local magnetic properties and insulation layer may be damaged.
- for cutting metal sheet with edges tapered at a prescribed angle
  - the punching technology does not guarantee the success
  - the EDM, LBM and WJM offer the capability of cutting various shapes in a controlled manner. However, the high temperature produced during EDM or LBM cause changes of the local magnetic properties. On the other hand, the WJM does not affect the structure of the superficial layers and produces a surface free of burrs and rags.
- for cutting short stack of laminations
  - the EDM and LBM have good capability for cutting on various contours but the high temperatures affect the structure of the superficial layers. Therefore, according to the machine design the laminations need surface treatment in order to restore the initial properties.
  - the WJM provides clean surfaces without heat damage.

It may be concluded that the AWJM seems to be the most appropriate technology for cutting laminations with tapered edges. The EDM and LBM are also good candidates for cutting laminations to be used in saw toothed air gap SRM. However, they have the disadvantage of adversely affecting the properties of the surface layer of the workpiece. The punching operation is more effective from the point of view of the time used to produce a stack but it will require special dies if tapered edges need to be cut.

## Cutting technology employed for the saw - toothed air gap SRM prototype

The lamination stack of the Shark SRM with saw-toothed air gap was cut using EDM. This decision was taken as the University workshop owns such a machine Charmille-Robofil 330. The cutting process consists of several steps and it is described in the following paragraphs.

The Shark SRM to be manufactured has the saw-toothed shape shown in Fig. 6.5 a. The lamination material has the thickness of 0.5 [mm]. The pitch of the Shark teeth,  $l_{shk}$ , is 4[mm] and the total stack length  $l_{stk}$  is 60 [mm], which gives a number of 15 Shark teeth. The main dimensions are given in Appendix A.2.

The technological process consists of several steps:

- stator stack forming
  - a complete lamination stack, having the inner diameter equal to the minimum Shark diameter  $D_{sg}$ , was cut initially (see Fig.6.5 a)
  - then groups of four laminations (half a Shark tooth) were formed at the prescribed angle  $\beta$  using the wire EDM.
- rotor stack forming
  - a complete lamination stack, having the outer diameter equal to the maximum Shark rotor diameter  $D_{r1}$  was initially cut (see Fig.6.5 b)
  - then each group of four laminations (half a Shark tooth) was formed at the prescribed angle  $\beta$  using the wire EDM.

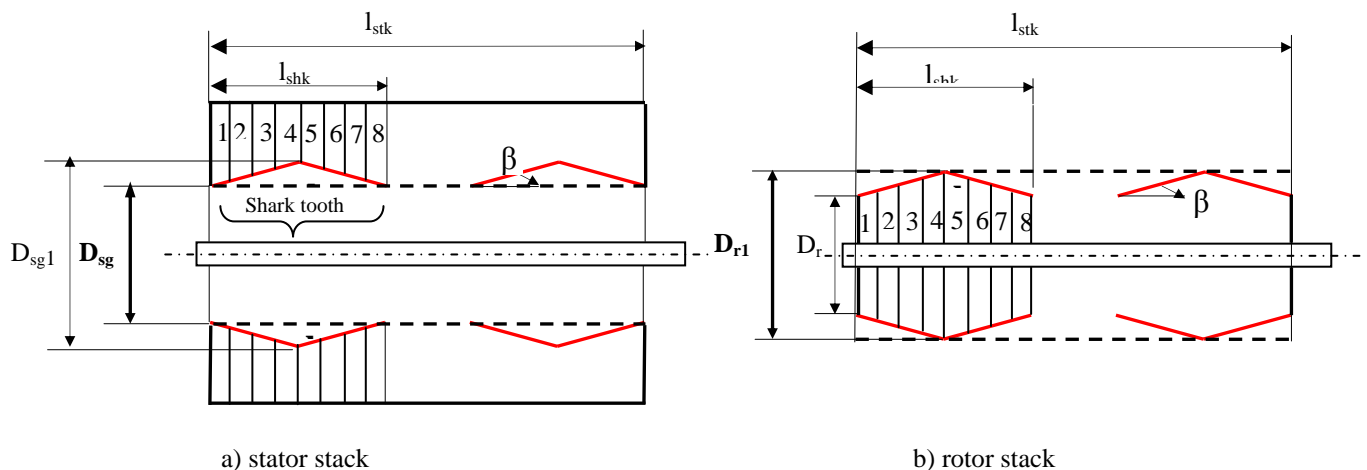


Fig.6.5 Schematic of the technologic process



### 6.3 Assembly solutions

Possible solutions to assemble the stator and the rotor stacks of the saw-toothed air gap SRM, are considered in this section. These possibilities fall into the following categories:

- (a) Simultaneous assembly of the stator and rotor laminations by alternately adding stator and rotor laminations.
- (b) Split the stator stack into two parts, insert the windings directly and then assemble the two stator parts in the final position (see Fig.6.6). However, *cut 1* from Fig. 6.6 does not completely solve the problem of coil insertion, because the coils of the two sectioned poles cannot be directly inserted. Therefore, *cut 2* is considered more appropriate from the point of view of coil insertion in the Shark SRM.
- (c) Individual stator poles are wound separately. There are various versions of this solution for example to split the stator into teeth and yoke sections, to split the stator into teeth sections connected by a thin flange, to split the stator into teeth sections, connected by joints allowing for relative movement of the sections. These solutions are already used in industrial manufacturing [109] and are illustrated in Fig.6.7.
- (d) Reduced number of Shark teeth. The stack of the Shark SRM consists of one single or one half of a Shark tooth, as it is shown in Fig. 6.8. However, this solution degrades the magnetic performances because the angle  $\beta$  is limited to a low value, to preserve a large available winding area. In chapters 3 and 4, it was shown that the performance of the Shark magnetic circuit, keeping the tooth pitch constant, was improved by increasing the height of the Shark teeth or the angle  $\beta$ .
- (e) The selection of single or two phase Shark SRMs with configuration (4/2, 8/4, 12/6), would allow for direct insertion of the rotor stack into the stator stack, as shown in Fig.6.9.

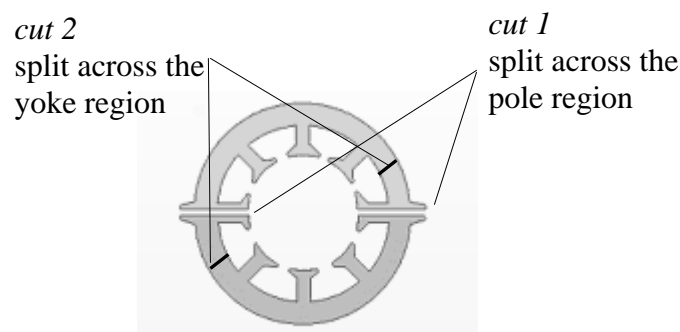


Fig.6.6 Stator split into two parts facilitates the assembly of the Shark SRM. (source Mitsui High-tec).

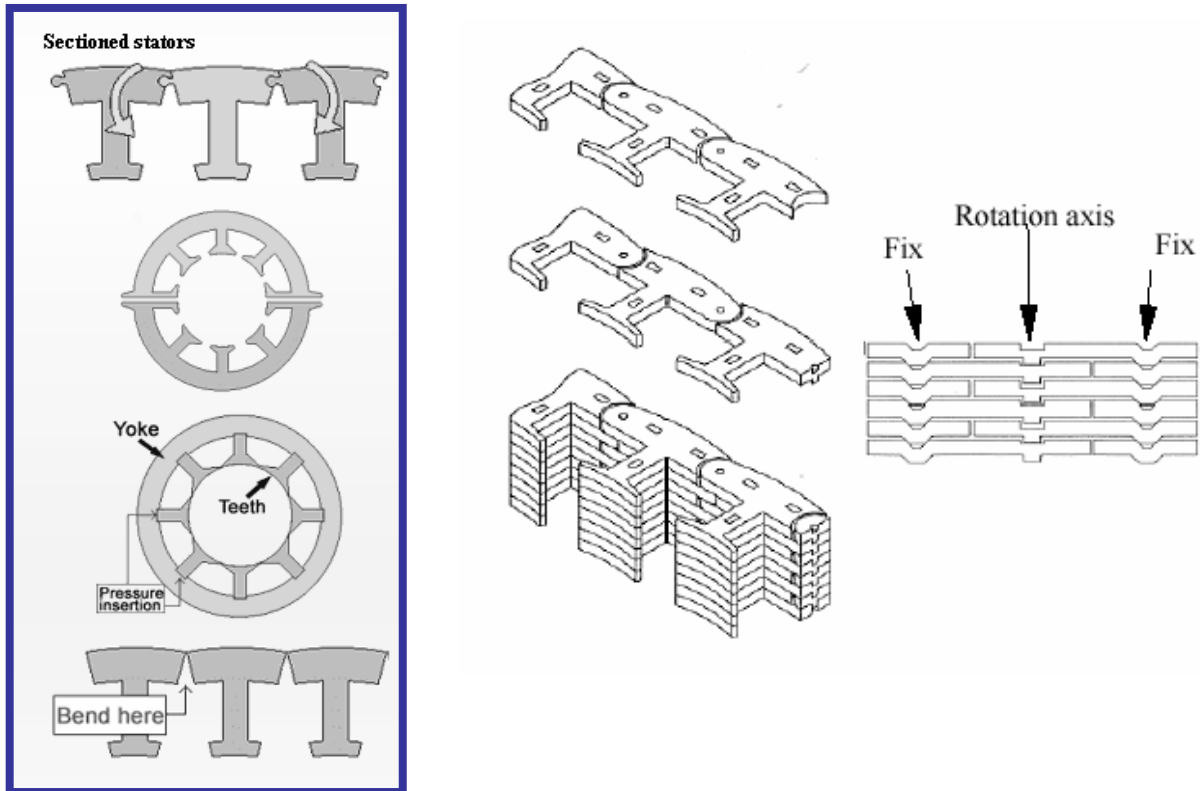


Fig.6.7 Illustration of the assembly solution of Shark structures by split stator [116]

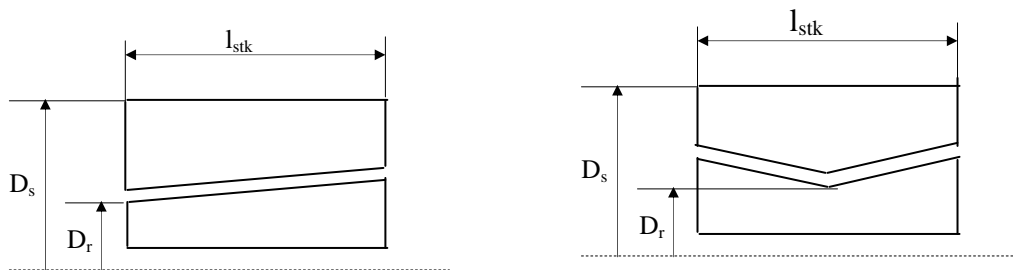


Fig.6.8 Illustration of the assembly solution of Shark structures with reduced number of teeth

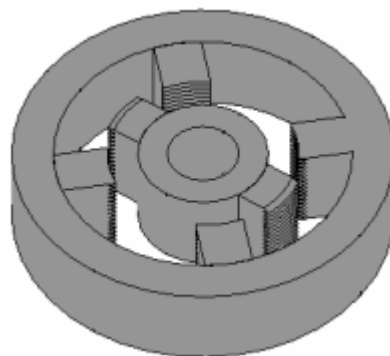


Fig.6.9 Sketch showing the cores of a two-phase SRM motor

## 6.4 Windings

Once the stator and rotor stacks are assembled, the coil insertion is the next step. At this point two situations may occur. One is that the stator stack is split into two parts such as to allow the coils to be directly slipped into place. The second case is that of the stator lamination made from a single piece. In this second case, the stator and the rotor stacks must be assembled by interweaving the stator and rotor laminations as discussed in section 6.3. This assembly complicates the insertion of the coils. The following discussion focuses on this latter solution because it was used to manufacture the Shark SRM to be tested in this project.

### 6.4.1 Insertion of the coil into slots

The problem in the Shark SRM, with the assembly as described in 6.1 is that the coils cannot be inserted directly into the slots. Coil assembly has to be done with the stator and rotor stacks already assembled. It means that the coils may be wound by one of two methods. One method is to sew the coils into slots using a shuttle. This operation would be time consuming. The second method is to wind the coils separately and then slip them into place as shown in this section.

The idea is to place the rotor into the position, which gives the maximum access to the stator slot and place the coil with one side into the slot as shown in Fig.6.10.

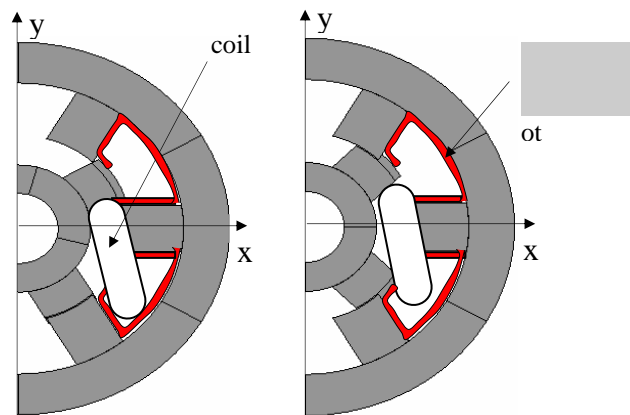


Fig.6.10 Illustration of the process of coil insertion into a slot of a Shark SRM.

Then the rotor is gradually rotated to allow the second side of the coil to slip into position. However, this solution is almost impossible, because the coil is very big and it cannot easily be inserted using the available space between the stator and rotor poles. Therefore, the coil of each pole was divided into two half coils, which are easier to insert into the slot. The complete process is illustrated in Fig.6.11.

The coil has also to be protected against insulation damage during insertion by rubbing against the Shark teeth.

Attention must be paid to the way the coil is slipped from position a to position b because it is very likely that the outer turns of the coil will chafe by rubbing against the Shark teeth on the surface of the stator and rotor poles (Fig.6.11 b and c). In order to prevent chafing two actions may be taken:

- Install a protective layer at the surface of the Shark indentation
- Protect the coils by packing them in a protective material

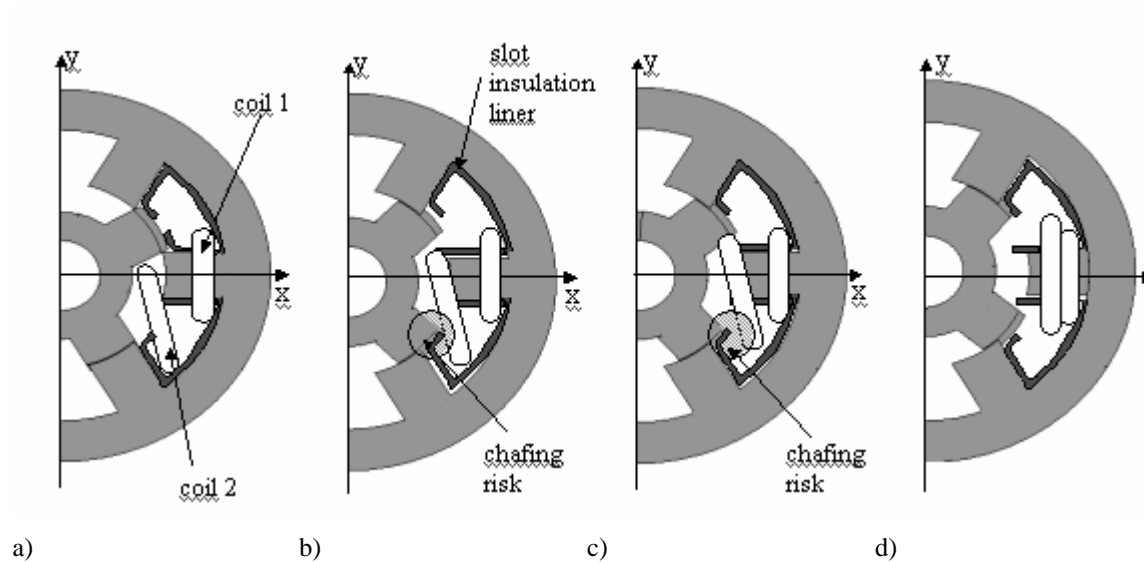


Fig.6.11 Coil insertion for the saw toothed air gap Shark SRM.

A better fill factor of the winding area may be achieved by reshaping the coils, to fill more at the bottom of the slot.

## 6.5 Axial mounting

As discussed in chapter 4, the Shark SRM is characterised by the presence of axial forces. Axial forces are produced on each side of the Shark teeth. In the case of a perfect axial alignment of the Shark teeth, the axial forces acting on each side of each Shark tooth are equal and cancel each other. When a small axial displacement exists between the stator and the rotor stacks, an unbalanced magnetic field is produced. Consequently, the axial force components are no longer equal and a resultant axial force acts on the rotor body. The action of this force is to increase the initial displacement exacerbate the problem. The analysis of chapter 4 highlighted quantitatively this effect of axial displacement.

The axial force may make the operation of the Shark SRM impossible, if inappropriate assembly of the machine were performed. In order to identify solutions for this problem, these situations, which may cause axial displacement were initially identified as:

- inaccurate axial alignment (Fig.6.12 a), which is likely to happens as there is no possibility to check the alignment accurately.
- lamination stacks extension at the air gap end due to the tightening of the stacks (Fig.6.12 b).

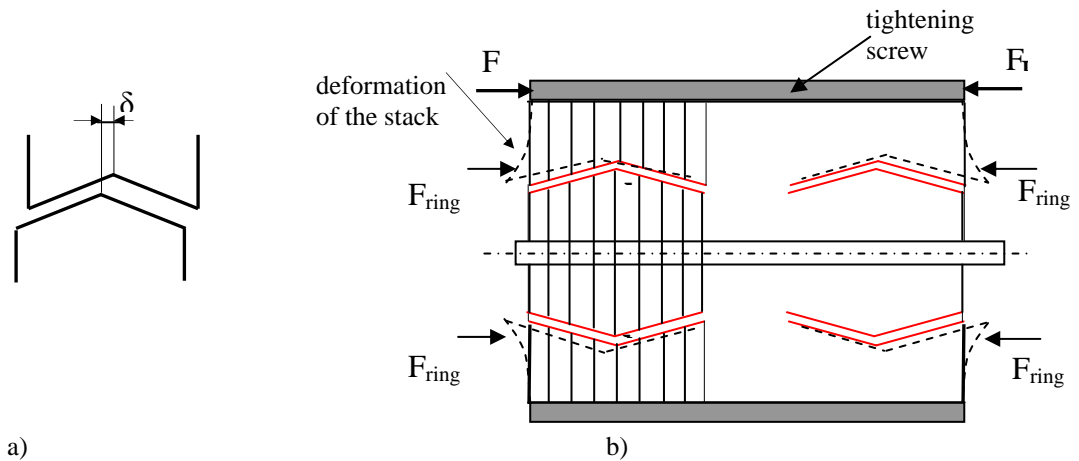


Fig.6.12 Schematics of misaligned Shark teeth. a) inaccurate mounting. b) lamination stack extension due to the tightening force

The solutions to be considered are mainly of two natures:

- (a) Measure to prevent any initial misalignment. The extension of the stator stack may be avoided by using two support rings mounted one at each end of the stator stack. The two rings press the stator stack in the region of the Shark teeth tips ( $F_{ring}$  in Fig.6.12 b), assuring that the two ends are parallel.
- (b) Measure to prevent axial movement of the rotor in the stator stack, during operation. To prevent this, spring washers are mounted behind the bearings to oppose to the maximum axial force, which may be produced in the air gap of the Shark SRM.

## 6.6 Summary and conclusions

In this chapter, the manufacturing process of a three-phase 6/4 Shark SRM was discussed. It was shown that the main difficulties are caused by the presence of the saw-toothed air gap. These problems fall into several categories such as: insertion of the coils into slots, insertion of the rotor stack into the stator stack, prevention of the axial movement of the rotor. Based on the experience gained during the manufacturing process, suggestions are made for a simple assembly of the Shark SRM.

The winding technology was also considered for the prototype Shark SRM. Of course, the easiest solution is the direct insertion of the coils when the general assembly allows it. Otherwise, the method of rotor rotation and coil slipping or the sewing of the coil may be employed. For the machine built in the workshop, the first method was employed as it allows the forming of the coils prior the insertion into slots.

The axial alignment and movement under the action of the axial forces was also considered in this chapter. The general actions to be taken are to prevent the initial misalignment and prevent axial movement of the rotor body under the axial forces. The solutions employed in the prototype built for this project were respectively a ring that forces the two ends of the stator stack to be parallels and wave-springs which preload the bearings and prevent any undesired axial movement.

## Chapter 7

### Summary and Conclusions

The research documented in this report is rooted in the efforts to reduce the energy consumed by electric motors. This work was motivated by the idea that the efficiency of a specified electric motor may be improved by replacing the usual cylindrical air gap by a non-linear air gap. This idea is not new, other reports addressing this subject being published prior to this work [1], [2], [3], [4], [5], [6]. However, no systematic analysis has been reported. The focus in these publications was mostly to prove that the concept work. It may be appreciated that the applicability of this concept, called Shark in [1], was not considered seriously, probably because of the assembly difficulties caused by the non-linear air gap. However, these problems may be overcome by nowadays technologies [117]. Therefore, it was appreciated that a detailed analysis of the effect of the Shark air gap on the performances of electric motors might be of interest. The methodology of the study was determined by the lack of analysis tool for Shark air gap machines. As 'vehicle' for this study, a Switched Reluctance Machines was considered due to its simple geometry.

The study considered the linear analysis and the Finite Element Analysis as main tools capable of providing basic knowledge of the magnetic behaviour of various air gap shapes applied in SRM. Based on these data, an analytical model, describing the magnetisation characteristics of the Shark SRM in aligned and unaligned rotor positions, was conceived. The modelling principle was to adapt one of the existing models of cylindrical air gap SRM such as to account for the influence of the Shark profiles in the air gap. This model was used to generate family of characteristics showing the relative improvement in terms of converted energy of the Shark SRM with respect to a cylindrical air gap SRM, having identical main dimensions.

The calculations were verified by measurements on two machines having cylindrical and saw-toothed air gap. Furthermore, an Induction Motor and a brushless DC motor were compared to the two SRMs.

In the following paragraphs each chapter of this report are summarised and their achievements are confronted to the objectives of this project.

#### 7.1 Summary of the thesis

#### **Linear and finite element analysis**

It was appreciated that a step-by-step analysis shall be performed as to identify as many as possible features of the proposed air gap shapes. Therefore, a linear analysis was made initially, providing

basic information about various Shark profiles. This was followed by finite element analysis of various Shark air gaps, allowing for consideration of the non-linear properties of the magnetic material and highlighting the saturation mechanisms specific to each Shark air gap.

Various air gap shapes such as saw-toothed, square-wave, trapezoidal, elliptical air gaps were considered. Some of them were gradually eliminated (elliptical air gap) from the study because it was considered that the manufacturing process would be too complicated.

There were built Finite element models of various Shark SRMs and 2D FEA was the solution preferred such as to save computation time. To account properly for the effect of the Shark air gap, the axial cross-section of the motor was modelled instead of the radial cross-section of the motor.

The effect of each dimension of the Shark profile on the energy conversion process was studied by using these models.

The ultimate goal of this analysis was to select the optimum Shark air gap, by optimum Shark air gap being understood the shape and dimensions of the Shark profile.

The finite element analysis revealed that:

- The saw-toothed air gap SRM produces, at any value of the excitation current, more flux linkage than the CSRSM
- The square-wave air gap SRM produces, at low current, more flux linkage than the CSRSM and the saw-toothed air gap SRM
- The square-wave air gap SRM produces, at high current, less flux linkage than the CSRSM
- The Shark SRM with trapezoidal teeth is the generalisation of the saw-toothed and square-wave geometries. Its magnetisation characteristic has values between the characteristics of the saw and square wave air gap SRM. Its shape is affected by the value of the parameter  $l_{top}$ , which defines the geometry of the Shark tooth. For  $l_{top} / l_{shk} = 0.5$ , the trapezoid tooth takes the shape of the square-wave tooth, whilst for  $l_{top} / l_{shk} = 0$ , it has the shape of the saw tooth.

It resulted as well that the saturation of the Shark profile occurs at different locations according to the specific shape:

- At the tip of the Shark tooth in the saw profile
- At the root of the Shark tooth in the square wave profile

There were also revealed the possibilities to improve the flux linkage induced in the magnetic circuit of the Shark SRM. These solutions were formulated such as to reflect the influence of each dimension of the Shark profile. They are summarised below.

**For Shark teeth having tooth pitch constant:**

- **Saw profile:** flux linkage increases as the height of the tooth increases
- **Square wave profile:** at low current the flux linkage increases with the increase in height but at high current the flux linkage decreases as the height of the tooth increases

For Shark teeth having  $l_{shk} / h_{shk} = \text{constant}$ :

- **Saw profile:** the flux linkage is, at all current values, bigger than that of the CSRSM as long as the active region of the air gap is not smaller than 90% of the total air gap area.
- **Square wave profile:** The flux linkage, at low current, increases by increasing the tooth pitch, as long as the active region of the air gap is not smaller than 85% of the total air gap area.

**For the condition  $h_{shk} = \text{constant}$ :**

- **Saw profile:** the flux linkage increases as the length,  $l_{shk}$ , increases
- **Square wave profile:** at low current the flux linkage increases with the decrease of the length,  $l_{shk}$ . At high current the flux linkage decreases as the length,  $l_{shk}$ , decreases.

This analysis revealed a clear difference between the saw and square-wave tooth. This is that the flux linkage induced in a SRM, having saw-toothed air gap, exceed at any current value the flux linkage of the corresponding SRM, having cylindrical air gap. On the other hand, the flux linkage induced in a SRM, having square-wave air gap is affected by saturation such as at a certain current, its magnetisation curve, which exceeded that of the CSRSM, will cross over and become smaller than that of the corresponding CSRSM.

Because the saturation plays an important role in SRM, this difference determined the selection of the saw-toothed air gap. This shape produces more flux linkage at all current values.

The optimum dimensions of the saw profile were determined by using the energy gain calculated as the ration of the energy converted in a Shark SRM to that converted in a corresponding CSRSM. The dimensions selected were a Shark tooth pitch of 4 [mm] and an angle  $\beta$  of 45 [deg].

**Analytical models of the Shark profiles**

The results of the previous studies were used to make an analytical model of the Shark SRM in aligned and unaligned rotor positions. This was wanted as a quick evaluation tool, which may be used as a substitute to the finite element analysis. The analytical model proposed by this work was thought such as to use the existing models of the cylindrical air gap SRM. To do this the air gap dimensions of the Shark SRM were converted to the dimensions of an equivalent cylindrical air gap



SRM. The conversion was made such as the static flux linkage characteristics of the two motors were identical /similar.

The model was tested for two SRM configurations, by comparing the calculated flux linkage curves of Shark SRM having different dimensions to those provided by FEA. However, more verifications are necessary.

This model was then used to analyse the influence of the Shark profile dimensions on the energy converted in the machine. The study of the relative performance of the CSRSM and Shark SRM, considering and neglecting the reduction of the winding area cause by the Shark profile, indicated that the optimum dimensions of the Shark air gap are relatively independent of the winding layout.

By using the above model, the components of the forces produced in the Shark SRM were analysed. It was shown that each Shark profile produces axial forces, which in the case of an axially unsymmetrical air gap will determine a resultant axial force. If the axial movement of the rotor is not prevented, the resultant axial force may determine the failure of the operation. It resulted that the radial force produced in a Shark SRM is smaller than that produced in a CSRSM, a smaller radial component being produced by increasing the angle  $\beta$ . On the other hand, the shape of the air gap makes difficult a precise axial alignment of the stator and rotor stacks. Thus a resultant axial component will be produced, whose magnitude increases generally by increasing the angle  $\beta$ . However, at  $\beta$  larger than 25-30 [deg], the axial force seems to decrease by increasing  $\beta$ .

## Measurements and comparison of various motor technologies

To verify the finite element and the analytical calculations, two demonstration SRMs, having cylindrical and saw-toothed air gap and identical main dimensions, were built in the University workshop. Static and steady-state tests were made such as to reveal the similarities and the differences between the two structures.

In addition, they were compared to other motor types such as an induction motor and a brushless Dc motor. These motors were designed such as to provide 550 [W], in operating conditions defined by 2800 [rpm] and 1.9 [Nm]. They had all to fit into a Grundfos frame for standard induction motor MG 71. However, the comparison was unfair for the BLDCM, which was optimised for a different working point than the IM and the CSRSM. Furthermore, the IM was tested only at rated voltage but it was shown [96] that this does not affect the results at the operating point, specified above.

The steady-state tests of the CSRSM and its Shark counterpart shown that the Shark SRM produces in identical operation conditions, the same output power as the CSRSM, by using less input power. The efficiencies measured for the Shark SRM were with 2 to 5 % points better than those measured for the CSRSM. The improvement of efficiency is more significant at low speed and load torque. This is explained by that the saturation of the iron material diminishes the effect of the Shark air gap. The power factor of the Shark SRM was also improved relative to that of the CSRSM.

## Manufacturing considerations

Considerations about manufacturing process were made and some solutions, simplifying the assembly of Shark structures, were suggested. The difficulties of assembling a Shark structure were identified as:

- Forming the air gap shape
- Assembling the stator and the rotor stack
- Inserting the coils into slot
- Preventing the axial displacement of the rotor under the action of the axial force

To suggest solutions to each of these problems different technologies for cutting lamination stack were discussed. Then the latest technologies for economical assembling of stator and rotor stacks and for winding production and insertion into slot were reviewed. One of them [117] is seen as a way opener for the application of the Shark concept in SRM. It was also shown that a single or a two-phase machine avoids any assembly difficulties. Furthermore, extending the application of the Shark principle to linear machines may be another possibility.

### 7.2 Future work

The analysis reported in this thesis highlighted also some subjects for further investigation such as:

- To analyse the magnetisation curves at intermediate rotor positions. It was seen from measurements that even for the saw-toothed air gap the magnetisation characteristics of the Shark SRM and CSRSM cross over at intermediate rotor positions. This may be explained by the local saturation of the stator and rotor poles at positions around the corner position, which may have a strong influence on the saw-toothed profiles. To do this 3D FEA is necessary.
- To study the force production in steady-state operation and their effect on vibration and noise of the Shark structure. The vibration of SRMs continues to be an impediment for its acceptance in applications, in spite of a variety of solutions to reduce it. Therefore, the reduction of the radial force determined by the saw-toothed air gap may be worth to investigate. By using such an air gap shape, the reduction of the radial force becomes an inherent feature of the machine and no other solution may be needed.
- To investigate new manufacturing solutions. The latest assembly technology [117], may open the way of the Shark SRM to applications. Therefore a detailed research of the implications the mentioned solution may have on producing Shark SRM may be of interest.



## Appendix A

### Appendix A.1

#### Design data for the standard Induction Motor

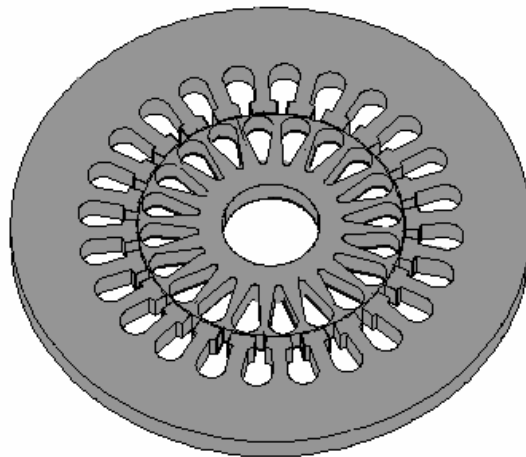


Fig.A.1 Illustration of the Induction Motor

##### a) Design data

Table A.1 Design data for the Induction Motor, Grundfos design, MG71

Phases	m	3
Rotor poles	$N_r$	2
Stator slots	$N_s$	24
Shaft diameter [mm]	$D_{sh}$	20.0
Rotor pole root diameter [mm]	$D_{br}$	36.4
Rotor crown diameter [mm]	$D_r$	54.4
Stator pole root diameter [mm]	$D_{bs}$	83.2
Stator outside diameter [mm]	$D_s$	106.5
Air gap length [mm]	g	0.3
Stack length [mm]	$l_{stk}$	60.0
Turns per phase	$N_{turn}$	420
Wire diameter [mm]	Wdia	0.475
Lamination tickness [mm]/steel	-	0.5/Lossil 400-50
Rated speed [rpm]	n	2800
Rated power [kW]	$P_m$	0.55
Rated DC link voltage [V]	$V_{dc}$	400
copper mass [Kg]		0.95
iron mass [Kg]		3.02
Al mass [Kg]		0.22

b) Measurement results

Table A.2 Results of the steady-state test on the standard Induction Motor

	Motoring Applied torque in % of rated torque	1 150 [%]	2 125 [%]	3 100 [%]	4 75 [%]	5 50 [%]	6 25 [%]
6	Ambient Temperature	20	20	20	20	19	19
7	Stator winding temperature	68.23	63.31	56	50	46	42
8	Frequency, in Hz	50	50	50	50	50	50
9	Synchronous speed [rpm]	3000	3000	3000	3000	3000	3000
10	Slip Speed [rpm]	311	245	178	122	75	36
11	Speed [rpm]	2689	2755	2822	2878	2925	2964
12	Line-to-Line Voltage [V]	387	386	387	387	387	387
13	Line Current [A]	1.80	1.52	1.25	1.05	0.88	0.8
14	Stator Power [W]	1094	874	686	519	358	203
15	Core Loss [W]	17.93	17.93	17.93	17.93	17.93	17.93
16	Stator I <sup>2</sup> R Loss	164.99	113.86	73.29	49.30	33.78	27.29
17	Power Across air gap [W]	911.08	742.19	594.77	451.77	306.29	157.78
18	Rotor I <sup>2</sup> R Loss	94.44	60.62	35.28	18.37	7.65	1.89
19	Friction and Windage Loss [W]	6.106	6.409	6.72	6.99	7.22	7.418
20	Total Conventional Loss [W]	283.46	198.81	133.24	92.59	66.58	54.52
21	Torque [Nm]	2.85	2.32	1.854	1.40	0.941	0.471
22	Efficiency %	75.20	76.60	79.86	81.29	80.51	72.02
23							
24	Shaft Power [W]	800.15	669.32	547.9	421.9	288.23	146.2
25	Apparent Total Loss [W]	293.85	204.7	138.1	97.1	69.77	56.8
26	Stray-Load Loss [W]	10.39	5.87	4.88	4.51	3.19	2.28
	Rs [ohm]	16.97	16.42	15.63	14.90	14.54	14.11
	cosφ	0.9	0.86	0.82	0.73	0.61	0.4

## Appendix A.2

### Design data for the cylindrical air gap Switched Reluctance Motor

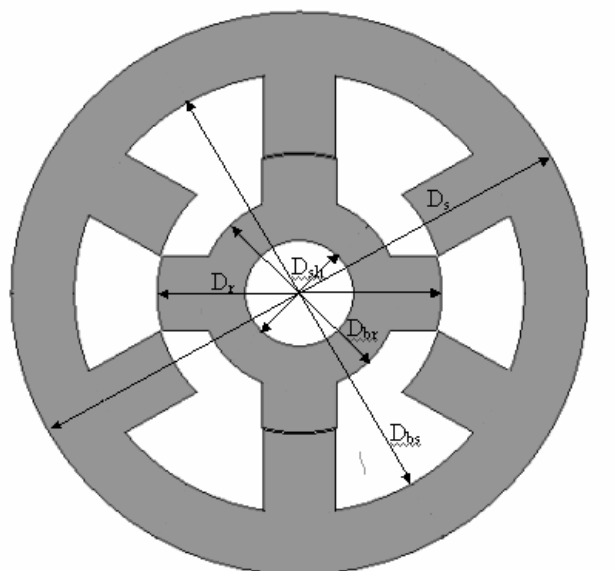


Fig. A.2  
the Cylindrical  
Motor (CSRSM)

Illustration of the cross-section of  
air gap Switched Reluctance

#### a) Design data

Table A.3 Design data for CSRSM - Danfoss design.

Phases	m	3
Rotor poles	$N_r$	4
Stator poles	$N_s$	6
Shaft diameter [mm]	$D_{sh}$	20.0
Rotor pole root diameter [mm]	$D_{br}$	36.4
Rotor crown diameter [mm]	$D_r$	52.6
Stator pole root diameter [mm]	$D_{bs}$	83.2
Stator outside diameter [mm]	$D_s$	106.5
Air gap length [mm]	g	0.3
Stack length [mm]	$l_{stk}$	60.0
Rotor pole angle [deg]	$\beta_r$	30.8
Stator pole angle [deg]	$\beta_s$	29.2
Turns per pole	$N_{turn}$	278
Wire diameter [mm]	Wdia	0.475
Lamination thickness [mm]/steel	-	0.5/Lossil 400-50
Rated speed [rpm]	n	2800
Rated power [kW]	$P_m$	0.55
Rated DC link voltage [V]	$V_{dc}$	500
copper mass [Kg]		0.48
iron mass [Kg]		2.59

b) Measurement results

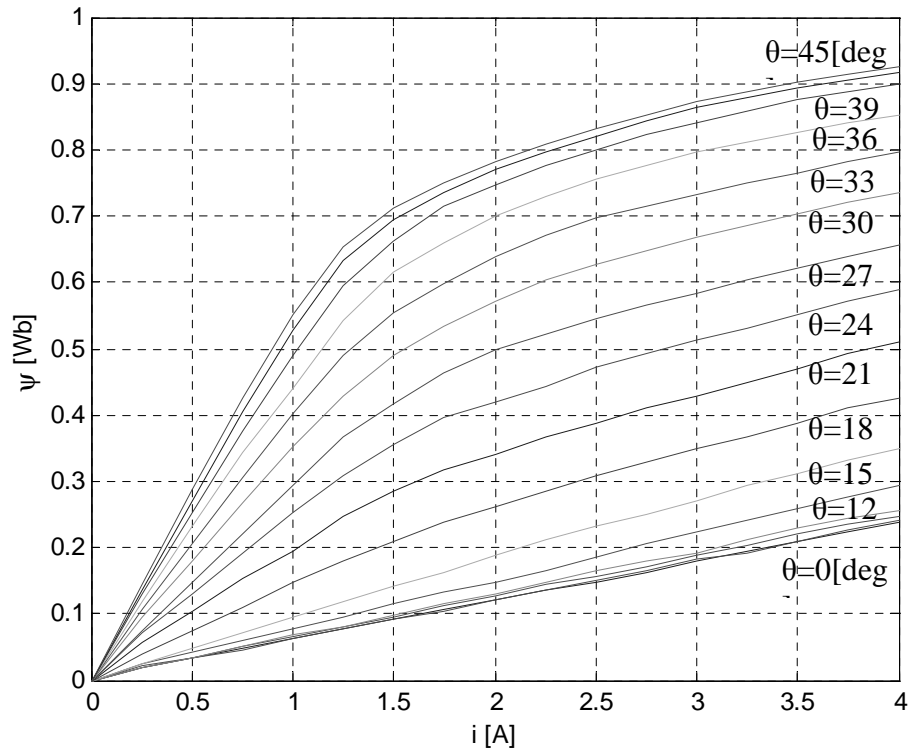


Fig.A.3 Static flux linkage characteristics at different rotor positions and current values

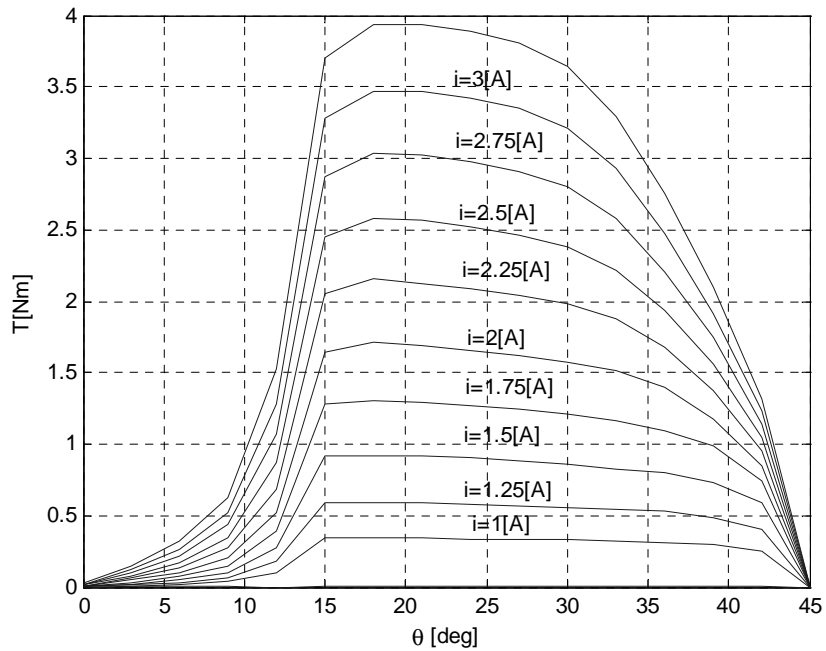


Fig.A.4 Static torque characteristics at different rotor positions and current values

### Appendix A.3

#### Design data for the Shark air gap Switched Reluctance Motor

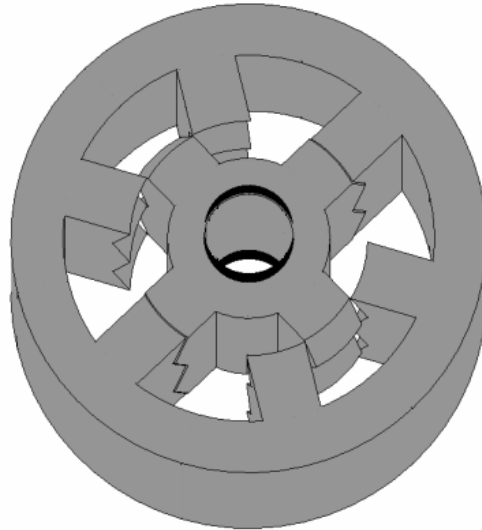


Fig.A.5 Illustration of the cross-section of the saw-toothed air gap Switched Reluctance Motor

a) Design data

Table A.4 Design data for the saw-toothed air gap SRM.

Phases	m	3
Rotor poles	$N_r$	4
Stator poles	$N_s$	6
Shaft diameter [mm]	$D_{sh}$	20.0
Rotor pole root diameter [mm]	$D_{br}$	36.4
Rotor crown diameter [mm]	$D_r$	52.6
Stator pole root diameter [mm]	$D_{bs}$	83.2
Stator outside diameter [mm]	$D_s$	106.5
Air gap length [mm]	g	0.3
Stack length [mm]	$l_{stk}$	60.0
Rotor pole angle [deg]	$\beta_r$	30.8
Stator pole angle [deg]	$\beta_s$	29.2
Turns per pole	$N_{turn}$	278
Wire diameter [mm]	Wdia	0.475
Lamination thickness [mm]/steel	-	0.5/Lossil 400-50
Rated speed [rpm]	n	2800
Rated power [kW]	$P_m$	0.55
Rated DC link voltage [V]	$V_{dc}$	500
copper mass [Kg]		0.48
iron mass [Kg]		2.59



a) measurement results

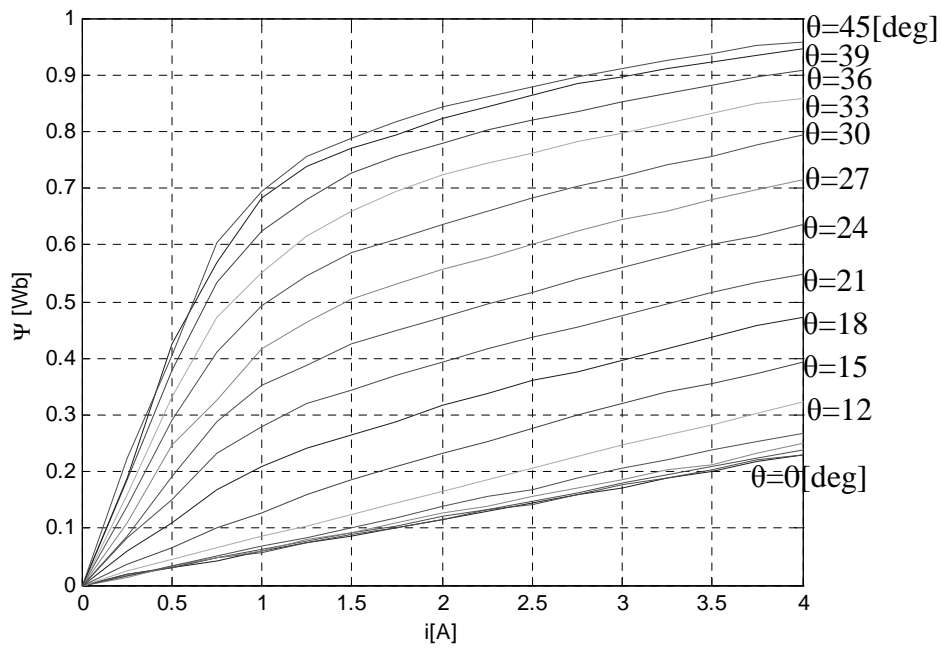


Fig.A.6 Static flux linkage characteristics for the saw-toothed air gap SRM

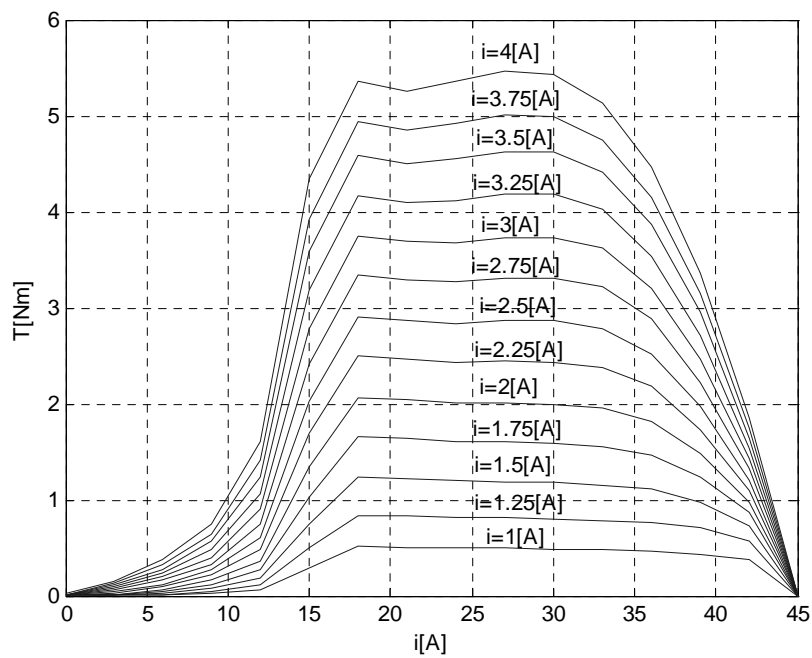


Fig. A.7 Static torque characteristics for the saw-toothed air gap SRM

## Appendix A.4

### Design data of the brushless DC motor

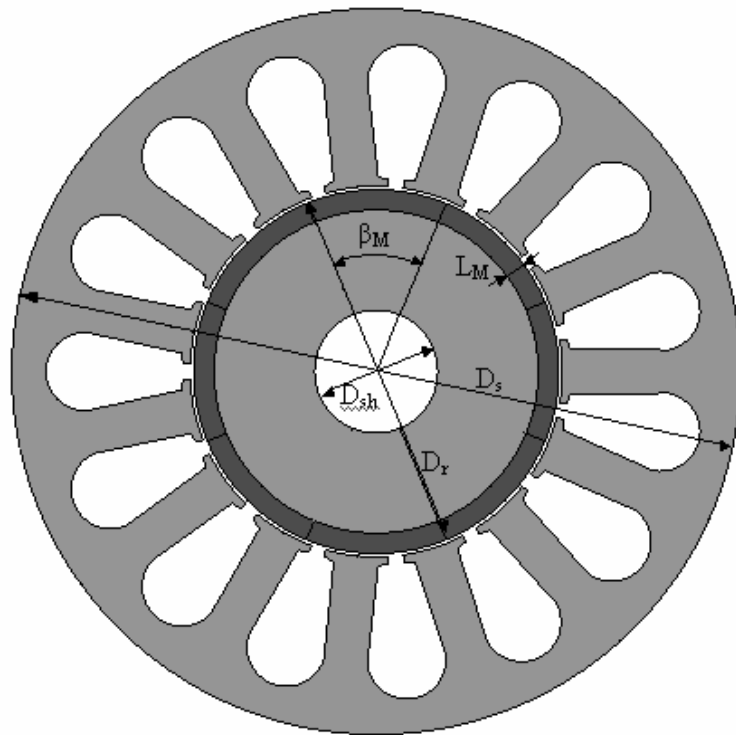


Fig. A.8 Illustration of the brushless DC motor

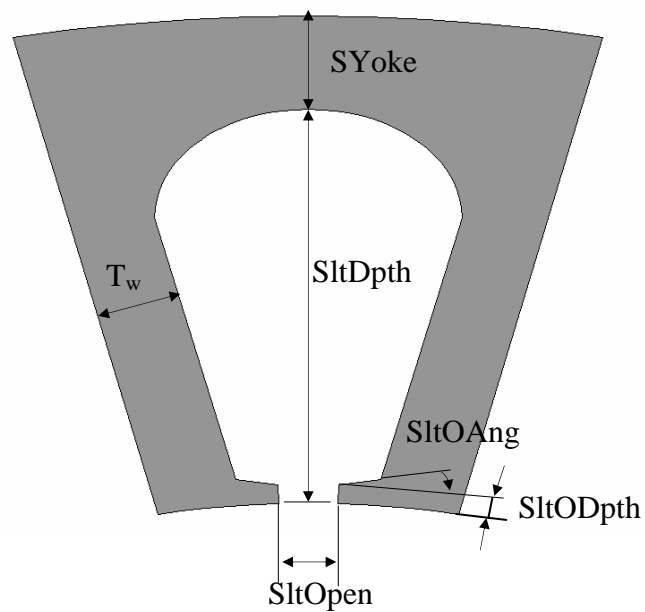


Fig.A.9 Illustration of the slot design of the brushless DC motor

a) Design data for the Grundfos BLDCM

Table A.5 Design data for the BLDCM

Phases	ph	3
Stator slots	$N_s$	15
Poles	$N_r$	8
Shaft diameter [mm]	$D_{sh}$	18.0
Rotor diameter – at magnet surface [mm]	$D_r$	53.4
Stator outside diameter [mm]	$D_s$	106.5
yoke tickness	SYoke	5.0
Air gap length [mm]	g	0.5
Stack length [mm]	$l_{stk}$	40.0
Magnet pole arc	$\beta_M$	180
Tickness of the magnet in direction of magnetisation [mm]	LM	3
<b>Slot dimensions</b>		
Stator tooth width [mm]	$T_w$	6.5
Slot depth [mm]	SltDpth	21.05
Slot open [mm]	SltOpen	2.2
Radial depth of stator tooth tip (slot opening depth) [mm]	SltODpth	1.0
Slot opening angle [deg]	SltOAng	22.5
Turns per phase	$N_{turn}$	225
Wire diameter [mm]	Wdia	0.709
Lamination tickness [mm]/steel	-	0.5/Lossil 400-50
Rated speed [rpm]	n	2800
Rated power [kW]	$P_m$	0.55
Rated DC link voltage [V]	$V_{dc}$	500
copper mass [Kg]		0.78
iron mass [Kg]		1.65
magnet mass [Kg]		0.11

## Appendix B

### Appendix. B.1

#### Definition of the air gap layers and of the reading lines for saw-toothed and square-wave air gaps

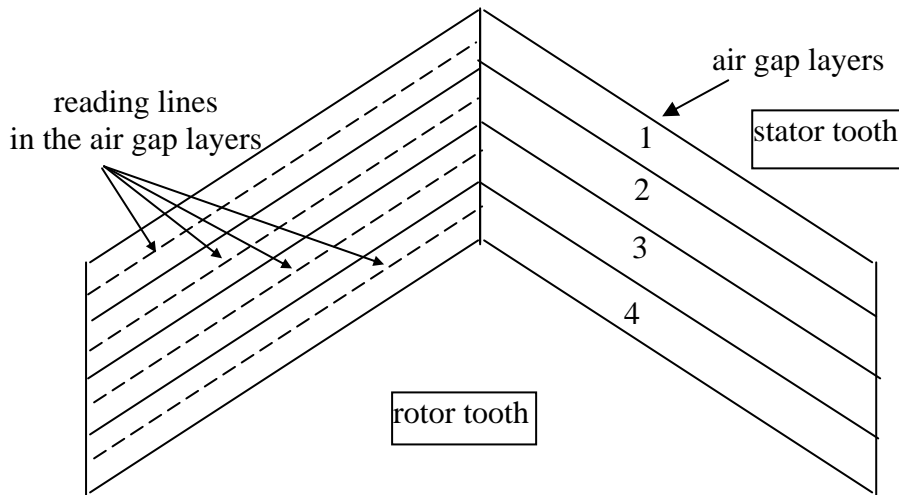


Fig.B.1 Saw-toothed air gap – air gap layers and reading lines

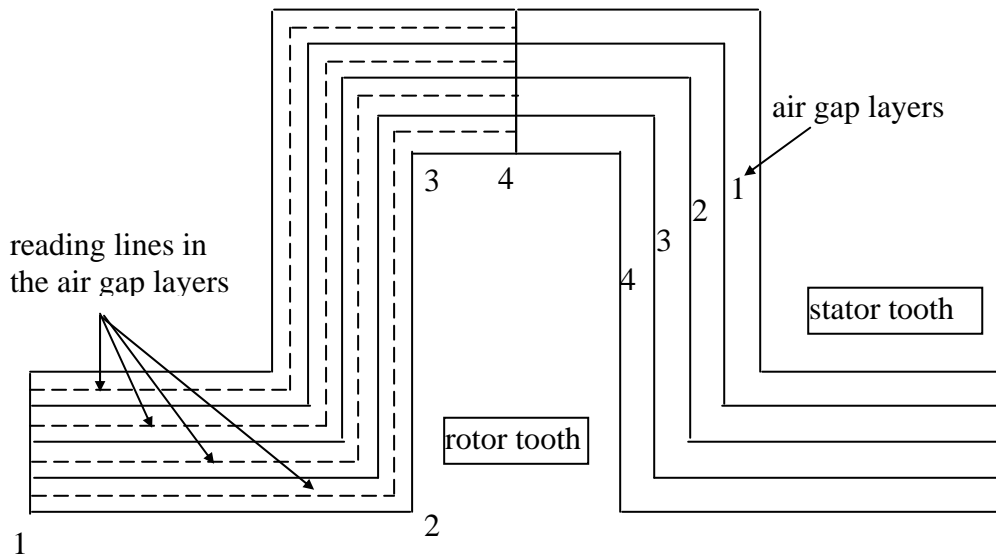


Fig.B.2 Square-wave air gap– air gap layers and reading lines

## Appendix B.2

### Air gap error distribution in saw-toothed and square-wave air gaps

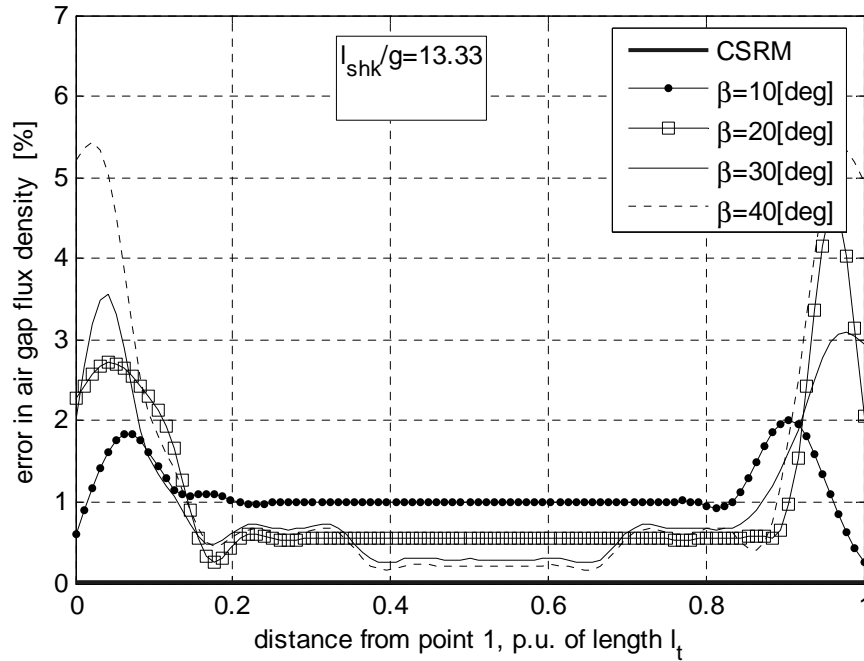


Fig.B.3 Local error distribution in saw-toothed air gap

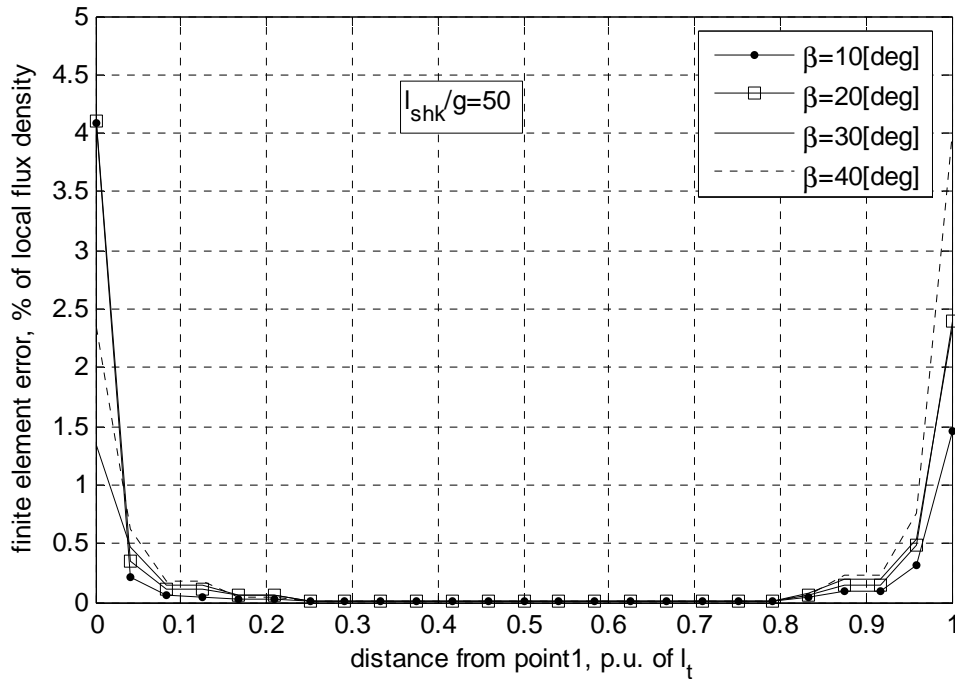


Fig.B.4 Local error distribution in saw-toothed air gap

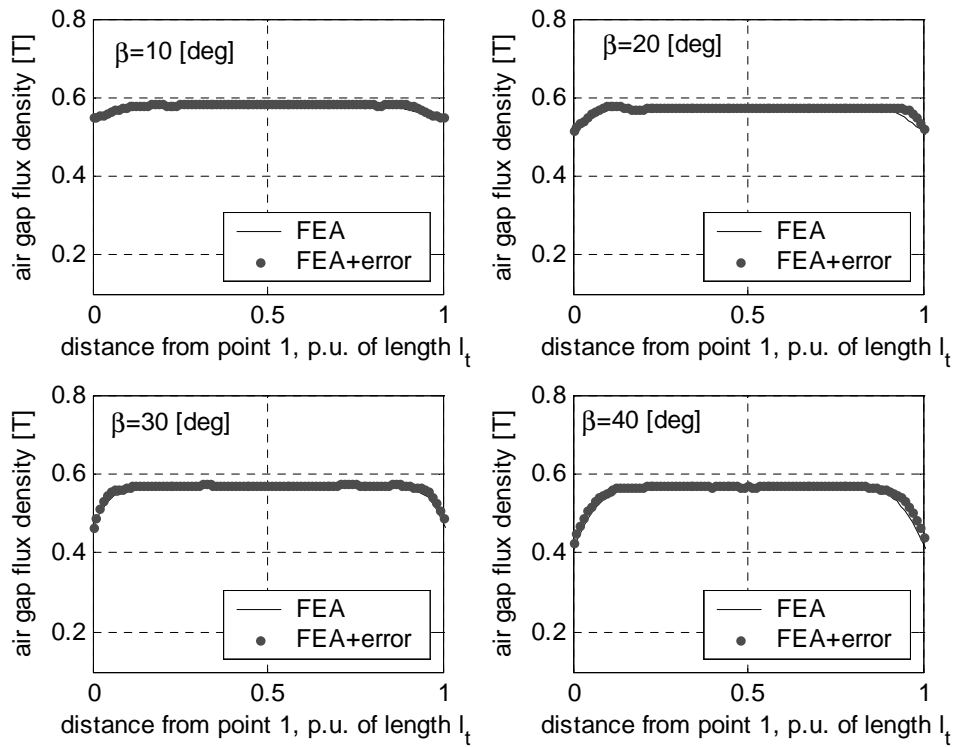


Fig.B.5 Saw toothed air gap SRM

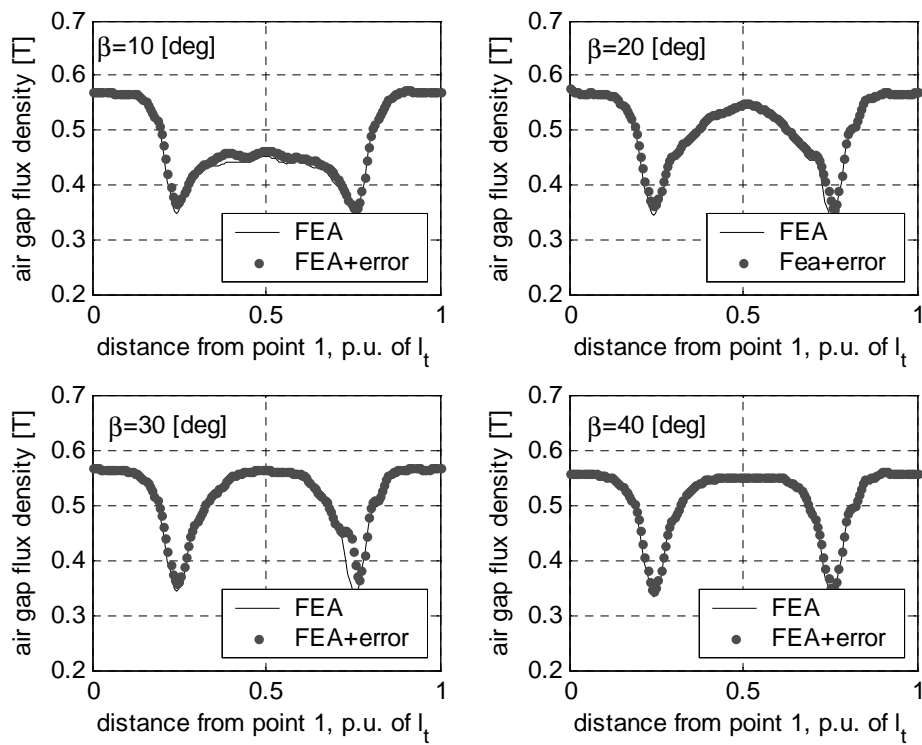


Fig.B.6 Square-wave air gap SRM

### Appendix B.3 Saw-toothed air gap SRM

#### Flux density distribution in the air gap layers

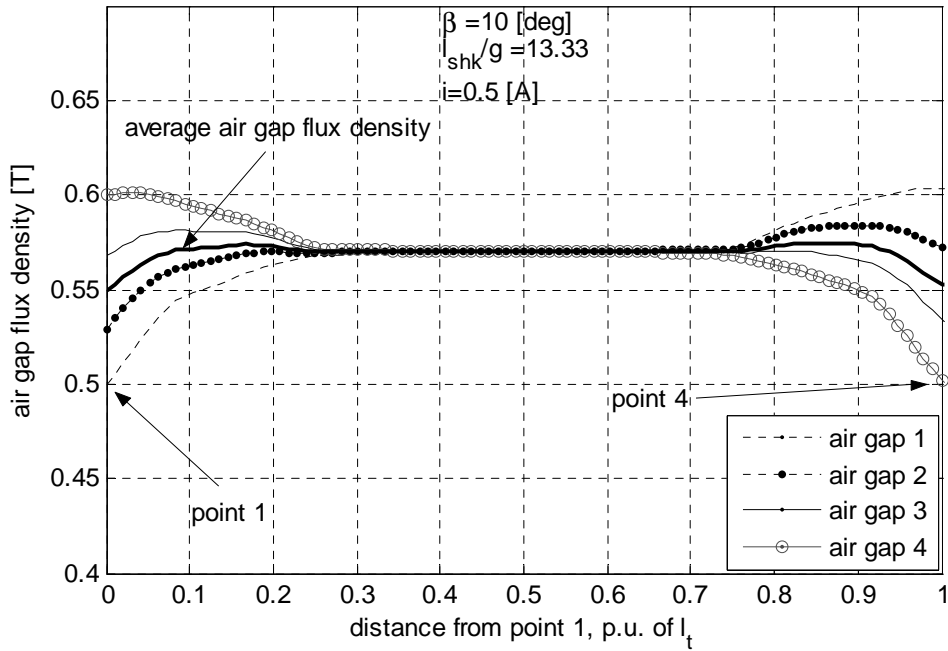


Fig.B.7 Flux density distribution in the four layers of the air gap in a Shark SRM ( $\beta=10$ [deg]), at low current

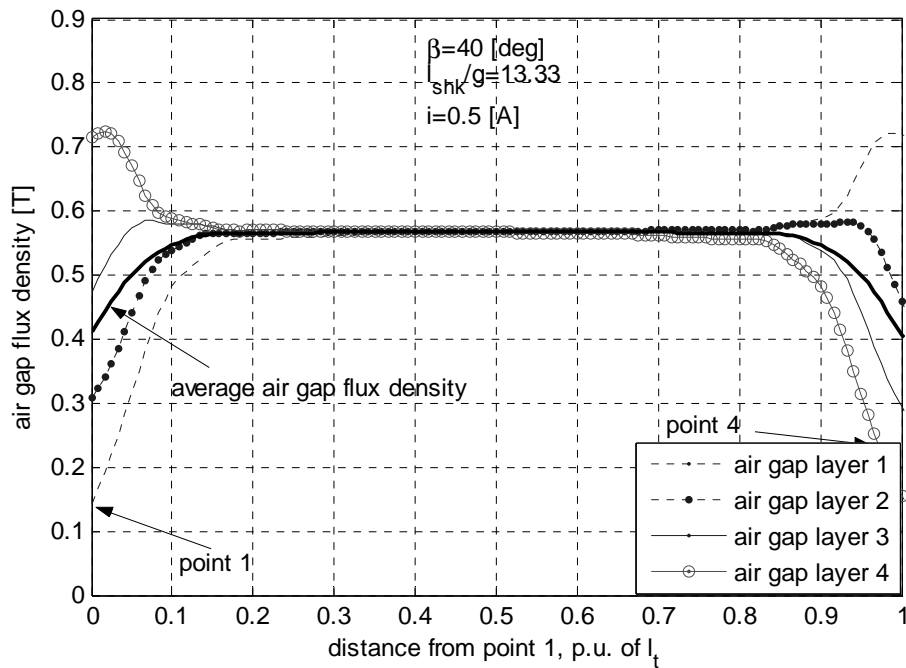


Fig.B.8 Flux density distribution in the four layers of the air gap in a Shark SRM ( $\beta=45$ [deg]), at low current

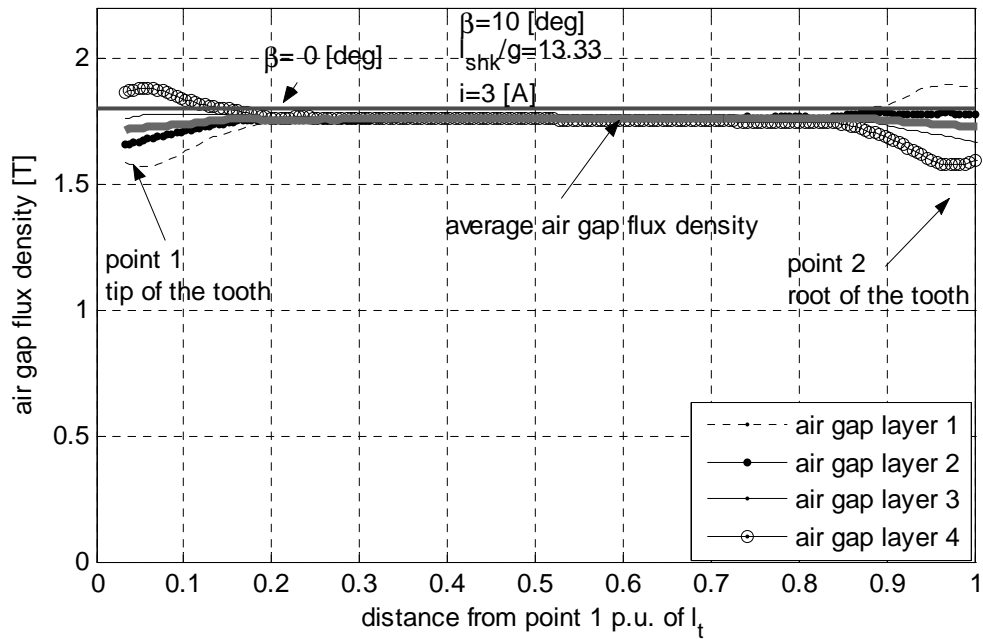


Fig.B.9 Flux density distribution in the four layers of the air gap in a Shark SRM ( $\beta=10$ [deg]), at high saturation level

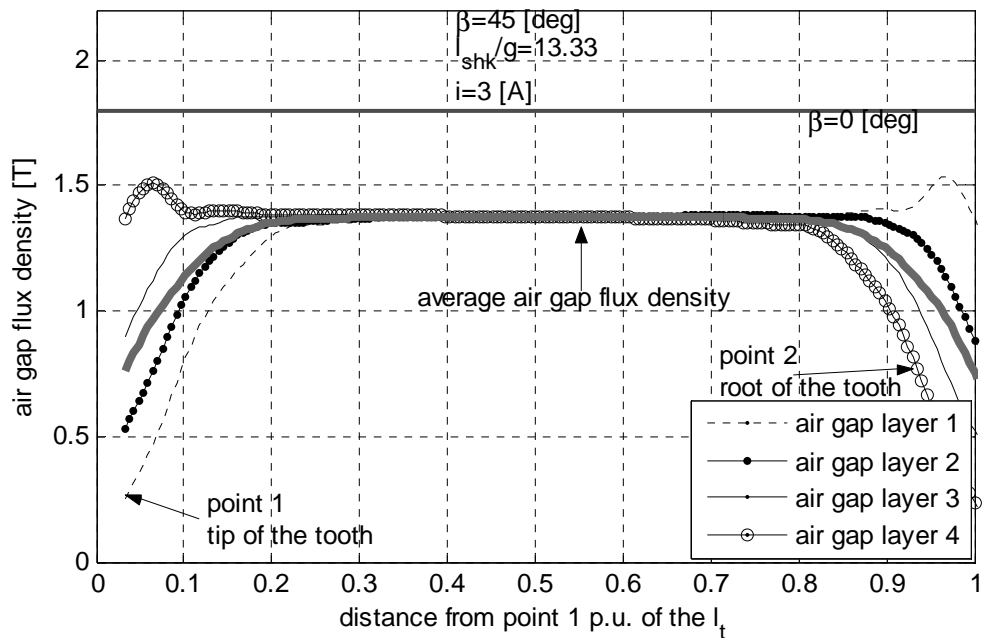


Fig.B.10 Flux density distribution in the four layers of the air gap in a Shark SRM ( $\beta=45$ [deg]), at high saturation level



### Appendix B.4 Square wave air gap SRM

#### Flux density distribution in the air gap layers

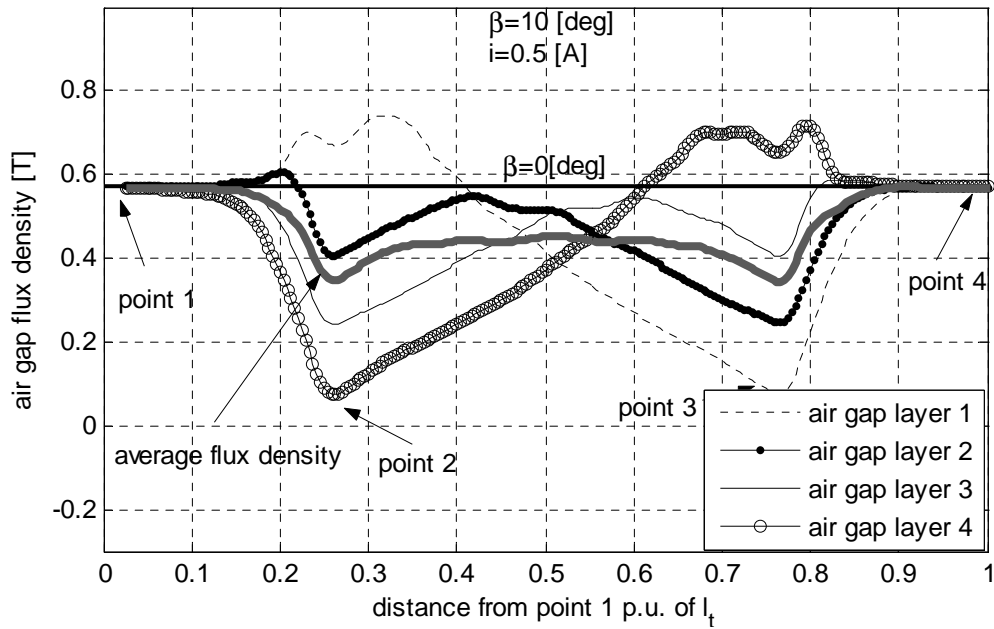


Fig.B.11 Flux density distribution in the four layers of the air gap in a Shark SRM ( $\beta=10$ [deg]), at low current

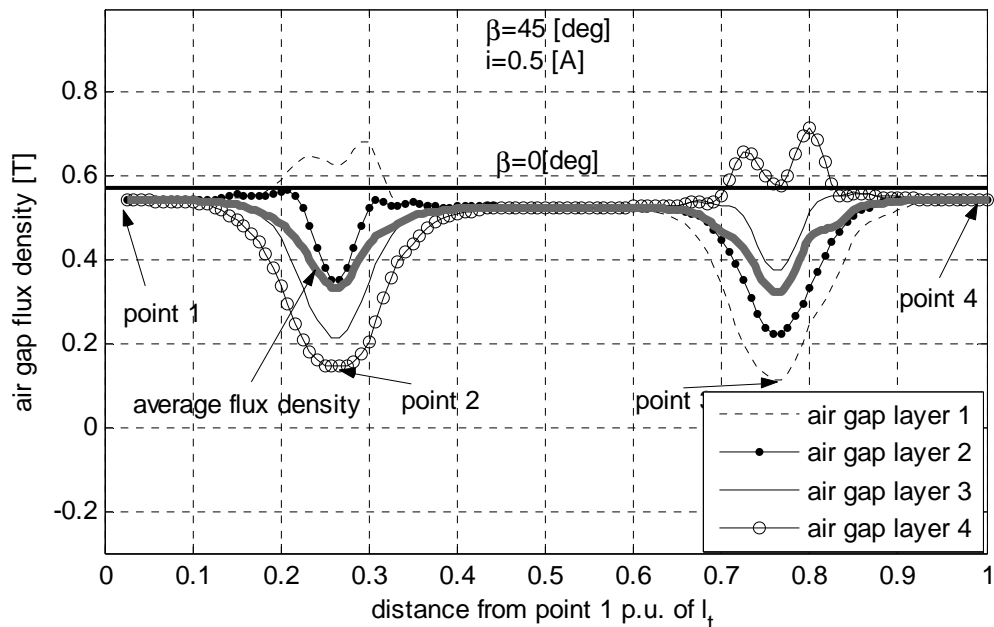


Fig.B.12 Flux density distribution in the four layers of the air gap in a Shark SRM ( $\beta=45$ [deg]), at low current

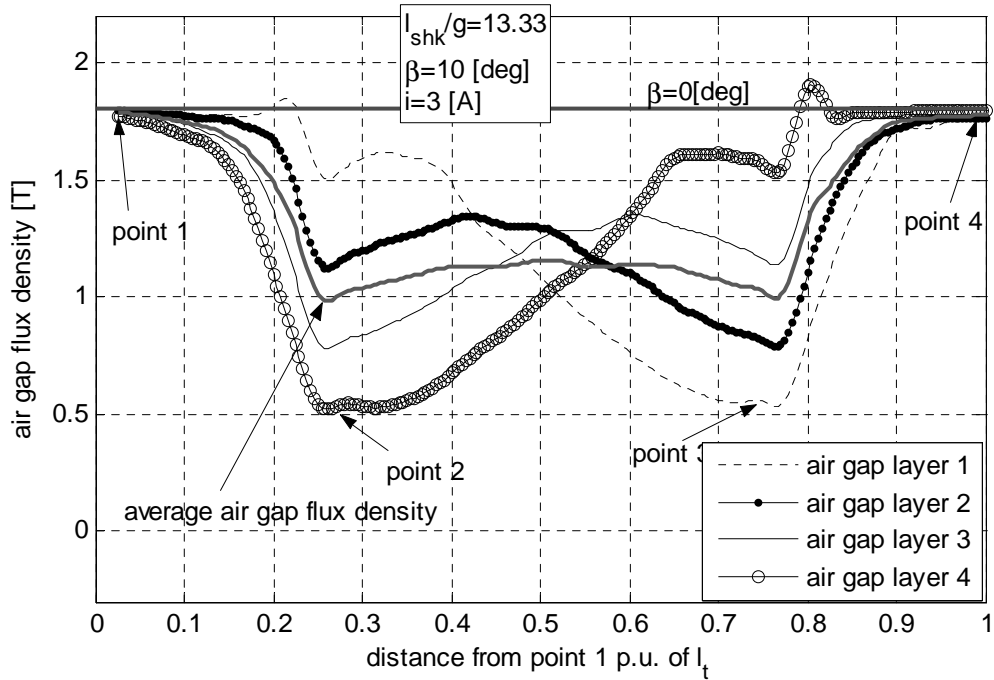


Fig.B.13 Flux density distribution in the four layers of the air gap in a Shark SRM ( $\beta=10[\text{deg}]$ ), at high current

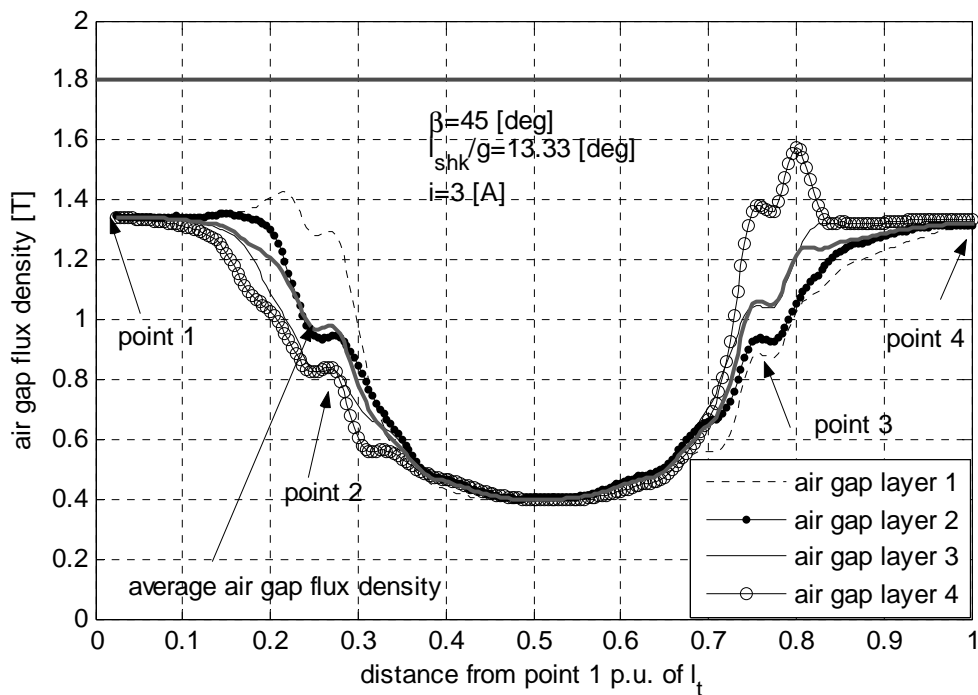


Fig.B.14 Flux density distribution in the four layers of the air gap in a Shark SRM ( $\beta=45[\text{deg}]$ ), at high current

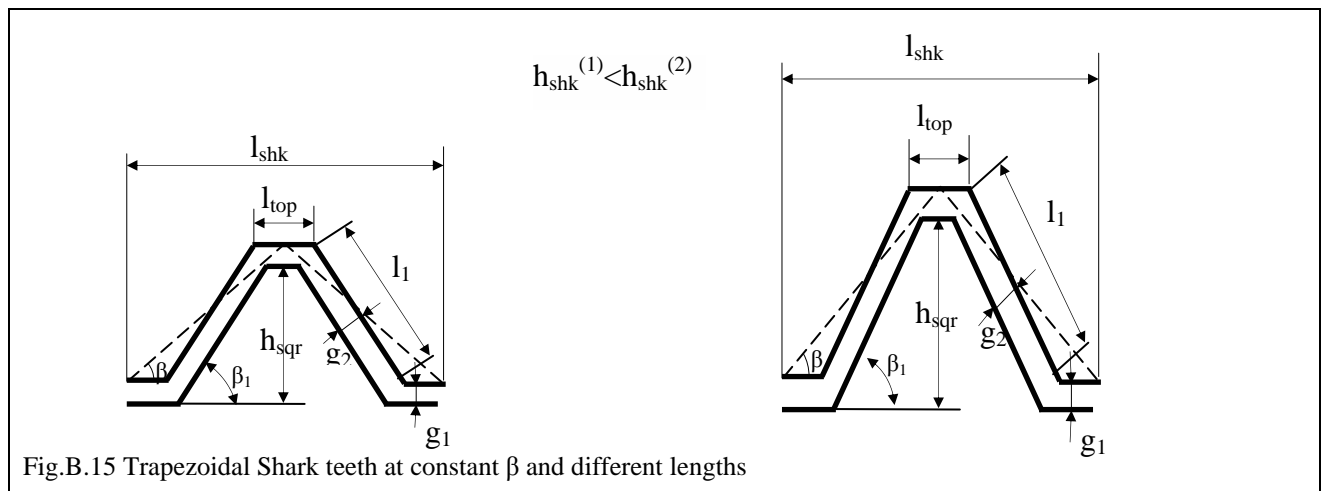
## Appendix B.5 Trapezoidal toothed air gap

The analysis performed for the saw and square wave toothed air gap is considered also for the trapezoidal air gap SRM. Because the trapezoidal profile is a generalisation of the saw and square profiles, the air gap flux density distribution are not presented as is was done in the two previous cases. Two situations are analysed for the trapezoidal profile:

- a) constant  $I_{shk}$  and variable  $\beta$
- b) constant  $\beta$  and variable  $I_{shk}$ .

### a) constant $I_{shk}$ and variable $\beta$

This case is illustrated in Fig.B.15. The trapezoidal shape is built based on the dimensions of the saw shaped Shark tooth. The trapezoidal profile is a generalisation of the saw and square wave profiles. Function of the value taken by the parameter  $l_{top}$ , the trapezoidal profile can be a saw ( $l_{top}=0$ ) or a square wave profile ( $l_{top}=0.5$ ). Therefore the magnetisation characteristics of the trapezoidal profile have shapes and values between those of the saw and square wave toothed air gap SRM.



To illustrate the magnetic behaviour of this profile, the magnetisation curves for Shark profiles with constant  $l_{shk}$ ,  $l_{top}$  equal to 0.4 of the tooth length  $l_{shk}$  are presented in Fig.B.16. It results that its behaviour is similar to the saw toothed air gap Shark SRM in the sense that the Shark magnetization characteristics do not cross over the reference curve. At wider  $l_{top}$ , the magnetisation characteristics look similar to those of the square profile. The current at which the crossing of the Shark and CSRSM happens is smaller for wider  $l_{top}$ , as shown in Fig.B.17.

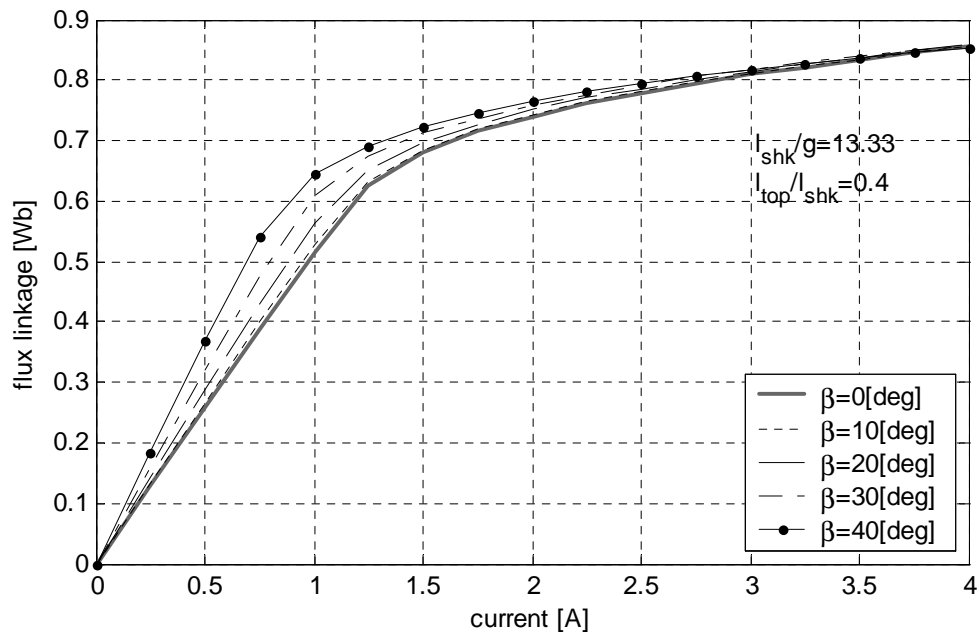
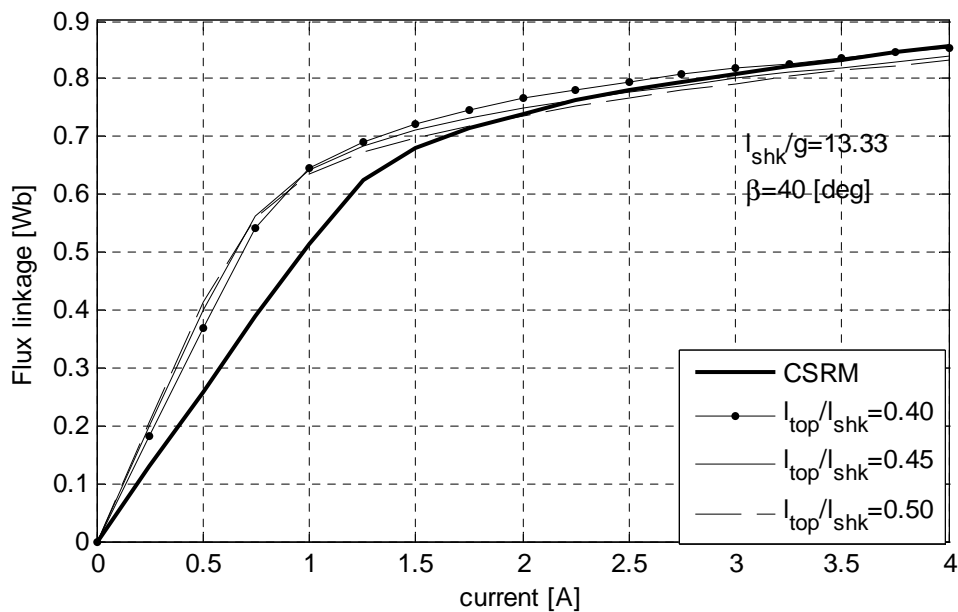

 Fig.B.16 Magnetisation characteristics for trapezoidal air gap Shark SRM ( $l_{top}/l_{shk}=0.4$ )


Fig.B.17 Crossing point between the magnetisation characteristics of the trapezoidal Shark SRM and CSRMs

Previously, it was mentioned that the trapezoidal profile is a generalisation of both saw and square profiles. This statement is supported by the magnetisation characteristics shown in Fig. B.16 and by the air gap density distribution from Fig. B.18. Here it can be seen that the profile of the average flux density distribution combines the features of the distribution for a saw profile. The flux density values along the horizontal faces reaches the flux density of the CSRMs (Fig.B.18). The resemblance to the square profile is shown by the profile of the distribution (Fig.B.18).

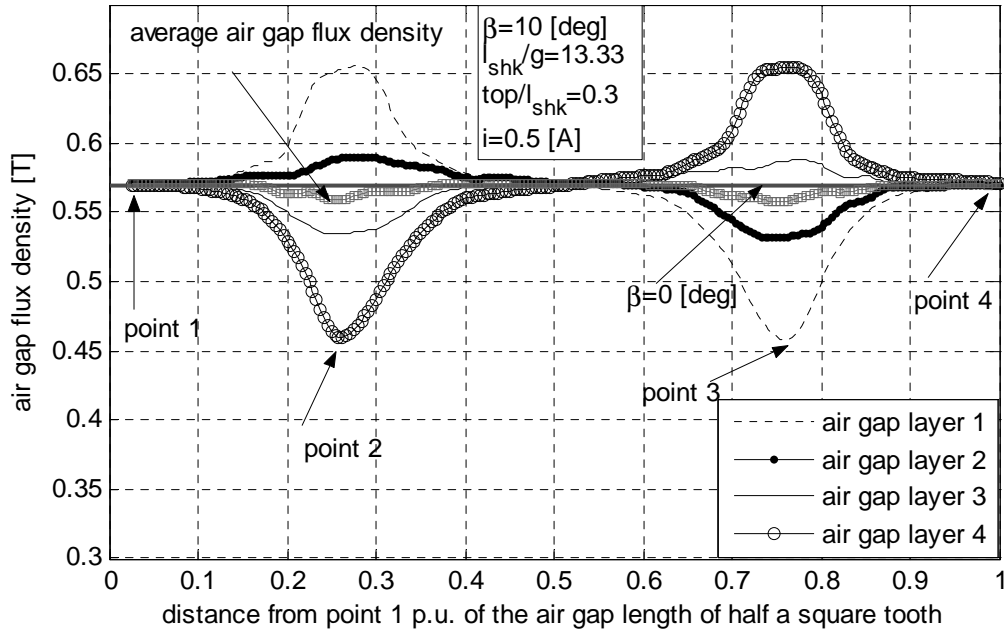


Fig.B.18 Flux density distribution in the trapezoidal air gap

**b) Influence of  $l_{shk}$  at constant  $\beta$**

This situation is illustrated in Fig.B.19, where two Shark teeth, with length and height modified as that  $\frac{h_{shk}}{l_{shk}} = const.$ , are shown.

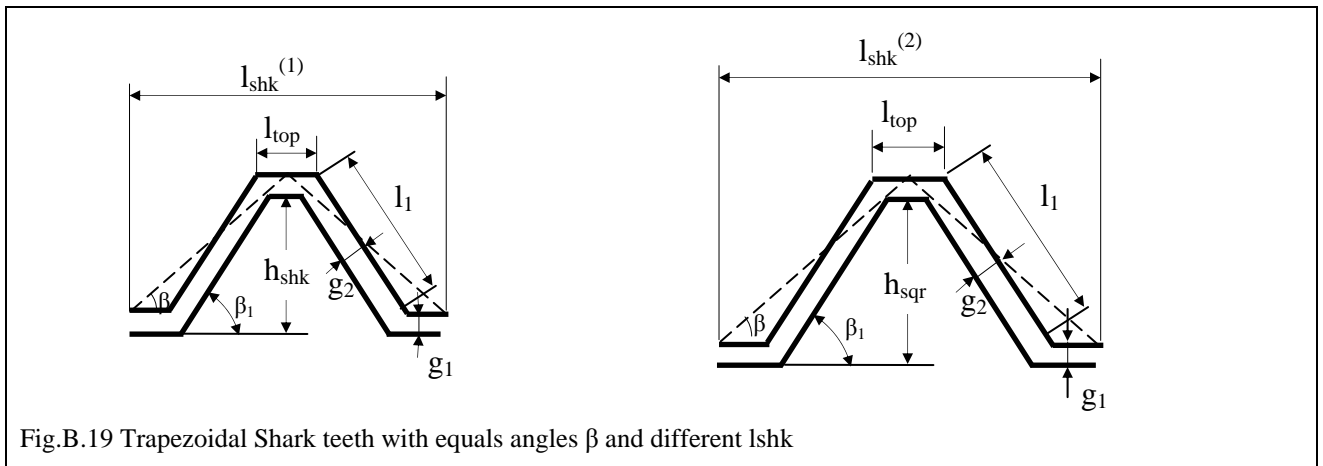


Fig.B.19 Trapezoidal Shark teeth with equal angles  $\beta$  and different  $l_{shk}$

The corresponding magnetisation characteristics are plotted in Fig.B.20 for  $\beta=40$ [deg] and different lengths of the Shark tooth. At long Shark teeth the magnetisation characteristic is above the characteristic of the reference machine for the whole range of current. Once the length of the Shark tooth decreases the magnetisation characteristics of the Shark SRM cross over the reference curve. The current at which the crossing happens is smaller for shorter teeth. This behaviour is similar to what was observed for the saw and for the square profiles.

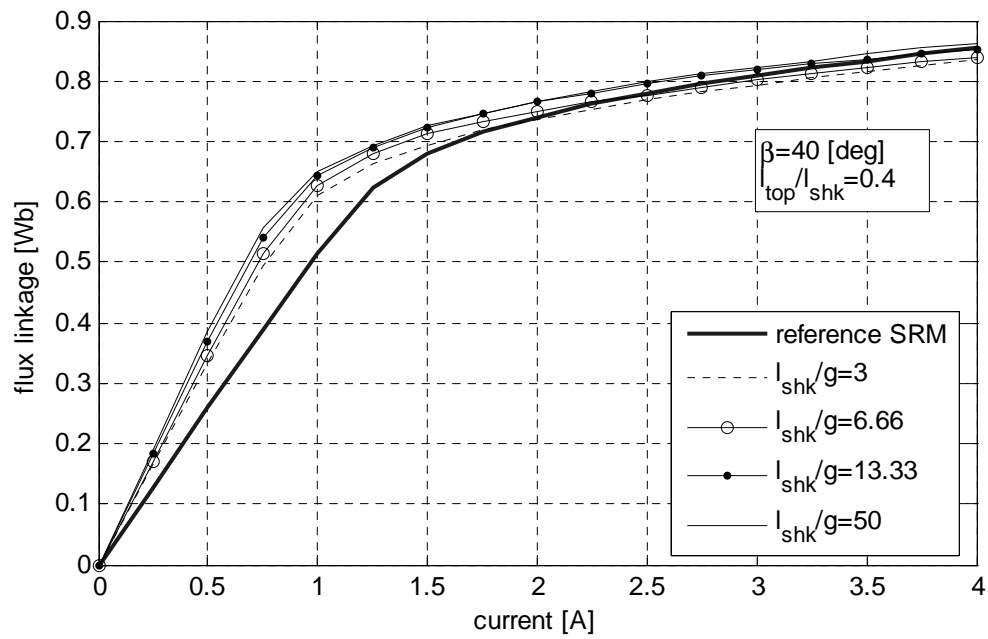


Fig.B.20 Magnetisation characteristics of the Shark SRM with trapezoidal air gap ( $I_{top}/I_{shk}=0.4$ )

## Appendix C

### Appendix C.1 Langevin function approach

The idea of this approach is to express the magnetisation characteristic of the Shark SRM by using the Langevin function [73]. The Langevin function is defined for modeling the BH curves of the magnetic materials [73], [74] and it expresses the magnetisation,  $M$ , as function of the saturation magnetisation,  $M_s$ , the effective magnetic field,  $H_e$  and a parameter,  $a$ , which characterises the shape of the BH curve. The expression of the function as given in [70] is:

$$M(H_e) = M_s \cdot \left( \coth\left(\frac{H_e}{a}\right) - \left(\frac{a}{H_e}\right) \right) \quad (\text{C.1})$$

where:  $H_e$  is the effective field intensity, which by the coefficient  $\alpha$  considers the interactions between the separate magnetic domains (for details see [74]),  $H_e = H + \alpha \cdot M$ .

In this approach, the flux linkage characteristic of the Shark SRM is expressed by using the Langevin function. The field variables in the Shark SRM are related to the field variables in the cylindrical air gap SRM (CSRSM) by the following procedure.

1. The flux linkage,  $\Psi$ , of the Shark SRM is expressed by the general equation:

$$\Psi(H_e) = \Psi_s \cdot \left( \coth\left(\frac{H_e}{a}\right) - \left(\frac{a}{H_e}\right) \right) \quad (\text{C.2})$$

where:  $H_e$  is the equivalent field intensity in the Shark SRM,  $\Psi_s$  is the saturation flux linkage and  $a$  is a parameter, which characterises the shape of the curve.

In order to obtain the dependence of the flux linkage on the phase current the equivalent field intensity,  $H_e$ , has to be expressed function of the field intensity in the cylindrical air gap machine and the parameters of the magnetic circuit of the Shark SRM.

The equivalent field intensity,  $H_e$ , is expressed function of the field intensity in the CSRSM,  $H$ , and the actual flux linkage,  $\Psi$ , given by equation (C.2):

$$H_e = H + \alpha \cdot \Psi \quad (\text{C.3})$$

where  $\alpha$  and  $a$  are functions of both material properties and the dimensions of the Shark profile.

2. The initial values of the coefficients  $a$  and  $\alpha$  are estimated from the BH curve of the magnetic material used in analysis
3. The dependence of the coefficients  $a$ ,  $\alpha$  and  $\Psi_s$  on the dimensions of the Shark tooth and on the air gap length is determined based on a large amount of FEA data.

The resulted parameters account for both the properties of the magnetic material and the effect of the particular shape of the Shark air gap. From the described steps it results that this approach has two main drawbacks:

- a) These are that this approach uses the analytical expression for the BH curve, which proves do not be very accurate and requires knowledge of the coefficients which are material dependents.
- b) the data used to get the dependence on Shark parameters are provided by the FEA of the axial cross-section. The curve-fitting algorithm makes that this method is a combination of numeric and analytic calculations. Therefore, this approach is not suitable for calculation, because it requires too many empirical data.

### Appendix C.2 Calculation of the winding area

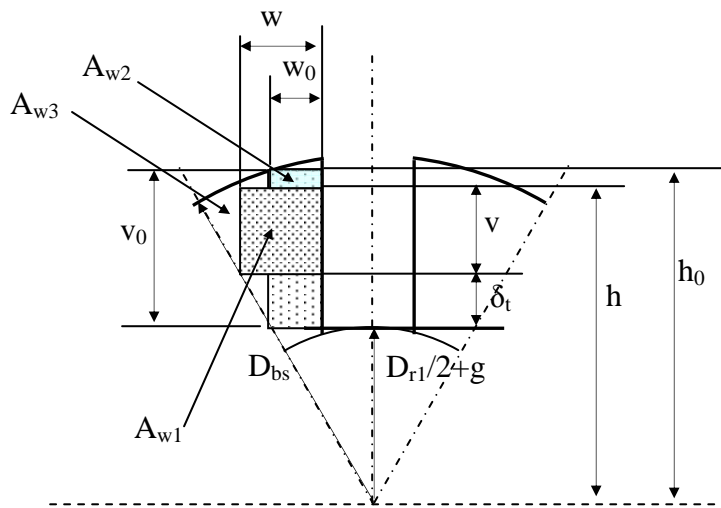


Fig.C.1 Illustration of the slot region

The initial winding area is:

$$A_{w0} = w_0 \cdot v_0 \quad (C.4)$$

The total winding area, of the machine having Shark air gap may be determined by

$$A_w = A_{w1} + A_{w2} + A_{w3} \quad (C.5)$$

where:



$$\begin{aligned}
 A_{w1} &= w \cdot v \\
 A_{w2} &= w_0 \cdot (h_0 - h) \\
 A_{w3} &= \frac{1}{2} \cdot \left( \alpha \cdot \frac{D_{bs}}{2} \right) \cdot \sqrt{v^2 - \left( \alpha \cdot \frac{D_{bs}}{2} \right)^2}
 \end{aligned} \tag{C.6}$$

The dimensions used in the above expression may be determined by;

$$w + \frac{p}{2} = \left( \frac{D_{r1}}{2} + g + \delta_t \right) \cdot \tan \left( \frac{1}{2} \cdot \frac{2 \cdot \pi}{N_s} \right) \tag{C.7}$$

$\delta_t$  – height of the Shark tooth

$$\begin{aligned}
 w &= \left( \frac{D_{r1}}{2} + g + \delta_t \right) \cdot \tan \left( \frac{1}{2} \cdot \frac{2 \cdot \pi}{N_s} \right) - \frac{p}{2} \\
 w_0 &= \left( \frac{D_{r1}}{2} + g \right) \cdot \tan \left( \frac{1}{2} \cdot \frac{2 \cdot \pi}{N_s} \right) - \frac{p}{2}
 \end{aligned} \tag{C.8}$$

$$h = \sqrt{\left( \frac{D_{bs}}{2} \right)^2 - w^2} \tag{C.9}$$

$$h_0 = \sqrt{\left( \frac{D_{bs}}{2} \right)^2 - w_0^2}$$

$$v = h - \left( \frac{D_{r1}}{2} + g + \delta_t \right) \tag{C.10}$$

$$v_0 = h_0 - \left( \frac{D_{r1}}{2} + g \right)$$

$\delta_t$  being equal to the height of the Shark tooth

$$\frac{N_{turns}}{N_{turns0}} = \frac{A_w}{A_{w0}} \tag{C.11}$$

**Appendix C.3 Verification of the analytical model of a 6/4 SRM**

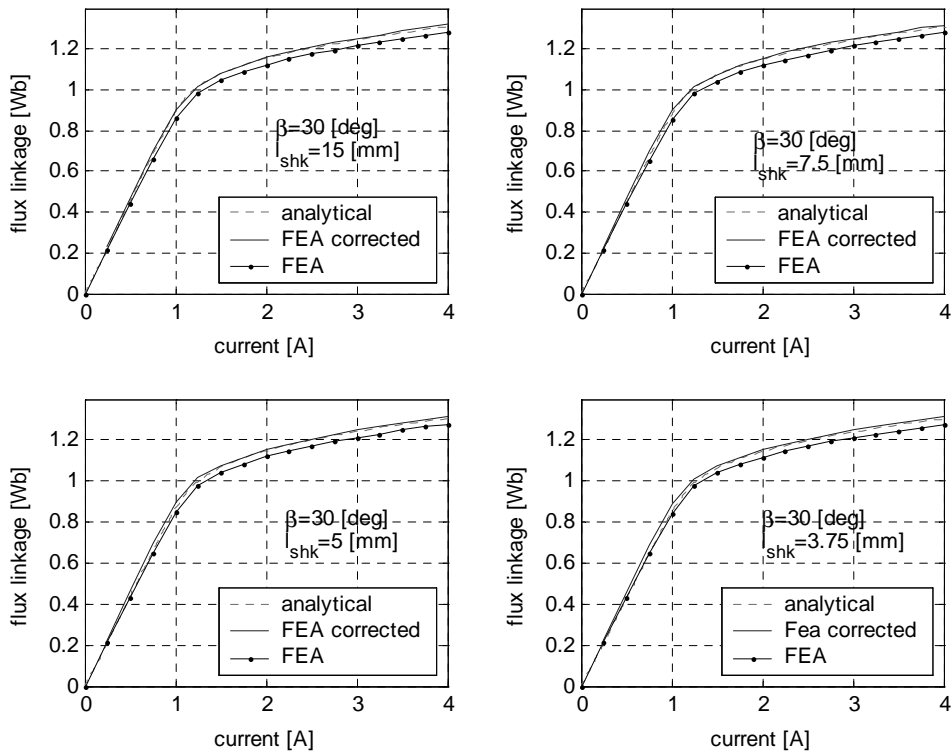


Fig.C.2 Magnetisation characteristics of Shark SRM, calculated by FEA and by analytical model

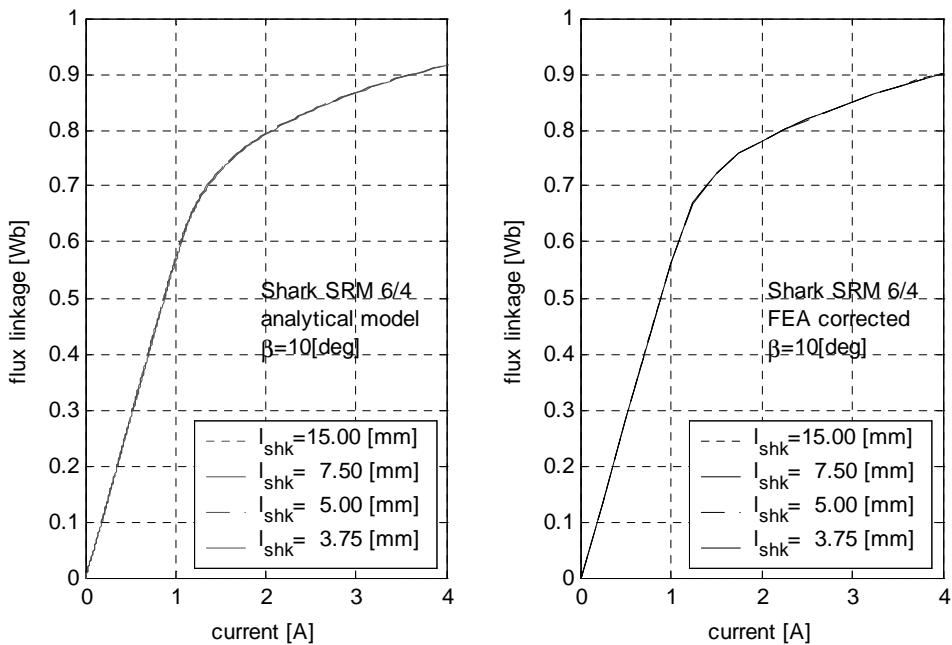


Fig.C.3 Magnetisation characteristics of Shark SRM, calculated by FEA and by analytical model

## Appendix C.4

### Verification of the analytical model for a 12/8 SRM

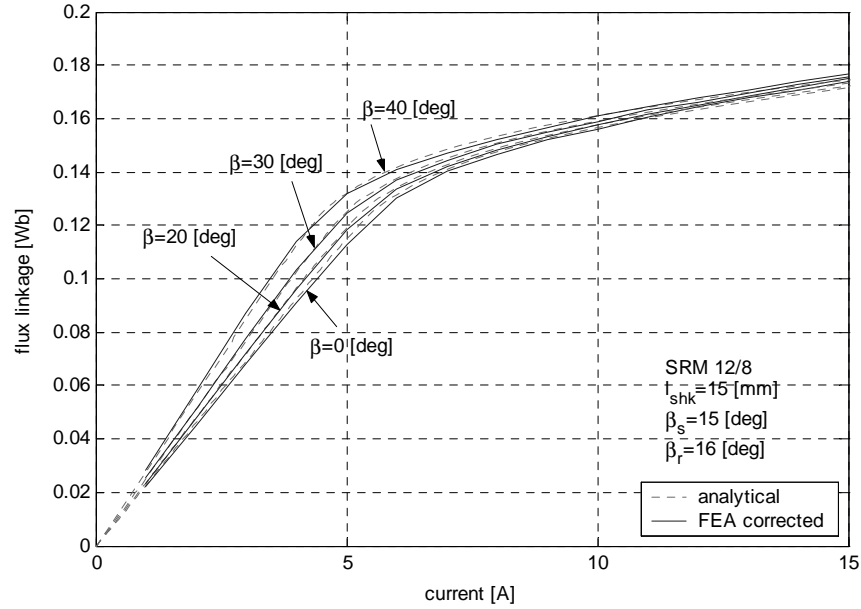


Fig.C.4 Magnetisation characteristics of Shark SRM, calculated by FEA and by analytical model, illustrating the influence of the angle  $\beta$

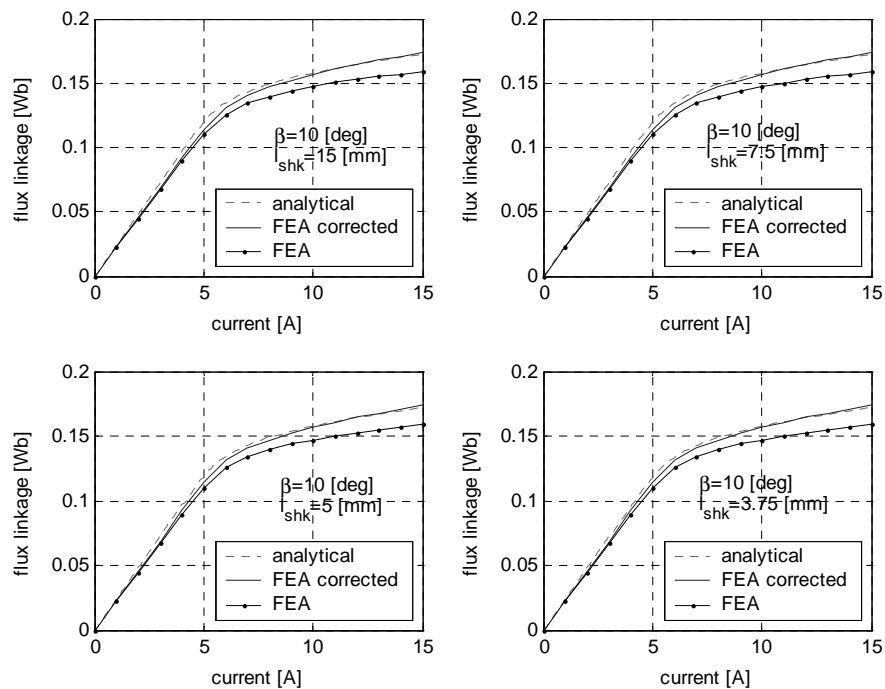


Fig.C.5 Magnetisation characteristics of Shark SRM, calculated by FEA and by analytical model, illustrating the influence of the Sharl tooth pitch,  $l_{shk}$

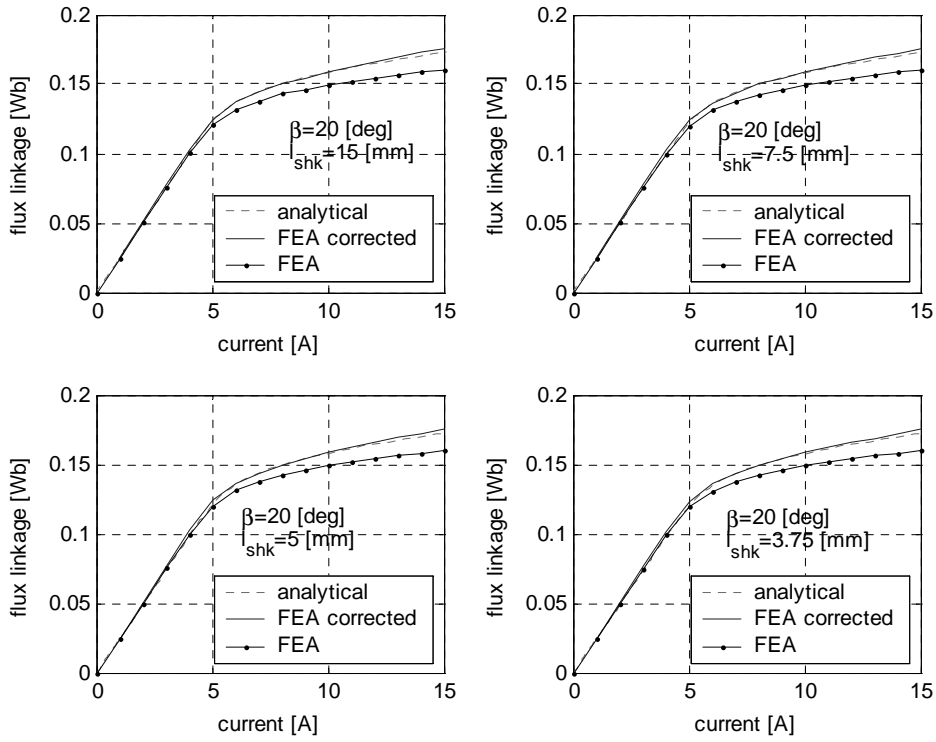


Fig.C.6 Magnetisation characteristics of Shark SRM, calculated by FEA and by analytical model

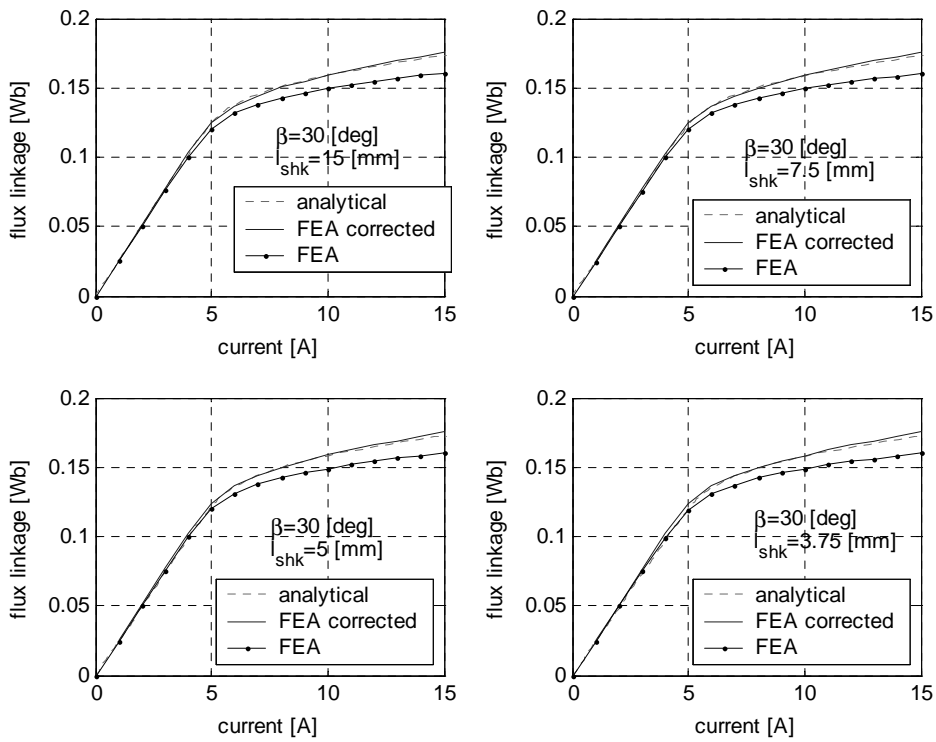


Fig.C.7 Magnetisation characteristics of Shark SRM, calculated by FEA and by analytical model

## Appendix C.5

### Permeance ratio

Permeance ratio determined for the CSRSM and Shark SRM with the dimensions given in Appendices A.2 and A.3. These ratio indicates which is the path preferred by the flux lines in the specified magnetic circuits

	CSRSM	Shark SRM
$P_1/P$	0.0038	0.0041
$P_2/P$	0.1042	0.1102
$P_3/P$	0.1989	0.1690
$P_4/P$	0.0834	0.0895
$P_5/P$	0.2382	0.2557

## Appendix C.6

**Illustration of the total radial and axial forces produced on each side of the Shark teeth at low and high current.**

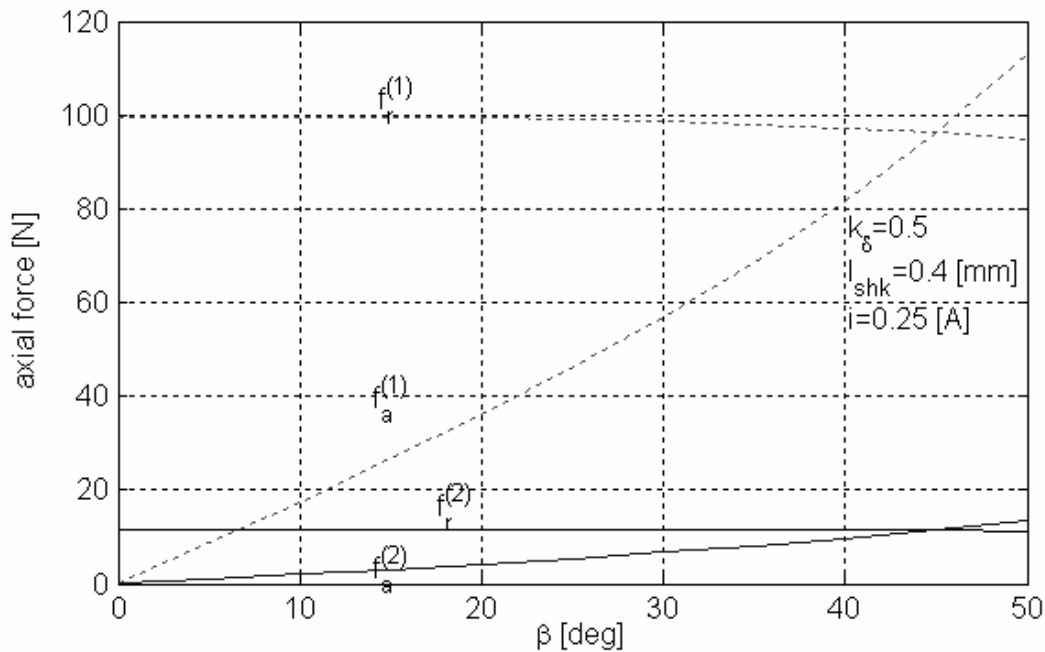


Fig.C.8 Radial and axial forces on the two sides of the Shark profile

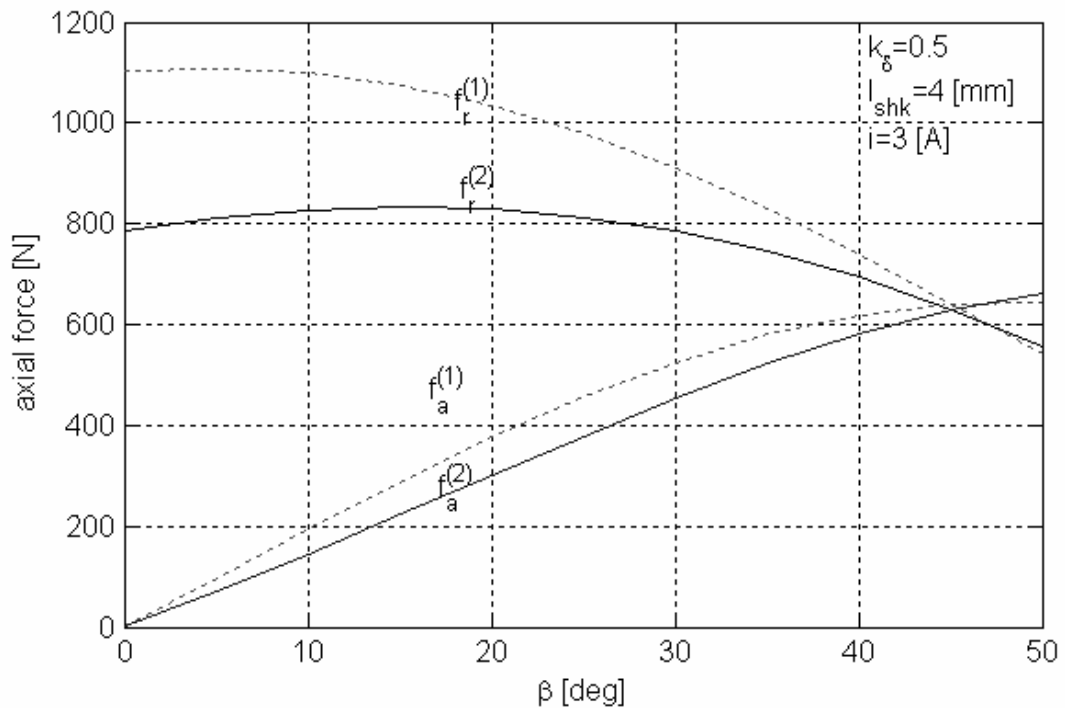


Fig.C.9 Radial and axial components on the two sides of the Shark profile

## Appendix D

### Appendix D.1

#### Estimation of the relative prices of different motor types

Assuming known the mass of the materials used in a specified motor ( $j$ ) the price may be determined by:

$$price^j = \sum_i a_i \times m_i^j \times pr_i \quad (D.1)$$

where  $i = Cu, Al, Fe, PM$ ,  $a_i = 1, 0$  if material  $i$  is or not used the motor  $j$ ,  $m_i^j$  is the mass of material  $i$  used in motor  $j$ , and  $pr_i$  is the price of material  $i$ .

The prices of different material are expressed function of iron price,  $pr_{Fe}$ , as following:

$$pr_i = K_i \times pr_{Fe}, \text{ with } K_{Fe} = 1 \quad (D.2)$$

With this definition, the expression of the cost of material used in a motor becomes:

$$price^j = \sum_i a_i \times m_i^j \times K_i \times pr_{Fe} \quad (D.3)$$

---

## References

- [1] P.O.Rasmussen, F.Blaabjerg, J.K.Pedersen, J.Jensen, "Switched Reluctance-Shark Machine - More torque and less acoustic noise", Industry Applications Conference, 2000. Conference Record of the 2000 IEEE , Volume: 1 , 8-12 Oct. 2000, Page(s): 93 -98 vol.1.
- [2] J.Y.Lim, H.S.Kim, J.Y.Oh, D.H.Cheong, J.C. Kim, "A performance of Single Phase Switched Reluctance Motor having both Radial and Axial air gap", Industrial Electronics Society, 1998. IECON '98. Proceedings of the 24th Annual Conference of the IEEE , Volume: 2 , 31 Aug.-4 Sept. 1998 , Page(s): 905 -910 vol.2.
- [3] S.P.Randall, UK Patent Application: GB 2315607 A, 04.02.1998, Switched Reluctance Drives Limited, United Kingdom.
- [4] Backhaus, Rolf, P42 14 038.2, 22 april 1993, Deutsches patentamt.
- [5] Woodward, Richard,.C. Jr, US patent PCT/US95/09737, 15 feb. 1996.
- [6] Davenport, Norban, Earl, US patent PCT/US95/08846, 8 feb. 1996.
- [7] "Energy-saving motors", European agreement,  
<http://www.schorch.de/news/downloads/EFF1.pdf> .
- [8] Paolo Bertoldi, Anibal T. de Almeida, Hugh Falkner, 'Energy efficiency improvements in electric motors and drives', Berlin, Springer, 2000.
- [9] Herbert Auinger, Sabine Stengel, "Classified according to efficiency", Siemens Drive Switch & Control, pp14-15, nr. 4, 1999.
- [10] Claus. B. Rasmussen, "Modelling and Simulation of Surface Mounted PM Motors, PhD thesis, Aalborg University, ISBN 87-89179-15-3, 1996.
- [11] Nema Premium Efficiency Electric Motor program, <http://www.nema.org>
- [12] M.Mikkelsen, "Sparemotorer er godt-men E-motorer er ofte meget bedre".  
<http://www.grundfos.com/web/homeDK.nsf/Webopslag/40CFE172D3876593412565AE003B1137>.
- [13] I.E.Chabu, S.I.Nabeta, J.R.Cardoso, "Design Aspects of 4:2 Pole- 2 Phase Switched Reluctance Motors", Electric Machines and Drives, 1999. International Conference IEMD '99 , 9-12 May 1999, Page(s): 63 -65.
- [14] H.C. Lovatt, J.M. Stephenson, "Influence of Number of Poles per Phase in switched Reluctance Motors", IEE Proced-B, vol 139, no. 4, pp307-314, july 1992.
- [15] C.Neagoe, A.Foggia, R.Krishnan, "Impact of Pole Tapering on the Electromagnetic Torque of the Switched Reluctance Motor", Electric Machines and Drives Conference Record, 1997, IEEE International , 18-21 May 1997, Page(s): WA1/2.1 -WA1/2.3.



- [16] T.J.E. Miller, "Brushless Permanent-Magnet and Reluctance Motor Drives", Clarendon Press, Oxford Science Publication, 1989.
- [17] J.A.Kline 'Opportunities for Switched Reluctance Motor-Drives', Record of 1999 Annual Pulp and Paper Industry Technical Conference, Seattle, WA, USA, 21 - 25 June, 1999, pp 42 - 47.
- [18] K.Atallah, F. Caparelli, C.M.Bingham, P.H. mellor, D. Howe, C. Cossar, L. Kelly, P.Kjaer, J.Gribble, T.J.E Miller, R. Capewell, C. Whitley, "Comparison of Electrical Drive Technologies for Aircraft Flight Control Surface Actuation", Proceedings of EMD '99, the 9th International Conference on Electrical Machines and Drives, IEE Conference Publication No. 468, Canterbury, UK, 1 - 3 September, 1999, pp 159 - 163.
- [19] Iqbal Husain, M.N.Anwa, 'Fault Analysis of Switched Reluctance Motor Drives', Proceedings of IEMDC '99, IEEE International Electric Machines and Drives Conference, Seattle, WA, USA, 9 - 12 May, 1999, pp 41 - 43.
- [20] T.Sawata, P. Kjaer, C.Cossar, T.J.E.Miller, Y.Hayashi, 'Fault-tolerant Operation of Single-Phase Switched Reluctance Generators', Proceedings of APEC '97, IEEE 12th Annual Applied Power Electronics Conference and Exposition, Atlanta, GA, USA, 23 - 27 February, 1997, Vol. 1, pp 553 - 558.
- [21] Jack A.G, Mecrow B.C, 'Safety Critical Drives for Aerospace applications', Proceedings of ICEM '94, International Conference on Electrical Machines, Paris, France, 5 - 8 September, 1994, Vol. 1, pp 91 - 96.
- [22] Stephenson, J.M.; Hughes, A.; Mann, R., 'Online torque-ripple minimisation in a switched reluctance motor over a wide speed range', Electric Power Applications, IEE Proceedings- , Volume: 149 Issue: 4 , July 2002, Page(s): 261 –267.
- [23] Cheng-Tsung Liu, Yan-Nan Chen, Ming-Huei Lee, Yue-Jen Lee, 'Operational Characteristics of a Zero-Torque Linear Switched-Reluctance Machine for Magnetic levitation and propulsion System', Conference Digest of INTERMAG '97, 35th IEEE International Magnetics Conference, New Orleans, LA, USA, 1 - 4 April, 1997, Paper BR-08.
- [24] El-Khazendar, 'A Battery-supplied traction drive for electric vehicles', Proceedings of ICEM '94, International Conference on Electrical Machines, Paris, France, 5 - 8 September, 1994, Vol. 1, pp 226 - 231.
- [25] K.H.Rahman, B.Fahimi, G. Uresh, A.V.Raharathnam, M.Ehsani, 'Advantages of Switched Reluctance Motor Application to EV and HEV: Design and Control Issues', Conference Record of IAS '98, the 1998 IEEE Industry Applications Society 33rd Annual Meeting, St. Louis, MO, USA, 12 - 15 October, 1998, Vol. 1, pp 327 - 334.
- [26] J.M.Miller, A.R.Gale, P.J.McCleer, F.Leonardi, J.H.Lang, 'Starter-Alternator for Hybrid Electric Vehicle: Comparison of Induction and Variable Reluctance Machines and Drives', Conference Record of IAS '98, the 1998 IEEE Industry Applications Society 33rd Annual Meeting, St. Louis, MO, USA, 12 - 15 October, 1998, Vol. 1, pp 513 - 524.

- [27] J.G.W.West, 'DC, Induction, Reluctance and PM Motors for Electric Vehicles', IEE Colloquium on 'Motors and drive systems for battery powered propulsion', 15<sup>th</sup> April 1993.
- [28] L.Chang, 'Control of a Switched Reluctance Motor for Automotive Applications', Proceedings of CCECE '98, 11th IEEE Canadian Conference on Electrical and Computer Engineering, Waterloo, ON, Canada, 24 - 28 May, 1998, Vol. 1, pp 393 - 396.
- [29] S.K.Mondal, S.N.Bhadra, S.N.Saxena, 'Application of current-source converter for use of SRM Drive in transportation area', Proceedings of PEDS '97, the 2nd IEEE International Conference on Power Electronics and Drive Systems, Singapore, 26 - 29 May, 1997, Vol. 2, pp 708 - 713.
- [30] N.Abut, B.Cakir, U.Akca, N.Erturk, 'Fuzzy control applications of SR Motor Drive for Transportation Systems', Proceedings ITSC '97, the IEEE Conference on Intelligent Transportation System, , 9 - 12 November, 1997, pp 135 - 140.
- [31] D.A.Torrey, S.E.Childs, S de Haan, 'A Variable-Speed Wind Turbine Based on a Direct-Drive Variable-Reluctance Generator', Proceedings of Windpower '94, Minneapolis, MN, USA, May, 1994, pp 513 - 522.
- [32] I.Haouara, A.Tounzi, F.Piriou, ' Study of a Variable Reluctance Generator for Wind Power Conversion', Proceedings of EPE '97, 7th European Conference on Power Electronics and Applications, Trondheim, Norway, 8 - 10 September, 1997, Vol. 2, pp 631 - 636.
- [33] R. Cardenas, W.F.Ray, G.M.Asher, 'Switched Reluctance Generators for wind Energy Applications', PESC '95 Record. 26th Annual IEEE Power Electronics Specialists Conference, Atlanta, USA, 18 - 22 June, 1995, Vol. 1, pp 559 - 564.
- [34] H.M.B. Metwally, W.R.Anis, 'performance Analysis of PV Pumping Systems using Switched Reluctance Motor Drives', Energ. Convers. Mgmt, vol. 38, no.1 pp 1-11, 1997, Elsevier Science Ltd, ISBN 0196-8904/97.
- [35] C.A Ferreira, S.R.Jones, B.T.Drager, W.S.Heglund, 'Design and Implementation of a Five Horsepower, Switched Reluctance Fuel-Lube, Pump Motor Drive for a Gas Turbine Engine', IEEE Transactions on Power Electronics, Vol. 10, No. 1, January, 1995, pp 55 - 61.
- [36] T.L Skvarenina, S.Pekarek, O.Wasynczuk, P.C. Krause, 'Simulation of Switched Reluctance, More Electric Aircraft Power System using a Graphical User Interface', Proceedings of IECEC '96, IEEE 31st Intersociety Energy Conversion Engineering Conference, , 11 - 16 August, 1996, Vol. 1, pp 143 - 147.
- [37] J.S.Cloyd, 'A Status of the United States Air Force's More Electric Aircraft Initiative', Proceedings of IECEC '97, IEEE 32nd Intersociety Energy Conversion Engineering Conference, , 27 July - 1 August, 1997, Vol. 1, pp 681 - 686.
- [38] Gregory.L.Fronista, 'An Electromechanical Actuator for a Transport Aircraft Spoiler surface', Proceedings of IECEC '97, IEEE 32nd Intersociety Energy Conversion Engineering

- Conference, , 27 July - 1 August, 1997, Vol. 1, pp 694 - 698.
- [39] T.J.E Miller, 'Optimal Design of switched Reluctance Motors', IEEE Transactions on Industrial Electronics, Vol. 49, No. 1, February, 2002, pp 15 - 27.
- [40] P.O.Rasmussen, "Design and Advanced Control of switched Reluctance Motors", PhD thesis, Aalborg University, Denmark, january 2002, ISBN 87-89179-40-4.
- [41] [http://www.srdrives.com/fr\\_index.htm](http://www.srdrives.com/fr_index.htm).
- [42][http://www.emotron.se/emotron/common\\_objects.nsf/framesets/index?opendocument](http://www.emotron.se/emotron/common_objects.nsf/framesets/index?opendocument).
- [43] R.J.Babiyak, 'Clean solution – LGE adapts SR technology for vacuum cleaners', Appliance manufacturers, pp 48, september, 2001.
- [44] T.J.E Miller, 'Switched Reluctance Motors and their Control', Magna Physics publishing ISBN 1-881855-02-3, Clarendon Press, Oxford.,1993, OUP ISBN 0-19-859387-2.
- [45] J.V.Byrne, J.G.Lacy, ' Characteristics of saturable stepper and reluctance motors', Proceedings of IEE Conf. on Electrical Machines and Drives, London, 1982, pp93-95.
- [46] J.M. Stephenson, M.A. El-Khazendar, 'Saturation in doubly salient reluctance motors', IEE Proceedings, vol 136, Pt.B, No.1, january 1989.
- [47] Yue Li; Lloyd, J.D.; Horst, G.E.; 'SRM with DC Assisted Excitation', Industry Applications Conference, 1996. Thirty-First IAS Annual Meeting, IAS '96., Conference Record of the 1996 IEEE , Volume: 2 , 6-10 Oct. 1996, Page(s): 801 -807 vol.2 .
- [48] Oyama, J.; Higuchi, T.; Abe, T.; Koga, T.; "Efficiency and power-factor of novel hybrid type switched reluctance motor", Industry Applications Conference, 2002. 37th IAS Annual Meeting. Conference Record of the , Volume: 1 , 13-18 Oct. 2002, Page(s): 1 -5 vol.1.
- [49] Torok, V., Loreth, K., "The world's simplest motor for variable speed control? The Cyrano motor, a PM-biased SR-motor of high torque density", Power Electronics and Applications, 1993., Fifth European Conference on , 13-16 Sep 1993Page(s): 44 -45 vol.6.
- [50] A.J.Hutton, T.J.E.Miller,"Use of flux screens in switched reluctance motors", Electrical Machines and Drives, 1989. Fourth International Conference on, 13-15 Sep 1989, Page(s): 312 –316.
- [51] HorstG.A., "Isolated segmental Switched Reluctance Motor", United States patent Nr.5,111,096, 5 may 1992.
- [52] Mecrow, B.C.; Finch, J.W.; El-Kharashi, E.A.; Jack, A.G.; "Switched reluctance motors with segmental rotors ", Electric Power Applications, IEE Proceedings, Volume: 149 Issue: 4 , July 2002 , Page(s): 245 –254.
- [53] Vlado Ostovic, "Dynamics of Saturated Electric Machines", 1989, Springer Verlag, Berlin

Heidelberg New York, ISBN 3-540-97079-7.

- [54] Vector Field, User Guide –ver. 7.5.
- [55] Courant, R., "Variational Methods for the Solution of Problems of Equilibrium and Vibration", Bull. Am. Math. Soc., vol. 49, pp. 1-43, 1943
- [56] R.P. Deodhar, 'The Flux-MMF Diagram Technique and its Applications in Analysis and Comparative Evaluation of Electrical Machines', Ph.D thesis, Univ of Glasgow, 1996.
- [57] A.M.Michaelides, C. Pollock, 'Effect of end core flux on the performance of the switched reluctance motor', IEE Proc-Electr. Power appl., vol 141, no 6, nov.1994.
- [58] A.B.J. Reece, T.W. Preston, 'Finite Element Methods in Electrical Power Engineering', Oxford University Press, 2000.
- [59] Henneberger, G., Kuppers, S., 'Field calculation and dynamic simulation of a claw-pole alternator', Electrical Machines and Drives, 1995, 7<sup>th</sup> International Conference on (Conf. Publ. No.412), 11-13 Sep. 1995, Page(s): 286 –290.
- [60] Guo, Y.G., Zhu, J.G., Watterson, P.A., Wu, W. 'Comparative study of 3D flux electrical machines with soft magnetic composite cores', Industry Applications Conference, 2002. 37th IAS Annual Meeting. Conference Record of the, Volume :2, 13-18 Oct.2002 , Page(s): 1147 -1154 vol.2.
- [61] J.Corda, A.M. Tataru, P.O. Rasmussen, E. Ritchie, ' Analytical estimation of torque enhancement of the SR machine with saw-shaped (shark) pole surfaces', IEE Proc-Electr. Power Appl., vol. 151, No 2., march 2004.
- [62] T.J.E. Miller, M. McGilp, 'Nonlinear theory of the switched reluctance motor for rapid computed-aided design', Electric Power Applications, IEE Proceedings Volume: 137 6 , Nov. 1990 , Page(s): 337 –347.
- [63] P.Materu, R.Krishnan, 'Analytical Prediction of SRM Inductance Profile and Steady-State Average Torque' Torque", Industry Applications Society Annual Meeting, 1990, Conference Record of the 1990 IEEE , 1990 , Page(s): 214 -223, vol.1.
- [64] A.Radun, "Analytical Calculation of the Switched Reluctance Motor's Unaligned Inductance", IEEE Trans. on Magnetics, vol. 35, no.6, pp.4473-4481, nov.1999.
- [65] T.J.E.Miller, M.Glinka, M.McGilp, C.Cossar, G.Gallegos-Lopez, D.Ionel, M.Olaru, 'ultra-fast Model of Switched Reluctance Motor', Industry Applications Conference, 1998. Thirty-Third IAS Annual Meeting. The 1998 IEEE, Volume: 1 , 1998 , Page(s): 319 -326 vol.1.
- [66] Y.Tang, 'Characterization, Numerical Analysis and Design of switched Reluctance Motor for Improved Material productivity and Reduced Noise', Industry Applications Conference, 1996. Thirty-First IAS Annual Meeting, IAS '96, Conference Record of the 1996 IEEE,

Volume: 2 , 1996 , Page(s): 715 -722 vol.2.

- [67] A. Michaelides, C. Pollock, C. Jolliffe, 'Analytical computation of Minimum and Maximum Inductances in Single and Two phase Switched Reluctance Motors' motor", IEE Proc.-Electr. Power Appl, vol. 141, no.6, pp. 308-316, 1994.
- [68] J. Corda, M. Stephenson, 'Analytical Estimation of the Minimum and Maximum Inductances of a Double-Salient Motor', Proceeding of the International Conf. On Stepping Motors and Systems, Univ. Leeds, pp.50-59, sept. 1979.
- [69] Byrne, J.V, Lacy, J.G., 'Characteristics of saturable stepper and reluctance motors', IEE Conference on Small Electrical Machines, London, UK, CP136, pp 93-96.
- [70] Byrne J.V., 'Tangential forces in overlapped pole geometries incorporating ideally saturable material, IEEE Trans., 1972, MAG-8, (1), pp. 2-9.
- [71] Byrne J.V., O'Dwyer J.B. 'Saturable Variable Reluctance Machine Simulation Using Exponential Functions', Proceed. of the International conference on Stepping Motors and Systems, Univ. of Leeds, July 1976, pp 11-16.
- [72] Carter F.W. 'The magnetic field of the dynamo-electric machine', pp. 1115-1138.
- [73] M. Langevin, Ann de Chem. et Phys. 5 (1905) 70.
- [74] D.C. Jiles, 'Theory of Ferromagnetic Hysteresis', Journal of Magnetism and Magnetic Materials, 61 (1986), pp 48-60, Amsterdam, Holland.
- [75] Chi-Yao Wu, C. Pollock, 'Analysis and reduction of vibration and acoustic noise in the switched reluctance drives', Proceedings of IAS'95, vol.1, pp.448-455, 1995.
- [76] G.E. Horst, 'Noise reduction in a switched reluctance motor by current profile manipulation', US patent 5.461.295, oct. 1995.
- [77] A. Michaelides, C. Pollock, 'Reduction of noise and vibration in switched reluctance motors: new aspects', Proceedings of IAS'96, vol 2, pp 771-778, 1996
- [78] F.W. Carter, 'Note on air gap and interpolar induction', IEE Journal, 1900, vol. 29, pp. 925-932.
- [79] K.C. Mukherji, S. Neville, 'Magnetic permeance of identical double slotting – Deduction from analysis by F.W. Carter', Proc. IEE, vol.118, no.9, pp. 1257-1264 september 1971.
- [80] M.A. Mueller, 'Switched Reluctance Machine with Rotor Skew', Proceed. of ICEM'98, vol.3, pp.1680-1685, 1988.
- [81] Byrne J.V., 'Tangential forces in overlapped pole geometries incorporating ideally saturable material, IEEE Trans., 1972, MAG-8, (1), pp. 2-9.

- [82] Per Sandholdt, 'Modeling and Test of Electrical Drive Systems ', ISBN 87-89179-38-2, Aalborg University, Denmark, june 2001.
- [83] Simovert manual.
- [84] Y. Hayashi, The Miller, 'A new approach to calculating core losses in the SRM'.
- [85] PN Materu, R. Krishnan, 'Estimation of Switched Reluctance Motor Losses', IEEE Trans Ind. Appl. , vol 28, no. 3, pp 668-679, may/june 1992.
- [86] J.Reinert, R. Inderka, R.W. De Doncker, , 'A novel method for the prediction of losses in switched reluctance machines', EPE'97, Trondheim, pp. 3.608-3.612.
- [87] J. R. Hendershot, Jr, 'Brushless DC Motors without permanent magnets', Integrated Engineering software, [http://www.integratedsoft.com/papers/techdocs/tech\\_6mx.pdf](http://www.integratedsoft.com/papers/techdocs/tech_6mx.pdf), pp, 1-13.
- [88] A. Boglietti, A Cavagnino, M. Lazzari, M.Pastorelli, 'Predicting iron losses in soft magnetic materials with arbitrary voltage supply: an engineering approach', IEEE Trans. On Magn., vol. 39, n0. 2, pp. 981-989, march 2003.
- [89] Th. Durbaum, A. Brockmeyer, 'Calculating core losses in transformers for arbitrary magnetizing currents. A comparison approach of different approaches', pp. 1463-1468.
- [90] J.Reinert, A. Brockmeyer, RW.A De Doncker, , 'Calculation of losses in ferro- and Ferrimagnetic materials based on the modified Steinmetz equation', Industry Applications, IEEE Transactions on , Volume: 37 , Issue: 4 , July-Aug. 2001, pp.1055 – 1061.
- [91] MR Harris, TJE Miller, 'Comparison of design and performance parameters in Switched Reluctance and Induction Motors', Electrical Machines and Drives, 1989. Fourth International Conference on, 13-15 Sep 1989, pp.303 – 307.
- [92] S. Huang, J- Luo, F. Leonardi, TA.Lipo, ,A general approach to sizing and power density equation for comparison of electrical machines', IEEE Trans. on Ind. Appl., vol. 34, no. 1, pp. 92-97, jan/feb 1998.
- [93] HC Lovatt, ML. McClelland, JM. Stephenson, 'Comparative performance of singly salient reluctance, switched reluctance and induction motors', Electrical Machines and Drives, 1997, pp 361-365, 1-3 sept 1997.
- [94] R.Krishnan, 'Criteria for the comparison of motor drive systems in motion control', Intelligent Control and Instrumentation, 1992. SICICI '92. Proceedings., Singapore International Conference on , Volume: 1 , 17-21 February 1992 , pp.127 – 133.
- [95] R.Krishnan, AS Bharadwaj, 'A comparative study of various motor drive systems for aircraft applications', IAS 1991,vol.1, pp. 252-258, 28 sep 1991.

- [96] F. Abrahamsen, 'Energy Optimal Control of Induction Motor Drives', ISBN 87-89179-26-9, Aalborg University, Denmark, feb.2000.
- [97] H.C. Lovatt, M.M. Clelland, J.M. Stephenson, "Comparative performance of singly Salient Reluctance, Switched Reluctance and Induction Motors", EMD'97, Conf. Proc., pp. 361-365, 1-3 sept, 1997.
- [98] P.O Rasmussen, G. Andersen, L. Helle, F. Blaabjerg, J.K. Pedersen, 'Fully Automatic Characterization System for Switched Reluctance Motor', ICEM'98, vol.3, pp. 1692-1698, Istanbul, Turkey.
- [99] S. Huang, J- Luo, F. Leonardi, TA.Lipo, 'A comparison of Power Density for Axial Flux Machines Based on General Purpose Sizing equations', IEEE Trans. on Energy. Conversion, vol. 14, no. 2, pp. 185-192, june 1999.
- [100] T.J.E. Miller, 'Converter requirements of the switched reluctance drive', IEEE Trans. on Industry Applications, vol. IA-21, no. 5, sept/oct, 1985, pp. 1136-1144.
- [101] S. J. Salon, 'Finite element analysis of electrical machines', Boston: Kluwer Academic Publishers, 1995.
- [102] IEC Standard 60034-2: Rotating electrical machines. Part2: Methods for determining losses and efficiency of rotating electric machinery from test (excluding machines for traction vehicles), bureau Central de la Commission Electrotechnique Internationale, Geneve, Suisse, 1972.
- [103] P.C. Kjaer, P. Nielsen, L. Andersen, F. Blaabjerg, 'New energy optimizing control strategy for switched reluctance motors', IEEE Trans. on Industry Applications, vol. 31, no.5, pp 741-747, 1995
- [104] Roger C. Beccera, mehrdad Ehsani, Timothy J.E. Miller, 'Commutation of SR Motors', IEEE Trans. on Power Electronics, vol.8, no.3, pp. 257-263, july 1993
- [105] D.A. Torrey, J.H.Lang, ' Optimal-efficiency excitation of variable-reluctance motor drives', IEE Proceeding-B, vol. 138, no. 1, pp. 1-14, january 1991.
- [106] F.J.Bartos, 'Forward to the Past' with SR Technology, Control Engineering, june 2002.
- [107] A.G. Jack, B.C. Mecrow, J. Haylock, 'A Comparative study of permanent magnet and switched reluctance motors for high performance fault tolerant applications', Industry Applications, IEEE Transactions on, Volume: 32 , Issue: 4 , July-Aug. 1996, pp. 889 – 895.
- [108] D.E. Cameron, J.H. Lang, S.D. Umans, 'The origin and reduction of acoustic noise in doubly salient variable-reluctance motors', IEEE trans. on Industry Applications, vol. 28, no. 6, pp.1250-1255, Nov-Dec. 1992.
- [109] Chi-Yao Wu, C. Pollock, 'Analysis and reduction of vibration and acoustic noise in the

- switched reluctance drive', IEEE trans. on Industry applications, no.1, pp. 91-98, January-February, 1995.
- [110] A. Michaelides, C. Pollock, 'Reduction of noise and vibration in switched reluctance motors: new aspects', Industry Applications Conference, 1996. Thirty-First IAS Annual Meeting, IAS '96, Conference Record of the 1996 IEEE , Volume: 2 , 6-10 Oct. 1996, pp.771 – 778, vol.2.
- [111] Serope Kalpakjian, 'Manufacturing engineering and technology', 3<sup>rd</sup> edition, 1998, Addison-Wesley Publishing Company, ISBN 0-201-84552-0.
- [112] Ivana Suchy, 'Handbook of Die design', McGraw-Hill, 1998, ISBN 0 –07-066671-7.
- [113] <http://www.gordonenglang.co.uk/hardness>.
- [114] AKSteel, 'Selection of Electrical Steel for Magnetic Cores', product data bulletin, 2000.
- [115] 'Laser beam vs. Water Jet Machining', [http://www.teskolaser.com/waterjet\\_cutting.html](http://www.teskolaser.com/waterjet_cutting.html).
- [116] Hiroyuki Akita, Yuji Nakahara, Nobuaki Miyake, Tomoaki Oikawa, 'New Core Structure and Manufacturing Method for High Efficiency of Permanent Magnet Motors', IAS 2003, Salt lake City, Utah, oct 12-16,2003.
- [117] D.W.J.Pulle, 'Performance of split-coil switched reluctance drive', IEE Proceedings, vol135, Pt. B, no.6, november 1988
- [118] Dirk Alexander philips, 'Switched Reluctance Drives: New Aspects', IEEE transaction on Power Electronics, vol. 5, no. 4, october 1990
- [119] Yuefeng Liao, Feng Liang, Thomas A. Lipo, 'A Novel Permanent Motor with Doubly Salient Structure', Industry Applications, IEEE Transactions on , Volume: 31 , Issue: 5 , Sept.-Oct. 1995, Pages:1069 - 1078
- [120] Y.G.Desouky, B.W.Williams, J.E. Fletcher, 'Conducting screen utilization in switched reluctance motors', IEEE Transaction on Energy Conversion, vol. 14., no. 4, december 1999
- [121] R. Hamdy, J.E. Fletcher, B.W. Williams, S.J. Finney, 'High-Speed Improvements of a Two-Phase Switched Reluctance Machine Utilizing Rotor-Conducting Screens', IEEE Transaction on energy conversion, vol. 17. no. 4 december 2002





## Publications

1. 'Shark motor. Analysis of the basic tooth shape', A.M Tataru, P.O. Rasmussen, E. Ritchie, Summer seminar on Nordic Network for MultiDisciplinary Optimized Electric Drives 2001, pp 20-24, june 15-17 2001, Hals, Denmark
2. 'Analytical calculation of the aligned inductance of a Shark SRM', Ana-Mari Tataru, Ewen Ritchie, Peter Omand Rasmussen, Proceeding of 15<sup>th</sup> Int. Conf. on Electrical Machines ICEM2002, august 25-28 2002, Brugge, Belgium
3. 'Saturation in doubly salient Shark Reluctance Motor', Ana-Mari Tataru, Ewen Ritchie, Peter Omand Rasmussen, Proceeding of PEDS 2003, oct. 12-16 2003, Singapore
4. 'Torque enhancement in non-cylindrical air gap switched reluctance motor (Shark motor )', J.Corda, A.M.Tataru, P.O.Rasmussen, E. Ritchie, IEE Proceeding 2004